

STAVEBNÍ OBZOR

číslo 3/2020



Obsah:

24	COMPARATION OF THE ECONOMIC CYCLE ON LABOUR MARKET IN THE CONSTRUCTION INDUSTRY AND IN THE NATIONAL ECONOMY OF THE CZECHIA <i>Božena Kadeřábková, Emilie Jašová</i>
25	SEISMIC PERFORMANCE EVALUATION OF A MASONRY BUILDING SUBJECTED TO NEAR AND FAR FIELD GROUND MOTIONS <i>Özden Saygılı</i>
26	DYNAMIC CONSTRUCTION CONTROL METHOD FOR A DEEP FOUNDATION PIT WITH SAND-PEBBLE GEOLOGY <i>Xuansheng Cheng, Bingbing Luo1, Haibo Liu, Qingchun Xia, Chaobo Chen</i>
27	SUGARCANE STRAW ASH EFFECTS ON LIME STABILIZED LATERITIC SOIL FOR STRUCTURAL WORKS <i>Olugbenga Oludolapo Amu, Christopher Ajiboye Fapohunda, Oluwaseun Adedapo Adetayo, Moronfolu Festus Ilesanmi</i>
28	ESTIMATION OF SWELLING PRESSURE OF EXPANSIVE SOILS REINFORCED WITH GRANULAR PILE <i>Kundan Meshram, P.K. Jain</i>
29	SEISMIC PERFORMANCE OF TANK FOUNDATIONS IMPROVED WITH STONE COLUMNS <i>Saeid NikKhah Nasab</i>
30	EFFECT OF WATER-CEMENT RATIO, CEMENT DOSAGE, TYPE OF CEMENT AND CURING PROCESS ON THE DEPTH OF CARBONATION OF CONCRETE <i>Malek Jedidi, Omrane Benjeddou, Chokri Soussi</i>
31	STUDY ON OPTIMAL COMBINATION SETTLEMENT PREDICTION MODEL BASED ON LOGISTIC CURVE AND GOMPERTZ CURVE <i>Bolin Wang, Xu Wang, Xuening Ma</i>
32	COHESION TEST OF A SINGLE IMPREGNATED AR-GLASS ROVING IN HIGH-PERFORMANCE CONCRETE <i>Tomáš Vlach, Jakub Řepka, Jakub Hájek, Richard Fürst, Zuzana Jirkalová, Petr Hájek</i>
33	DEM STUDY ON THE PENETRATION OF JACKED PILES INTO LAYERED SOFT CLAY <i>Suchun Yang, Mingyi Zhang, Songkui Sang</i>

34	EXPERIMENTAL RESEARCH INTO THE RESPONSE OF HISTORICAL STRUCTURE TO THE EFFECTS OF NATURAL SEISMICITY <i>Tomáš Čejka, Aneta Libecajtová</i>
35	ESTIMATION OF DISPLACEMENT CAPACITY OF RECTANGULAR RC SHEAR WALLS USING EXPERIMENTAL AND ANALYTICAL DATABASE <i>Florin Pavel, Petru Panfilii, Ehsan Noroozinejad Farsangi</i>

COMPARATION OF THE ECONOMIC CYCLE ON LABOUR MARKET IN THE CONSTRUCTION INDUSTRY AND IN THE NATIONAL ECONOMY OF THE CZECHIA

Božena Kadeřábková¹, Emilie Jašová²

1. Czech Technical University in Prague, Faculty of Civil Engineering, Department of Economics and Management, Thákurova 7, Prague 6, Czech Republic; kaderabb@fsv.cvut.cz
2. Charles University, Faculty of Social Sciences, Smetanova nábřeží 6, Prague 1, 110 01, Czech Republic, ekonomka_2@hotmail.com

ABSTRACT

This paper is focused on economic cycle on the labor market in the entire national economy of the Czech Republic and in particular in the construction industry of Czechia. Authors use indicators of price level development. Analysis applies methods of the Hodrick–Prescott filter, Kalman filter and Stochastic trend to improve the informative value and credibility of reached conclusions. Phases of economic cycle on the labor market can be verified by comparison with the actual development of unemployment and gross domestic product. Special attention is given to unstable periods on the labor market, and we focus on determining reasons for their existence, their duration and manifestation.

The analysis revealed negative gaps in the period of economic transformation but there were periods with positive unemployment gaps in the years 2007 and 2008 too.

We used the development in the last period to predict the development in the near future. This ad hoc estimate is compared with model estimate made on an extended time series up to the end of the year 2018.

KEYWORDS

NAIRU, HP filter, Kalman filter, Stochastic trend, Unemployment gap, Labor market

INTRODUCTION

Aim of this paper is to measure the economic cycle on the labor market with the use of price indicator an HP filter (Hodrick-Prescott filter), Kalman filter and Stochastic trend method. Phases of economic cycle reached by said methods are then verified in the paper by comparing them with the development of actual unemployment rate and added value with the delay being two or three quarters. Researched periods are the periods of economic transformation, period of significant positive unemployment gaps in the years 2007 and 2008, period of the last recession and the following period of boom. Ad hoc prediction was then compared with the model estimate, which was made on an extended time series up to the end of the year 2018. Paper is divided into several chapters. First part shows methods leading to the estimation of NAIRU. In the second part, an analysis of the predicted development of an economic cycle in the conditions of the entire national economy and in the construction industry is made. This includes a prediction of said development in the near future. Last part of the paper offers a summary of the results of the analysis.



OVERVIEW OF METHODS

To examine the economic cycle, we used the NAIRU value defined by J. Tobin [1]. A. G. Akerlof, T.W. Dickens and L. G. Perry [2] also helped the spread of this concept. To estimate it, it is necessary to apply econometric models and methods, because it is an unobservable variable.

In this paper, we use the following methods:

HP filter - these methods divide the unemployment rate into a trend (NAIRU) and a cyclical part. The downside of this method is that it is often based on random and in many cases improbable assumptions, mainly centered around the NAIRU smoothing value coefficient. Among other authors applying this method were also P. Richardson et al. [3] and M. Hájek and V. Bezděk [4].

Kalman filter a Stochastic trend estimate variable NAIRU in every moment of the studied period. In the case of **Kalman filter**, behavioural equations explaining inflation are used to properly estimate NAIRU. NAIRU is specified as a random walk in reaction to shocks. Main disadvantage of this method is its inability to identify basic structural relationships. This method was used by authors such as S. Fabiani and R. Mestre [5] and L. Boone [6].

Stochastic trend is a method used with the aim to improve the explanatory power and credibility of a NAIRU estimate. S. Fabiani and R. Mestre [7] claim, that NAIRU follows the process of a random walk, but extended by variable stochastic shift (so-called local linear trend).

We then compare our estimated NAIRU values with the actual development of an unemployment rate, by which we get positive or negative values of an unemployment gaps. These are used as an alternative way of determining the phases of the economic cycle, because quarterly changes of GDP are one of the main ways as how to measure a cycle.

To estimate the development of the entire national economy we use consumer price index, and we use a construction work price index in the construction industry. Time series of consumer price index and construction work price index are then transformed in a way to be able to formulate adaptive formation of expectations (annual change in time t – annual change in time t-1). For a description of a development on a labour market, we use registered unemployment rate given by Ministry of Labour and Social Affairs of CR and specific unemployment rate in a construction industry, which we had to calculate ourselves, because of lack of any officially published statistics [8]. Among other explanatory variables are annual changes of exchange rates and import prices. Unemployment rates for each season were cleaned by moving multiplicative average. All-time series used passed the ADF test [9], and their stationary was confirmed. Time series were also cleaned using Census X12 method [9]. To choose the best suited model to approximate the analysed data in a case of Kalman's filter and method of Stochastic trend, cleaned R^2 was used. For the testing of the normality of residues, the Jarque-Bera test was used [9]. For testing the auto correlation of residues, the Breusch-Godfrey test was used [9]. For testing the heteroscedasticity of residues, the Wald test was used [9]. For measuring the bearing capacity of multicollinearity, the Variable inflation factor was used [9]. Time series covered the period between 1st quarter of 1994 and 4th quarter of 2012. Due to frequency of used time series being quarterly, smoothing parameter with a value of 1600 was used during an analysis using a method of HP filter. This value of smoothing is internationally recognized.

COMPARATION OF ESTIMATE OF DEVELOPMENT OF ECONOMIC CYCLE ON THE LABOUR MARKET WITH THE ACTUAL DEVELOPMENT

Whole period is divided into a 1995 to 2012 subperiod and another subperiod after year 2012 to the end of the year 2018.

Comparison of model values and an actual development between the 1995 and 2012

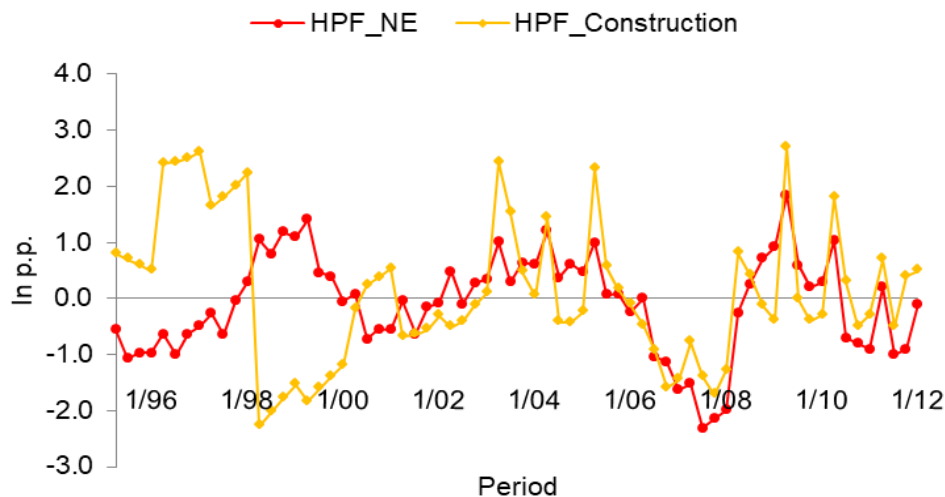


Fig. 1 - Development of unemployment gap in national economy according to HP filter and in the construction industry in Czechia (Source: Own calculations based on data by Ministry of Labour and Social Affairs and Czech Statistical Office)

Model phase of recession (4th quarter of 1998 to 1st quarter of 2001) on the labour market was consistent with the annual unemployment rate rise (+1,1 p.p.). **Positive gaps** (approx. 5,0 p.p., see Figure 1) were identified in the period from 4th quarter of 2006 to the 1st quarter of 2009. Model did not take into account the decline of situation on a labour market when showing NAIRU values. The phase of boom overlapped with the rise of GDP, which was on average 4,3 %. According to this method, effect of the last recession on labour market manifested itself in the period between 2nd quarter of 2009 and 1st quarter of 2011 and with the exception of the last two quarters was consistent with the actual development of national economy. In the period between 2nd and 4th quarter of 2011, a phase of boom with the positive unemployment gap of 0,2 p.p. appeared. **Phase of recession** followed in the 1st quarter of 2012 (unemployment rate declined annually by 0,4 p.p. and GDP by only 0,1 %) and also in the 4th quarter of 2012 (GDP fell by 1,3 %). Gradual decline of positive unemployment gap in the last quarter of 2012 while maintaining the fall in GDP (-1,6 %) and rise in unemployment rate to 8,9 % indicates continuation of a phase of recession. In the construction industry, the start of transformation can be found in 1st quarter of 1996 (3 full quarters later than in the industry) and ends at same time as in the industry (4th quarter of 1998). Model development is consistent with the annual decline of added value (by 5,4 %) and with the acceleration of the specific unemployment rate to the value of 6,4 %. **Positive gaps** amounting to 1,0 p.p. were observed between the 4th quarter of 2006 and 4th quarter of 2008. Beginning of this period is one quarter behind the industry, the end of this period, however, overlaps. The model phase of boom on a labour market is consistent with the development of the actual economy (added value rose by 3,9 % and specific rate of unemployment fell annually by 0,9 p.p.). The effect for the last recession on a labour market manifested itself from the 1st quarter of 2009 to the 2nd quarter of 2011. The start was in the same quarter as it was in the industry, but the end of the recession was the full one quarter later than in the construction business. Specific unemployment rate in the observed period rose annually by 1,2 p.p. and added value rose only by 0,4 %. Phase of boom in the period between 3rd quarter of 2011 and 2nd quarter of 2012 is consistent with the one observed in the industry. Average positive gap amounting to 0,3 p.p. was consistent with the development of the specific unemployment rate (annual fall by 0,4 p.p.), but it wasn't consistent with the fall of the added value (annual fall by 5,0 %). Slight decrease of the

negative unemployment gap in the last quarter of 2012 (from +0,19 to +0,17) and a frequent changing of the phases since the 2nd quarter of 2011 showed a great probability of a positive gap in the 2nd half of 2013.

Comparison of model values and the actual development from 2012 to 2018

In this part, the development of the economic cycle in the national economy and in selected industries is observed in the period between the 1st quarter of 2013 and 4th quarter of 2018. For describing the development on the labour market, we are still using the registered unemployment rate provided by Ministry of Labour and Social Affairs. This time series can be used after 2013 only because the fact, that the data published for 2012 are using both the new and old methodology, which allows us to calculate a conversion coefficient. Additional estimate allowed us to confirm anticipated in our estimates after extending the time series with new observations. Furthermore, it allowed to verifying predictions, which we made from the trends in the development of data from the end of the 2012 for the near future, the year 2013. Development of the cycle to the 4th quarter of 2018 is also shown, including the prediction for a year 2019.

Tab. 1 - Impact of extending the time series on a prior estimate of NAIRU and gap in national economy and in chosen industries in Czechia - in p.p. (Source: Own calculation based on data provided by Ministry of Labour and Social Affairs and Czech Statistical Office)

Period	NAIRU_NE	NAIRU_Construction	Gap_NE	Gap_Construction
1/06	0,0	0,0	0,0	0,0
	0,0	0,0	0,0	0,0
	0,0	0,0	0,0	0,0
	0,0	0,0	0,0	0,0
1/07	0,0	0,1	0,0	-0,1
	0,0	0,1	0,0	-0,1
	0,0	0,1	0,0	-0,1
	0,0	0,1	0,0	-0,1
1/08	0,1	0,1	-0,1	-0,1
	0,1	0,1	-0,1	-0,1
	0,1	0,1	-0,1	-0,1
	0,1	0,2	-0,1	-0,2
1/09	0,1	0,2	-0,1	-0,2
	0,2	0,2	-0,2	-0,2
	0,2	0,2	-0,2	-0,2
	0,2	0,2	-0,2	-0,2
1/10	0,2	0,2	-0,2	-0,2
	0,2	0,2	-0,2	-0,2
	0,3	0,2	-0,3	-0,2
	0,3	0,2	-0,3	-0,2
1/11	0,3	0,2	-0,3	-0,2
	0,3	0,1	-0,3	-0,1
	0,3	0,1	-0,3	-0,1
	0,3	0,1	-0,3	-0,1
1/12	0,3	0,0	-0,3	0,0
	0,3	-0,1	-0,3	0,1
	0,3	-0,2	-0,3	0,2
	0,3	-0,3	-0,3	0,3

From the comparison of estimate of NAIRU gained by using HP filter and an unemployment rate gap for the entire national economy we can see, that extending the time series by years 2013 to 2018 impacted the previously estimated values with the rising intensity of NAIRU in the national economy. While between the years 1994 and 2006 no changes in NAIRU and gap were mapped (see Table 1), in the period from 1st quarter of 2007 to the 3rd quarter of 2008, the difference ranges from 0,0 to 0,1 p.p., in the period from the 4th quarter of 2008 to the 3rd quarter of 2010, the differences are already ranging from 0,1 to 0,2 p.p, in the period from the 4th quarter of 2010 to the 2nd quarter of 2012, the interval is from the 0,0 to 0,3 p.p, in the 3rd quarter of 2012 the difference is between 0,2 and 0,4 and in the 4th quarter of 2012, the values were between 0,2 and 0,5 p.p.

Quality of ad hoc prediction for year 2013 from the alternative methods (such as Kalman filter and Stochastic trend), which allows us more complex assessment of phases of economic cycle can be seen in Table 2.

Tab. 2 - Comparison of ad hoc unemployment gap prediction for the year 2013 and its development after time series extension to the year 2018 - in p.p. (Source: Own calculation based on data provided by Ministry of Labour and Social Affairs and Czech Statistical Office and Czech National Bank)

Estimation method	Period	NE_Gap	Construction_Gap
Estimating from tendencies towards the end of 2012 using the HP filter method	1/13	Continuation and further deepening of the recession phase but also a variant with its exhaustion in the second half of the year.	The probability of turning into a positive gap in the second half of 2013.
Estimating from tendencies towards the end of 2012 using the Kalman filter method	1/13	Continuation and further deepening of the recession phase but also a variant with its exhaustion in the second half of the year.	The continuation and further deepening of the positive gap, but also the variant with its exhaustion in the first half of the year.
Estimating from tendencies towards the end of 2012 using the Stochastic trend method	1/13	The continuation of the positive gap only in Q1 2013, the possible recession phase could cover the remaining part of the year.	Sustaining the recession phase in the early part of 2013 and the boom phase in the second half of the year.
Estimation after prolongation of the HP filter method	1/13	1,13 2 0,47 3 0,54 4 0,93	2,86 1,04 -0,22 -0,66

In case of comparing ad hoc prediction of the unemployment gaps in the entire national economy for the year 2013 using all methods and the estimate of HP filter, we can see the correct placement of the phase of recession, while the former HP filter and Kalman filter results indicated a certain degree of doubts about said recession being present for the entire year 2013. Slightly more optimistic were ad hoc predictions for the year 2013 using the methods of HP filter and Kalman filter. The most conformity between the extrapolated data from 2012 and results obtained by using HP filters after extending time series to the year 2018 can be seen in the construction industry. Interestingly, in the industry, trends resulting from the application of models on the data all the way to the year 2012 were the most reliable in predicting the correct development using the method of Stochastic trend.

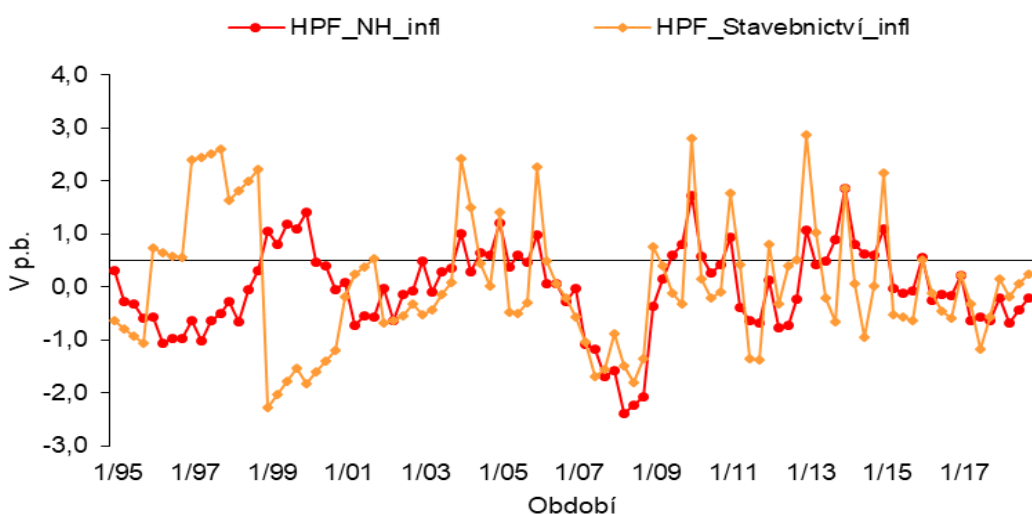


Fig. 2 - Development of unemployment gap in national economy according to HP filter and in the construction industry after extending the time series all the way to the 4th quarter of 2018 (Source: Own calculations based on data by Ministry of Labour and Social Affairs and Czech Statistical Office)

Phase of recession estimated for the entire national economy in the year 2013 and continuing all the way up to the 1st quarter of 2015 was consistent with the annual growth of unemployment rate (+0,3 p.p.). It was also consistent with the development of GDP, which shows the beginnings of this phase as early as in the 2nd quarter of 2012. Positive gaps amounting to roughly 0,2 p.p. (see Figure 2) were found in the period from the 2nd quarter of 2015 to the 4th quarter of 2018. Observed phase of boom overlapped with the decrease in the unemployment rate by 1,4 p.p. and was also accompanied by growth of (by 3,7 %). In the construction industry, negative gaps were observed as early as in the 3rd quarter of 2012 to the 1st quarter of 2015, with added value growing only by 0,5 % and specific unemployment rate growing by 0,1 p.p. Positive gaps in the period directly following and lasting all the way to the 2nd quarter of 2018 was in average roughly 0,3 p.p. and was in accordance with the annual growth of the added value and with the decrease in the specific unemployment rate (by 1,2 p.p.). Negative gap was then observed in the second half of 2018 being roughly 0,2 p.p., and added value growing only by 0,9 % with specific unemployment rate stagnating and being same as at the same time last year.

CONCLUSION

From the analysis of the ability of individual methods to correctly depict the influence of the transformation of the economy on the labor market consistent with the development of the actual real economy, it can be concluded, that, in Czechia, we can accept the conclusions made by authors [7]. These conclusions were about using local linear trend to improve the credibility of the estimate of NAIRU. Method of Stochastic trend reacted to the actual development of the economy nearly the same as the Kalman filter and substantially more accurately than the HP filter.

In the construction industry, the period of transformation of the economy and phases of the economic cycle was predicted correctly by used methods and was consistent with the actual development of the economy. Even though Stochastic trend was consistent with the actual development of the economy, results gained by this method did not cover the entire observed period and it is therefore impossible to agree with the authors [7] about their proposed extension of random walk. It needs to be added, that the Kalman filter with the smoothing factor of 0,6 reacted to the process of transformation in the Czech economy and in the construction industry by giving

negative or unrealistically low positive NAIRU values. Another reason for unrealistically great gaps in this period can be seen in the fluctuations in oil prices, exchange rates, import prices and in regulated prices, which disturbed the substitution relation between unemployment and the deflation of household consumption.

Another extraordinary incident that was recorded by all three methods was the period of extensive positive unemployment gaps. The consistency of estimation made using Stochastic trend with the actual data supports the proposal of modifying the random walk, as made by the authors S. Fabiani and R. Mestre [7]. Method of the Stochastic trend reflected actual economy equally the HP filter did (while the Kalman filter reported the beginning of the said phase with a delay). Positive gaps consistent with the actual development of the economy were also observed in the construction industry. Reason for such high positive gaps both in the national economy and construction industry while using Kalman filter can be explained by said model being unable to reflect the last significant improvement of the situation on the labor market in the NAIRU value.

All methods reacted to the emerging recession. Using the method of Stochastic trend, the effect of the last recession on the labor market in the national economy was consistent with the actual data. Specifically, it was the period from the 2nd quarter of 2009 to the 1st quarter of 2011, which was consistent with the results provided by HP filter and one quarter earlier than the prediction provided by Kalman filter. Start of the latest recession in the construction industry was determined very differently by individual methods. All the methods, with the exception of the Kalman filter (estimates the phase of boom contrary to the actual economic data) agree with and place the end of the phase of the recession at the end of the year 2012. Stochastic trend reflected the transition between the phases of boom and recession with the significant delay. It needs to be pointed out that the disadvantage of too tightly copying estimated NAIRU values and the development of the actual specific unemployment rate. *The problem was that beside low values of the calculated unemployment gap, there was also frequent changing of the phases of the cycle. (Negative and positive states of the calculated unemployment gaps.)*

The evaluation of the national economy until the end of year 2012 with methods used is inconclusive. Using Stochastic trend, development of the national economy in the period between 2nd quarter of 2011 and 4th quarter of 2012 was meant to be characteristic by the fact, that the labor market was in the phase of boom. Using the Kalman filter as well as HP filter, we got the phase of the boom ending by the end of the 3rd quarter of the year 2012 and in the following year the labor market once again entered the phase of recession. Both the Kalman filter and the HP filter turned out to be much better suited for the analysis of the latest period than the Stochastic trend.

Consistency of the extrapolation of the development in the year 2013 from the estimates provided by the individual methods using the data until the end of the year 2012 with the results given by using HP filter after extending time series as the way to the end of the year 2018 confirmed the correct placement of the recession phase in the entire national economy. The most consistent was the estimation in the industry made by using the HP filters for the year 2013 and the extrapolation made on the results until the end of the year 2012 using the Stochastic trend method. Little more optimistic were former estimates concerning the year 2013 with these using the methods HP filter and the Kalman filter. The most consistency with the results that were obtained by extrapolation of the data from the year 2012 and the estimation made by using the HP filter from extended time series was found in the construction industry.

Estimations made by using HP filter on the most recent data confirmed two more phases of the economic cycle in the national industry in the period after the year 2012 and three more phases in our chosen industry. Phase of the recession estimated for the entire national economy started in the 1st quarter of the year 2013 but in the construction industry it



already started by the 3rd quarter of 2012. In both said cases, these model estimates were verified by annual unemployment rate growth (in the national economy and in the construction industry). The phase of the recession ends by the 1st quarter of the year 2015. Start of the positive gaps both in the national economy and in the construction was located to the 2nd quarter of the year 2015. While in the entire national economy this positive period lasted until the end of the year 2018, in the construction industry, this period only lasted until the 2nd quarter of 2018. The observed phase of boom was on all levels consistent with the annual decline in unemployment rate and with the growth of the added value. The following period can be characterized by very shallow recession in the construction industry in the two last quarters of 2018, specifically the 3rd and the 4th quarters of 2018. Specific unemployment rate in the construction industry was the same as it was in the 2017, while in the industry, it saw an annual decrease of 0,3 p.p. Both in the construction industry and in the industry as a whole, a rise in the negative unemployment gaps can be registered, which makes continuation of this phase into 2019 very probable. In the entire national economy, a decreasing intensity of positive gap can be registered since the 3rd quarter of 2018 and it can signal slow end of the phase of the boom, which could then change into a shallow recession in the second half of 2019.

REFERENCES

- [1] Tobin, J. (1997): *Supply Constraints on Employment and Output: NAIRU versus Natural Rate*. Cowles Foundation Paper 1150. Yale University, New Haven. 1 s.
- [2] Akerlof, G. A.; Dickens, W. T.; Perry, G. L. (1996): The Macroeconomics of Low Inflation. Brookings Papers on Economic Activity, Brookings Institution. Washington, D.C.
- [3] Richardson, P., Boone, L., Giorno, C., Meacci, M., Rae, D., Turner, D. (2000): *The concept, policy use and measurement of structural unemployment: estimating a time varying NAIRU across 21 OECD countries*. OECD WP. 38 s.
- [4] Hájek, M., Bezděk, V. (2000): Estimation of potential product and production gap in the Czech Republic. Working Paper, 2000, č. 16, Czech National Bank. 21 s. (in Czech)
- [5] Fabiani, S.; Mestre, R. (2000): Alternative measures of the NAIRU in the euro area: estimates and assessment. ECB WP.
- [6] Boone, L. (2000): Comparing Semi-Structural Methods to Estimate Unobserved Variables. The HPMV and Kalman filter Approaches OECD. Economics Department Working Papers No. 240.
- [7] Fabiani, S., Mestre, R. (May 2001): A system approach for measuring the euro area NAIRU. ECB WP. 65 s.
- [8] Kadeřábková, B., Jašová, E. (2011): *Analysis of the NAIRU indicator at the sectoral level*. Political Economy, University of the Economics, Prague, 4, ISSN 0032-3233. (in Czech)
- [9] Eviews. 2013. EViews Version 7.2 Help Topics.

Czech Statistical Office

Consumer price index, <http://www.czso.cz/csu/csuf/aktual-isc>
Manufacturing price index, <http://www.czso.cz/csu/csuf/aktual-ipc>
Construction price index, <http://www.czso.cz/csu/csuf/aktual-ipc>
Import price index, http://www.czso.cz/csu/redakce.nsf/i/ceny_vd_ekon

Czech National Bank

http://www.cnb.cz/cs/financni_trhy/devizovy_trh/kurzy_devizoveho_trhu/denni_kurz.jsp

Ministry of Labour and Social Affairs

Registered unemployment rate, <http://www.mpsv.cz/cs/869>



SEISMIC PERFORMANCE EVALUATION OF A MASONRY BUILDING SUBJECTED TO NEAR AND FAR FIELD GROUND MOTIONS

Özden Saygılı

*Yeditepe University, Faculty of Engineering, Department of Civil Engineering,
Istanbul, 34755, Turkey; ozden.saygili@yeditepe.edu.tr*

ABSTRACT

On October 23, 2011 an earthquake occurred approximately 20 km north of the province of Van, Turkey with a magnitude of Mw 7.2. Following the main earthquake, 111 aftershocks with magnitudes of 4.0 and above occurred. The state of damage was very severe and considerable amount of unreinforced masonry buildings were affected highlighting the need for investigating the seismic design of unreinforced masonry buildings in the affected area. In this paper, seismic behaviour of a two story masonry building designed according to the 2019 Turkish Building Seismic Code is presented. The main objective of this activity was to study the near field and far field synthetic ground motions, artificial ground motions and evaluating the responses to get reliable information on the seismic response of masonry buildings.

KEYWORDS

Masonry buildings, Seismic analysis, Near-field seismic motion, Time history analysis

INTRODUCTION

Located in a major earthquake zone in Turkey, most of the buildings especially in rural areas are in form of masonry construction. Historical ones are generally unreinforced stone or brick masonry. Modern masonry buildings are generally reinforced and confined masonry constructed with fired clay bricks or concrete blocks. This structural type of brick masonry is also widely used for housing in most of the countries due to its advantages of brickwork, aesthetic appearance and economy of the construction [1], [2], [3], [4]. In many countries a considerable amount of research was carried out and continues to contribute to improvement of seismic codes for masonry buildings. In Turkey, this type of construction became popular in recent times but there is no specific design code for masonry buildings. It is important to investigate the seismic behaviour of masonry buildings since large mass of walls could result in serious damages under earthquake ground motion. In this study a two-story masonry building was designed according to the recently adopted 2019 Turkish Building Seismic Code (2019 TBSC) [5]. Structural performance of the masonry building was investigated under seismic excitations. Dynamic analyses were performed under real and simulated ground motions. Near field and far field synthetic ground motions were generated compatible with the target spectrum. Due to the characteristics of earthquakes, near field ground motions have long period velocity pulses that are not shown in far field ground motions. Besides, the effect of ground motion of a moderate-large earthquake recorded in a near-field, mostly differ from the effects recorded far from the earthquake source [6]. This research also aims to investigate the seismic response of a two-story masonry building due to near-field and far-field ground. Therefore, the City of Van located in Turkey was chosen as the study area. The city is under the influence of the 40 km long Bitlis fault zone which passes about 20 km north of the city



and the South Anatolian fault. The region of Van is under the influence of the north-south compression and contraction zone as a result of the proximity of the Arabian plate to the north towards the Eurasian plate. There are three different categories of faults falling in the Van region; strike-slip, thrust to reverse and oblique-slip normal [7]. A simplified tectonic unit and seismic activity of Van and its surroundings is given in Figure 1. These maps were constructed with Generic Mapping Tools (GMT). On October 23, 2011 the Van earthquake occurred approximately 20 km north of the province of Van with a magnitude of Mw 7.2 with a right-lateral strike-slip mechanism. Following the main earthquake, 111 aftershocks with a magnitude of Mw 4.0 and above occurred. According to the Disasters and Emergency Situations Directorate of Turkey (AFAD), this earthquake resulted in the death of approximately 604 people, 4,152 people were injured, and 6,017 buildings collapsed [8]. Another earthquake of Mw 5.7 took place on 9 November 2011. In addition to that, after October 23, 2011, 5527 earthquakes ranging in size from 1.4 to 5.7 occurred in the Van earthquake region for about 1 year [9], [10].

GROUND MOTION DATA SETS

The ground motion recorded in field within a distance of about 20 km from the fault rupture is typically known as near-field ground motion. Although there is no clear definition for the distance range of near and far field, if the site is about 50 km around the fault then the ground motion is considered as a far-field earthquake. Near-field ground motions distinctively have higher acceleration, more limited frequencies and different pulses in time histories as far as far field ground motion is concerned. In addition to that, forward directivity and fling step effects are common characteristics of near-field ground motions. These effects result from rupture mechanism, residual ground displacement and slip direction of rupture relative to the site. At the beginning of the record, large pulses are observed due to transfer of a major portion of the fault's energy to the site when the rupture propagation of the fault towards a site with a velocity close to the shear wave velocity. Seismic waves observed at site with radiation pattern of the fault oriented in the fault-normal direction get close to each other and generate a large pulse which decreases the duration of the fault waves reaching the structure [11], [12]. Although most of these pulses are observed from the radiation pattern of the fault oriented in the fault-normal direction, the fault parallel direction could result in strong pulses, too [13], [14]. Fling-step effect is the relative slip between the hanging wall and footwall which produces large amplitude unidirectional velocity pulse and a monotonic step in displacement time history [15], [16]. These pulses result in the occurrence of static permanent ground displacements due to tectonic deformation associated with fault rupture [17]. As these near field effects can lead to higher seismic demands, it is important to take seismic design of structures located in the near-field zone into consideration [14], [18], [19], [20], [21]. 2019 TBSC provides regional variations in the shape of the response spectrum for site conditions, earthquake source and path. In this study for the target spectrum, a reduced design acceleration spectrum was created under a horizontal earthquake effect according to the 2019 TBSC. The soil profile in the selected area is composed of thick, medium solid-hard silt and silt sand and gravel sand layers ranging from clay to medium tight-tight. The shear wave velocities obtained in the central districts of Van province according to SPT-N values vary between 261.3 m / s and 357.7 m / s [22], [23]. Taking into account the site properties proposed by the National Earthquake Hazard Reduction Program (NEHRP), the site is medium tight-hard as class D [24].

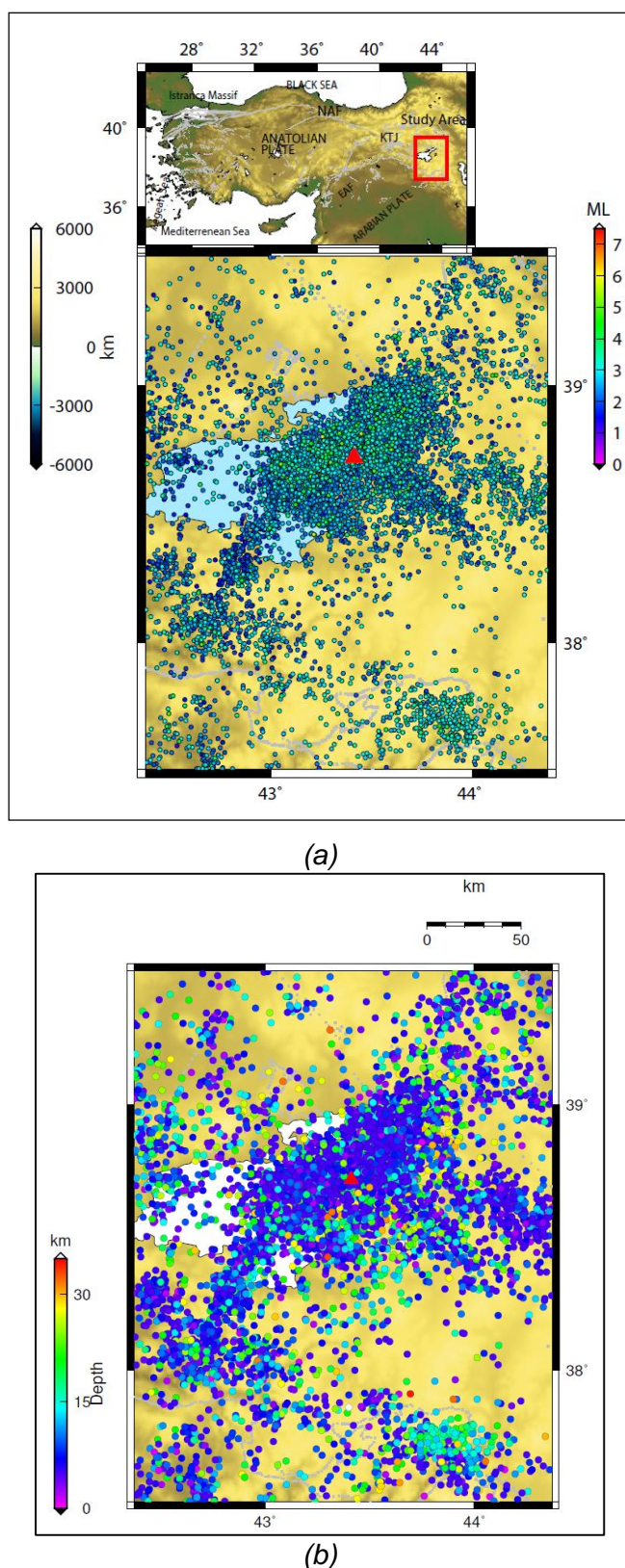


Fig. 1 – A simplified tectonic units and seismic activity of Van and surroundings

Two different earthquake ground motion levels were taken into consideration for the generation of synthetic accelerograms. The first ground motion level has a 2% probability to be exceeded in 50 years. Return period of this ground shaking is approximately 2475 years. The second ground motion level has a 10% probability to be exceeded in 50 years. Return period of this ground shaking is approximately 475 years. For each earthquake ground motion level a total of eight near field, eight far field synthetic excitations and eight artificial ground motions were generated based on the adaptation of a random process to a target spectrum of the region. SeismoArtif provides a user defined spectrum to generate artificial accelerograms [25]. The accelerogram was defined using target spectrum and adapting its frequency content using the Fourier transform. Halldorson and Papageorgiou algorithm was used for the generation of synthetic motions applied both in the near-fault and in the far-field region [26]. The correction of the random process was performed for each iteration using Equation 1 [27]:

$$F(f)_{i+1} = F(f)_i \left[\frac{SRT(f)}{SR(f)_i} \right] \quad (1)$$

where,

- $F(f)_{i+1}$, $F(f)_i$ are the data of the accelerogram in the frequency domain;
- $SR(f)_i$ is the data response spectrum relative to the accelerogram of that iteration due to frequency f .
- $SRT(f)$ is the data of target spectrum relative to the accelerogram of that iteration due to frequency f .

At each iteration a Fourier transformation was applied to move from time domain to frequency domain. In order to generate the synthetic accelerogram, Gaussian white noise was multiplied by Saragoni & Hart envelope shape [28]. Soil effects were considered as linear based on NERPH class D ($V_{s30} = 255$ m/s). The smallest and largest periods of the target response spectrum were used to determine the frequency range within the power spectral density function. In order to establish the elastic response spectra, linear dynamic analysis was performed using Newmark integration method to solve the single degree of freedom system of equations of motion [29]. In addition to these synthetic ground motions (SGM), artificial ground motions (AGM) were generated through the use of a Saragoni and Hart (1974) envelope shape and a power spectral density function which was calculated from the velocity target spectrum of earthquake ground motion level 1 and level 2. Sinusoidal wave Equation 2 was used to generate the steady state motion:

$$W(t) = \sum_i A_i \sin(w_i t + \phi_i) \quad (2)$$

where,

- A_i is the amplitude and
- ϕ_i is the phase angle of the i^{th} sinusoidal wave.

In order to simulate the transient behaviour for the artificial ground motions, $GM(t)$ the steady state motions were multiplied by Saragoni and Hart (1974) envelope shape, $I(t)$ in which the phase angles are in the interval of $[0, 2\pi]$, with a uniform probability distribution by Equation 3:

$$GM(t) = I(x) \sum_i A_i \sin(w_i t + \phi_i) \quad (3)$$

For the ground motion level 1, peak ground acceleration (PGA) of near field and far field synthetic ground motions varies between 0.51 g and 0.53 g. For the same ground motion level peak ground velocity (PGV) values which are often considered as the indicator of damage potential are in the range of 0.50 m/sec and 0.76 m/sec. For the ground motion level 2, peak ground acceleration (PGA) of near field and far field synthetic ground motions is about 0.27 g. For the same ground motion level peak ground velocity values vary between 0.31 m/sec and 0.53 m/sec.



Furthermore ground motion record of October 23, 2011 Van earthquake (ML 6.7) was downloaded from the Disaster and Emergency Management Authority (AFAD) Strong Motion Database. The earthquake lasted for approximately 80 s. Acceleration time histories of Van Earthquake are given in Figure 2. Comparison of target spectrum and response spectrum of ground motions are shown in Figure 3 and Figure 4.

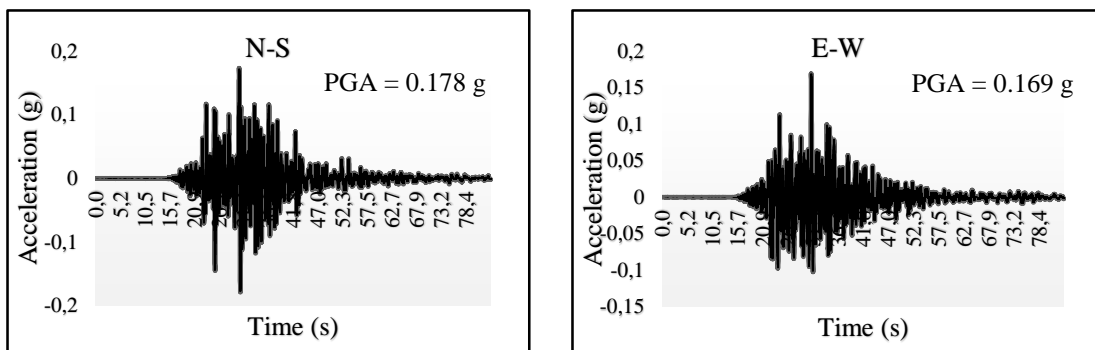


Fig. 2 – Acceleration histories of Van NS and EW components

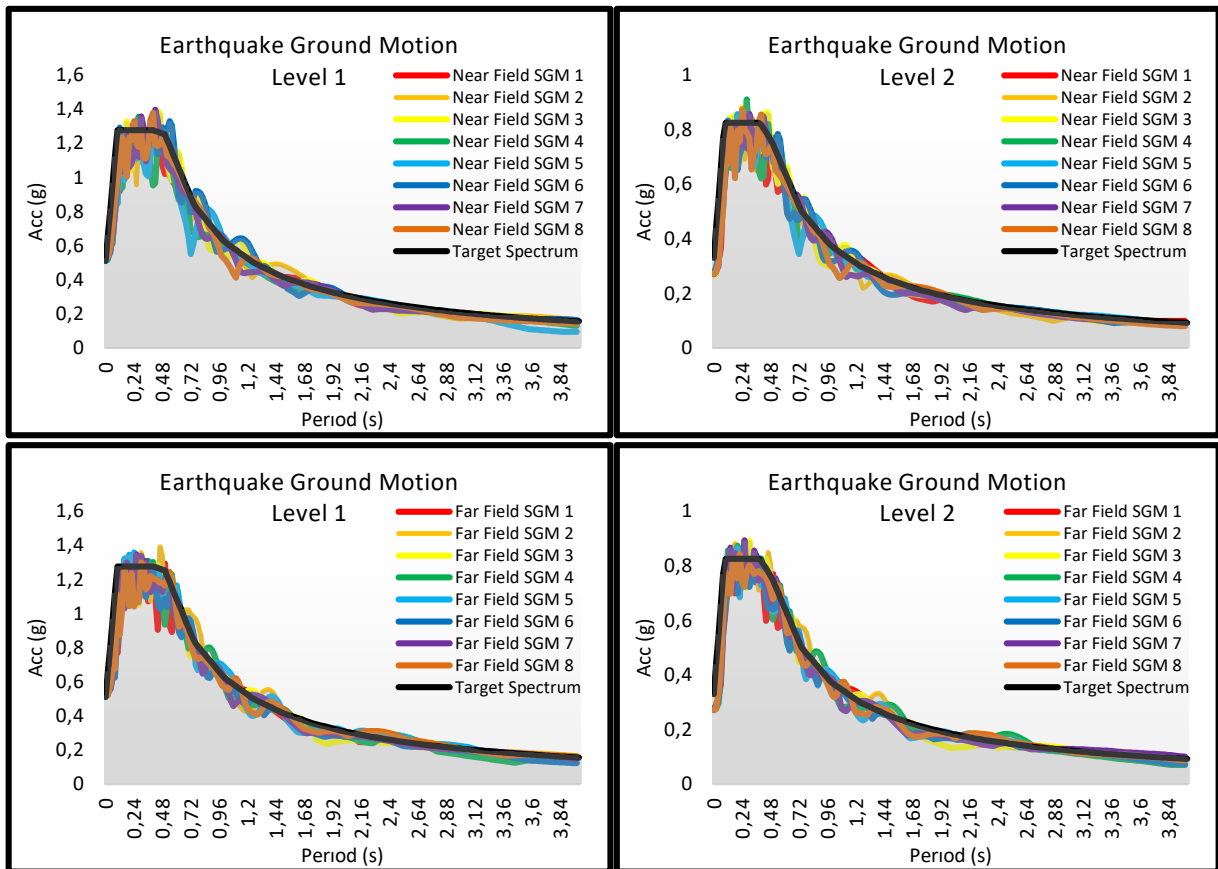


Fig. 3 – Comparison of target spectrum and response spectrum of synthetic ground motion (SGM) for ground motion level 1 and level 2

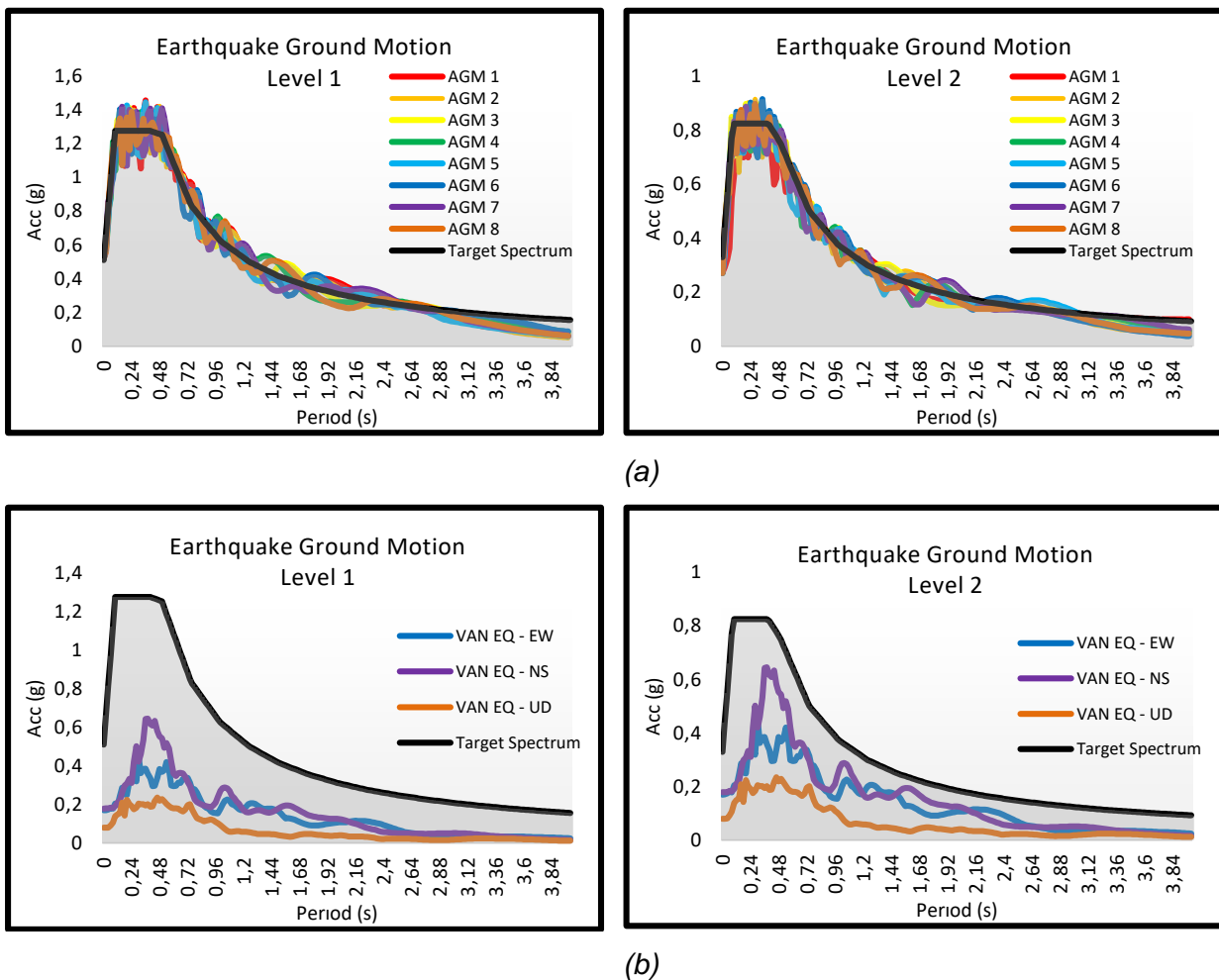


Fig. 4 – Comparison of target spectrum and response spectrum of artificial ground motion (AGM) for ground motion level 1 and level 2 (a), comparison of target spectrum and response spectrum of October 23, 2011 Van Earthquake (b)

DESCRIPTION OF NUMERICAL MODEL

For the numerical modelling, finite element modelling (FEM) software SAP2000 was used to create the two-story masonry building. The two story masonry building was considered to be designed for dead load, live load and seismic load according to the 2019 TBSC. The masonry building that was considered for this study was a double story building consisting of three bays in each direction of 10.25 m long and 12 m wide. The wall was 0.25 m thick and the total height of masonry buildings was 5.90 m. In the building, tops of openings in the story were at the same level. The plan of the building consisted of a continuous lintel band through all walls just above the openings but it was not considered in the numerical model. The wall was discretized into small number of elements. The structural members of the masonry building were slabs, beams and bearing walls. The slab was reinforced concrete and was supported by horizontal beams on the masonry walls. In order to integrate concrete slab and masonry walls with each other and distribute the horizontal loads to the masonry walls; rigid diaphragm behaviour was adopted. By this way, the shear force induced by the walls was compensated by the in-plane rigidity of the walls. In the numerical model floor, the slab has a degree of freedom of translation in two in-plane directions and rotation about the vertical direction. At 4 m intervals in the masonry walls vertical beams were designed according to 2019 TBSC. These vertical beams and proper connection between wall and

diaphragms would lead to ductile behaviour governed by the in plane response of the masonry walls.

In the Eurocode 8 of Part 1 and Part 3, the conditions of limit for the design or assessment of masonry buildings refer to a damage limitation and to an ultimate limit state. According to Eurocode 8, three different performance criteria are included: damage limit state of the occurrence of damage and the associated limitations of use. The Ultimate limit or Life Safety limit state that the structure should remain without global or local collapse that the structure continue to carry the gravity load demands of buildings and a residual load bearing capacity [30]. In the FEMA E-74, earthquake damage to non-structural elements are given in three types of risks: Life Safety limit state, Property Loss limit state and a Functional Loss limit state [31]. In the FEMA 273, the given performance criteria applied for structural components and unreinforced masonry infill walls are Immediate Occupancy, Life Safety and Collapse Prevention [32]. According to the given definitions for the performance of masonry buildings in 2019 TBSC, if the shear strength of all the walls of the masonry building in both directions is sufficient to meet the shear forces generated by the applied earthquake effects, it is concluded that the building provides a Limited Damage Performance Level. This level of performance corresponds to the level of damage in which the building damage is limited, i.e. non-linear behaviour is limited. If the contribution of the walls that do not meet this condition to the shear force is lower than the 40% in the earthquake direction applied on any floor, the building will be considered to provide the Controlled Damage Performance Level. This level of performance corresponds to the level of damage to the structural components which is not serious and often repairable to ensure safety. If this rate exceeds 40%, the building is considered to be in a Collapse State. In this study, the resulting shear force was compared with the safety shear strength of the wall, taking into account the vertical normal force on the wall and the bearing strength of the wall. Wall areas were calculated by removing gaps such as doors and windows. For the safety of the structural system, the torsional rigidity relative to the vertical axis of the building was determined according to the 2019 TBSC. Masonry walls were designed such that the stress calculated by dividing the design force acting on the masonry wall in the vertical direction by the cross-sectional area excluding door and window openings on the wall is not greater than the allowable compressive stress for the wall. In addition to that, the masonry walls were designed such that the design strength of vertical load was greater than the design normal force acting in the vertical direction to the masonry wall. To this aim, the following equations (2019 TBSC) given in Table 1 were used:

Tab. 1 - 2019 Turkish Building Seismic Code given design equations

Characteristic shear strength of masonry wall, f_{vk}	
$f_{vk} = f_{vk0} + 0.4\sigma_{vertical} \leq 0.10f_b$	Initial shear strength of masonry wall, f_{vk0} obtained from TBSC 2019 $f_{vk0} = 0.30 \text{ MPa}$
Vertical compression stress	
$\sigma_{vertical} = \frac{N_{Ed}}{lt}$	Axial force, N_{Ed} Wall cross-section length, l Wall thickness, t
Shear strength of masonry wall design	
$V_{Rd} = lt \frac{1.5f_{vdo}}{b} \sqrt{1 + \frac{N_{Ed}}{1.5ltf_{vdo}}}$	$V_{Rd} = f_{vdo} t l_c$
$f_{vdo} = \frac{f_{vk0}}{\gamma_m}$	
Strength reduction coefficient, γ_m is 0.2 determined according to the TBSC 2019	

The initial shear strength of the masonry wall, f_{vk0} is determined according to the 2019 TBSC. Accepted compressive strength of the masonry wall, f_b is 20 MPa. The elasticity and shear modulus of the masonry walls was calculated according to the relationship between characteristic compressive strength of masonry wall and elasticity given in 2019 TBSC.

Eigen frequencies and displacement mode shapes of model are shown in Figure 5. The first period is approximately 0.067 seconds which is very close to the second mode 0.055 sec due to the almost symmetric plan those corresponds to a bending mode shape on both orthogonal horizontal planes. Mode 3 involves shear and torsional movements. Mode 1 and mode 2 are predominant translation modes that exhibit a high relative modal mass in both orthogonal direction and little or near zero in rotation. Modal analysis provided valuable information insight into the dynamic characteristics of the masonry numerical model. In addition to that, as the modal contribution to the displacement depends on the static properties of the system and the dynamic response of the system under earthquake excitation time history analyses were performed.

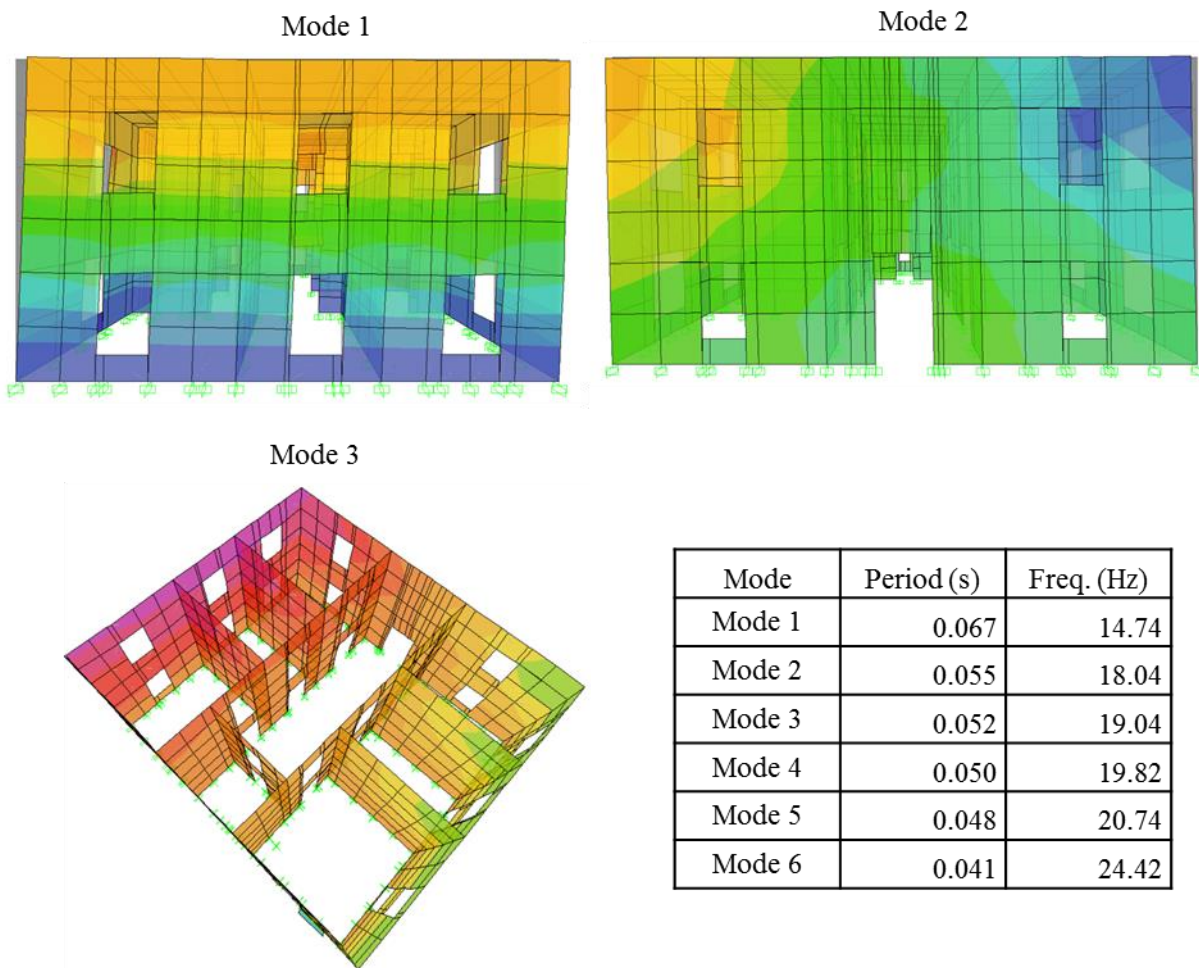


Fig. 5 – Eigen frequencies and displacement mode shapes

SEISMIC RESPONSE ANALYSIS OF A MASONRY BUILDING

Seismic ground motions were applied as base excitation to the numerical model. It was assumed that the structure was subjected to the earthquake in both horizontal directions. Due to the fact that the seismic effects in two orthogonal directions are unlikely to reach their maximum value at the same time, the 30 percent orthogonal loading rule was applied. For the time history analysis under synthetic and artificial ground motions, 100% of the earthquake was combined with



30% of the earthquake in the orthogonal direction. During near field and far field seismic excitations, depending on the direction of ground motion, in-plane and out-of-plane forces occurred on the masonry walls. For out-of-plane, shear force and bending moment were developed in the weak direction of the masonry wall due to the weakness of the out-of-plane stiffness of the masonry wall. Horizontal inertia forces transmitted from the slab were transmitted by the in-plane forces formed on the walls in the direction of force. Under near and far field earthquakes when the torsional moment increases the shear force in one part of the masonry walls in the earthquake direction, it decreases the shear force in the other part. It created a shear force on the masonry walls for those which were not parallel to the direction of seismic loading.

Variation of top displacement and base shear force under artificial earthquakes, near and far field earthquakes for ground motion level 1 and ground motion level 2 are given in Figure 6. A brief inspection of the values indicates that the maximum roof displacements that the masonry building experienced are under near field excitations created for ground motion level 1. The duration of the artificial ground motions was about 20 sec. while for the near field and far field ground motions duration was about 10 sec. and 14 sec., respectively. As the near field ground motions have higher accelerations and more limited frequencies in time histories than the far field ground motion, the selected building experienced the highest responses in terms of deformation and stresses under near field synthetic excitations. The Masonry building was exposed to artificial ground motions for 20 sec. which resulted in the highest base shear forces in both ground motion levels. Furthermore, PGV of synthetic and artificial ground motions and roof drift ratios were compared for each ground motion set (Figure 7). Drift ratios were found by dividing the roof displacement with the story height. Considering the set of ground motion level 1; PGV of the synthetic loadings were in the range of 50 cm/sec and 76 cm/sec and PGV of the artificial loadings were in the range of 50 cm/sec and 58 cm/sec. For the second ground motion level, PGV of the synthetic loadings varied between 31 cm/sec and 53 cm/sec while PGV of the artificial loadings were in the range of 27 cm/sec and 36 cm/sec. It is evident for the near field synthetic and artificial excitations of both ground motion levels; the drift ratio increases with the increase of PGV which is not clear for far field ground motion data set. Considering the ground motion level 1, although the PGVs are in about the same range for artificial and far field ground motions, higher drifts were observed under far field loadings. Furthermore, during seismic analysis in addition to the horizontal shear forces induced in the walls in the related direction of seismic loading, under vertical loads, shear forces and bending moment occurred in slabs but shear forces were more effective on the behaviour of walls of masonry buildings than the bending moment. The designed building had damage of the ductile type distributed at many locations due to the absorption of a good amount of energy received from the seismic excitations. Close the opening tensile stresses occurred under compression which would result in cracks. As expected, the masonry structure experienced maximum tensile stresses observed under near field earthquake for ground motion level 1 and minimum tensile stress occurred under the October 23, 2011 Van Earthquake.

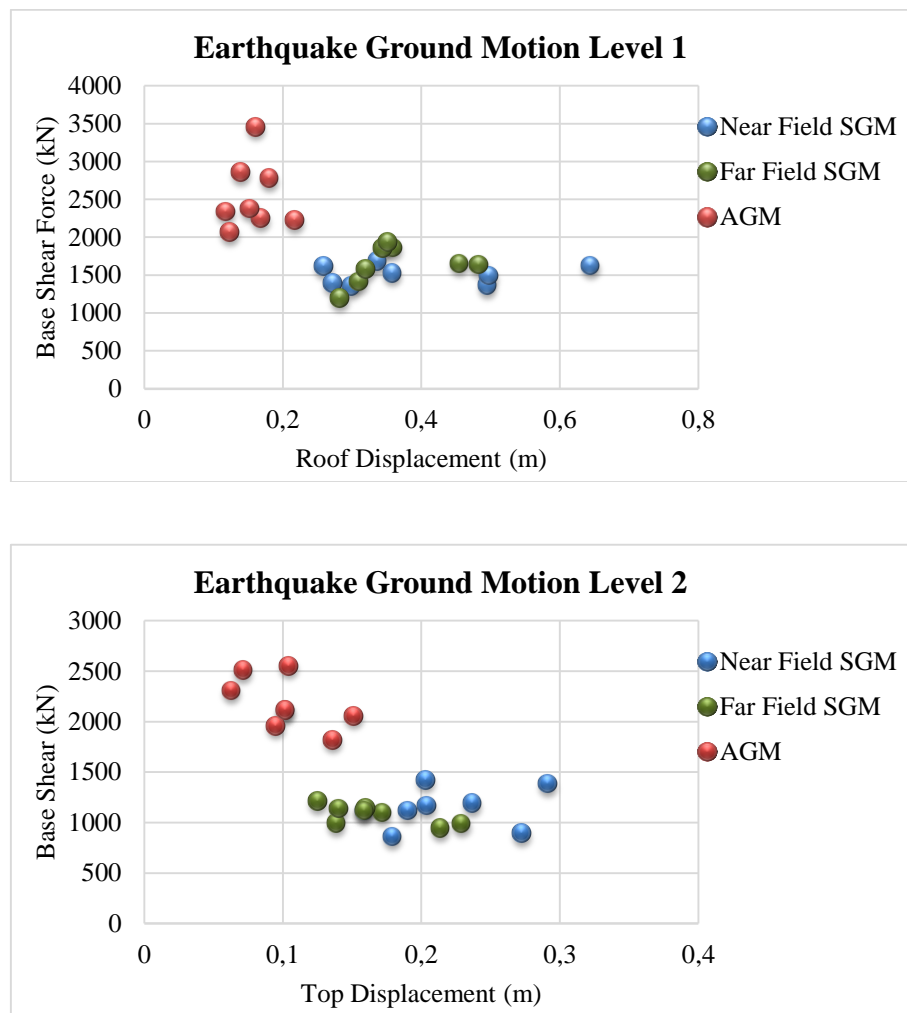


Fig. 6 – Variation of top displacement and base shear force under artificial earthquakes (AGM), near and far field synthetic earthquakes (SGM) for ground motion level 1 and ground motion level 2

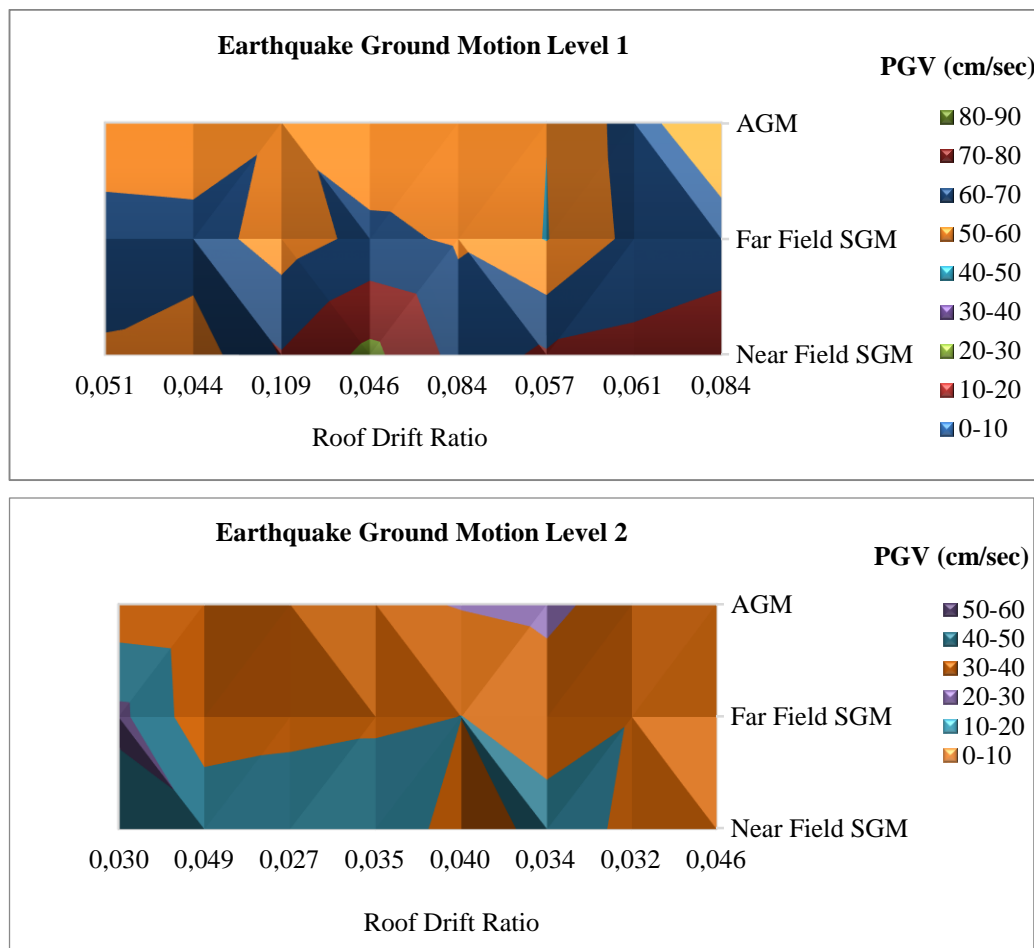


Fig. 7 – Variation of drift ratio and peak ground velocity (PGV) under artificial earthquakes (AGM), near and far field synthetic earthquakes (SGM) for ground motion level 1 and ground motion level 2

CONCLUSION

The response of masonry buildings subjected to seismic excitations depends basically on their failure mechanism and deformation characteristics. Considering the in-plane response of sliding shear failure of the masonry wall, displacement capacity was generally very large. When the principal tensile stress exceeds the in-plane tensile strength of the masonry wall, diagonal shear mode occurs. This case can be described by loss in strength and stiffness of masonry wall with limited displacement capacity. Another failure mechanism of flexural failure occurs generally in slender masonry walls due to the large ratio of moment to shear. In addition to these failure modes, rocking response can be observed due to second order effects. This study evaluates the seismic capacity of two story masonry buildings designed according to the TBSC 2019. In addition to the capacity curves determined by pushover analyses performed in two principal directions, time history analyses were also performed which led to the following conclusions:

- Near field ground motions is characterized by long period velocity pulses due to the directivity effect and the permanent tectonic deformation at the site which is referred to as the fling effect. Therefore, slender structures such as masonry minarets or towers with long natural time periods could be subjected to larger seismic demands under near field seismic excitations. But the

inspection of the results indicates that these effects could also be accounted for the selected non slender masonry building with a short natural time period.

- The maximum roof displacements that the masonry building experienced under near field excitations created for ground motion level 1 were significantly higher than those for the other earthquakes.
- Under the lateral shear force applied at roof level, the total displacement at the same level can be considered to be comprised of a displacement of the gross wall acting as a cantilever additional deflections resulting from flexibility of piers. For the ground motion level 2, under far field excitations, artificial ground motions and the October 23, 2011 Van Earthquake, the masonry building showed closed to an elastic behaviour. On the other hand, for the ground motion level 1, under near field excitations, the masonry building showed an inelastic behaviour.
- For the two levels of synthetic and artificial near field motions considered in this study, tensile stresses observed close the openings were significantly higher than the far field responses which would result in cracks. Therefore, in the design process, the location and size of the openings should be defined to optimize the performance under ground motion. Although, for ground motion level 2 under far field excitations, artificial ground motions and the October 23, 2011 Van Earthquake masonry walls passed the range of linear elastic limit a bit, under other earthquakes the deformation levels are well beyond the elastic limit.
- It can be concluded that the selected two story masonry building designed according to the 2019 TBSC can stably withstand inelastic actions without collapse. Results indicate that near field motions play an important role in seismic resistant design of masonry structures. Near field synthetic motions produced greater displacement responses in the masonry building than far field seismic excitations. However, it should be noted that in the case of stiff soils, the reverse can happen in that far field motions can result in higher responses than near field ground motions. Therefore, more analysis results of various masonry buildings subjected to near and far field seismic motion in stiff soil are needed. Major findings should be stated with respect to relevant literature. Recommendations for future research should also be made.

REFERENCES

- [1] Tomazevic M., 1999. Earthquake-resistant design of masonry buildings. Imperial College Press, London (UK).
- [2] EERI/IAEE, 2000. World housing encyclopedia. Earthquake Engineering Research Institute and the International Association for Earthquake Engineering. www.worldhousing.net.
- [3] El-Gawady M., Lestuzzi P., Badoux M., 2004. A Review of Conventional Seismic Retrofitting Techniques for URM. In: Proceedings, 13th International Brick and Block Masonry Conference.
- [4] D'Ayala D., Bostenaru M., Goretti A., Yakut A., Tomazevic M., 2005. Application of the World Housing. Encyclopedia Geophy Res Abstr, 7, 01649.
- [5] TBSC, 2019. Turkish Building Seismic Code (Türkiye Bina Deprem Yönetmeliği) Afet ve Acil Durum Yönetimi Başkanlığı.
- [6] Grimaz S. and MaliSan P., 2014. Near Field Domain Effects and Their Consideration in the International and Italian Seismic Codes. Bollettino di Geofisica Teorica ed Applicata 55(4): 717-738.
- [7] Koçyiğit A., 2013. New Field and Seismic Data about the Intraplate Strike-Slip Deformation in Van Region, East Anatolian Plateau E. Turkey. J. Asian Earth Science, 60, 586-605.
- [8] AFAD, 2011. Disasters and Emergency Situations Directorate of Turkey, 28 November 2011.
- [9] KOERI, 2011. Van earthquake (Mw 7.2) evaluation report as of 27 October 2011, Bogaziçi University, Kandilli Observatory and Earthquake Research Institute, 3.
- [10] KOERI, 2012. Son Depremler, Kandili Rasathanesi ve Deprem araştırma Enstitüsü, Boğaziçi Üniversitesi, <http://www.koeri.boun.edu.tr/sismo/zeqmap/gmapt.asp> (Son Erişim: 26 Nisan 2012).

- [11] Somerville P., Smith N., Graves R., Abrahamson N. 1997. Modification of Empirical Strong Ground Motion Attenuation Relations to Include the Amplitude and Duration Effects of Rupture Directivity. *Seismological Society Letters*, 1(68): 180-203.
- [12] Tehranizade M. and Movahed H. 2011. The Investigation of Steel Moment-Resisting Frames in Tall Structures in Near-Fault Range. *Journal of Civil Engineering and Mapping*, 5(44): 621-633.
- [13] Bray JD., Rodrigues-Marek, A., 2004. Characterization of Forward-Directivity Ground Motions in the Near-Fault Region. *Soil Dynamics and Earthquake Engineering*, 11(24): 815-828.
- [14] Davoodi M., Sadjadi M., 2015. Assessment of Near-Field And Far-Field Strong Ground Motion Effects on Soil Structure SDOF System. *International Journal of Civil Engineering*, 13.
- [15] Abrahamson N. and Somerville P., 1996. Effects of the Hanging Wall and Footwall on Ground Motions Recorded During the Northridge Earthquake. *Bulletin of the Seismological Society of America*, 86(1B), S93-S99.
- [16] Somerville P. G., 2002. Characterizing near fault ground motion for the design and evaluation of bridges. Paper presented at the Third National Conference and Workshop on Bridges and Highways, Portland, Oregon.
- [17] Bozorgnia B., Bertero V., 2004. *Earthquake Engineering: from Engineering Seismology to Performance-Based Engineering*, Florida, CRCPress.
- [18] Malhorta P., 1999. Response of Buildings to Near-Field Pulse Like Ground Motion. *Earthq. Eng. Struct. Dynamics*, 28(11): 1309–1326.
- [19] Alavi B., Krawinkler, H., 2001. Effects of Near-Fault Ground Motions on Frame Structures. John A. Blume. *Earthquake Engineering Center Stanford, California*, No. 138.
- [20] Rodriguez-Marek A., Bray JD., 2006. Seismic Site Response for Near-Fault Forward-Directivity Ground Motion. *Journal of Geotechnical and Geoenvironmental Engineering ASCE*, 1611-1620.
- [21] Li S., Xie L., 2007. Progress and Trend on Near-Field Problems in Civil Engineering. *Acta Seismological Sinica*, 1(20): 105-114.
- [22] Acarlar M., Bilgin E., Elibol E., Erkal T., Gedik İ., 1991. Van Gölü Doğu ve Kuzeyinin Jeolojisi. MTA Genel Müdürlüğü, No: 1061.
- [23] Selçuk L., Aydin H., 2012. Kuvaterner Yaşılı Alüvyal Zeminlerin Kuvvetli Yer Hareketine Etkisi: 2011 Van Depremleri. *Jeoloji Mühendisliği Dergisi*, 36(2).
- [24] BSSC, 2009. The 2003 NEHRP Recommended Provisions for the Development of Seismic Regulations for New Buildings and Other Structures, Building Seismic Safety Council, FEMA, Washington D. C.
- [25] SeismoSoft 2012. SeismoArtif, version 1.0.0 2012: SeismoArtif's help system 2002–2012. Seismosoft Ltd.
- [26] Halldorsson B. and Papageorgiou A. S., 2005. Calibration of the Specific Barrier Model to Earthquake Of Different Tectonic Regions. *Bulletin of the Seismological Society of America*, 95, 1276—1300.
- [27] Mucciarelli M., Spinelli A., Pacor F., 2004. Un Programma per la Generazione di Accelerogrammi Sintetici "Fisici" Adeguati Alla Nuova Normativa. *Proceedings of XI Congresso Nazionale L'Ingegneria Sismica in Italia*, Genova, Italy.
- [28] Saragoni G.R., Hart G.C., 1974. Simulation of Artificial Earthquakes. *Earthquake Engineering-and Structural Dynamics*, 2, 219-267.
- [29] Newmark, N.M., 1959. A Method of Computation for Structural Dynamics. *Journal of the Engineering Mechanics Division ASCE*, 85(3): 67-94.
- [30] CEN., 2004. European Standard Eurocode 8: Design of Structures for Eathquake Resistance. EN 1998-1:2004, Comité Européen de Normalisation, Bruxelles.
- [31] FEMA E74, 2012. Reducing the Risks of Nonstructural Earthquake Damages, Federal Emergency Management Agency, Practical Guide.
- [32] FEMA 273, 1997. NEHRP Guidelines for the Seismic Rehabilitation of Buildings, Federal Emergency Management Agency, U.S. Department of Homeland Security, Washington DC, USA.

DYNAMIC CONSTRUCTION CONTROL METHOD FOR A DEEP FOUNDATION PIT WITH SAND-PEBBLE GEOLOGY

Xuansheng Cheng¹, Bingbing Luo¹, Haibo Liu¹, Qingchun Xia¹ and Chaobo Chen²

1. School of Civil Engineering, Lanzhou University of Technology, Lanzhou, No. 287, Langongping Road, 730050, China; chengxslut@sina.com, 2031663951@qq.com, 2459612631@qq.com, 278962530@qq.com
2. China Railway 21st Bureau Group Co., LTD., No. 921, Beibinhe West Road, Lanzhou, China; 694874282@qq.com

ABSTRACT

Taking the water-rich sand and pebble geology deep foundation pit of Jinfu Station of Chengdu Metro Line 6 as the research object, combined with the ladder excavation method of slotting, utilizing finite difference software FLAC 3D as well as on-site monitoring result, the deformation law of the diaphragm wall during the dynamic excavation of the foundation pit is analysed, and the influence of the relative stiffness between the vertical and horizontal walls of the foundation pit on the lateral deformation of the retaining structure is discussed. The results show that while using the ladder excavation method of slotting, the maximum lateral displacement of the underground diaphragm walls decreases gradually with the excavation depth of the foundation pit, which occurs at the intersection of the middle point of the oblique excavation line and the step distance section of the transverse excavation. Additionally, the lateral displacement increases closer to the excavation section. The lateral displacement of the envelope enclosure mainly depends on the relative constraint stiffness of the vertical and horizontal underground diaphragm wall of the foundation pit. The use of the ladder layered excavation method of slotting can effectively reduce the lateral displacement of the underground diaphragm wall. The simulated result and on-site monitoring result are nearly the same. These results can provide a corresponding theory and engineering basis for the selection of excavation methods for the same type of sand and pebble stratum foundation pit.

KEYWORDS

Sand and pebble geology, Deep foundation pit, Numerical simulation, Dynamic control, Lateral displacement

INTRODUCTION

With the rapid development of China's economy, the construction of urban rail transit has also achieved sustained and rapid development. During the construction of urban infrastructure such as the Chengdu Metro, unfavourable engineering geological conditions such as water-rich sand and pebble strata have brought greater difficulties to the construction of engineering foundation pits and have created technical problems that require solving. The geological conditions in Chengdu mostly consist of sand and pebble strata, and they are widely distributed. There are also large differences in the spatial distribution of the strata. Sand-pebble formations have a skeleton structure, a rich porosity, a large particle dispersion, almost zero cohesion, poor disturbance resistance, and easy water permeability. These strata are typical in mechanically unstable formations. During the excavation of foundation pits, due to insufficient research on this type of geological condition and unknown engineering characteristics, engineering accidents such as overall instability of the foundation pit and ground collapse are often caused. Therefore, it is of



great theoretical and practical significance to study the dynamic construction control method of sandy pebble geological deep foundation pits.

Scholars have adopted different methods to study different approaches to engineering and technical problems in the excavation of deep foundation pits. Liao et al [1] used the field monitoring data of the shotcrete anchoring of a deep foundation pit in Chengdu to obtain the deformation law of deep foundation pits in Chengdu area and its influence range, and proposed a new type of supporting strength, stability calculation method and deformation control method for deep foundation pit. Yu et al [2] verified the necessity of 3D analysis for foundation pit engineering. Ou et al [3] gave the deformation characteristics of foundations pits for the Taipei soft soil area, while Wang et al [4] gave the deformation characteristics of foundation pits under soft soil conditions. Ou et al [5,6] explored the changes in the lateral movement of the wall and the settlement of the ground surface behind the wall in different regions and under different stratum conditions, as well as the characteristics of time and space. Tong et al [7] used the particle discrete element method to analyse the changes in the surrounding ground settlement during the excavation of the deep foundation pit. Finno et al [8] obtained the range of influence of the pit angle effect for the Chicago stratum. Feng et al [9] analysed the overall deformation of the subway station foundation pit in consideration of the spatial effects. Li et al [10] discussed the space-time laws of the ground subsidence, pile displacement, supporting axial force and pit bottom bulging of the foundation pit. Wang et al [11] established a numerical analysis model of the deep foundation pit supporting structure to analyse the settlement and deformation laws.

As can be seen above, there are few studies on the influence of the relative stiffness of the vertical and horizontal walls of the foundation pit on the lateral deformation of the retaining structure for the long-strip subway foundation pit in the water-rich area with sand and pebble geology. In addition, the general excavation of foundation pits usually only considers the impact of layered excavation on the lateral displacement of the underground diaphragm wall of the subway foundation pit, and there are few studies on the impact of soil excavation methods and support erection timing. At the same time, there is still a lack of systematic, comprehensive and detailed research on the dynamic construction control methods of deep foundation pits in sand and pebble geology. Therefore, using the FLAC 3D finite difference software, combined with the grooved stepped foundation pit excavation method, the deformation law of the underground continuous wall during the dynamic excavation of the foundation pit is analysed and studied; the relationship between the relative rigidity of the transverse wall and the longitudinal wall of the foundation pit is discussed; the influence of earth excavation method and support erection on lateral displacement of underground diaphragm wall of subway foundation pit is studied, which has important practical guiding significance for solving practical engineering problems.

Excavation method for the stepped sand-pebble layer of a deep foundation pit

This research relies on Jinfu Station of Chengdu Metro Line 6, the intermediate station of the first and second phases of the project. The foundation pit of the standard section of the station is 20 m wide, approximately 20.36-21.5 m deep and 311.3 m long. The half-cover digging construction method is adopted for construction, and the supporting system adopts a type of supporting pile + internal support. The support system for the excavation standard section of the foundation pit adopts a reinforced concrete support + three steel supports, and the diagonal wells are used at the end wells. The top of the pile is provided with a reinforced concrete crown beam, the first support is supported on the concrete crown beam, and the steel support is supported on the steel enclosure.

Vertical excavation method of the foundation pit sand-pebble layer

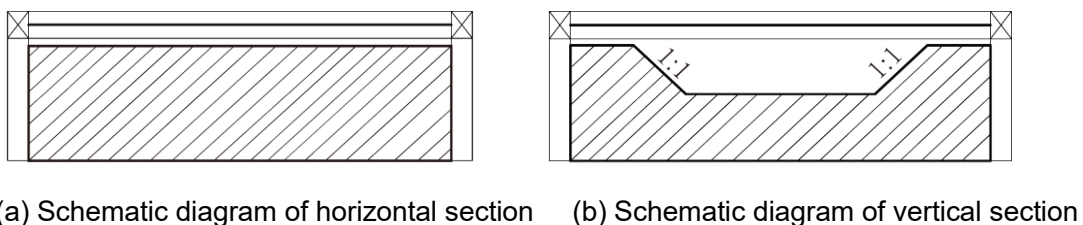
For the excavation of the vertical soil of the foundation pit, four layers of excavation were used. The first excavation reached the design elevation of the bottom of the first concrete support. The second excavation depth was 7.5 m, excavated for three times respectively, each excavation depth was 2.5 m; the third excavation depth was 6.0 m, excavated for three times respectively,



each excavation depth was 2 m; the last excavation was excavated to the design base level. The specific excavation method of each layer is described as follows.

Excavation of the first layer of earthwork

The first layer of earthwork is excavated as a whole to form a plane at the bottom of the crown beam. After the template is installed, the first layer of the concrete support is poured. After the concrete support reaches the design strength, excavation from the north to the south is used to excavate the second layer of soil grooves. During the excavation, the support plane is reserved for the construction plane, ensuring the groove width in the middle of the foundation pit is 9 m. The soil on both sides of the steps is stable. A schematic diagram of the excavation section of the first layer of earthwork is shown in Figure 1.



(a) Schematic diagram of horizontal section (b) Schematic diagram of vertical section

Fig. 1 – Schematic diagram of the excavation section of the first layer of earthwork

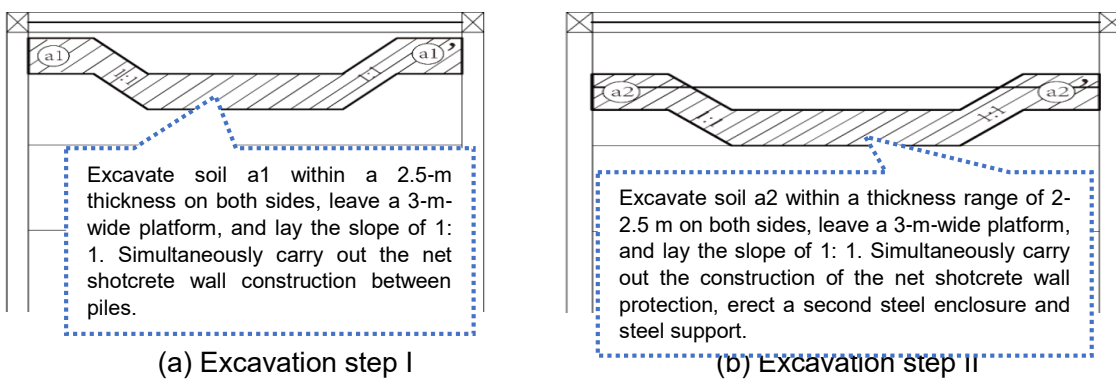


Fig. 2 – Vertical concrete excavation diagram of the second layer of earthwork

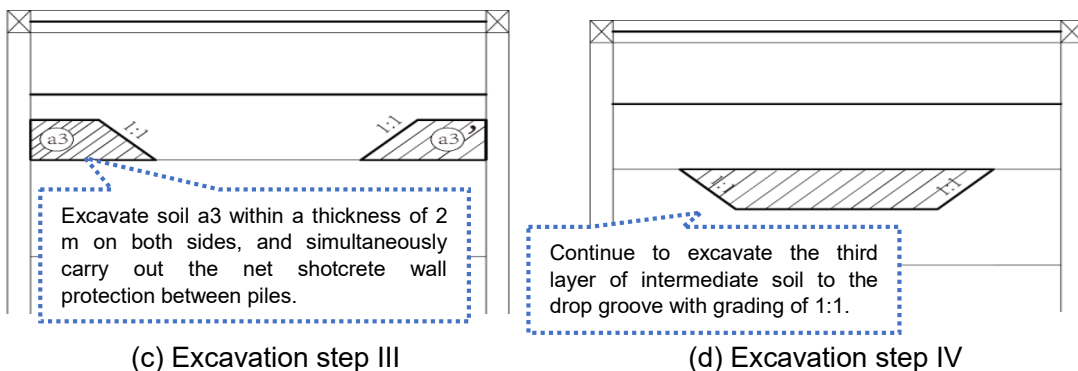


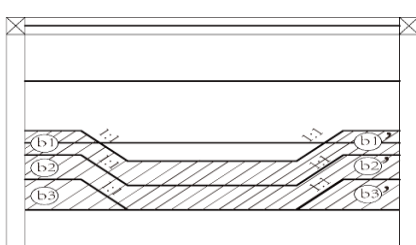
Fig. 2 – Vertical concrete excavation diagram of the second layer of earthwork

Excavation of the second layer of earthwork

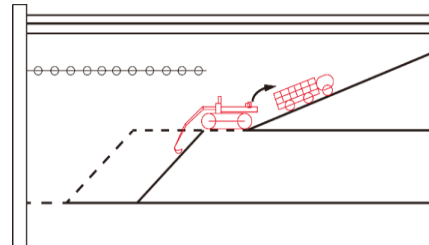
The excavation depth of the second layer of earthwork is 7.5 m, which is excavated for three times, and each excavation depth does not exceed 2 ~ 2.5 m. The concrete vertical excavation of the second layer of earthwork is shown in Figure 2.

Excavation of the third layer of earthwork

The excavation depth of the third layer of earthwork is 6 m, which is excavated for three times, and each excavation depth does not exceed 2 m. The middle slot is excavated first in the horizontal direction, the sides of the slot are sloped at 1:1, and the soil in b1, b2, and b3 are excavated on both sides in sequence. Platforms with a width of 3 m are left on both sides of each excavation. Soil spraying is carried out on the soil platform. A third steel enclosure and steel support is erected after the b1 soil is excavated. A schematic diagram of the excavation section of the third layer of earthwork is shown in Figure 3.



(a) Excavation step (b₁-b₁, b₂-b₂, b₃-b₃ part)

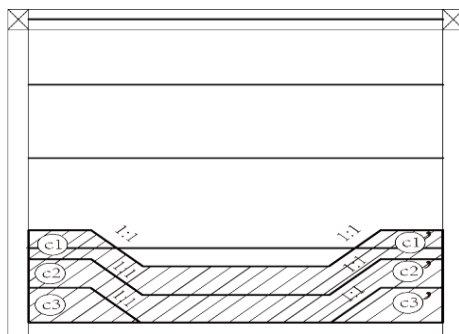


(b) Mechanical operation diagram

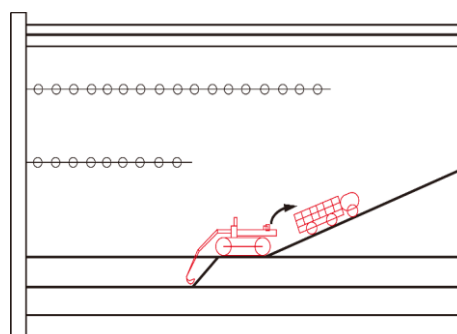
Fig. 3 – Schematic diagram of the vertical excavation section of the third layer

Excavation of the fourth layer of earthwork

The excavation depth of the fourth layer of earthwork is 6.4 m, and it is excavated three times; each excavation depth does not exceed 2 ~ 2.4 m. The middle slot is excavated first in the horizontal direction, both sides of the slot are sloped at 1:1, and the soil in c1, c2, and c3 is excavated on both sides in sequence, leaving a 3 m wide platform on each side of the excavation. Soil spraying is carried out on the soil platform. Where the excavation reaches 300 mm above the ground of the foundation pit, manual excavation should be used to remove the remaining earthwork. Over-excavation is strictly prohibited to minimize disturbance to the foundation soil. A schematic diagram of the excavation section of the fourth layer of earthwork is shown in Figure 4.



(a) Excavation step (c₁-c₁, c₂-c₂, c₃-c₃ part)



(b) Mechanical operation diagram

Fig. 4 – Schematic diagram of the excavation section of the fourth layer of earthwork

MODELLING AND SIMULATION

Calculation parameters and models

The irregular and convex edge part of the foundation pit on the actual site is simplified to a regular rectangular end well. According to St. Venant's theorem, the model boundary is 5 times deeper than the excavation boundary of the foundation pit and 3 times deeper in the depth direction.

The parameters of Tables 1~3 are derived from experience and engineering practice. The support is simulated using beam elements in Table 1, and the beam element parameters can be seen in Table 2; the plastic-hardening constitutive model, and the soil parameters of each layer can be seen in Table 3. During the excavation process, the precipitation process of the foundation pit is no longer considered. The final calculation model of the solid unit is $420\text{ m} \times 140\text{ m} \times 60\text{ m}$.

Tab. 1 - Main parameters of the underground diaphragm wall

Diaphragm Wall	E/GPa	ν	Thickness t/m	$\rho/(\text{kg}/\text{m}^3)$	$k_n/(\text{N}/\text{m}^3)$
Inside	24.00	0.20	0.85	2500	1.8×10^{10}
Outside	24.00	0.20	0.85	2500	1.8×10^{10}
Diaphragm Wall	$k_s/(\text{N}/\text{m}^3)$	c/kPa	$\psi/^\circ$	$f_t/(\text{N}/\text{m}^2)$	$c_r/(\text{N}/\text{m}^2)$
Inside	1.8×10^{10}	7.00	6.00	0.00	2500
Outside	1.8×10^{10}	14.00	12.50	0.00	2500

Tab. 2 - Support unit parameters

Support	Section size /mm	Density $\rho/(\text{kg}/\text{m}^3)$	E/GPa	Cross-sectional area S/m^2	I_y/m^4	I_z/m^4
RC Support	1200×1400	2500	25.0	1.68	0.2016	0.2744
Steel support	$\phi 609$ ($t=6$)	7800	200	0.0298	1.32×10^{-3}	1.32×10^{-3}



Tab. 3 - Soil layer parameters of the plastic-hardening model

Model parameters	Miscellaneous fill [12]	Clay [12]	Sand [12]	Loose sand-pebble	Medium dense sand-pebble	Compact sand-pebble
p^{ref} /kPa	100.00	100.00	100.00	100.00	100.00	100.00
E_{50}^{ref} /MPa	6.00	8.00	30.00	27.27	20.07	14.86
E_{ur}^{ref} /MPa	18.00	24.00	90.00	109.07	80.29	59.44
E_{oed}^{ref} /MPa	6.00	4.00	30.00	8.19	11.12	10.10
v_{ur}	0.20	0.20	0.20	0.20	0.20	0.20
c' /kPa	0.00	5.00	1.00	0.00	0.00	0.00
$\phi'/^{\circ}$	15.00	25.00	32.00	26.05	34.65	42.05
$\psi/^{\circ}$	0.00	0.00	2.00	14.29	13.51	13.43
m	0.65	0.80	0.50	0.22	0.42	0.63
k_0^{nc}	0.44	0.50	0.47	0.56	0.43	0.33
R_f	0.90	0.90	0.90	0.34	0.79	0.90

Numerical simulation conditions

The site adopts the stepped excavation construction method of the slot, combined with the longitudinal excavation method, and according to the vertical excavation of the soil layer, the simulation conditions are set as shown in Figure 5. The first floor is excavated to the first concrete support design elevation position (R1), and the concrete support is applied. Then, after the groove excavation (R2) of the remaining soil layer is finished, the excavation of the remaining soil layer is performed from the lower left corner to the upper right corner according to the simulation condition setting table during the simulation. The excavation of each layer is divided into two steps. The first step is to excavate the slot (*Z) in the middle, and the second step is to clean up the steps (*B) on both sides. When excavating to the support design elevation, support erection is carried out in time. The excavation method of the entire foundation pit adopts a backward angled excavation method, and the foundation pit is excavated in turn.

CALCULATION RESULTS AND RESULTS ANALYSIS

To accurately obtain the lateral movement of the underground continuous wall during the stepped excavation of the slotted groove, when the fourth soil excavation in the first section reached the design elevation of the bottom of the foundation pit, data was recorded (the excavation simulation condition setting chart is the excavation condition of the top left corner without filling background). The data is recorded after each excavation (the excavation simulation condition setting chart shows the conditions of completing the same filling background colour). The names of the data are recorded as working conditions I ~ X, respectively.



Total excavation depth / m	Excavation number	Layer number	Layer depth / m	Excavation conditions										
21.3	First layer excavation	First floor	1.4	R1										
				R2										
	Second layer excavation	a1	2.5	a11Z a11B	a12Z a12B	a13Z a13B	a14Z a14B	a15Z a15B	a16Z a16B	a17Z a17B	a18Z a18B	a19Z a19B	a10Z a110B	
		a2	2.5	a21Z a21B	a22Z a22B	a23Z a23B	a24Z a24B	a25Z a25B	a26Z a26B	a27Z a27B	a28Z a28B	a29Z a29B	a210Z a210B	
		a3	2.5	a31Z a31B	a32Z a32B	a33Z a33B	a34Z a34B	a35Z a35B	a36Z a36B	a37Z a37B	a38Z a38B	a39Z a39B	a310Z a310B	
	Third layer excavation	b1	2.0	b11Z b11B	b12Z b12B	b13Z b13B	b14Z b14B	b15Z b15B	b16Z b16B	b17Z b17B	b18Z b18B	b19Z b19B	b110Z b110B	
		b2	2.0	b21Z b21B	b22Z b22B	b23Z b23B	b24Z b24B	b25Z b25B	b26Z b26B	b27Z b27B	b28Z b28B	b29Z b29B	b210Z b210B	
		b3	2.0	b31Z b31B	b32Z b32B	b33Z b33B	b34Z b34B	b35Z b35B	b36Z b36B	b37Z b37B	b38Z b38B	b39Z b39B	b310Z b310B	
	Fourth layer excavation	c1	2.0	c11Z c11B	c12Z c12B	c13Z c13B	c14Z c14B	c15Z c15B	c16Z c16B	c17Z c17B	c18Z c18B	c19Z c19B	c110Z c110B	
		c2	2.0	c21Z c21B	c22Z c22B	c23Z c23B	c24Z c24B	c25Z c25B	c26Z c26B	c27Z c27B	c28Z c28B	c29Z c29B	c210Z c210B	
		c3	2.4	c31Z c31B	c32Z c32B	c33Z c33B	c34Z c34B	c35Z c35B	c36Z c36B	c37Z c37B	c38Z c38B	c39Z c39B	c310Z c310B	

Note: Z--Middle slotted soil; B--Step soil on both sides.

Fig. 5 – Setup diagram of the excavation simulation conditions

Horizontal displacement of the underground continuous wall in the x direction

The cross-sectional position diagram of the horizontal displacement data point in the X direction of the underground diaphragm wall is shown in the Figure 6.

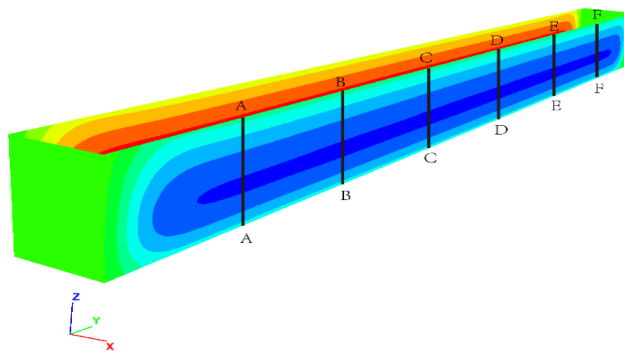


Fig. 6 - Cross-section location of horizontal displacement data points in X direction of underground diaphragm wall

During the excavation of the foundation pit, to obtain the displacement change of the underground continuous wall in the x direction, six sections were taken as the data extraction surface, and the distance between adjacent sections was 50 m. The data obtained for each section is shown in Figure 7.



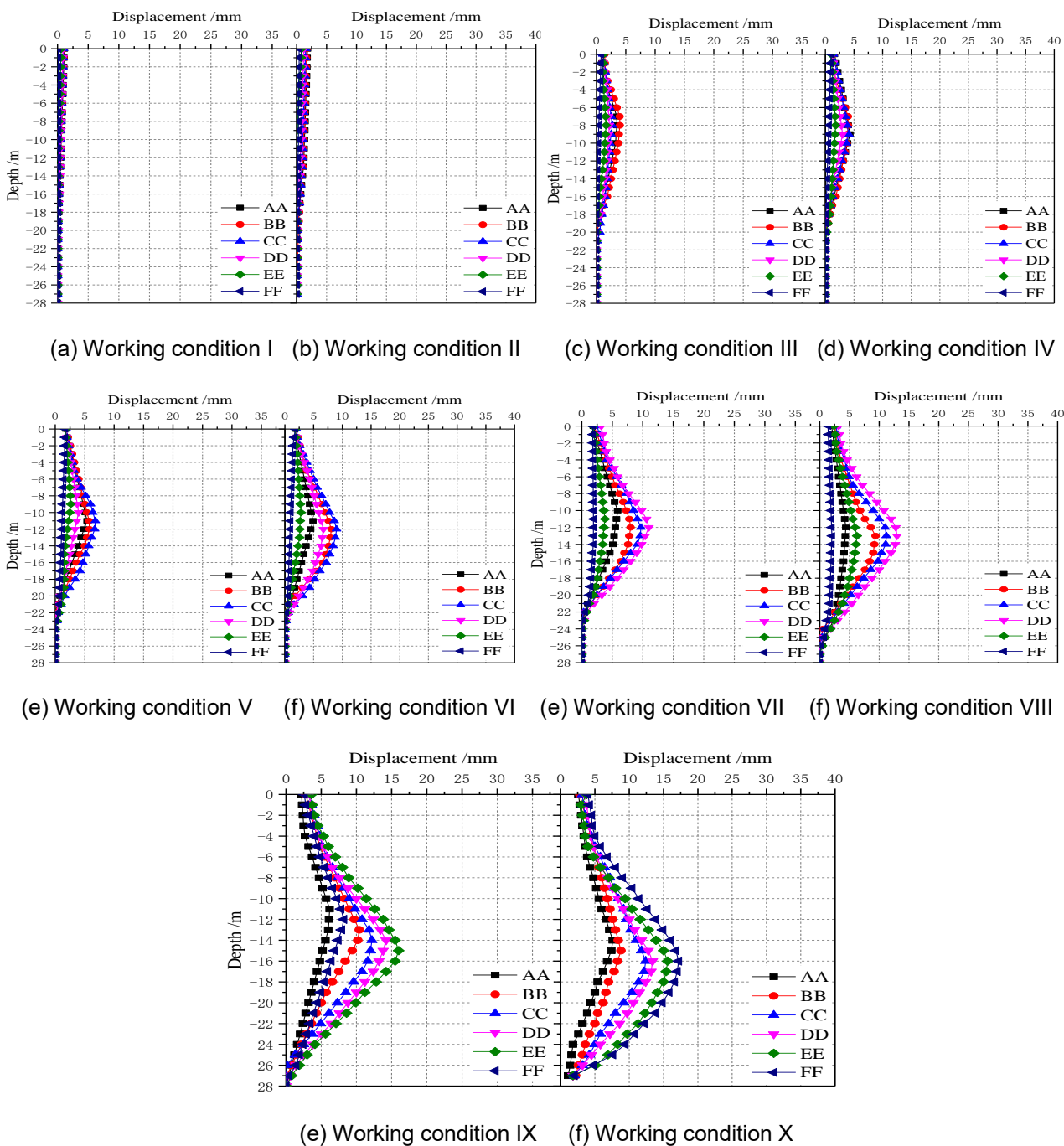


Fig. 7 – Horizontal displacement of the underground diaphragm wall in the x direction

It can be seen from Figure 7 that during the excavation of the foundation pit, the first and second working conditions were excavated to the design elevation of the foundation pit, and the entire foundation pit was excavated to a lesser extent. The difference in the earth pressure on both sides of the underground continuous wall was not sufficient to resist the embedded rigidity at the bottom of the underground continuous wall, and because of the stepped excavation of the slotted groove, the support was erected in time, and the maximum side shift was 2.2 mm. Later, inclined-angle retrogressive excavation was adopted, and the excavation construction step was 30 m. It can be seen from working conditions III and IV that as the excavation of the foundation pit gradually increased, the lateral movement of the underground continuous wall gradually increased, and the maximum moving section appeared at the intersection of the midpoint of the diagonal

excavation line and the excavation section. Second, the maximum lateral displacement section was on the adjacent side of the maximum lateral displacement surface. The closer to the cross section of the lateral excavation construction step, the larger the lateral displacement was. The maximum lateral displacement was 4.8 mm. When the excavation reached working conditions V or VI, the excavation volume of the soil inside the foundation pit exceeded half of the total excavation volume of the soil. The difference in the earth pressure on both sides of the underground diaphragm wall gradually approached the bending resistance provided by the embedded end of the underground diaphragm wall, which caused the tendency of the underground diaphragm wall to rotate. The maximum excavation depth of the foundation pit was close to 16.9 m after the excavation to working conditions VII and VIII, and the supporting system was fully applied. The maximum lateral displacement of the underground continuous wall was 13.2 mm. When the excavation reached working conditions IX and X, the lateral movements of the underground continuous wall at section AA were almost equal, which indicates that the internal forces of the underground continuous wall were redistributed to reach a stable and relatively balanced state with each envelope system. The lateral movement of the underground continuous wall in the x direction was 17.6 mm.

Horizontal displacement of the underground continuous wall in the Y direction

The cross-sectional position diagram of the horizontal displacement data point in the Y direction of the underground diaphragm wall is shown in Figure 8.

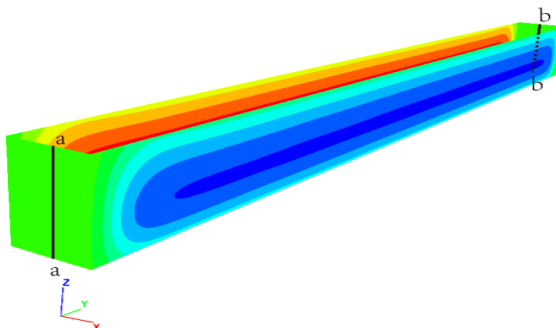


Fig. 8 - The position of the cross section of the horizontal displacement data point in the Y direction of the underground diaphragm wall

To obtain the deformation evolution mechanism of the horizontal underground diaphragm wall and to study the constraint of the horizontal wall of the end well of the foundation pit on the vertical underground diaphragm wall, the middle section is taken at the lateral wall on both sides, and the calculation results are shown in Figure 9.

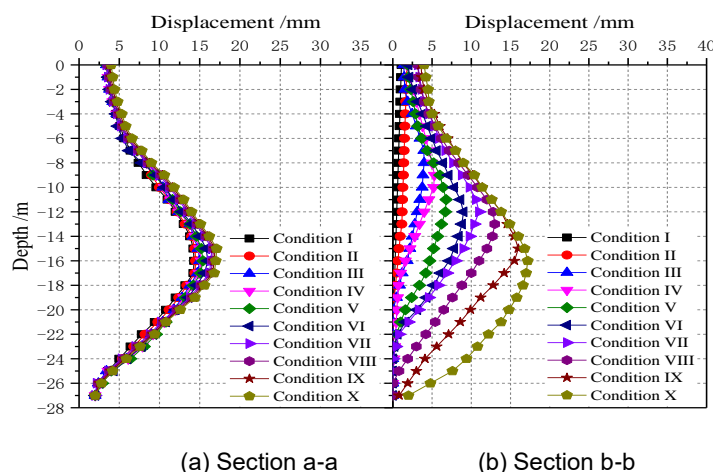


Fig. 9 – Horizontal displacement of the underground diaphragm wall in the y direction

When extracting the result, the fourth condition soil in the first section has been excavated to the design elevation at the bottom of the foundation pit, and the lateral movement of its underground continuous wall has stabilized, as shown in Figure 9 (a). The minimum lateral displacement of the underground continuous wall in section a-a is 14.3 mm. During the gradual excavation of the foundation pit, the lateral displacement of the underground continuous wall gradually increases due to the redistribution of the internal forces of the underground continuous wall and its supporting system. The maximum lateral shift value is 17.1 mm. During the excavation process, the shape of the lateral shift curve of section a-a did not change. For section b-b, since the excavation of the soil is from the original unexcavated state until the excavation reaches the base design elevation, during the entire excavation process, when the excavation depth of the foundation pit is small, the bottom of the underground continuous wall has a larger embedded stiffness, the lateral deformation of the foundation pit retaining structure is similar to that of the "cantilever beam", and the maximum lateral displacement mainly occurs at the top of the wall, at approximately 1.1 mm. With the increase in the excavation depth, the position of the maximum displacement of the underground continuous wall gradually moves down. When the foundation pit is excavated to the first concrete design elevation, the first concrete support did not reach the design strength during construction. The overall rigidity of the foundation pit did not improve. Thus, the top lateral deformation of the retaining wall of the underground continuous wall of the foundation pit is completely determined by the longitudinal (horizontal) relative stiffness of the wall. With the increase in the excavation depth, it can be seen that the lateral stiffness of the retaining structure of the foundation pit is significantly stronger than that of the longitudinal side. The relative restraint effect along the wall is related to the excavation depth. The larger the longitudinal dimension of the foundation pit, the closer the plane deformation of the foundation pit to the plane strain state. During the subsequent excavation process, the height of the maximum lateral deformation of the underground continuous wall gradually develops from the top of the underground continuous wall to the deep soil. When excavated to the design elevation of the bottom of the foundation pit, the maximum lateral deformation in the y direction is 16.8 mm.

Analysis of on-site monitoring results of horizontal displacement of underground diaphragm wall

In order to verify the rationality of the numerical simulation result, the horizontal displacement of the underground diaphragm wall during the on-site excavation of the deep foundation pit was monitored and analysed. Therefore, the representative a-a section of the short side direction and b-b section of the long side direction of the deep foundation pit are selected to analyse the on-site monitoring data of underground diaphragm wall, and the change law curves are drawn, as shown in Figure 10.



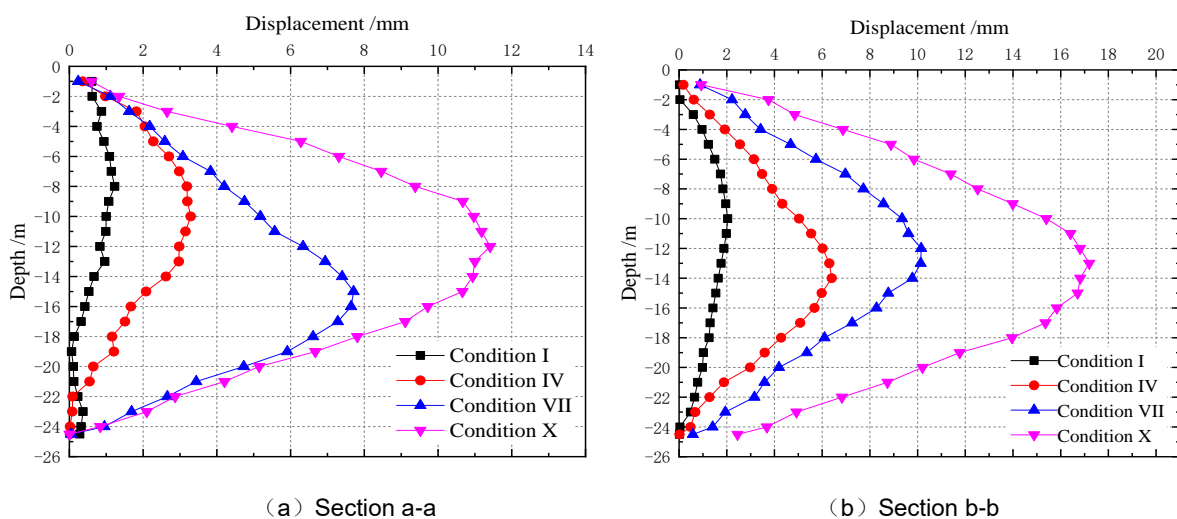


Fig. 10 – On-site horizontal displacement of underground diaphragm wall

In Figure 10, it can be seen that when the excavation depth of the foundation pit is small, the lateral displacement value of the underground diaphragm is small. The maximum horizontal displacement of the diaphragm wall in the deep layer gradually decreases with the increase of the excavation depth of the foundation pit. The maximum value appears near the excavation surface. The deep horizontal displacement of the diaphragm wall shows a “big belly” shape. When the foundation pit is excavated to the designed bottom elevation, the maximum side displacement of a section of the short side about the foundation pit is 11.41 mm, the maximum side displacement of b-b section of the long side direction is 17.2 mm, and the side displacement of the long side of the foundation pit is much larger than that of the short side. It indirectly indicates that during the excavation of the foundation pit, the lateral displacement of the diaphragm wall mainly depends on the relative restraint stiffness of the diaphragm wall in the vertical and horizontal directions of the foundation pit.

Comparison and analysis of simulated result and on-site monitoring result

By analysing and comparing the numerical simulation value curves (Figure 7 and Figure 9) with the on-site monitoring value curve (Figure 10), it can be easily seen that during the construction process, the displacement of the underground diaphragm wall is small; and the change law of lateral displacement of the two changes consistently with the increase of excavation depth, both appear as “big belly-shaped”; at the same depth, the displacement value error of the two is small, which verifies that the simulation calculation results are credible and proves the rationality of the numerical test method; meanwhile, it reveals that the stepped excavation construction method can effectively control the displacement of the underground continuous wall.

Grooved step construction control method

Combined with the previous studies of the research group, the overall layered foundation pit excavation method is adopted. When the foundation pit is excavated to the design elevation of the pit bottom, the maximum lateral displacement of the underground continuous wall is 28.5 mm, while the maximum lateral displacement of the underground continuous wall obtained by the stepped excavation construction method is 17.6 mm. Compared with the overall performance, the layered foundation pit excavation method reduces the maximum side shift by 38%. It can be concluded that during the excavation of the foundation pit, the stepped excavation of the groove is very effective in reducing the deformation of the foundation pit, and during the earthmoving process, the method of reserving steps on both sides of the foundation pit can be used for more



than just subsequent erection. The support provides a good working surface and plays a beneficial role in controlling the lateral deformation of the foundation pit retaining structure. In the actual design of the foundation pit enclosure structure, the stiffness of the underground diaphragm wall can be appropriately reduced, and construction cost can be achieved through strict control of the construction technology.

CONCLUSIONS

For the simulation method during the excavation of the foundation pit, in order to reduce the calculation, cost in the simulation process, the overall layered excavation method is generally adopted. In this paper, we take the actual subway foundation pit Jinfu station as an example, combined with the actual construction conditions on site, adopting the grooved stepped excavation method, the finite difference software FLAC 3D is used to simulate the excavation process of the foundation pit. The simulated result and on-site monitoring result are nearly the same, which verifies the rationality of finite element method. The specific conclusions are drawn as follows:

- 1) During the excavation process, the larger the longitudinal dimension of the foundation pit, the closer the deformation evolution mechanism of the underground diaphragm wall to the plane strain problem. The grooved stepwise excavation method is adopted. As the excavation depth of the foundation pit gradually increases, the position of the maximum lateral displacement of the underground continuous wall gradually moves down and appears at the midpoint of the diagonal excavation line and the lateral excavation. As the cross position of the step section moves closer to the excavation section, the side shift becomes greater.
- 2) During the excavation of the foundation pit, the lateral constraint of the end well of the foundation pit is significantly greater than the longitudinal constraint. The lateral displacement of its retaining structure is mainly determined by the relative constraint stiffness ratio of the vertical and horizontal underground diaphragm wall of the foundation pit. In the past, the foundation pit has been simplified to consider the plane strain problem, which failed to correctly reflect the constraints provided by the end well on the vertical underground diaphragm wall, and the design was too conservative.
- 3) By comparing the simulated result and on-site monitoring result, it is found that the error between them is small, and their displacement changing trend law is very similar, verifying the reliability of simulation method.
- 4) The slotted stepwise layered excavation method can effectively reduce the lateral movement of the underground continuous wall by 38% compared with the overall excavation method. During the groove drawing process, the two side steps provide an effective working surface for the erection of the support.

ACKNOWLEDGMENTS

This research is supported in part by the Science and Technology Project in China Railway 21th Bureau Group Co. LTD. (Grant number: 17C-5).

REFERENCES

- [1] Liao X.B., Chen Y., Zhu M., 1998. Design for anchor-shotcrete support structure and its application to protecting wall works of deep foundation pit in Chengdu area. *The Chinese Journal of Geological Hazard and Control*, Vol.9: 108-113. <https://doi.org/10.16031/j.cnki.issn.1003-8035.1998.01.020>
- [2] Yu J. L., Gong X.N., 1999. Spatial behavior analysis of deep excavation. *Chinese Journal of Geotechnical Engineering*, Vol. 21: 21-25.



- [3] Ou C., Hsieh P. G., Chou D. C., 1993. Characteristics of ground surface settlement during excavation. Canadian Geotechnical Journal, Vol.30, 758-767. <https://doi.org/10.1139/t93-068>
- [4] Wang J.H., Xu Z.H., Wang W.D., 2007. Analysis of deformation behavior of deep excavations supported by permanent structure. Chinese Journal of Geotechnical Engineering, Vol. 29: 1899-1903.
- [5] Ou C.Y., Chiou D.C., Wu T.S., 1996. Three-dimensional finite element analysis of deep excavations. Journal of Geotechnical Engineering, Vol. 122: 337-345. [https://doi.org/10.1061/\(ASCE\)0733-9410\(1996\)122:5\(337\)](https://doi.org/10.1061/(ASCE)0733-9410(1996)122:5(337))
- [6] Wang J. H., Xu Z. H., Wang W. D., 2010. Wall and ground movements due to deep excavations in shanghai soft soils. Journal of Geotechnical and Geoenvironmental Engineering, Vol.136: 985-994. [https://doi.org/10.1061/\(ASCE\)GT.1943-5606.0000299](https://doi.org/10.1061/(ASCE)GT.1943-5606.0000299)
- [7] Tong J.J., Wang M.N., Yu L., et al., 2014. A study of the land subsidence around the deep foundation pit of the Chengdu subway station. Hydrogeology & Engineering Geology, Vol. 42:97-101. <https://doi.org/10.16030/j.cnki.issn.1000-3665.2015.03.16>
- [8] Finno R.J., Blackburn J. T., Roboski J. F., 2007. Three-dimensional effects for supported excavations in clay. Journal of Geotechnical and Geoenvironmental Engineering, Vol.133: 30-36. [https://doi.org/10.1061/\(ASCE\)1090-0241\(2007\)133:1\(30\)](https://doi.org/10.1061/(ASCE)1090-0241(2007)133:1(30))
- [9] Feng C. L., Zhang D.L., 2018. The general deformation mode and its application of subway station foundation pit in sandy cobble stratum. Chinese Journal of Rock Mechanics and Engineering, 37:4395-4405. <https://doi.org/10.13722/j.cnki.jrme.2018.0722>
- [10] Li S., Zhang D.L., Shao Y.D., 2019. Research on spatio-temporal law of deep excavation deformation under complicated environment in Beijing Subway Station. Journal of Beijing Jiaotong University, Vol. 43: 29-36. <https://doi.org/10.11860/j.issn.1673-0291.20190040>
- [11] Wang M.N., Zeng Z.Q., Zhao Y.T., et al., 2019. Study on deformation rules of earth's surface and support structure for deep foundation pit in bad gradation pebble stratum. Journal of Railway Science and Engineering, Vol.16: 646-653. <https://doi.org/10.19713/j.cnki.43-1423/u.2019.03.012>
- [12] Brinkgreve R.B.J., Engin E., Swolfs W.M., et al., 2013. PLAXIS 3D 2013 User's Manuals, The Netherlands: Plaxis BV, Delft.



SUGARCANE STRAW ASH EFFECTS ON LIME STABILIZED LATERITIC SOIL FOR STRUCTURAL WORKS

Olugbenga Oludolapo Amu¹, Christopher Ajiboye Fapohunda¹,

Oluwaseun Adedapo Adetayo¹, Moronfolu Festus Ilesanmi²

1. *Federal University Oye Ekiti, Faculty of Engineering, Department of Civil Engineering, Ekiti State, Nigeria; oluwaseun.adetayo@fuoye.edu.ng*
2. *Obafemi Awolowo University, Faculty of Technology, Department of Civil Engineering, Ile-Ife, Osun State, Nigeria*

ABSTRACT

The research examined the appropriateness of sugarcane straw ash (SSA) as a modifier in lime stabilized lateritic soil with a view of improving the Geotechnical considerations of the soil structures. Elementary and Geotechnical investigations were performed on the lime stabilized soil samples and also when varying percentages of SSA were introduced. The elementary tests incorporated the moisture content, specific gravity, molecule size examination, and Atterberg's limits, while the Geotechnical were: compaction, California Bearing Ratio (CBR), and unconfined compression test. The lateritic samples were stabilized with 7% optimum of lime by weight, while SSA contents were gradually introduced at optimum lime up to 12.5% bulk of the soil. The addition of the SSA to the lime stabilized lateritic soil diminished the plastic indices from 25.09 to 21.98%, 24.76 to 21.09% and 19.43 to 15.37%; increased the unsoaked CBR values from 6 to 12%, 6 to 10% and 8 to 10 % and the unconfined compressive strengths from 88.10 to 126.13 kPa, 73.8 to 114.1 kPa and 52.17 to 127.85 kPa for tests A, B and C respectively. Concluding, the expansion of sugarcane straw debris improved the Geotechnical considerations of the lime stabilized lateritic soil tests for structural works.

KEYWORDS

Lateritic soil, Lime-stabilized soil, Sugarcane Straw Ash (SSA)

INTRODUCTION

Stability of civil infrastructures such as buildings, highways, and so on requires that they are found on firm and strong soil strata. However, it is not unusual to encounter on new sites, especially in the establishment of new built environment, soils that are not suitable for founding building and highway infrastructures. Removal of such soil and replacement with better soil from borrowing pit may prove expensive [1]. More often, it is more economical to employ one of the soil improvement methods on such soil, with a view to improving its Geotechnical properties before it is used as foundation material. The most widely recognized technique for soil improvement is soil sturdiness. Soil sturdiness includes the treatment of soils so as to improve their building properties with the end goal that they become progressively reasonable for development [2]. Although, many techniques of soil stabilization exist, a synthetic admixture adjustment which depends on the utilization of an admixture to change the compound properties of the soil to accomplish the ideal impact of improved Geotechnical performance has gained ascendancy in recent years. Notable materials that have been used or found by researchers to be suitable as a soil stabilizer includes: lime [3-7]; cement [8]; eggshell powder [9]; blast furnace slag [10]; fly ash [11]; marble dust [12];



stone dust [13]; used lubrication oil [14]; sugar cane bagasse ash [15-17], rice husk ash [16], saw dust ash [18], ground nut ash [19] and sugar cane straw ash [20]. These materials are either used singly or in combination, and for different types of soil. The present work investigates the effects of sugarcane straw ash (SSA) on the Geotechnical considerations of lime-stabilized lateritic soil for structural works. Lateritic soils are the most abundant materials in Nigeria, and indeed all over the world, especially in humid tropical and subtropical zones [21] on which most civil infrastructures (roads, buildings, and so on) are founded. In its regular state, lateritic soils for the most parts have a low bearing limit and low quality because of high mud content. According to [22], the quality and steadiness of lateritic soils cannot be ensured under burden within the sight of dampness. According to [21], the difficulties encountered when laterites are used include: (i) poor compaction because of high dampness content, (ii) affect ability to vacillations in dampness, where quality might be fundamentally decreased with a slight increment in water substance, and (iii) genuine agglomeration and trouble in compaction in the field. It is along these lines basic, consequently, to improve the Geotechnical considerations of laterite to make it fit for founding civil engineering infrastructures. Some admixtures that have been found in stabilizing laterite include: banana leaf ash [22]; cassava peel ash [23]; lime-cement mix [24]; palm piece shell debris [19], saw dust debris [18], lime [21], groundnut husk ash [19]. Many of these admixtures are waste materials, and as such, their use in soil stabilization is an innovative solution to the problems associated with waste disposal. The present work investigates the possibility of using sugarcane straw ash as a stabilizing agent of lime-stabilized lateritic soil. Though [25] researched the impact of SSA on the Geotechnical considerations of concrete balanced out lateritic soil, where the results showed improved Geotechnical properties. Similarly, an investigation conducted by [5] on lateritic soil using lime-sugarcane bagasse (SB) yielded improved geotechnical properties of optimum lime-SB of 4:1. Also, [2] experimented with the possible use of SSA as a stabilizing agent for lateritic soil. However, literature is scarce on the use of lime and sugarcane straw ash (SSA) together as balancing out specialist. Along these lines, the point of this work is to evaluate the impact of SSA on the Geotechnical properties of lime-settled lateritic soil for structural works.

RESEARCH QUESTION

Lime is created by consuming limestone. It responds promptly on contact with water in the soil to frame slaked lime or calcium hydroxide ($\text{Ca}(\text{OH})_2$). This response produces heat and the pH esteem increments to roughly 12.5 [26]. It is a condition for the ensuing pozzolanic responses, in which mud particles in the soil respond with the calcium hydroxide to frame the quality improving response items. Knowing that sugarcane straw, from which the sugarcane ash (SSA) is derived, being a waste, presently has no value and also constitutes an environmental nuisance, will its presence enhance pozzolanic activities of lateritic soil, and thus becomes a valuable material? What will be the impacts of SSA on lime balanced out lateritic soil, in relation to the sustenance condition for pozzolanic response for improved Geotechnical properties? This is the fundamental research question about this investigation.

METHODOLOGY

The materials utilized in this investigation are, lateritic soil, hydrated lime, sugarcane straw ash, and portable water. The lateritic soil utilized was gathered from three distinct areas (tests A, B, C). The global positioning of the locations of tests A, B, and C are separately, 70° 31' 02.51" N, 40° 30' 48.74" E; 70° 31' 02.94" N, 40° 30' 48.48" E; and 70° 31' 04.70" N, 40° 30' 46.01" E. The samples were kept dry inside jute bags marked to indicate description, area and date of examining. The different soil samples were spread independently for air drying, to permit incomplete disposal of characteristic water which may influence investigation. After the drying time frame, irregularities in the samples were somewhat pounded with negligible weight and from there on sieved with strainer



No. 4 (4.76mm opening) to get the last samples for the tests. Hydrated lime was used because it does not set by reaction with water like hydraulic lime. The hydrated lime was kept in a safe bag under room temperature to forestall any contact with dampness or potentially whatever other outer elements that can influence its property. The sugarcane straw was gathered from a sugarcane farm in Igboya Ile-Ife, Nigeria. The straws were spread out on the ground and air dried to encourage simple consuming. After air drying, the sugarcane straws were singed straightforwardly into debris and gathered in polythene sacks, put away under room temperature until utilized. The sugarcane straw ash (SSA) was sieved through the BS sifter 212 µm to get fine debris.

Experimental investigations

Both preliminary and Geotechnical tests were completed on the soil samples A, B and C. The preliminary tests did on soil samples were, moisture content, specific gravity, molecule size examination, and Atterberg's limits, while, the Geotechnical investigations were, compaction, California Bearing Ratio (CBR), and unconfined compression test. All these were done as per relevant universal standard systems as stipulated in [27]. All the soil samples were stabilized with optimum 7% lime by weight. The lime-stabilized samples were then treated with SSA in varying percentages of 6%, 8%, 10% and 12.5% bulk of soil samples, in order to determine the optimum prerequisite of SSA required for the modification of the different samples. At the point when the samples were stabilized with 7% lime, the Geotechnical properties were determined and these were utilized as a control against which the Geotechnical considerations of the lime stabilized soil changed with sugarcane straw ash (SSA) were compared.

RESULTS AND DISCUSSION

Preliminary results of the soil samples

The results of the preliminary properties of the soil samples appear in Table 1. It can be observed in the Table 1 that soil samples A, B and C are delegated as A-7-6, A-7-5, and A-7-5 separately.

Tab. 1 - Preliminary results of soil tests

Property	Sample A	Sample B	Sample C
Natural Moisture Content	8.49	12.63	10.55
Specific Gravity	2.44	2.38	2.94
AASHTO Arragement	A-7-6	A-7-5	A-7-5
Liquid Limit	73.88	65.95	60.40
Plastic limit	27.27	33.72	30.83
Plasticity Index	46.61	32.23	29.57
Maximum Dry Density (kg/m ³)	1466	13881	1431
Optimum Moisture Content (%)	23.50	29.40	27.40
CBR (%)	6	3	5
UCS (kg/m ²)	81.25	68.10	52.77

All the soil samples have their liquid limits more noteworthy than 41% and plasticity indices more prominent than 11%. As per the AASHTO table for classification, soils having a place with this class are viewed as reasonable for poor material and are not appropriate as subgrade material. Therefore, soil stabilization becomes very relevant. The poor quality of the samples is further reinforced by high liquid limit and plasticity indices, thus necessitating application of soil improvement measures, as per soils used for similar research work by [28-29].

Atterberg limits characteristics

The Atterberg limits characteristics of lime-stabilized lateritic soil containing SSA are shown in Table 2. In relation to the Atterberg limit traits of the soil as shown in Table 1, it can be observed that the use of SSA caused a decrease in the plasticity record of the lime-balanced out lateritic soil at some points along the process.

The watched decline of the plasticity record of soil tests with SSA upgrades its qualification for use as construction materials. According to [30] and [29] a decrease in P.I gives a sign of a progressively steady soil with checked expanded usefulness.

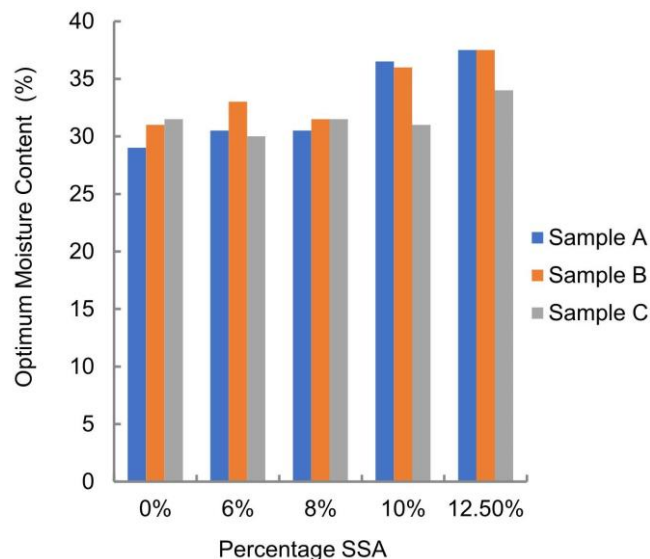
Tab. 2 - Summary of Atterberg's limits

Samples	Percentage SCSA (%)	Liquid Limit, LL (%)	Plastic Limit, PL (%)	Plasticity Index, PI (%)
A	0	67.63	42.54	25.09
	6	70.4	44.35	26.05
	8	66.59	44.61	21.98
	10	66.4	43.59	22.81
	12.50	66.60	41.30	25.30
B	0	60.68	35.92	24.76
	6	62.8	38.26	24.54
	8	63.53	40.35	23.18
	10	63.93	42.15	21.78
	12.50	62.25	41.16	21.09
C	0	60.35	40.92	19.43
	6	56.46	41.09	15.37
	8	59.5	40.73	18.77
	10	59.18	42.99	16.19
	12.50	56.62	40.27	16.35

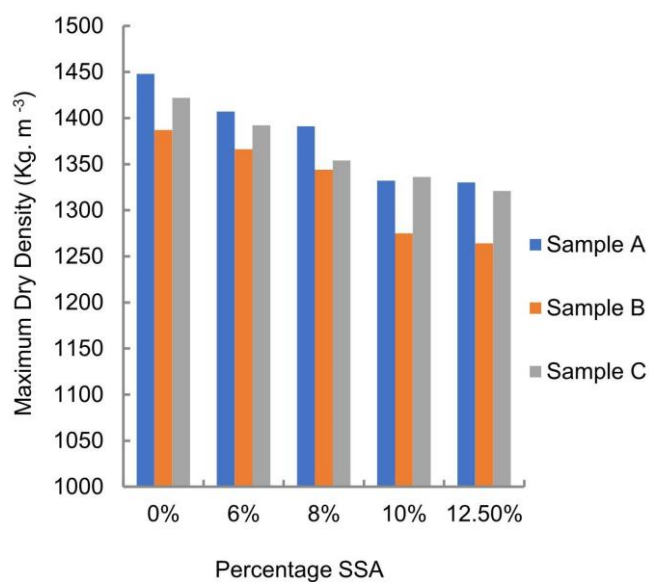
Results of the compaction tests

The compaction qualities of the lime-stabilized soil modified with sugarcane straw ash (SSA) as far as characteristics, moisture content and the maximum dry density are presented in Figure 1. From Figure 1, all the samples dynamically display higher moisture content with expanding substance of SSA. The expansion in moisture content is presumably because of the extra water held inside the flocculated soil structure coming about because of lime cooperation for the pozzolanic responses to occur [28-29]. The extra water held in the muddled soil structure because of the permeable property of sugarcane straw ash which could likewise bring about higher

moisture content in the soils [3]. The figure additionally shows decreases in the maximum dry densities of the treated soils with expanding SSA.



(a) Effect of SSA on the Optimum Moisture Content



(b) Effect of SSA on the Maximum Dry Density

Fig. 1 - Characteristics of Lime-stabilized Soil Modified by SSA

The decrease in dry density is an impression of the expanded obstruction offered by the muddled soil structure to the compactive exertion [31]. Likewise, adding to the decrease in the dry density is the specific gravity of the sugarcane straw ash, which is lower than that of the normal soil tests, in this manner the less heavy and smaller particles fill the voids of the muddled soil network to give a less thick lattice [32]. According to [33], a reduction in dry density shows that a low compactive vitality is required than the regular soil to accomplish its greatest dry density and accordingly, the expense of compaction will be diminished. The compactive attributes of lime-

stabilized soil modified with SSA of higher optimum moisture content and lower density can be used to reduce or eliminate volumetric changes in soil, caused by alternate wetting and drying [34].

GEOTECHNICAL CHARACTERISTICS

CBR Test Results

The CBR method, according to [18], is a solid handy method for finding the quality of the sub-level (bearing limit of soil) and assessing the necessary thickness of pavement to fulfil a given stacking. The consequences of the unsoaked CBR tests, suggested for tropical soil [1], to evaluate the bearing capacity of lime-stabilized lateritic soil containing SSA, are plotted and appeared in Figure 2. For all the samples, there is a typical pattern that can be observed, which is, increment in CBR values with SSA followed by decrease upon consistent expansion of SSA. An expansion in CBR esteem means that improved Geotechnical properties [1]. The expansion in the CBR estimation of the samples can be credited to improved conditions for pozzolanic exercises, by guaranteeing that the pH value is maintained at around 12.5 [26]. The pozzolanic activities will result in the strength-forming C-S-H gel hydration products. The CBR values of the normal soil tests are 6, 3 and 5% of tests A, B and C separately. The CBR estimations of 6, 6 and 8% were recorded on expansion of 7% lime to tests A, B and C individually.

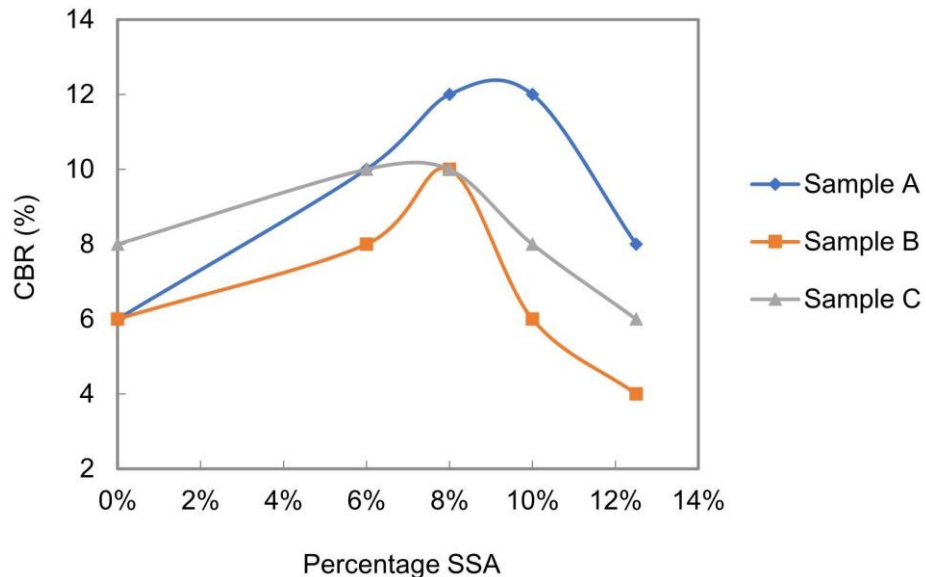


Fig. 2 - Effects of SSA on the Unsoaked CBR of the Tests Samples

The highest CBR values of 12%, 10% and 10% were recorded at 8% SSA and 7% lime combinations of tests A, B and C individually. The expansion in CBR esteem after expansion of lime is most likely because of the development of different solidifying specialists due to pozzolanic response between the silica present in soil and lime. As indicated by [35], a CBR estimation of 7–20 % is suggested for Highway sub-base and 0–7 % of the sub-level materials. It is obvious that the CBR values of lime-stabilized lateritic soil containing SSA up to 8%, can be used as highway subbase and subbase materials.

Unconfined compression test

The unconfined compression strength (UCS) test is the principle test prescribed for the assurance of the necessary measure of added substances to be utilized in modification of the soils [18]. The general guideline for a given kind of modification is that the higher the compressive

quality, the better is the nature of the settled material. The results of the unconfined compression tests on lime-stabilized lateritic soil samples containing SSA are shown in Figure 3.

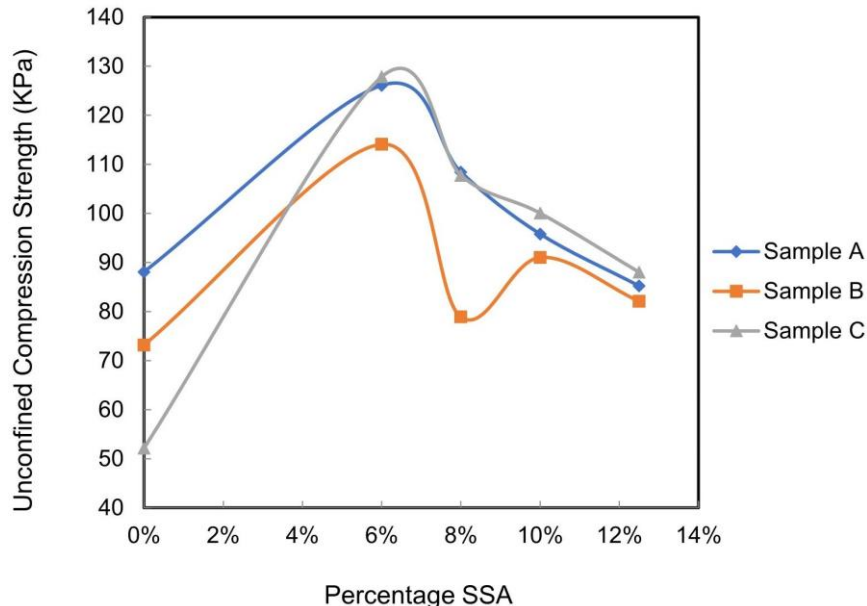


Fig. 3 - Effects of SSA on the Unconfined Compression Strength of the Soil Samples

It may be very well seen from Figure 3 that the unconfined compressive quality, increased with the expansion of SSA up to 6% and then decreased for all the samples. It can be explained that beyond 6%, the necessary condition for pozzolanic activities, in lime-based medium, which is a pH of about 12.5 [26] is disrupted. However, comparing the numerical values of UCS obtained for the samples; the unconfined compressive strength of the natural soil samples rose respectively, for samples A, B and C from 81.25, 68.10 and 52.27 KN/m² to 88.1, 73.18 and 52.37 KN/m² when lime was added. The compressive strength further increased with the addition of SSA, but the optimum values at 6% were 126.13, 114.1 and 127.85 KPa respectively, for tests A, B and C. It is likewise notable that UCS is the principal determinant for consistency of soil [32]. Additionally, according to [33], the UCS esteems between 0-25 kN/m² demonstrates exceptionally delicate soil, between 25-50 kN/m² shows delicate soil, between 50-100 kN/m² shows medium soil, between 100-200 kN/m² shows firm soil, between 200-400 kN/m² shows extremely hardened soil and more noteworthy than 400 kN/m² demonstrates hard earth. It may be very well seen that the unconfined compression quality of the samples A, B and C transformed from the underlying state medium consistency to hardened consistency at 6% SSA and optimum lime stabilization.

CONCLUSIONS

From the analysis of the results of this investigation, the following conclusions were made:

- 1) The expansion of SSA in lime-settled lateritic soil brought about a decrease in plasticity record at all levels for all the samples.
- 2) Introduction of SSA in lime-settled lateritic soil brought about increment in CBR values up to a level. However, the peak values for CBR for all the samples occurred at 8% addition of SSA.
- 3) The overall results showed that, lime-stabilized lateritic soils containing SSA up to 8% by weight of soil are able to sustain the conditions necessary for pozzolanic reaction for improved Geotechnical properties.

The addition of SSA in lime-stabilized lateritic soil increased the UCS, but the optimum values for all the samples were obtained at 6%

Though, optimum performances were obtained at 8% for CBR tests and 6% for UCS, by considering the lower bound principle, it can be concluded that 6% of SSA in lime-stabilized lateritic will results in optimum geotechnical performance of the soil.

REFERENCES

- [1] Ola S. A., 2013. Essentials of Geotechnical Engineering, 3rd ed., University Press PLC, Ibadan Nigeria
- [2] Amu O. O., Ogunniyi S. A., Oladeji O. O., 2011a. Geotechnical properties of lateritic soil stabilized with sugarcane straw. American Journal of Scientific and Industrial Research, Vol. 2, pp. 323-331.
- [3] Amu O. O., Bamisaye O. F., Akomolafe I. A., 2011b. The suitability and lime stabilization requirement of some lateritic soil samples as pavement material. International Journal of Pure and Applied Science Technology, Vol. 2, No. 1, pp. 29- 46.
- [4] Barasa P. K., Too D., Jonah K., Mulei S. M., 2013. Stabilization of expansive clay using lime and sugarcane bagasse ash. International Journal of Science and Research (IJSR), Vol. 4, No. 4, pp. 2112-2117.
- [5] Barasa P. K., Jonah K., Mulei S. M., 2015. Stabilization of expansive clay using lime and sugarcane bagasse ash. Mathematical Theory and Modeling, Vol. 5, No.4, pp. 124-134.
- [6] Dang L. C., Hasan H., Fatahi B., Jones R., Khabbaz H., 2016). Enhancing the engineering properties of expansive soil using bagasse ash and hydrated lime. International Journal of GEOMATE, Vol. 11, No. 25, pp. 2447 - 2454.
- [7] Hasan H., Dang L., Khabbaz H., Fatahi B., Terzaghi S., 2016. Remediation soils using agricultural waste bagasse ash. Procedia Engineering, Vol. 14, No. 3, pp. 1368–1375.
- [8] Ramteke N. B., Saxena A., Arora T. R., 2014. Stabilization of black cotton soil with sand and cement as a subgrade for pavement. International Journal of Engineering Sciences & Research Technology, Vol. 3, No. 6, pp. 688-692.
- [9] Ahmed B., Rahman A., Das J., 2015. Improvement of subgrade CBR value by using Bagasse ash and Eggshell powder. International Journal of Advanced Structures and Geotechnical Engineering Vol. 4, No. 2, pp. 86-91.
- [10] Chavan P., Nagakumar M. S., 2014. Studies on soil stabilization by using bagasse ash International Journal of Scientific Research Engineering and Technology (IJSRET), pp. 89-94.
- [11] Rajakumaran, K. (2015). An experimental analysis on stabilization of expansive soil with steel slag and fly ash. International Journal of Advances in Engineering and Technology, Vol. 7, No. 6, pp. 1745-1752.
- [12] Ali R. H., Khan A. A., Shah T., 2014. Expansive soil stabilization using marble dust and bagasse ash. International Journal of Science and Research (IJSR), Vol. 3, No. 6, pp. 2812-2816.
- [13] Mudgal A., Sarkar R., Sahu A. K., 2014. Effect of lime and stone dust in the geotechnical properties of black cotton soil. International Journal of GEOMATE, Vol. 7, No. 2, pp. 1033-1039.
- [14] Sadeq J. A., Ochepo J., Salahudeen B. A., 2016. Effect of used oil contamination and bagasse ash on some geotechnical properties of lateritic soil. Leonardo Electronic Journal of Practices and Technologies, Vol. No. 28, pp. 119-136.
- [15] Salim R. W., Ndambuki J. M., Adedokun D. A., 2014. Improving the bearing strength of sandy loam soil compressed earth block bricks using sugarcane bagasse ash. Sustainability 6, 3686-3696; doi:10.3390/su6063686.
- [16] Yadav A. K., Gaurav K., Kishor R., Suman S. K., 2017. Stabilization of alluvial soil for subgrade using rice husk ash, sugarcane bagasse ash and cow dung ash for rural roads. International Journal of Pavement Research and Technology, Vol. 10, pp. 254–261.
- [17] Ojeda-Farías O., Mendoza-Rangel J. M., Baltazar-Zamora M. A., 2018. Influence of sugar cane bagasse ash inclusion on compacting, CBR and unconfined compressive strength of a subgrade granular material. Revista ALCONPAT, Vol. 8, No. 2, pp. 194 – 208. doi: <http://dx.doi.org/10.21041/ra.v8i2.282>.
- [18] Butt W. A., Gupta K., Jha J. N., 2016. Strength behaviour of clayey soil stabilized with saw dust ash. International Journal of Geo-Engineering, Vol. 7, No. 18, pp. 2-9.
- [19] Nnochiri E. S., Ogundipe O. M., Oluwatuyi O. E., 2017. Effects of palm kernel shell ash on lime-stabilized lateritic soil. Slovak Journal of Civil Engineering, Vol. 25, No. 3, pp. 1-7. doi:10.1515/sjce-2017-0012.
- [20] Chakraborty A., Borah A., Sharmah D., 2016. Stabilization of expansive soil using sugarcane straw ash (SSA). ADBU-Journal of Engineering Technology, AJET. Vol. 4, No. 1, pp. 2348-7305.



- [21] Tan Y., Hu, M., Li D., 2016. Effects of agglomerate size on California bearing ratio of lime treated lateritic soils," International Journal of Sustainable Built Environment, pp. 168–175. <http://dx.doi.org/10.1016/j.ijsbe.2016.03.002>.
- [22] Nnochiri S. E., Aderinlewo O. O., 2016. Geotechnical properties of lateritic soil stabilized with banana leaves ash. FUOYE Journal of Engineering and Technology, Vol. 1, No. 1, pp. 116-119.
- [23] Bello A. A., Ige J. A., Ayodele H., 2015. Stabilization of lateritic soil with cassava peels ash. British Journal of Applied Science and Technology, Vol. 7, No. 6, pp. 642-650. doi: 10.9734/BJAST/2015/16120.
- [24] Todingrara Y. T., Tjaronge M., Harianto T., Ramli M., 2017. Performance of laterite soil stabilized with lime and cement as a road foundation. International Journal of Applied Engineering Research, Vol. 12, No. 14, pp. 4699-4707.
- [25] Onyebuchi M., Abdulhameed M., Yeke E., Michael T., 2018. Effect of sugarcane straw ash on cement stabilized lateritic soil for use as flexible pavement material. Journal of Emerging Technologies and Innovative Research (JETIR), Vol. 5, No. 2, pp. 563-567.
- [26] Axelsson K., Johansson S., Andersson R., 2002. Stabilization of organic soils by cement and pozzolanic reactions - Feasibility Study (Report 3). The Swedish Deep StabilizationResearchCentre. <http://www.swedgeo.se/sd.htm>.
- [27] British Standards BS: 1377-1., 2016. Methods of test for soils for Civil Engineering purposes. General requirements and sample preparation.
- [28] Jha J. N., Gill K. S., 2006. Effect of rice husk ash on lime stabilization. Journal of the Institution of Engineers, Vol. 87, pp. 33-39.
- [29] Mtallib M. O. A. and Bankole G. M., 2011. The improvement of the index properties and compaction characteristics of lime stabilized tropical lateritic clays with Rice Husk Ash (RHA) Admixtures. EDGE, Vol. 16.
- [30] Martirena J. F. H., Middendorf B., Gehrke M. and Budelmann H., 1998. Use of wastes of the sugar industry as pozzolana in lime-pozzolana binders: Study of the reaction. Cement and Concrete Research. Vol 28, pp. 1525–1536.
- [31] Nagaraj T. S., 1964. Discussion on Soil – lime research at Iowa State University ASCE, Vol. 90, No. 6, pp. 225-226.
- [32] Das B. M., 2000. Fundamental of Geotechnical Engineering, 4th ed., Thomson Learning, New York.
- [33] Muntohar G.D., Hantoro G., 2000. Influence of rice husk ash and lime on engineering properties of a clayey sub-grade. Dept of Civil Engineering, Muhammadiyah University of Yogyakarta, Indonesia.
- [34] Bowles J. E., 1998. Foundation Analysis and Design, McGraw Hill International Book Company, London.
- [35] ARRA, 2008. Asphalt Recycling and Reclaiming Association (ARRA), Soil stabilization. 2011 annual meeting presentation. #3, Church Circle Annapolis, Maryland.

ESTIMATION OF SWELLING PRESSURE OF EXPANSIVE SOILS REINFORCED WITH GRANULAR PILE

Kundan Meshram and P.K. Jain

Department of Civil Engineering, Maulana Azad National Institute of Technology Bhopal-462003 (M.P.), India; email: kundan.transpo@gmail.com

ABSTRACT

Constructing over expansive soils often severely damage the structure due to high swell-shrinkage behaviour and loss of strength owing to fluctuating water content. Due to the above reasons construction on or using expansive soils is considered to be unsafe. The technique of such soil improvement by installation of granular piles (also known as stone columns) is popular to marshy lands, marine clays, loose sand, silty or clayey sand, and compressible soils. Granular piles improve swelling properties of expansive soil. In the present study six expansive soils were used. The one of them was the naturally available black cotton soil and others were derived from it by mixing bentonite in different proportions. Test beds of these soils were prepared at different initial moisture contents and the granular pile of sand was installed in these beds by the method of removal. Besides initial moisture content, properties of expansive soils, the spacing between the piles (expressed by s/d ratio; s = spacing between the piles and d = diameter of a pile) and the relative density of granular pile forming material were the variables of the study. Multiple linear regression analysis on the test data has been performed and equations for predicting swelling pressure of soil bed without pile and inclusion with granular pile have been developed.

KEYWORDS

Granular pile; S/d ratio; Swelling pressure; Relative density of sand

INTRODUCTION

Expansive soil deposits occur in the arid and semi-arid region of the world and are problematic to engineering structures because of their tendency to heave during wet season and shrink during dry season [1-2,25]. Light structures such as highways, railroads, runways, and other lifeline structures, constructed over such soils often get severely damaged due to high swell-shrinkage behaviour and loss of strength owing to fluctuating water content. Due to the above reasons construction on or using expansive soils is considered to be unsafe. The traditional techniques of ground improvement like lime stabilization, cement stabilization; fly ash stabilization, etc. have difficulty of mixing the stabilizer to the soil properly and are limited to treat the soil to shallow depth only. Ample examples are available which show failure of roads and embankments, boundary walls and uneven settlement of building floors and damage to lightly loaded structures founded on such soils. The annual cost of damage to structures, worldwide, due to construction on such soils is enormous [3-5]. Hence the search for developing a new technique for expansive soil improvement still remains alive and relevant.

Now-a-days, granular pile/stone column (also known as stone column) is one of the soil stabilization technique used in expansive soil [6]. It is also used for improvement of loading bearing capacity in marshy lands, marine clays, loose sand, silty or clayey sand, and compressible soils [7-16,33] and the rate of consolidation [17-20]. Unlike other soils, loss of strength is not the only



aspect, but swelling and shrinkage is another serious problem with expansive soils; hence effect of inclusion of granular piles on swelling behaviour of expansive soils reinforced with granular pile needs to be studied.

In the present study, test beds of expansive soils were prepared at different initial moisture contents and the granular pile of sand was installed in these beds by the method of removal. Granular pile was constructed full length of mould. The initial moisture content, percentage fines, liquid limit, plasticity index and dry density are very important factors which affect the swelling pressure of expansive soils. The spacing between piles is generally expressed by s/d ratio, where, 's' is the spacing between piles and 'd' is the effective influence diameter of the granular pile as per unit cell concept [21]. Empirical models were developed for estimating swelling pressure exerted by expansive soils without and with granular pile.

LITERATURE REVIEW

Unit cell concept

Granular piles should be installed preferably in an equilateral triangular pattern which gives the densest packing, although a square pattern may also be used.

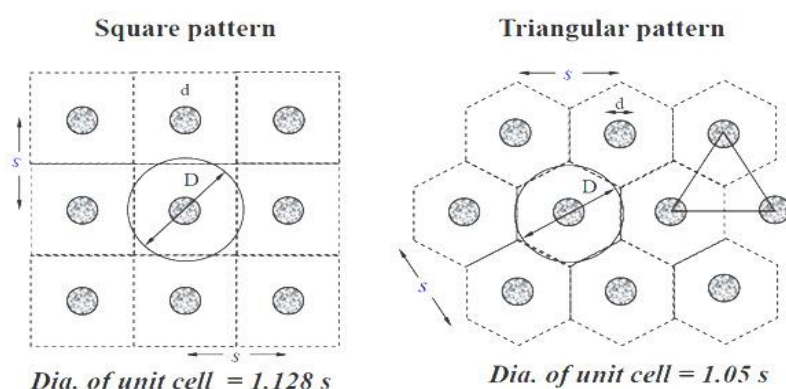


Fig. 1- Typical granular piles arrangement (after IS 15284(Part-I): 2003[21])

Where, D_e = effective diameter and "s" is the spacing of granular piles.

Estimation swelling pressure of expansive soils

Regression models, for estimating swelling pressure of expansive soils were developed by many researchers, are shown in Table 1.

Tab. 1 - Empirical relationships for estimating swelling pressure of expansive soils

Investigators	Empirical relationships	Remarks
[26]	$\log P_s = -2.132 + 0.0208LL + 0.000565 \gamma_d - 0.0269w$	$P_s = \text{kg/cm}^2$, $\gamma_d = \text{kg/m}^3$
[27]	$Sp = 3.5817 \times 10^2 PI^{1.12} (C^2/w^2) + 3.7912$	$P_s = \text{Psi}$
[28]	$P_s = -227.27 + 2.14 w + 1.54LL + 72.49 \gamma_d$	$P_s = \text{N/cm}^2$ $\gamma_d = \text{g/cm}^3$
[29]	$\log P_s = -4.812 + 0.01405PI + 2.394 \gamma_d - 0.0163 w$ $\log P_s = -5.020 + 0.01383PI + 2.356 \gamma_d$	$P_s = \text{kg/cm}^2$, $\gamma_d = \text{g/cm}^3$
[30]	$Sp = 135 + 2(C+PI - w)$	$P_s = \text{kPa}$
[31]	$\log Ps = 0.0276PI - 365.2118 \gamma_d^{-2.4616} - 0.0320 w + 2.2292$ $\log Ps = 0.0239PI - 1285.3723 \gamma_d^{-3.2768} - 0.0396 + 2.3238$	$P_s = \text{kPa}$ $\gamma_d = \text{kN/m}^3$
[32]	$S_p = 1.9319 S^{1.2897}$	$S_p \leq 300 \text{ kPa}$,

S = Swelling in percent, $Sp/ P_s/ S_p$ = Swelling Pressure, LL = Liquid Limit (%), PI = Plasticity Index, γ_d = dry density of soil, w = water/moisture content, C = clay percent,

Most of the test performed for measurement of swelling pressure of expansive soil by Oedometer test. There is no arrangement to construction of granular pile in oedometer test.

In the present work, empirical models were developed for swelling pressure of test beds without pile and reinforced with granular pile.

DATA COLLECTION

The study has been conducted on six different expansive soils in which one was the natural black cotton soil and others were the mixture of black cotton soil with bentonite clay as presented in Table 2.

Tab. 2 - Expansive soils used in the present work

S.N.	Soil samples	Combination	Type of Soil
1	SS1	Black Cotton (BC) Soil	Natural
2	SS2	BC soil+ 10% Bentonite	Prepared
3	SS3	BC soil+ 20% Bentonite	Prepared
4	SS4	BC soil+ 30% Bentonite	Prepared
5	SS5	BC soil+ 40% Bentonite	Prepared
6	SS6	BC soil+ 50% Bentonite	Prepared

Liquid limit of these soils in range of 48-77%, plastic limit 22-36%, optimum moisture content 18-24%, and maximum dry density 15.4-14 kN/m³ were measured and procedure adopted to determination of these properties by IS 2720 (Part 5) [24], IS 2720 (Part 7) [23] respectively. The soils were classified as per IS: 1498-1970[22] and all were fall in CH i.e. clay of high plasticity and compressibility group. BC soil and bentonite both soils have expansive nature and check



performance of granular pile in worst ground condition. So both soils were mixed and made new soils.

The beds of soils were prepared in cylindrical moulds of three different sizes as shown in Table 3.

The consistency of the soils was varied by changing the initial moisture content ($w_f = 15\%, 17\% \text{ and } 20\%$). In the present study, granular piles were installed in an equilateral triangular pattern as suggested by IS 15284(Part-I): 2003[21]. Piles of three different diameters were installed in moulds of different diameters so as to have variation in s/d ratio of 2, 3 and 4 as given in Table 3.

Tab. 3 - Requirement of mould diameter for different s/d ratio

Mould Designation	s/d ratio	Pile diameter (mm)	Mould diameter (mm)	Mould Height (mm)
M ₁	2	48	100	220
M ₂	3	32	100	144
M ₃	4	25	105	115

Single pile was installed as full length of mould to reduce the swelling pressure of expansive soils. Constant volume method was adopted for determination of swelling pressure of expansive soils. Sand was used as the granular pile forming material. The piles were formed by filling sand at two relative densities 40% and 60%. For different combinations of pile-soil, and s/d ratio, total 108 composite specimens were prepared for swelling pressure determination. Corresponding to three moulds and at three different moisture contents, test beds of six soils without piles were also made for swelling pressure determination. Thus in total 162 swelling pressure tests were conducted. Swelling pressure of soils were estimated for basic soil parameters in case of unreinforced pile test beds, and pile parameters in case of granular pile reinforced clay beds. Summary of model tests conducted for determination of swelling pressure as shown in Table 4.

Tab. 4 - Summary of model tests conducted

S.N.	Test Series	Parameter measured	Initial Water Content (%)	s/d ratio	Granular Pile Diameter(mm)	D _r of Sand	No. of test conducted		
							Without pile	With pile	Total
1	TS1	Swelling pressure	15,17,20	2	48	40%	18	18	54
						60%		18	
2	TS2	Swelling pressure	15,17,20	3	32	40%	18	18	54
						60%		18	
3	TS3	Swelling pressure	15,17,20	4	25	40%	18	18	54
						60%		18	
Grand Total							54	108	162



The test results have been analysed using multivariate regression analysis for estimation of swelling pressure (S_p in kN/m²) and validation of regression models through 20% data set. The basic soil parameters considered were percentage fines (F), liquid limit (LL in %), plasticity index (PI), initial water content (w_i in %), dry density (γ_d , in kN/m³) and pile related parameters were s/d ratio (α) and relative density of sand (D_r , in kN/m³).

ESTIMATION OF SWELLING PRESSURE OF EXPANSIVE SOILS

In order to estimate swelling pressure (S_p) of expansive soils reinforced with granular pile, multivariate regression analysis (MRA) has been performed on the test data. Swelling pressure of a soil depends on clay content, initial moisture content, density of the soil and the type of mineral present in the soil. Further, in case of an expansive soil reinforced with granular pile, the pile characteristics such as D_r of the pile material, s/d ratio will also affect these properties. Hence MRA model for swelling pressure of soil bed without pile and with pile has been developed by taking following basic parameters as input.

(i) **Soil bed without pile:** Input parameters taken were percentage fines (F), liquid limit, (LL), plasticity index (PI), initial water content (w_i), and the dry density of the clay soil (γ_d). For different combinations of input parameters four equations have been developed and listed in Table 5. The performance parameters namely coefficient of correlation (R^2), root mean square error (RMSE) and mean absolute error (MAE) have been determined and listed in Table 6.

Tab. 5 - Regression models for swelling pressure of soil bed without granular pile

S.N.	Equation
(1)	$S_p = 82.87 + 1.358 LL - 4.802 w_i$
(2)	$S_p = 4702.684 - 41.328F - 1.428LL + 3.018PI - 39.135\gamma_d$
(3)	$S_p = 1972.077 - 19.523F + 1.993LL - 0.303PI - 4.802w_i$
(4)	$S_p = 2140.064 - 20.854F + 1.784LL - 0.100 PI - 4.583w_i - 2.389\gamma_d$

Tab. 6 - Performance parameters for swelling pressure of soil bed without granular pile

Equation No.	R^2	RMSE	MAE
(1)	0.710	11.380	7.781
(2)	0.669	12.145	8.789
(3)	0.722	11.139	7.691
(4)	0.722	11.135	7.696

(ii) **Soil bed with pile:** In the case of test beds reinforced with granular pile, besides F, LL, PI, w_i and γ_d of the clay soil, the relative density of granular fill material, D_r and s/d ratio (α) were also taken as input parameters. The developed equations, for different combinations of input parameters by MRA analysis, are shown in Table 7 and their performance parameters are given in Table 8.

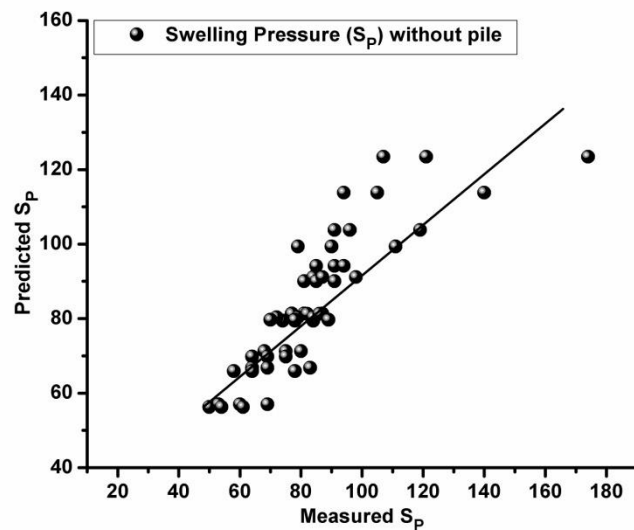
Tab. 7 - Regression models for swelling pressure of soil bed with granular pile

S.N.	Equation
(5)	$S_P = 1612.817 - 9.691F - 1.657LL + 1.628PI - 30.890\gamma_d + 6.444\alpha - 82.963D_r$
(6)	$S_P = -971.806 + 11.939F + 0.393LL - 3.586w_i + 6.444\alpha - 82.963D_r$
(7)	$S_P = -546.056 + 7.519F + 1.042LL - 0.99PI - 3.586w_i + 6.444\alpha - 82.963D_r$
(8)	$S_P = 21.466 + 3.021F + 0.336LL - 0.307PI - 8.071\gamma_d - 2.846w_i + 6.444\alpha - 82.963 D_r$

Tab. 8 - Performance parameters for swelling pressure of soil bed with granular pile

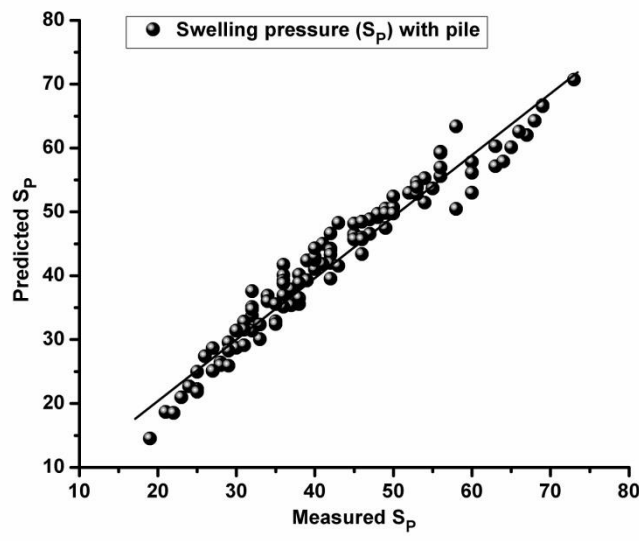
Equation No.	R ²	RMSE	MAE
(5)	0.892	4.073	3.396
(6)	0.933	3.211	2.529
(7)	0.945	2.890	2.280
(8)	0.951	2.742	2.237

From above mentioned regression models, it is found that equation (4), the incorporate parameters are percentage fines (F), liquid limit, (LL), plasticity index (PI), initial water content w_i, and the dry density of the clay soil (γ_d), gives the best correlation for estimation of swelling pressure (S_P) of the plain soil, shown in Figure 2(a).



(a)

Fig.2 - Relationship between measured and predicted swelling pressure for (a) without pile and (b) with pile



(b)

Fig.2 - Relationship between measured and predicted swelling pressure for (a) without pile; and (b) with pile

In case of expansive soil reinforced with granular pile, equation (8) estimate swelling pressure with high $R^2=0.951$, and low RMSE=2.742, MAE= 2.237, shown in Fig. 2(b).

Therefore, Equation (4) and (8) may be used to estimate swelling pressure of soil alone and that reinforced with granular pile.

CONCLUSIONS

Six expansive soils having variation in liquid limit and plasticity index and expansiveness have been taken in the present study. These soils were prepared for installation of a pile for different combinations of s/d ratio, D_r , of pile material and initial moisture content, w_i for the soils. The test data has been analysed and models for predicting swelling pressure of soils unreinforced and reinforced with granular material (pile) have been developed. Based on the analysis following conclusions are drawn:

1. Granular pile technique is promising technique for reducing the swelling pressure of expansive soil and it may install successfully at any season.
2. Regression equations that have high R^2 , least RMSE and MAE values are:

(i)For test beds without pile

$$S_p = 2140.064 - 20.854F + 1.784LL - 0.100 PI - 4.583w_i - 2.389\gamma_d$$

$$R^2 = 0.722, \text{ RMSE} = 11.135, \text{ MAE} = 7.696$$

(ii)For test beds with pile

$$S_p = 21.466 + 3.021F + 0.336LL - 0.307PI - 8.071\gamma_d - 2.846w_i + 6.444\alpha - 82.963 D_r$$

$$R^2 = 0.951, \text{ RMSE} = 2.742, \text{ MAE} = 2.237$$

REFERENCES

- [1] Chen, F.H., 1975. Foundations on expansive soils. Elsevier Scientific Publishing Co., New York.
- [2] Grim,R. E., 1968. Clay mineralogy. 2nd edn. McGraw-HillBook Company, New York, USA.
- [3] Gourley, C. S., Newill, D., Shreiner, H. D., 1993. Expansive soils: TRL's research strategy. Proc., 1st Int. Symp. on Engineering Characteristics of Arid Soils, London.
- [4] Puppala,A. J., Cerato, A., 2009. Heave distress problems in chemically-treated sulfate-laden materials. *Geo-Strata*, 10(2): 28– 30.
- [5] Jones,L. D., Jefferson, I.,2012. Expansive soils. Burland, J., Chapman, T., Skinner, H., Brown,M. Geotechnical engineering principles, problematic soils and site investigation. Edited by, ICE manual of geotechnical engineering, 5:413-441.
- [6] Meshram, K., 2016. Swelling behavior of expansive soils reinforced with granular pile. Ph.D. thesis, Maulana Azad National Institute of Technology Bhopal (M.P.), India.
- [7] Hughes,J. M. O., Withers, N. J., 1974. Reinforcing of soft cohesive soils with stone columns. *Ground Engineering*, 7 (3): 42-49.
- [8] Guetif, Z., Bouassida, M., Debats, J. M.,2007. Improved soft clay characteristics due to stone column installation. *Computers and Geotechnics*, 34(2):104-111.
- [9] Samadhiya, N. K.,Maheshwari, P., Basu, P., Kumar, M. B., 2008. Load settlement characteristics of granular pile with randomly mixed fibers. *Indian Geotech. J.*, 38(3):345-354.
- [10] Murugesan,S., Rajagopal, K.,2010. Studies on the behavior of single and group of geosynthetic encased stone columns. *Journal of Geotechnical and Geoenvironmental Engineering*, 136(1):129–139.
- [11] Black, J. A.,Sivakumar, V.,Madhav, M. R., Hamill, G. A., 2007. Reinforced stone columns in weak deposits: laboratory model study. *Journal of Geotechnical and Geoenvironmental Engineering*, 133(9):1154-1161.
- [12] Stuedlein,A. W., Holtz, R. D.,2012. Analysis of footing load tests on aggregate pier reinforced clay," *Journal of Geotechnical and Geoenvironmental Engineering*, 138(9):1091-1103.
- [13] Hanna, A. M.,Etezad, M., Ayadat, T., 2013. Mode of failure of a group of stone columns in soft soil," *International Journal of Geomechanics*, 13(1):87-96.
- [14] Zhang, L., Zhao, M., Shi, C., Zhao, H.,2013. Settlement calculation of composite foundation reinforced with stone columns.*International Journal of Geomechanics*, 13(3): 248–256.
- [15] Ali, K., Shahu, J. T., Sharma, K. G., 2014. Model tests on single and groups of stone columns with different geosynthetic reinforcement arrangement. *Geosynthetics International*, 21(2):103–118.
- [16] Rangeard, D.,Phan, P. T.,Martinez, J., Lambert, S., 2016. Mechanical behavior of fine-grained soil reinforced by sand columns: an experimental laboratory study. *Geotechnical Testing Journal*, 39(4):648-657.
- [17] Castro,J., Sagaseta, C., 2009. Consolidation around stone columns: Influence of column deformation. *International Journal for Numerical and Analytical Methods in Geomechanics*, 33: 851-877.
- [18] Castro, J., Cimentada, A.,da Costa, A. D.,Cañizal, J., Sagaseta, C., 2013. Consolidation and deformation around stone columns: comparison of theoretical and laboratory results. *Computers and Geotechnics*, 49:326-337.
- [19] Han,J., Ye, S. L., 2001. Simplified method for consolidation rate of stone column reinforced foundations. *Journal of Geotechnical and Geoenvironmental Engineering*, 127(7):597-603.
- [20] Han,J., Ye, S. L., 2002. A theoretical solution for consolidation rates of stone column-reinforced foundations accounting for smear and well resistance effects. *International Journal of Geomechanics*, 2(2):135-151.
- [21] Bureau of Indian Standards, 2003. Indian standard code of practice for design and construction for ground improvement-guidelines. Part 1: Stone columns. IS 15284 (Part 1), New Delhi, India.
- [22] Bureau of Indian Standards, 1970. Classification and identification of soils for general engineering purposes," IS 1498, First Revision, Reaffirmed 2007, New Delhi, India.
- [23] Bureau of Indian Standards, 1980. Indian standard code of practice for methods of test for soils: determination of water content dry density relation using light compaction. IS 2720 (Part 7), New Delhi, India.
- [24] Bureau of Indian Standards,1985. Indian standard code of practice for methods of test for soils: determination of liquid limit and plastic limit. IS 2720 (Part 5), New Delhi, India.
- [25] Harishkumar,K., Muthukumaran, K.,2011. Study on swelling and shrinkage behaviour and its improvement. *International Journal of Earth Sciences and Engineering*, 4(6):19-25.
- [26] Komornik,A., David, D.,1969. Prediction of swelling pressure of clays. *Soil Mech Found Eng.*, 95(1):209–225.

- [27] Nayak,N. V., Christensen, R. W.,1971. Swelling characteristics of compacted expansive soil. *Clays Clay Miner.*, 19: 251–261.
- [28] Erguler,Z. A., Ulusay, R. A.,2003. A simple test and predictive models for assessing swell potential of Ankara (Turkey) clay. *Eng .Geol.*, 67:331–352 .
- [29] Erzin,Y., Erol, O., 2004. Correlations for quick prediction of swell pressures. *Electron. J. Geotech. Eng.*, 9, paper 0476.
- [30] Sabtan, A. A., 2005. Geotechnical properties of expansive clay shale in Tabuk, Saudia Arabia. *J. Asian Earth Sci.*, 25:747–757.
- [31] Çimen, O., Keskin, S. N., Yildirim, H., 2010. Prediction of Swelling Potential and Pressure in Compacted Clay. *Arabian J. Sci. Eng.*, 37(6):1535–1546 .
- [32] Erzin,Y., Gunes, N., 2013. The unique relationship between swell percent and swell pressure of compacted clays. *Bull. Eng. Geol. Environ.*, 72:71–80.
- [33] Lajevardi, S. H.,Shamsi, H. R.,Hamidi, M., Enami, S., 2018. Numerical and experimental studies on single stone columns. *Soil Mechanics and Foundation Engineering*, 55(5):340-345.

SEISMIC PERFORMANCE OF TANK FOUNDATIONS IMPROVED WITH STONE COLUMNS

Saeid NikKhah Nasab

Buein Zahra Technical University, Faculty of Civil Engineering, Department of Geotechnical engineering, Qazvin, Buein Zahra,Iran;
saeid.nikkhah.nasab@gmail.com

ABSTRACT

Natural soil in engineering practices is not always considered to bear loads of above structures. In such a way, it is necessary to improve the quality of the soil before any constructions. Tanks are the structures that apply significant load to the beneath soil and they are usually constructed with circular foundations in shape. Seismic loads can apply irremediable damages to the structures and sometimes tanks are the highly important infrastructures during earthquakes. One of the most techniques that has been recently widely used on soft deposits and loose fine-grained soils is stone columns or singular piles. The stone columns increase the strength of loose soils and also decrease settlements induced by applying the loads. In this study, a linear numerical model of the structure-foundation-soil-stone column was simulated using the ABAQUS. Results show that with the increase of the length of stone columns a decrease in settlement occurred, while the increase of length more than a specific threshold had no significant effect to decrease the uplift and settlement.

KEYWORDS

Circular foundation, Acceleration, Stone column, Settlement, Uplift

INTRODUCTION

One of the existing structures in oil and petrochemical industries that can have economic and environmental catastrophes is steel tanks. Increasing use of firing, toxic and dangerous materials which cause the environment pollution and also waste resources is an example of unreplaceable and destruction of structures. Steel tanks located on soils can be constructed in two ways of braced and unbraced. The braced tanks are linked to their foundation using piles and anchors. In unbraced tanks, there is no linkage between the tank wall and its foundation. [1]

Primary seismic analysis investigations were introduced by Sivý et al. They proposed that foundation and tank wall are rigid [2]. During a drastic earthquake in Alaska in 1964, extreme damages to fluid tanks occurred. These damages were arising from lack of consideration of any flexibility for the tank wall in the design process. Ozdemir et al. analysed the problem of fluid-structure interaction by numerical methods and finally introduced a simple model in which the effect of flexibility of tank wall had considered [3]. Estekanchi and Alembagheri published an article in which the effect of higher turbulence mode contributions had been considered [4].

Ormeño et al. studied static uplift of steel tanks and concluded that the important resistant element against uplift is tank under sheet [5].

Malhorta et al. analysed the resistance of semi-infinite beam on a rigid bed against uplift [6].



Brown and Mikle also introduced a method of quasi-static simulation on nonlinear uplift of unbraced tank sheet based on results of the tank sheet uplift model. A simple method for analysing of cylindrical unbraced tanks' uplift was also developed [7].

One of the most techniques that has been recently widely used on soft deposits and loose fine-grained soils is stone columns or singular piles. These stone columns cause an increase in strength of loose soils and also decrease settlements induced by loadings [8].

Nowadays, stone columns are widely used to decrease the settlements of tanks. Stone columns were first used in 1830 in France and after 1950 they are widely used in many other countries [9].

In Iran, stone columns were used firstly with compaction method and since 1383 (Persian Calendar) vibrating methods were imported to create this kind of soil improvement technique. Laboratory investigations have been conducted on the use of lime and fly ash columns to increase the bearing capacity and also decrease settlements of clays [10].

Laboratory results showed that singular stone columns failed at top parts of the column due to bulging phenomenon. Based on the test results of single stone columns, it was concluded that every single column in columns group can deform independently and then failure. In other words, in this method, the effect of columns on adjacent ones is not considered [11]. Many laboratory and numerical investigations showed that it is not true to design and analysis of group stone columns without considering the effect of adjacent columns on each other [12-15]. In this research, numerical simulation is run to evaluate the effects of length and diameter of stone columns and settlement. Moreover, the sliding of the tank in different modes has been considered.

METHODS

The simulated geometry of the tank and its beneath soil using ABAQUS has been shown in Figure 1. The simulated geometry dimensions are 100 m of width, 100 m of length and 30 m of depth. Figure 2 shows the applied acceleration within the soil. The maximum acceleration of the applied earthquake occurs in the first 10 seconds. Soil strength parameters and steel tank dimensions are presented in Table 1. Table 2 presents the linear constitutive properties of material of the cylindrical steel tank. The thickness of the steel tank wall, $t = 0.004 \times R$ is performed as suggested by Jadhav and Jangid [16]. The dimensions of the circular footing of steel tank were selected with a height/radius ratio of 0.66 ($H/R=0.66$) that settled on the soil. In this study, the height and radius of the cylindrical tank footing were selected as 2 m and 3 m, respectively. Relatively fine mesh is used near the surface while a coarser mesh grid was used for farther distance from the centre of the foundation. Stone column and soil were modelled as the perfectly-elastic plastic using the Drucker-Prager model. The boundary conditions were chosen such that the horizontal displacement of the boundary is restricted in all directions, while vertical boundaries are restricted horizontally and free to move in the vertical direction. The acceleration boundary condition is applied at the bottom of the model. The acceleration time history of the earthquake is applied as a base excitation input to the steel tank along x- and y-axis. The base is fixed to a rigid foundation and is assumed to be excited by ground acceleration. The tank wall is modelled using three-node triangular and four-node quadrilateral shell elements, S3R and S4R, respectively. The analysis was performed under displacement controlled method. The model with boundary is used to include deformable foundation effects as a linear elastic soil medium. The Newmark's step-by-step method [17] assuming linear variation of acceleration over a small time interval is chosen for evaluating the response of the system. The tank and stone columns materials are assumed to be linear elastic. The soil medium is modelled as an isotropic elastic space. Provided the assumption is made that the base of the tank is rigidly attached to the foundation thereby linear elastic behaviour was carried out to determine its response.

The applied acceleration record below the tank is one of the El Centro earthquake data recorded in 1940 with a maximum peak of 0.5g. A surcharge (75 kPa) pressure was applied on the soil to simulate the loads from the steel tank. Additionally, analyses were carried out under static



loading in order to evaluate the effects of the stone column on settlements of stone column subjected to such loading.

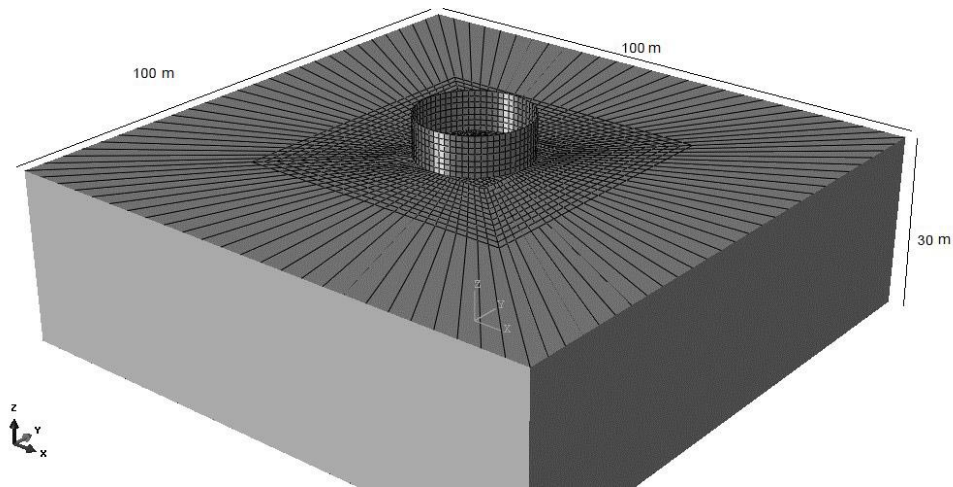


Fig. 1 - Simulated soil and tank

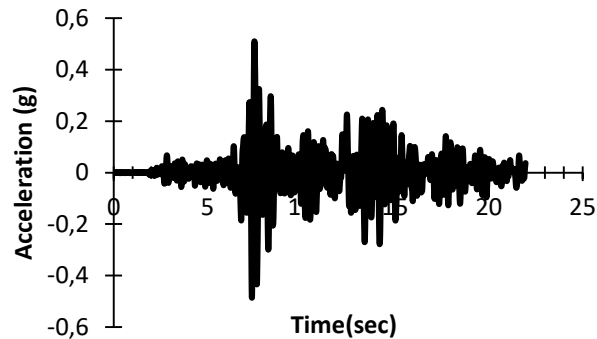


Fig. 2 - Applied earthquake acceleration beneath of the tank

Tab. 1 - Properties of soil

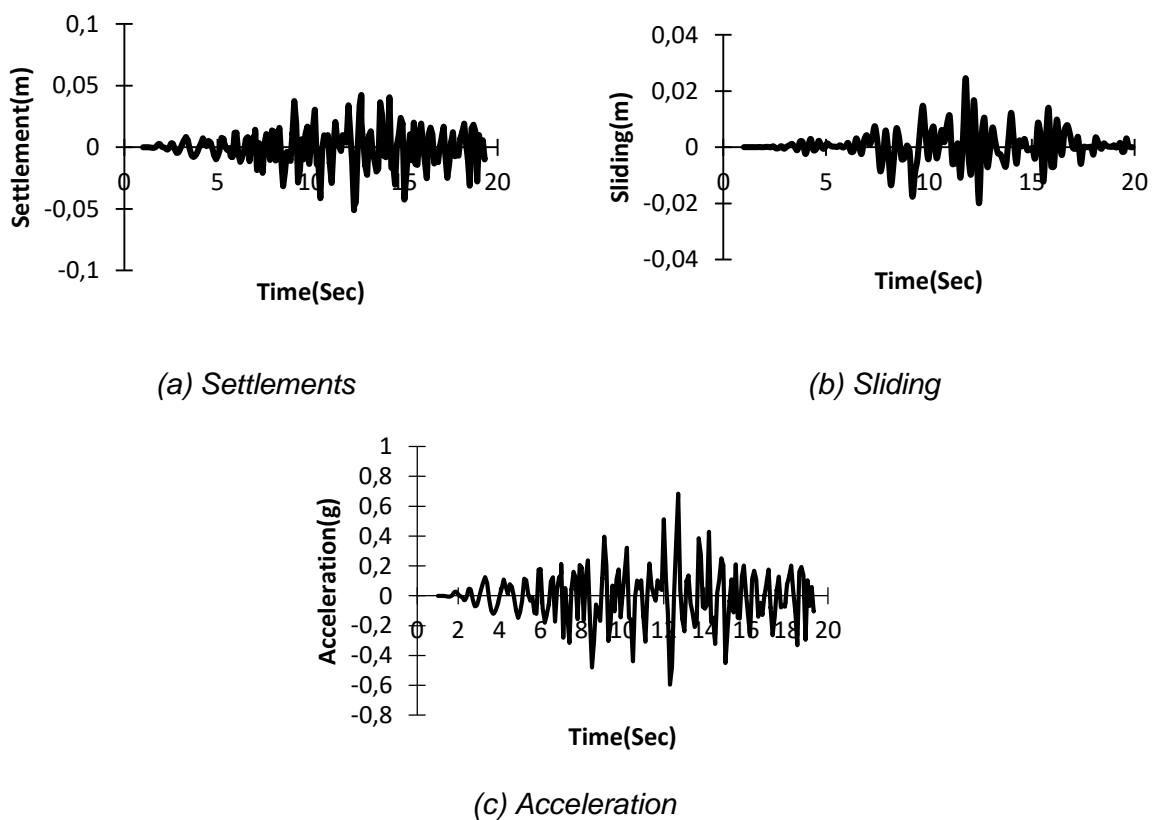
Module of elasticity (E) (kPa)	Poisson's ratio (v)	Unit weight (γ) (kg/m ³)	Friction angle (ϕ)	Cohesion (kpa)	Dilatancy angle (ψ)
Moderate compacted sand	7e6	0.35	1800	35	0
Stone column	20e6	0.25	2000	47	4

Tab. 2 - Parameters of cylindrical tank

Material	Module of elasticity (E) (kPa)	Poisson's ratio (v)	Unit weight (γ) (kg/m ³)	Height (m)	Radius (m)	Wall thickness (m)	
Cylindrical tank	Steel	2e8	0.3	7900	21	14	0.056

RESULTS

As shown in Figure 3, in the beginning, the tank was located on the soil with no stone column and also the amounts of uplift, settlement, slide and recorded accelerate is impressible for the tank on the soil without any improvement. After evaluation of the improved soil with the tank, it was observed that the vertical settlement of soil decreased due to the reinforcing effect of stone columns. Figures 4, 5 and 6 are related to settlement and uplift of the tank foundation and stone columns with the lengths of 8, 10 and 12 m and diameters of 0.4, 0.8 and 1.2 m. With the increase of the column's length, the more area of the soil was affected and simultaneously the improved soil showed more strength to the applied stress during the loading process.


Fig. 3 - Settlement (a), Sliding (b) and acceleration (c) of the tank without stone column

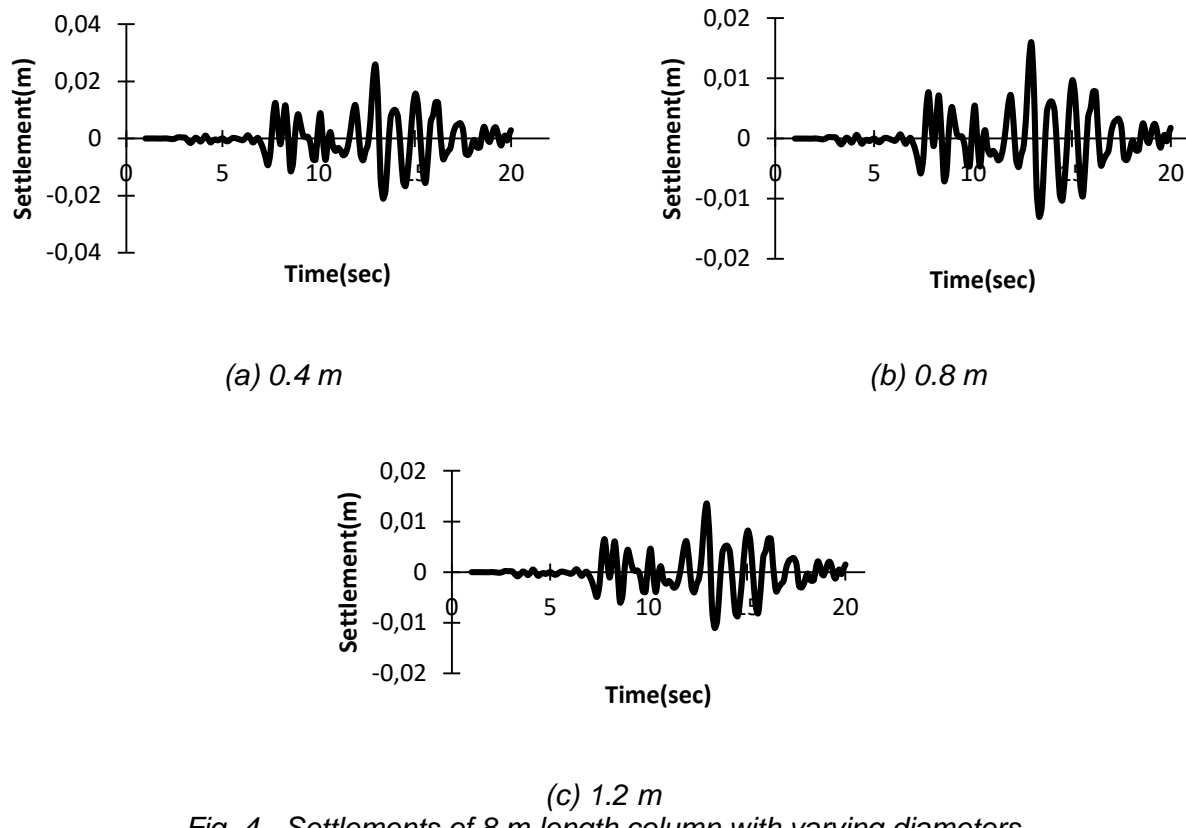
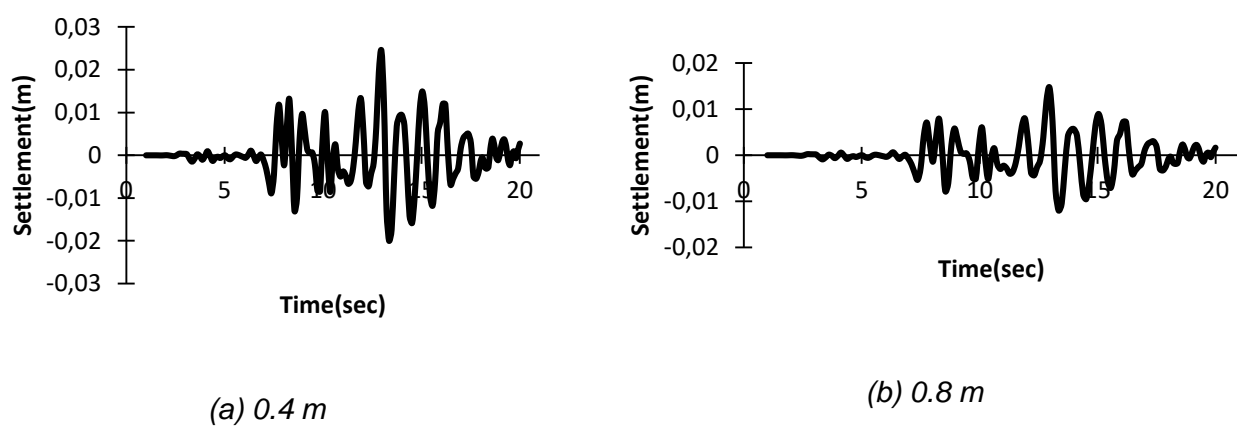
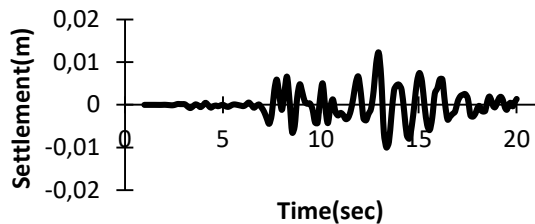


Fig. 4 - Settlements of 8 m length column with varying diameters





(c) 1.2 m

Fig. 5 - Settlement of 10 m length column with varying diameters

It is noticeable that in the present study, the centre to centre distance between all columns is 2 meters and also as it can be noticed that with the increase of the column's length, the settlement and uplift decrease. For instance, in a column with a diameter of 0.8 m and centre-to-centre distance of 2 m, with the increase of the column's length from 8 m to 10 m and then 12 m, the induced settlements decrease of about 7.7 % and 8.3 %, respectively. It is considered that with a constant diameter and centre-to-centre length, the further increase of the length after 8 m, would not have any significant effect on the settlement. Thus, the effect of centre-to-centre and the column's diameter up to a threshold length is more important.

As it can arise from the charts, the amounts of uplift and settlement significantly decreased with the improvement of the soil beneath the tank using stone columns. Furthermore, with the increase of the diameter of the columns from 0.4 m to 0.8 m, there is a significant decrease in uplift and settlement. Also, with the increase of the diameter of the columns from 0.8 m to 1.2 m, the amounts of uplift and settlement decreased but these decreases were more when the diameter was changed from 0.8 m to 1.2 m. Hence, the use of stone columns with 1.2 m in diameter does not seem to cost economically.

In terms of settlements, the use of stone columns has a significant effect on the decrease of the settlements of the tank. As shown in Figure 6, in the exact location of the tank, there are fewer settlements than other areas. This can be justified that by using the stone columns the settlements decreased.

According to uplift results from Figure 7, the settlements of the tank decreased using stone columns. Thus, it is the best way to reduce damages from earthquakes by using improvement techniques.

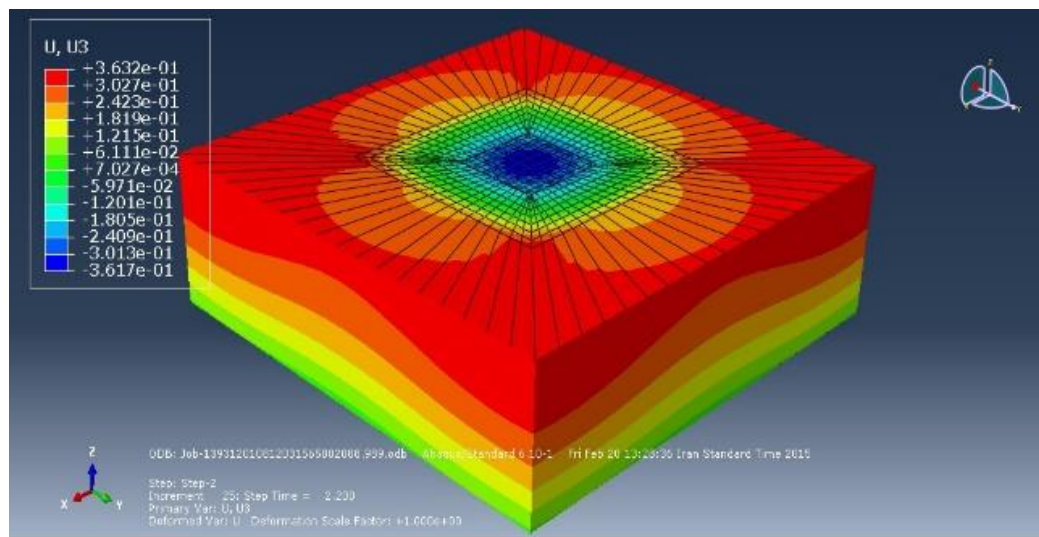


Fig. 6 - Vertical displacements of the foundation of tank using stone columns

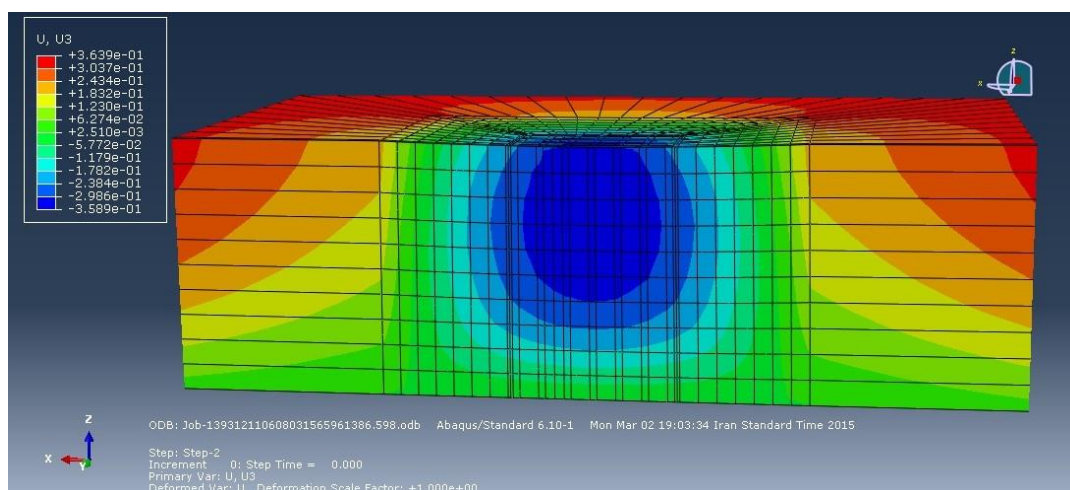


Fig. 7 - settlements of the foundation of tank using stone columns

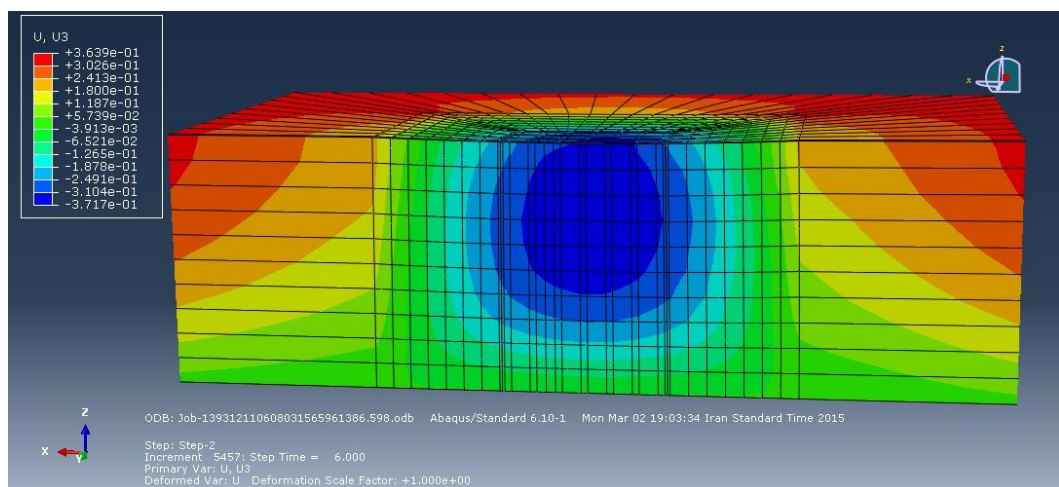


Fig. 8 - Settlements of the foundation of tank without using stone columns

CONCLUSION

The following results are derived from the numerical simulation of the tanks with and without stone columns to decrease the amounts of uplift, settlement and in consequence increase in bearing capacity of them:

- Increase of the length of the columns caused a reduction of settlement. This conclusion is obviously clear in the presented results. In a model with a stone column that has 0.8 m diameter and 2 m centre-to-centre distance, there was a 46% reduction in settlement compared with the model without any stone column. With the increase of the length of the columns from 8 m to 10 m and 12 m, a reduction of 62% and 64% was observed, respectively.
- The study of the diameter of the columns in settlement of the tank is an item which was evaluated in the present study. In soil with a stone column with a diameter of 0.8 m, the increase of the column's length from 0.4 m to 0.8 m, caused a 38% reduction in settlement and with the more increase of the diameter from 0.8 m to 1.2 m, only a 15% reduction were observed. The rate of this reduction with the increase of the diameter from 0.8 m to 1.2 m was less significant.

ACKNOWLEDGEMENTS

The author states that there is no conflict of interest.

REFERENCES

- [1] American Petroleum Institute (API), (1998) "Welded Storage Tanks for Oil Storage," API 650, American Petroleum Institute Standard, Washington D.C.
- [2] Sivý M., Musil M. (2017) Procedure for Seismic Analysis of Liquid Storage Tanks Using FEM Approach and Analytical Models. In: Beran J., Bílek M., Žabka P. (eds) Advances in Mechanism Design II. Mechanisms and Machine Science, vol 44. Springer, Cham. https://doi.org/10.1007/978-3-319-44087-3_28
- [3] Ozdemir, Z., Souli, M., & Fahjan, Y. M. (2010). Application of nonlinear fluid–structure interaction methods to seismic analysis of anchored and unanchored tanks. *Engineering Structures*, 32(2), 409-423.
- [4] Estekanchi, H. E., & Alembagheri, M. (2012). Seismic analysis of steel liquid storage tanks by Endurance Time method. *Thin-Walled Structures*, 50(1), 14-23.
- [5] Ormeño, M., Larkin, T., & Chouw, N. (2015). The effect of seismic uplift on the shell stresses of liquid- storage tanks. *Earthquake Engineering & Structural Dynamics*, 44(12), 1979-1996.
- [6] Malhotra, P. K., Wenk, T. and Wieland, M, (2000) "Simple Procedures for Seismic Analysis of Liquid Storage Tanks", *Structural Engineering International*, IABSE, Vol. 10, No. 3, pp 197-201.
- [7] Brown, S.; Mikle, G.N. (2010), Analysis of stone column reinforced foundations. *Int. J. Numer. Anal. Methods Geomech.* 22, 1001–1020. [https://doi.org/10.1002/\(SICI\)1096-9853\(199812\)22:12<1001::AID-NAG955>3.0.CO;2-I](https://doi.org/10.1002/(SICI)1096-9853(199812)22:12<1001::AID-NAG955>3.0.CO;2-I)
- [8] Wood, D.M.; Hu, W.; Nash, F.T.: Group effects in stone column foundation: model tests. *Geotechnique* 50(6), 689–698 (2005).
- [9] Malarvizhi, S. N. (2007). Comparative study on the behavior of encased stone column and conventional stone column. *Soils and Foundations*, 47(5), 873-885.
- [10] Bowles, Joseph E. 1988. Foundation analysis and design. New York: McGraw-Hill.
- [11] Ngo, N. T., Indraratna, B., & Rujikiatkamjorn, C. (2016). Load-deformation behavior of a stone column using the coupled DEM-FDM method. In *Geotechnical and Structural Engineering Congress 2016* (pp. 1618-1626).
- [12] Deb, K., Samadhiya, N. K., & Namdeo, J. B. (2011). Laboratory model studies on unreinforced and geogrid-reinforced sand bed over stone column-improved soft clay. *Geotextiles and Geomembranes*, 29(2), 190-196. <https://doi.org/10.1016/j.geotexmem.2010.06.004>
- [13] Elsawy, M. B. D. (2013). Behaviour of soft ground improved by conventional and geogrid-encased stone columns, based on FEM study. *Geosynthetics International*, 20(4), 276-285.



- [14] Jaiswal, O. R., Rai, D. C., & Jain, S. K. (2007). Review of seismic codes on liquid-containing tanks. *Earthquake Spectra*, 23(1), 239-260.
- [15] Papadrakakis, M., & Fragiadakis, M. (2017). EVALUATION OF CODE PROVISIONS FOR SEISMIC PERFORMANCE OF UNANCHORED LIQUID STORAGE TANKS.
- [16] Jadhav, M. B. and Jangid, R. S., "Response 26. of base-isolated liquid storage tanks", *Shock and Vibration*, Vol. 11, 2004, pp 33–45. DOI :10.1155/2004/276030
- [17] Rosenblueth, E. and Newmark, N.M. (1971). "Fundamentals of Earthquake Engineering", Preince-Hall, N.J.

EFFECT OF WATER-CEMENT RATIO, CEMENT DOSAGE, TYPE OF CEMENT AND CURING PROCESS ON THE DEPTH OF CARBONATION OF CONCRETE

Malek Jedidi^{*1,3} Omrane Benjeddou^{2,3}, Chokri Soussi²

1. Higher Institute of Technological Studies of Sfax, Department of Civil Engineering, Sfax, Tunisia.
2. Prince Sattam bin Abdulaziz University, College of Engineering, Civil Engineering Department, Alkharij, Saudi Arabia
3. University of Tunis El Manar, National Engineering School of Tunis, Civil Engineering Laboratory, Tunis, Tunisia; malekjedidi@yahoo.fr

ABSTRACT

In recent years, the durability of concrete has been the subject of a few research projects carried out by several scientific and technical centres. As a major cause of concrete degradation around the world, reinforcing steel corrosion requires our full attention. This article analyses one of the phenomena at the origin of these disorders, namely the carbonation of concrete, and proposes some provisions to guard against it. The article is divided into two parts; the first describes the causes and consequences of the chemical process of carbonation as well as the means to protect it. The second deals with the influence factors on carbonation such as the minimum cement dosage, the type of cement, the water-cement ratio (W/C) and the reinforcement coating. Indeed, prismatic specimens ($15 \times 15 \times 60 \text{ cm}^3$) and cubic specimens ($15 \times 15 \times 15 \text{ cm}^3$) were made for different mixtures and with a W/C ratio of 0.50, 0.55 and 0.60. The prismatic specimens were subjected to a carbonation test, while the cubic specimens were used to determine the compressive strength, the corresponding density and the immersion water absorption.

KEYWORDS

Durability, Carbonation depth, Concrete, Reinforcement corrosion, Cement, Dosage

INTRODUCTION

Concrete exposed to the air is subjected to an aging process that results from the reaction of carbon dioxide (CO_2) in the air with the alkaline constituents of the material. This reaction is called carbonation.

The carbonation of concrete is an inseparable phenomenon of this building material. During the lifetime of the structure, the carbon dioxide in the atmosphere enters the concrete from the surface of the material. A young concrete has a high pH which is around 12 to 13. This alkalinity leads to the formation, at the periphery of the reinforcements, of an almost impenetrable layer of iron hydroxides insulating the steel and stopping the process of corrosion. We talk about passivation of steel. During the life of the structure, the confrontation of concrete under the action of chemical environments such as sulfate reactions, alkaline reaction and carbonation can cause their degradation [1-3]. The concrete traps carbon dioxide at the level of 10 to 15% of the CO_2 emitted during the decarbonation of the limestone necessary for the manufacture of the cement. During the twentieth century, engineers learned to master certain problematic consequences of the carbonation phenomenon. At the end of the life of the structure, this time carbonation can be



exploited to fix CO₂ in the hardened cement paste of a demolition concrete. Recent results show that it is then possible to adjust up to 50 to 60% of additional CO₂. Moreover, this carbonation is particularly favourable for improving the quality of the recycled granulate from the demolition concrete, thus facilitating its reuse.

Unlike the harmful consequences of carbonation on the durability of concrete structures, carbonation is rather a beneficial phenomenon from the point of view of the concrete material itself. It is indeed to recognize that the carbonation of cement matrices based on CEM I type cement is achieved with a mass gain corresponding to the fixation of CO₂ in the hydrates. The fact that the molar volume of the calcium carbonate formed is greater than that of the hydrates leads to clogging of the microstructure which makes the concrete less permeable to aggressive agents (in this case CO₂ and O₂ gases, but also sulphate ions, chlorides, and more generally, aggressive waters such as seawater, selenite or magnesian waters, ...).

It has even been shown that carbonation makes it possible to increase the mechanical resistance of concrete and to make the material more chemically stable vis-à-vis swelling reactions (internal or external sulfatic reaction, alkali-aggregate reaction). On the other hand, the modulus of rigidity or modulus of elasticity is increased, which is not always perceived as an advantage because this can lead to embrittlement of thin parts and to a heterogeneity of resistance and shrinkage in the case of coatings of partially carbonated facades where surface cracks can be observed which stop at the level of the non-carbonate internal zone.

A lot of research has been done to find out the influence of the W/C ratio on the carbonation rate. Papadakis et al. [4] show that the depth of carbonation is doubled when the W/C ratio goes from 0.5 to 0.8. The study by Loo et al. [5] focused on the influence of the W/C ratio and the cement content. Their results have led to consider that the most important parameter is the W/C ratio and that the cement content remains by comparison insignificant.

Taylor et al. [6] observed a decrease in carbonate thicknesses when the cement content increases. Two concomitant explanations for the decrease in the rate of carbonation are noted in the literature [6,7]:

- On the one hand, the quantity of lime to carbonate per unit of volume increases with the dosage of cement. The carbonation time is then longer, the carbonation speed decreases. Note that the amplitude and depth of carbonation also decreases.
- On the other hand, the compactness of the material tends to increase with the dosage of cement. The decrease in the amount of mixing water, induced by a higher dosage of cement, reduces the porosity of the cement, thus slowing the penetration of CO₂ into the porous network. Consequently, the carbonation rate decreases.

Muller and Sickert [8] compared the carbonation resistance of concretes made from ordinary Portland cement or cement based on blast furnace slag. They have shown that cement mixes based on blast furnace slag carbonate much faster than Portland cement mixes for an identical W/C ratio. Their study has also shown that only cement concretes based on blast furnace slag are carbonated.

Kobayashi and Uno [9] studied the carbonation rate of concretes made with cements with different alkaline contents. Their results from accelerated carbonation and natural carbonation tests have shown that an increase in the alkali content leads to greater carbonation of the concrete. These authors also studied the influence of the alkali content at different W/C ratios; they showed that an increase of 0.6% in alkali is equivalent, from the point of view of carbonation, to an increase in W/C ratio of 0.10.

Loo et al. [5] have shown that the carbonation rate decreases with the duration of an underwater cure regardless of the compressive strength of the concrete at 28 days. They noted that after 14 days of treatment, the improvement is less. They also carried the carbonation coefficient as a function of the inverse of the square root of the compressive strength. They found that the points line up on the same straight line whatever the duration of the cure, which means

that the improvement in resistance due to the cure is the preponderant factor responsible for the reduction in the carbonation rate.

Fattuhi [10] studied the improvement brought by a cure of concrete under water. The results of the accelerated carbonation tests have shown that concretes subjected to a cure in water of 1, 3, 5, 7 and 28 days respectively have a carbonation rate of 66, 63, 42, 39 and 17% compared to a cure performed in the air.

Gruyaert et al. [11] have shown that a curing period longer than 1 month significantly improves the durability properties of slag cements. The effect of the cure is more appreciable for a slag cement because of its slower hydration kinetics [12,13]. However, for treatment duration of more than 3 months, the resistance to carbonation is no longer significantly modified. Furthermore, it seems that increasing the curing period does not have the same effect in the case of Portland cement or in the case of a composite cement [14]. The results of Lo and Lee [15] also tend towards this result. According to several authors [14,16], the effect of the cure on carbonation is minimal compared to the effect of the nature of the cement.

The carbonation of concrete is also correlated with other parameters such as mineral addition. Skenderovic [17] has shown that replacing part of the cement (10%) with silica fumes increases the rate of natural carbonation of the concrete although the porosity is considerably reduced. He explained this phenomenon by the lower quality of portlandite in concretes with silica fumes. In the study by Richardson et al. [18], the authors have shown that the addition of scilice fumes limits the depth of carbonation of the concrete. These contradictory results require further investigation to assess these additions under similar conditions of W/C ratio and curing of concrete samples.

For the addition of furnace slag, Skenderovic [17] and Malami et al. [19] have not obtained any significant change in the carbonation rate for cement replacements up to 30% and 15% respectively. They observed a significant increase in carbonation only for the replacement of 50% of the cement by slag.

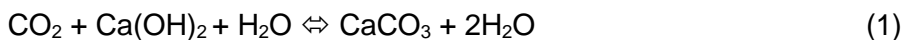
Papadakis et al. [4] studied the influence of fly ash on the depth of carbonation of concrete. The results of their analysis have been very marked when we exceed 15%. The replacement of aggregates with fly ash has an opposite effect but with a lesser tendency.

The main objective of this experimental study is to describe the causes and consequences of the chemical process of carbonation as well as the means to protect it. The influence of certain parameters on carbonation such as the minimum cement dosage, the type of cement, the water-cement ratio (W/C) and the reinforcement coating has also been studied.

CARBONATION AND CORROSION

Carbonation process

Carbon dioxide is diluted in the water contained in the porous structure of the concrete. This reaction allows the calcium hydroxide to dilute in turn in the interstitial water, to react with the CO₂ and to precipitate in the form of calcium carbonate, which lowers the pH of it to a value close to 9 [20-22]. Carbonation of hydrated calcium silicates (C-S-H) is also possible. The reaction is represented chemically as follows:



The carbonation of C-S-H, which contributes significantly to the fixation of CO₂ in the cement matrix, is responsible for important changes in the microstructure (Figure 1).

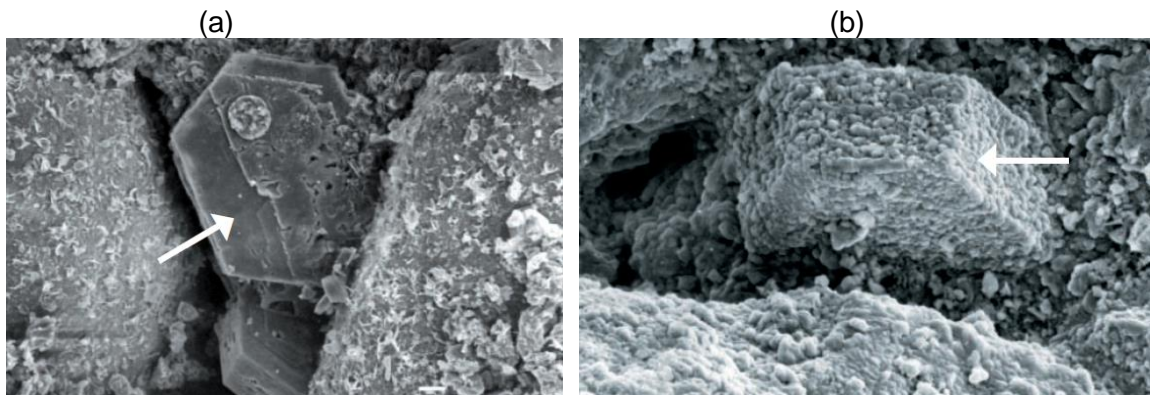


Fig. 1- Portlandite crystal observed under a scanning electron microscope (SEM). (a): Non-carbonated portlandite crystal; (b): Portlandite crystal in the process of carbonation.

Generally, corrosion of reinforcement begins with the drop in pH. At this stage, we notice a loss of passivity of the concrete against corrosion of the reinforcements. Table 1 gives the effect of pH drop on the state of corrosion of reinforcements

Tab. 1 - Effect of pH drop on the state of corrosion of reinforcements [23]

pH of concrete	State of reinforcement corrosion
< 9.5	Commencement of steel corrosion
8.0	Passive film on the steel surface disappears
< 7.0	Catastrophic corrosion occurs

For most concretes, the precipitation of calcium carbonate (CaCO_3) results in an improvement in the compactness of the structure and a slight increase in compressive strength. In reinforced concrete, however, this reaction may lead to degradation due to corrosion of reinforcement. Over time, the carbonation front, which is the demarcation between the carbonate zone of the concrete and the intact zone, progresses more and more deeply in the structure (Figure 2).

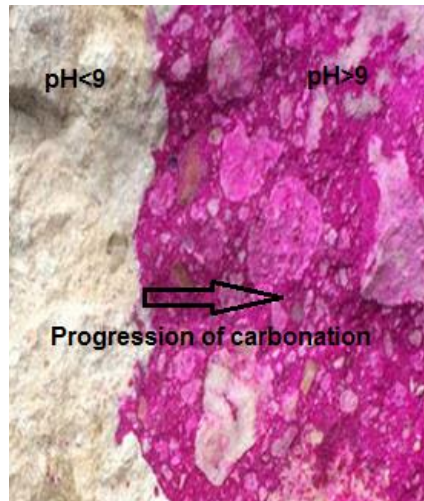


Fig. 2 - Progression of carbonation in concrete

However, the rate of carbonation decreases with time, since CO_2 must penetrate ever further into the concrete and the pores are clogged with calcium carbonate. The approximate depth of carbonation can be calculated using the following formula:

$$D = K_C \cdot (t)^{\frac{1}{2}} \quad (2)$$

Where, D is the carbonation depth (mm), K_c is the carbonation coefficient, a function of the quality of the concrete and its exposure [mm/(years) $^{1/2}$], t is the age of concrete (years).

The carbonation coefficient K_c gives an indication of the concrete's resistance to carbonation; it depends on the composition of the latter, the cure achieved and the exposure of the structure. In a concrete exposed to a specific medium, the higher the coefficient, the faster carbonation will be and therefore the lower the resistance to the phenomenon.

As soon as the carbonation front reaches the reinforcement, the pH decreases in the area of the concrete located on the periphery of the steel, the passivation layer is destabilized, dissolves and its protective action disappears. If the structure also contains water and oxygen, the reinforcements will begin to rust. The corrosion products formed will occupy a volume several times greater than that of steel, which will lead to cracking and crumbling of the concrete.

In general, it is found that the corrosion of the reinforcements induced by carbonation affects the elements more or less uniformly over long distances (generalized corrosion). It is also reported that the resistivity decreases and corrosion rate increases with an increase in the chloride content [24]. In fact, the modification of the chloride content causes a slight variation in the pH value. Table 2 describes the level of corrosion of reinforcement as a function of the chloride content in the concrete.

Tab. 2 – Level of corrosion in concrete containing chlorides [25]

Chloride content	Condition of concrete adjacent to reinforcement	Level of corrosion
Less than 0.4%	Carbonated	High
	Uncarbonated, made with cement containing less than 8% C ₃ A	Moderate
	Uncarbonated, made with cement containing 8% or more C ₃ A	Low
0.4% - 1.0%	As above	High
	As above	High
	As above	Moderate
More than 1.0%	All cases	High

Measurement of concrete carbonation depth

The phenolphthalein method was used to measure the depth of carbonation according to BS EN 14630 [26]. Phenolphthalein is a coloured indicator used to estimate the pH in weak acid or strong base assays. It changes colour depending on the pH value of the solution. When the concrete is not carbonated, the phenolphthalein becomes red and it remains colourless in the case of carbonated concrete.

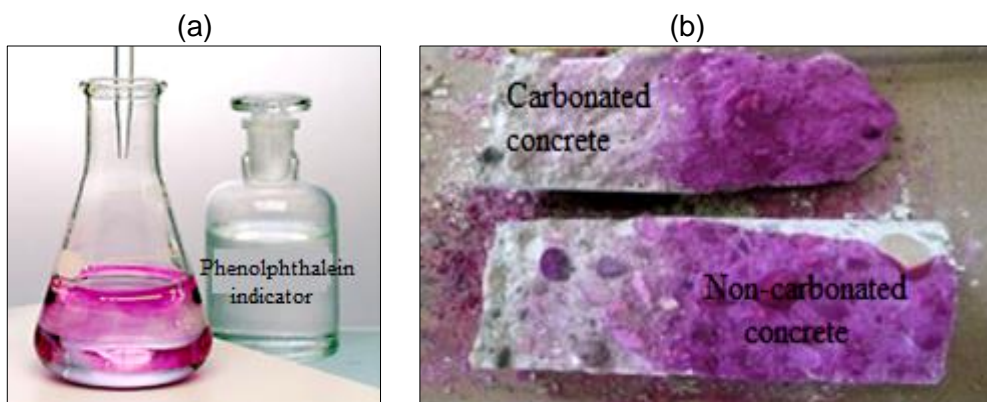


Fig. 3 - Phenolphthalein Test. (a): Phenolphthalein indicator; (b): Carbonated and non-carbonated concrete

The steps of the phenolphthalein test are as follows: (Figure 3):

- Break a relatively large surface or a concrete core in the lengthwise;
- Apply the phenolphthalein indicator solution to the surface to be tested. It is advisable to apply a light mist of water on the broken surface in the case of very dry concrete;
- Measure with a graduated ruler the distance between the edge of the red-purple coloured area and the exterior surface of the concrete and deduce the average depth of carbonation.

According to some authors [27-29], environmental conditions and exposure conditions influence the phenomenon of carbonation of concrete.

This procedure requires fairly large samples. To limit the damage due to sampling, another measurement method is used; this consists of drilling small holes 6 to 8 mm in diameter into the concrete and collecting the drilling powder on a sheet impregnated with phenolphthalein. In the case of a concrete slab, the powder can be sprinkled regularly with phenolphthalein. As soon as the drilling reaches the healthy concrete, the powder changes colour. The depth of the drilling then corresponds approximately to the depth of carbonation. The measurement should be made at least three times in each area examined to reduce the influence of local phenomena such as the presence of aggregates. It must also be taken into account that the depth of carbonation can be higher in cracks and angles.

Parameters influence carbonation kinetics

There are many models of carbonation that translate, more or less directly, the physicochemical resistance of concrete against the penetration of the carbonation front.

The parameters used relate to:

- The porosity of the concrete which conditions the "physical" resistance of the material to the diffusion of CO₂;
- The content of carbonatable hydrates: the higher it is, the more the concrete is able to "chemically" slow down the penetration of the carbonation front;
- The microstructure of the material (pore size) on which depends the hydrous state of the material which will condition the kinetics of penetration of the phenomenon. It is then essentially the liquid water permeability of the material that will be an indicator of relevant durability.

These models generally result in a slow evolution in the square root of the time of the carbonation depth. To fix ideas, with ordinary concrete preserved in an environment whose relative humidity is between 50 and 70%, the carbonation depth is 5 mm after one year, 10 mm after 4 years and 25 mm after 25 years.

The mechanism of concrete carbonation is affected by several internal and external factors. The Internal factors are cement type and content [27], curing conditions and curing time [30] and water cement ratio. The external factors are the relative humidity [31-33], sheltering, rain, CO₂ concentration and temperature [33,34].

Carbonation can also be the cause of disorders in the facade coatings generally corresponding to high-fat mortars (Ca(OH)₂) partially carbonated.

The acidification of the medium that results from the attack of CO₂ can be at the origin of the development of microorganisms (lichens, mosses, algae, etc.) that do not grow in a strongly basic medium. These microorganisms are at the origin of unsightly stains. It is possible to temporarily remove these traces by washing the wall with diluted bleach or using a suitable fungicide product.

METHODS AND MATERIAL

Principle

The fundamental element that controls the carbonation of concrete is the diffusion of CO₂ through the hardened cement paste. This is why the requirements impose limit values for the



water-cement ratio (maximum) and the cement (minimum) dosage. Exposure of concrete (moisture content) has an influence on the carbonation rate.

The purpose of this work is to determine the influence of various parameters on the concrete's resistance to carbonation. The parameters studied were:

- The type of cement;
- The cure of concrete;
- The water-cement ratio (W/C);
- The cement dosage.

In the absence of a standard test procedure, a method has been developed to characterize the concrete's resistance to carbonation and to examine the influence of the above parameters. This test method is deliberately simple in nature so that it can be used both for testing site samples and for testing as part of a certification.

Test method

The concretes used in the research were composed of calcareous aggregates, the dimensions of which were distributed in accordance with standard NF EN 480-1 [35].

Different types of cement were used (CEMI 32.5N, CEMI 42.5N and CEMII A-L 32.5N) in conformity with Tunisian Standard NT 47.01 and European standard EN 197-1:2000 produced by the Cement Company of BIZERTE. Table 3 shows the chemical composition and compressive strength at 28 days of cement.

Tab.3 - Chemical composition and properties of cement

Chemical composition	Type of cement			
	CEMI 32.5N (%)	CEMI 42.5N (%)	CEMIIA-L 32.5N (%)	
Insoluble Residue (IR)	≤ 5	≤ 5	-	
Sulphur Trioxide (SO_3)	≤ 3.5	≤ 3.5	≤ 3.5	
Magnesium Oxide (MgO)	≤ 5	≤ 5	≤ 5	
Chloride (Cl)	≤ 0.1	≤ 0.1	≤ 0.1	
Soundness (mm)	≤ 10	≤ 10	≤ 10	
Initial Setting Time (mn)	≥ 60	≥ 60	≥ 60	
Compressive strength at 28 days (MPa)	min 32.5	Max 52.5	min 42.5	Max 62.5
			min 32.5	Max 52.5

The mixtures were prepared with a W/C ratio of 0.50 and a cement dosage of 300 kg/m³. For cements CEM I 42.5 N and CEM II A-L 32.5 N, mixtures were also formulated with a W/C ratio of 0.55 and 0.60 (cement content 300 kg/m³) and cement dosages of 280 kg/m³ and 350 kg/m³ (W/C ratio of 0.50).

Prismatic specimens (15 x 15 x 60 cm³) and cubic specimens (15 x 15 x 15 cm³) were made for each mixture. The prismatic specimens were subjected to a carbonation test, while the cubic specimens were used to determine the compressive strength (at 28 days), the corresponding density and the immersion water absorption.

After a hardening of 24 hours, the samples were demolded and underwent two different treatments:

- An ideal cure: preservation for 56 days in an environment with (20 ± 2°C) and more than 90% relative humidity (RH);
- An unsatisfactory cure: preservation for 56 days in an environment at (20 ± 2°C) and (60 ± 2%) relative humidity (RH).

The long cure time (56 days) is intended to allow sufficient primary and secondary hydration. After this time, the specimens are dried for 14 days, and then stored at a temperature of 20 ± 2 °C and a relative humidity of 60 ± 2% until constant mass.



The prismatic specimens were stored for 56 days in the carbonation chamber, within which the CO₂ content is regulated at 1%, the temperature at (20 ± 2°C) and the relative humidity at (55 ± 5%). A number of prismatic specimens were split after 3, 7, 14, 28, 35, 42 and 56 days to measure the average carbonation depth.

The different samples were subjected to several tests: resistance in compression, determination of the corresponding density and the absorption of water by immersion. Subsequently, correlations between these characteristics were established.

Measurements of porosity accessible to water on the concrete samples were carried out. This method is now the subject of an AFPC-AFREM operating mode which therefore ensures a homogeneous practice of this test and which allows a comparative treatment of the results, regardless of the laboratory where they were obtained. The results obtained provided an indicator of the quality of the mixture which is well correlated with the compressive strength: when the porosity decreases (due to a decrease in the W/C ratio), the strength increases.

RESULTS AND DISCUSSION

Measurement of concrete carbonation depth

The approximate depth of carbonation was calculated using the formula (2). The mean carbonation depth as a function of the square root of the exposure time ($\sqrt{\text{days}}$) is given in Figure 4. When applying the phenolphthalein solution to the samples, it was noticed that the non-carbonated area takes on a dark pink colour, on the other hand the carbonated area remains colourless. Phenolphthalein therefore offers a simple reading of the depth of carbonation since the forehead is sharp and generates good colour contrasts. It was noted that concretes based on CEM II are more carbonated than concretes based on CEM I for all ages. We also observed on the samples that the carbonation front increases with the W/C ratio and with the time of exposure to CO₂.

It was also noted that after 35 days, the concretes based on CEM II were completely carbonated. This rapid carbonation is mainly due to the high value of the W/C ratio which influences the porosity and subsequently its permeability. On the other hand, the concretes based on CEM I were not entirely carbonated even after 56 days.

According to the carbonation models, the evolution of carbonate thickness follows a square root law of time. For our concretes, the depths measured over time do not strictly form a line segment. Indeed, several authors believe that the kinetics of accelerated carbonation does not obey a square root law of time. It associates the curvature of the kinetics curve of the carbonation front with the carbon dioxide depletion of the material by chemical carbonation reactions. Thus, it would not be a simple process of diffusion which follows kinetics in square root of time.

According to the results of Figure 4, it is noted that the kinetics ratio between the carbonation of concretes composed of CEM II and CEM I is associated with the lower content of portlandite in CEM II. As a result, a smaller amount of CO₂ is needed to consume the portlandite. These results are in agreement with the results of Papadakis et al. [4] who observed a faster rate of progression of the carbonation front in composite cement than in pure Portland cements.

The use of a concrete based on CEM I 42.5 and a W/C ratio = 0.50 made it possible to obtain a high performance concrete durable and resistant to carbonation. This result is mainly due to the good compactness of the concrete, which considerably reduces the penetration of CO₂ as well as the high reserve of Ca(OH)₂.

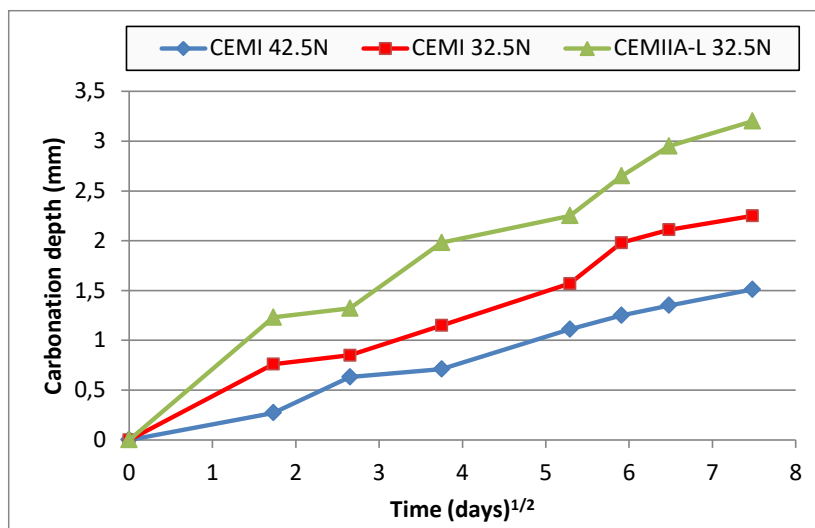


Fig. 4 - Determination of carbonation depth by linear regression coefficient

Effect of water-cement ratio (W/C)

The incidence of the W/C ratio was studied on concrete containing two types of cements (CEM I 32.5 N and CEM II/AL 32.5 N) dosed at a rate of 300 kg/m³. Figure 5 and 6 give the results obtained on three test pieces for each W/C ratio used. As expected, the resistance to carbonation increases as the W/C ratio decreases.

It is noted that the W/C ratio exerts a great influence on the porosity of the hydrated cement paste because it directly governs the initial spacing between the grains of cement suspended in the mixing water.

In fact, when the W/C ratio is low, the grains of cement become very close to each other and the carbonation decreases. The gaps between the cement grains are smaller and there is less chance of having a large void that cannot be completely filled by hydrates.

The reduction in the W/C ratio not only makes it possible to reduce the total volume of the capillary pores but it also makes it possible to reduce their diameter.

For a lower W/C ratio, the capillary porosity is in fact made up of a finer and more discontinuous network of pores.

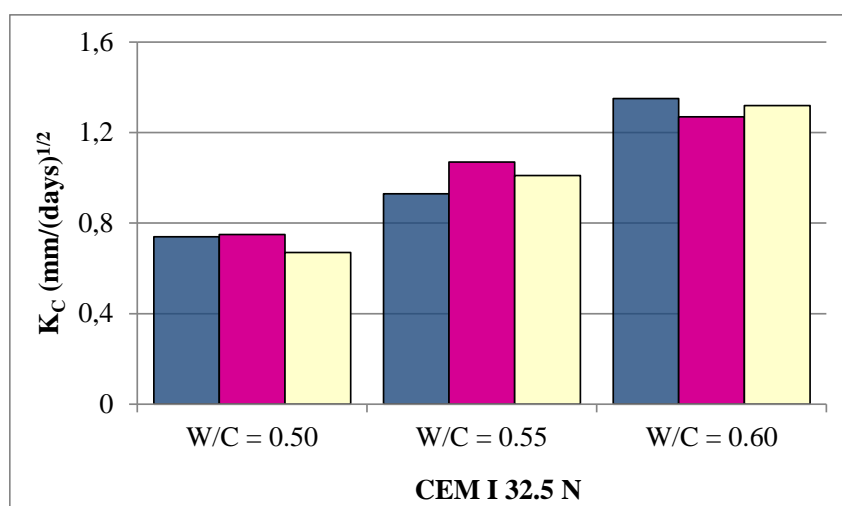


Fig. 5 - Effect of W/C ratio on K_C of cementitious concrete CEM I 32.5 N dosed at 300 kg/m³.

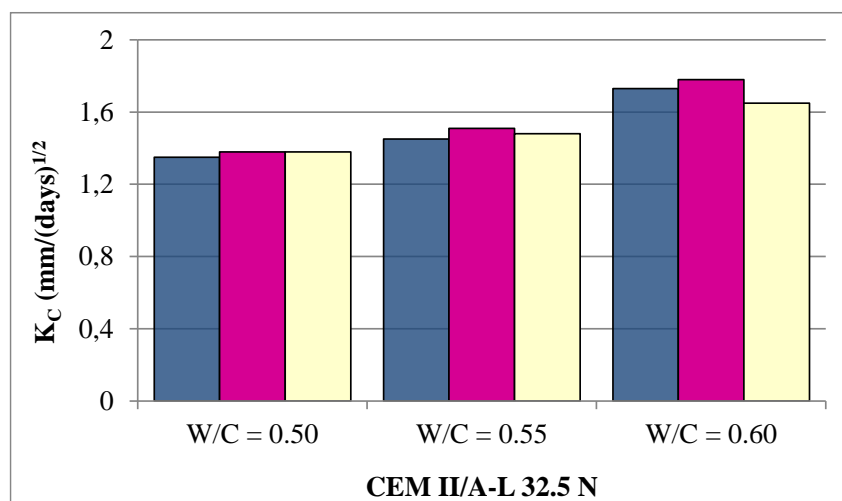


Fig. 6 - Effect of W/C ratio on K_c of cementitious concrete CEM II/A-L 32,5 N dosed at 300 kg/m³.

No macroscopic trace of carbonation was observed even after one month on the concrete containing cement CEM I, W/C = 0.50. Conversely, the concrete containing cement CEM II, W/C = 0.60 has a carbonation detectable from the first day of exposure to CO₂ and which turns out to be total from 20 days because of its high porosity.

It is also noted from the results of Figure 5 and 6 that the progression of the carbonation of the concrete containing the cement CEM I, W/C = 0.60 is similar to that of the concrete containing the cement CEM II, W/C = 0.50. This means that with regard to accelerated carbonation, increasing W/C from 0.50 to 0.63 is equivalent to moving from CEM I to CEM II.

Effect of cement dosage

The effect of cement dosage was also examined on cement-based concrete CEM I 42.5 N with a W/C ratio of 0.50. The results obtained on three specimens for each cement dosage are shown in the diagrams of Figure 7. We did not find any significant effect of the cement dosage on the carbonation resistance. However, it must be emphasized that the quantities of cement used during the study were relatively high and not very differentiated.

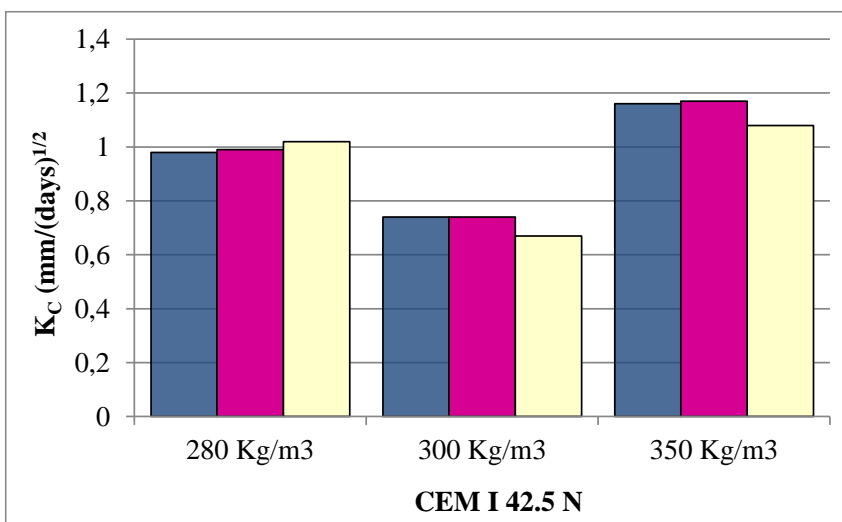


Fig. 7 - Effect of cement dosage on K_c of cementitious concrete CEM I 42,5 N.

Apart from the cement dosage, a major point influencing the degree of carbonation is the nature of the cement. Compound cements, which substitute part of Portland cement with mineral

additions (silica smoke, fly ash, blast furnace slag), carbonate differently depending on their compositions. In addition, a brief synthesis of the works relating to the effect of mineral additions on the rate of carbonation is proposed. Only the mineral additions used in the composition of the cements studied for this study are taken into account.

Effect of the type of cement

The carbonation coefficients K_C obtained with concretes formulated with different types of cement dosed at 300 kg/m³ and having W/C ratio of 0.50 are presented in Table 4.

The influence of the cement type has been demonstrated by comparing the carbonation coefficient of each cement with that of the CEM I 32.5 N (reference cement). Thus, it can be seen that with W/C ratio and identical dosages, the cement with additives (Calcareous Filler, Gypsum) have a higher carbonation coefficient than Portland cement. This unfavourable effect is accentuated, as the fineness of the cement decreases (passage from class 42.5 to 32.5 for the same type of cement).

Tab.4 - Carbonation coefficients K_C obtained with different cements and different curing processes

Cements	K_C (mm/ $\sqrt{\text{days}}$)		Unsatisfactory cure/Ideal cure
	Ideal cure	Unsatisfactory cure	
CEM I 32.5N	2.22	2.79	1.26
CEM II/A-L 32.5R	1.15	2.29	1.99
CEM I 42.5N	0.72	1.57	2.18

Effect of curing process

The cure consists of taking protective measures to reduce the evaporation of water on the concrete surface or to preserve its moisture content. For in-situ concrete, several cure classes have been defined. These correspond to a cure time of 12 hours or the time required to reach a given resistance in compression (Table 5). The cure class must be specified in the performance requirements.

Tab.5 - Cure class [26]

Cure class	Percentage of the value specified for the compressive strength at 28 days
Class 1(*)	-
Class 2	35%
Class 3	50%
Class 4	70%

(*) Provided that the setting does not exceed 5 hours and the temperature on the surface of the concrete is equal to or greater than 5 °C.

The results of research shown in Table 5 also show that the type of cure has a major influence on the resistance of concretes to carbonation. In fact, poor cure conditions lead to carbonation coefficients two times higher than those obtained on the series of specimens composed of the same cement but subjected to optimal conditioning.

Correlations with other common features

The carbonation coefficient is not a common evaluation criterion, nor is it a fast measuring device to control the quality of a concrete. This is why correlations with more conventional characteristics such as water absorption or compressive strength were established.

The absorption of water by immersion has been determined according to standard NBN B 15-215. The results of Figure 8 show that the absorption of water by immersion is between 4.4% and 6.3% for the concretes studied in the research.

We also note that the lowest carbonation coefficients were obtained with concretes with the lowest absorption values. However, the carbonation coefficients could not be directly correlated with the water absorption by immersion.

The type of cement, the W/C ratio, the cement dosage and the degree of hydration are also factors influencing the compressive strength of concrete; it was once common to consider that the resistance to carbonation was a function of the resistance in compression.

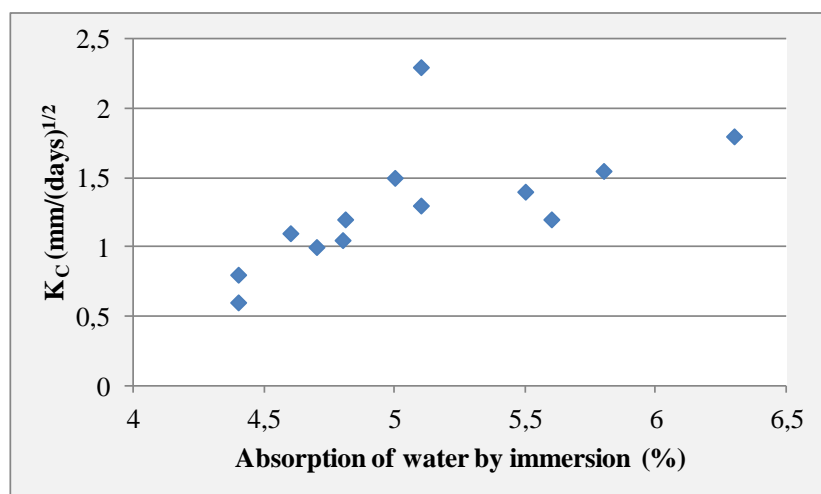


Fig. 8 - Correlation between K_c and absorption of water by immersion

However, as shown in Figure 9, there is no direct link between the carbonation coefficient and the compressive strength determined according to NBN EN 12390-3 at 28 days. At most it is noted that the carbonation coefficients are the highest in concretes of lower compressive strength and, conversely, the concretes that resist compression best also have the lowest carbonation coefficients.

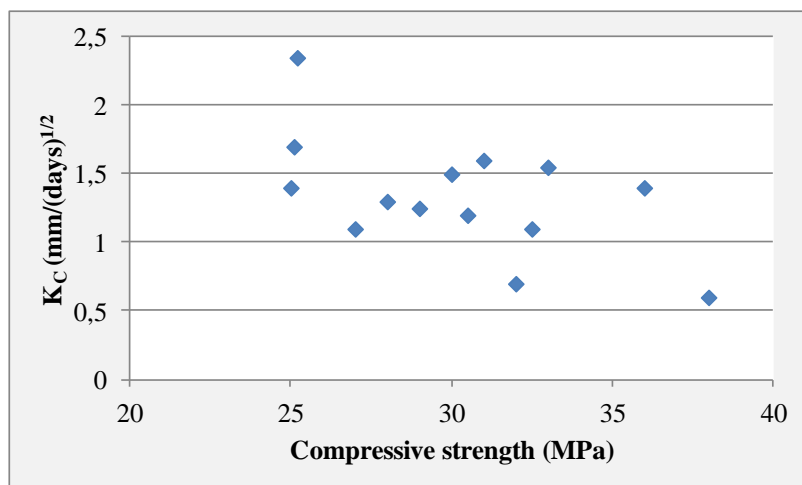


Fig. 9 - Correlation between K_c and compressive strength

CONCLUSION

The present paper has presented results of an experimental study conducted on prismatic and cubic specimens to analyse the phenomena of carbonation of concrete and proposes some provisions to guard against it. The following results have been deduced:

- The resistance to carbonation increases as the W/C ratio decreases for concrete containing two types of cements (CEM I 32.5 N and CEM II/A-L 32.5 N) dosed at 300 kg/m³.

- The cement dosage has no effect on the carbonation of the concrete specimens made with CEM I 42.5 N and W/C ratio of 0.50.
- The cements dosed at 300 kg/m³ and having W/C ratio of 0.50 with additives (Calcareous Filler, Gypsum) have a higher carbonation coefficient than Portland cement.
- The type of cure has a major influence on the resistance of concretes to carbonation. In fact, poor cure conditions lead to carbonation coefficients two times higher than those obtained on the series of specimens composed of the same cement but subjected to optimal conditioning.
- The carbonation coefficients could not be directly correlated with the water absorption by immersion.
- The carbonation coefficients do not have a direct link with compressive strength determined at 28 days.

REFERENCES

- [1] Monkman S., Mac Donald M., 2016. Carbon dioxide upcycling into industrially produced concrete blocks. Construction and Building Materials, 124:127-132.
- [2] Jedidi M., Abroug A., Moalla B., Benjeddou O., 2017. Non-destructive Testing for the Diagnosis and Repair of Reinforced Concrete Building. International Journal of Architecture, Engineering and Construction, 6(1): 20-28.
- [3] Mehta PK., 2001. Reducing the environmental impact of concrete: concrete can be durable and environmentally friendly. Concrete International, 61-66.
- [4] Papadakis VG., Fardis MN., Vayenas CG., 1992. Effect of composition, environmental factors and cement-lime mortar coating on concrete carbonation, Materials and Structures, 25: 293-304.
- [5] Loo YM., Chin MS., Tam CT., Ong KCG., 1994. A carbonation prediction model for accelerated carbonation testing of concrete, Magazine of Concrete Research, 46(168): 191-200.
- [6] Taylor R., Richardson IG., Brydson RDM., 2010. Composition and microstructure of 20-year old ordinary Portland cement-ground granulated blast-furnace slag blends containing 0 to 100% slag, Cement and Concrete Research, 40: 971–983.
- [7] Houst YF., Wittmann FH., 1989. Retrait de carbonatation, in: Durabilities of Structures IABSE, Lisbonne, pp. 255–260.
- [8] Muller A., Sickert G., 1995. Determination of the carbonation resistance of concrete on the basis of its capillarity and microstructure, Betonwerk + Fertigteil-Technik, N°11, pp. 70-88.
- [9] Kobayashi K., Uno Y., 1990. Influence of alkali on carbonation of concrete. Part I, Preliminary tests with mortar specimens, Cement and Concrete Research, vol. 19, N°5, pp. 821-826, 1990. Part II, Influence of alkali in cement on rate of carbonation of concrete, Cement and Concrete Research, 20(4): 619-622.
- [10] Fattuhi NI., 1988. Concrete carbonation as influenced by curing regime, Cement and Concrete Research, 18(3): 426-430.
- [11] Gruyaert E., Van den Heede P., De Belie N., 2012. Carbonation of slag concrete: Effect of the cement replacement level and curing on the carbonation coefficient - Effect of carbonation on the pore structure, Cement and Concrete Composites.
- [12] Gowripalan N., Cabrera JG., Cursens AR., Wainwright PJ., 1990. Effect of curing on durability, Concrete International Design and Construction, 12(2) 47-54.
- [13] Haque MN., 1990. Some concretes need 7 days initial curing. Concrete International: Design and Construction 1990, 12(2): 42-46, Concrete International: Design and Construction, 12: 42–46.
- [14] Balayssac JP., Detriche CH., Grandet J., 1995. Effects of curing upon carbonation of concrete, Construction and Building Materials, 9: 91–95.
- [15] Lo Y., Lee HM., 2002. Curing effects on carbonation of concrete using a phenolphthalein indicator and Fourier-transform infrared spectroscopy, Building and Environment, 37: 507–514.
- [16] L.J. Parrott, Some effects of cement and curing upon carbonation and reinforcement corrosion in concrete, Materials and Structures, 29, pp. 164–173, 1996.
- [17] Skenderovic B., 1992. Effects of some additives on dynamics of carbonation, 9th International Congress of Chemistry and Cement New Delhi, vol. V, pp. 377-380.
- [18] Richardson IG., Groves GW., Brough AR., Dobson CM., 1993. The carbonation of OPC and OPC/silica fume hardened cement pastes in air under conditions of fixed humidity, Advances in Cement Research, 5(18): 81-86.



- [19] Malami C., Kaloidas V., Batis G., Kouloumbi N., 1994. Carbonation and porosity of mortar specimens with pozzolanic and hydraulic cement admixtures, *Cement and Concrete Research*, 24(8): 1444-1454.
- [20] Saetta AV., Vitalicani RV., 2005. Experimental investigation and numerical modeling of carbonation process in reinforced concrete structures: Part II. Practical applications. *Cement and Concrete Research*, 35:958-967.
- [21] Jedidi M., Benjeddou O., 2018. Chemical Causes of Concrete Degradation. *MOJ Civil Engineering*, 4(1).
- [22] Thiery M., Dangla P., Belin P., Habert G., Roussel N., 2012. Carbonation kinetics of a bed of recycled concrete aggregates: a laboratory study on model materials. *WASCON*, Gothenburg, SWEDEN.
- [23] Berkely KGC., Pathmanaban S., 1990. Cathodic protection of reinforcement steel in concrete. London: Butterworths & Co. Ltd.
- [24] BB. Hope BB., Alan IPKC., 1987. Chloride corrosion threshold in concrete. *ACI Master Journal*. 84: 306-314.
- [25] Pullar-Strecker P. 1987. Corrosion damage concrete: assessment and repair. London: Butterworths.
- [26] BS EN 14630, 2006. Products and systems for the protection and repair of concrete structures. Test methods. Determination of carbonation depth in hardened concrete by the phenolphthalein method.
- [27] Parrott L.J., 1987. A Review of Carbonation in Reinforced Concrete Building Research Establishment, UK, Waterford.
- [28] Jiang L., Lin B.Y., Cai, Y., 2000. A model for predicting carbonation of high-volume fly ash concrete. *Cement and Concrete Research*, 30(5): 699-702.
- [29] Ceukelaire L.D., Nieuwenburg V.D., 1993. Accelerated carbonation of a blast-furnace cement concrete. *Cement and Concrete Research*, 23(2): 442-452.
- [30] Sanjuan M., Estévez E., Daniel del Barrio AC., 2018. Effect of curing time on granulated blastfurnace slag cement mortars carbonation, *Cement and Concrete Composition*, 90: 257–265.
- [31] Turcry PH., Oksri-Nelfia L., Younsi A., Ait-Mokhtar A., 2014. Analysis of an accelerated carbonation test with several preconditioning, *Cement Concrete Research*, 57: 70–78.
- [32] Chen CT., Ho CW., 2012. Influence of cyclic humidity on carbonation of concrete, *Journal Materials Civil Engineering* 25 (12): 1929–1935.
- [33] Leemann A., Moro F., 2017. Carbonation of concrete: the role of CO₂ concentration, relative humidity and CO₂ buffer capacity, *Materials Structures*, 50(1): 30.
- [34] Gruyaert E., Van den Heede P., De Belie N., 2013. Carbonation of slag concrete: Effect of the cement replacement level and curing on the carbonation coefficient—Effect of carbonation on the pore structure, *Cement and Concrete Composition*, 35 (1): 39–48.
- [35] NF EN 480-1, 2014. Admixtures for concrete, mortar and grout - Test methods - Part 1: reference concrete and reference mortar for testing.

STUDY ON OPTIMAL COMBINATION SETTLEMENT PREDICTION MODEL BASED ON LOGISTIC CURVE AND GOMPERTZ CURVE

Bolin Wang, Xu Wang and Xuening Ma

Department of Civil Engineering, Lan Zhou Jiao Tong University, Lan Zhou 730070, China; wang-bo-lin@163.com; publicwang@163.com; 65809626@qq.com

ABSTRACT

The Logistic and Gompertz embankment settlement prediction models have poor prediction accuracy for the late settlement of high-filled soil. This study proposes a combination of the two models based on their common characteristics and individuality, and their respective advantages and specific limitations. The minimum logarithmic error square sum of the combined model was used as the objective function to solve the optimal weighting coefficient. The optimal weighted geometric mean combination prediction model was deduced, to improve the confidence of the prediction accuracy of the settlement of high-filled soil. By fitting and analysing the measured settlement data of the engineered high-filled soil with each prediction model, the feasibility of the proposed optimal combination prediction model in the settlement prediction of high-filled soil was tested. It was found that the proposed optimal combination forecasting model was more accurate and adaptable compared to any single model, and was more reliable. Therefore, the proposed combination forecasting model could be used as an effective method to predict the settlement of high-filled soil in the later stages of settlement.

KEYWORDS

High-filled soil, Optimal combination model, Settlement prediction

INTRODUCTION

The central and western regions of China are occupied with cities in mountainous terrain. The continuous development of these urbanized areas has resulted in large cities expanding into surrounding areas, resulting in new urban districts, airports and railway and (highway) roads being built on land formed using high-filled soil. Uneven settlement and deformation of high-filled soil in hilly and gully terrain is of concern to geotechnical experts. Many structures built on high-filled soil have been destroyed or condemned due to the settlement of the foundations. The settlement of high-filled soil results in the deformation of the filling soil and the settlement of the foundation. Reported data indicate compression of the soil caused by the weight of the fill often accounts for 80%-90% of the total settlement [1-2]. After completion of the construction of the fill soil, uneven settlement often occurs over a long period to varying degrees. The settlement is primarily influenced by the filling speed, filling height, filling properties and local climatic conditions. This multi-dimensional problem based on time and space cannot be solved using empirical formulas [3]. The final settlement calculated using the finite element method based on the consolidation theory is often significantly different to the measured value. Therefore, it is necessary to understand the dynamic process of settlement of high-filled soil to accurately predict trends in settlement using data during the early period, to ensure safety and quality [4]. To date, there are three main methods used globally for predicting settlement of high-filled soil: the empirical formula deduction method, numerical simulation and the curve fitting method. The most commonly used curve fitting



methods include hyperbolic, modified hyperbolic, grey prediction, grey Theory-Markov, power function, exponential equations and Asaoka methods [5-14]. In recent years, the Logistic and Gompertz curves have been favoured as they reflect more accurately the relationship between settlement and time [15-18], however, the prediction accuracy is often limited by the amount of monitoring data, geographical conditions and construction technology. It is difficult to use a single prediction model to make an accurate prediction of settlement, resulting in low confidence of prediction precision.

The common characteristics and individuality of Logistic and Gompertz prediction models, together with their advantages and specific limitations are used in this study which combines the two models to calculate the optimal weighting coefficients. The sum of the minimum logarithmic error squares of the combined model was used as the objective function which derived the optimal weighted geometric mean of the combination prediction model. The prediction model was used to improve the prediction accuracy of the curve fitting method. The combined prediction model could be used as an effective method for predicting the late settlement of high-filled soil.

THE TWO SETTLEMENT PREDICTION MODELS

The Logistic model

In 1938, Pierre-Francois Verhulst proposed the Logistic model for predicting world population growth (Verhulst-Pearl model). Due to the development of inter-discipline fields, this model is widely used in ecology, medicine, economics and management. The model can be used for settlement prediction and its differential form can be rewritten as:

$$\frac{dy}{dt} = ky(1 - \frac{y}{A}) \quad (1)$$

where: y =settlement; t =time; k =immediate settlement rate; A =final settlement.

The integral of equation (1) is:

$$\int (\frac{1}{y} + \frac{1}{A-y}) dy = \int k dt \quad (2)$$

Solution:

$$y = \frac{A}{1 + Be^{-kt}} \quad (3)$$

where: B =parameter to be sought; e =Euler number.

The Gompertz model

The Gompertz model was put forward by the British statistician Benjamin Gompertz. It was originally used to describe the law of the growth and change of nature. Since its birth, the Gompertz model has played an important role not only in the field of biology, but also in market economy forecasting and traffic forecasting. The model can be used for settlement prediction and its differential form can be rewritten as:

$$\frac{dy}{dt} = -k \ln \frac{y}{A} \quad (4)$$

where: y =settlement; t =time; k =immediate settlement rate; A =final settlement.

The integral of equation (4) is:



$$\int \frac{d(\ln y - \ln A)}{\ln y - \ln A} = - \int k dt \quad (5)$$

Solution:

$$y = Ae^{-Be^{-kt}} \quad (6)$$

where: B = parameter to be sought; e = Euler number.

Then, the first derivative of equations (3) and (6) can be obtained:

$$\left. \begin{aligned} \frac{dy}{dt} &= \frac{ABke^{-kt}}{(1+Be^{-kt})^2} > 0 \\ \frac{dy}{dt} &= ABk e^{-Be^{-kt}} \cdot e^{-kt} > 0 \end{aligned} \right\} \quad (7)$$

The second derivative of equations (3) and (6) are:

$$\left. \begin{aligned} \frac{d^2y}{dt^2} &= \frac{ABke^{-kt}(Be^{-kt}-1)}{(1+Be^{-kt})^3} \\ \frac{d^2y}{dt^2} &= ABk^2 e^{-Be^{-kt}} \cdot e^{-kt} \cdot (Be^{-kt}-1) \end{aligned} \right\} \quad (8)$$

The limits of equations (3) and (6) are:

$$\left. \begin{aligned} \lim_{t \rightarrow \infty} \frac{A}{1+Be^{-kt}} &= A \\ \lim_{t \rightarrow \infty} Ae^{-Be^{-kt}} &= A \end{aligned} \right\} \quad (9)$$

Using the definition of consolidation degree U , equations (3) and (6) can be written:

$$\left. \begin{aligned} U &= \frac{y_t - y_0}{y_\infty - y_0} = \frac{(A/1+Be^{-kt}) - (A/1+B)}{A - A/1+B} \\ U &= \frac{y_t - y_0}{y_\infty - y_0} = \frac{Ae^{-Be^{-kt}} - Ae^{-B}}{A - Ae^{-B}} \end{aligned} \right\} \quad (10)$$

Equation (7) demonstrates that the Logistic and Gompertz curves increase monotonously, Equation (8) demonstrates that when $Be^{-kt}=1$ (that is $t=\ln B/k$) there is an inflection point in the curve, and Equation (9) demonstrates that when time is infinite, the maxima in both curves equals A . According to the properties of the two curves, the shape of the Logistic curve is an "S" shape, and the Gompertz curve has the characteristics of an "anti-S" shape distribution. This is in agreement with the proposal by Mei et al. that it is theoretically demonstrated that the settlement-time curve is an "S" shape when the load is linear or approximately linear [19]. Equation (10) demonstrates that when time equals zero, $U=0$, and when time approaches infinity, $U=1$. Therefore, the Logistic and Gompertz models can be used to predict the variation in settlement of high-filled soil over time.

SOLUTION OF THE MODEL

Using the Logistic and Gompertz models, settlement can be predicted for any time when the values of the parameters A, B and k are known. In order to improve the fit, nonlinear Gompertz and Logistic curves were converted into modified exponential curves using the basic principles of linear regression. The transformation of the modified exponential equations is shown in Table 1.

Tab. 1 - Transformation of the modified exponential equation

Model type	Model equation	Transformation process	Transformation model
Logistic	$y = \frac{A}{1 + Be^{-kt}}$	if $Y = 1/y$, $A' = 1/A$, $B' = B/A$, $k' = e^{-k}$	$Y = A' + B'k'^t$
Gompertz	$y = Ae^{-Be^{-kt}}$	$\ln y = \ln A - Be^{-kt}$, if $Y = \ln y$, $A'' = \ln A$, $B'' = -B$, $k'' = e^{-k}$	$Y = A'' + B''k''^t$

This study proposes the use of the Bryant method to solve the parameters of the curve. The three parameters in the model require that the measured y_t in the settlement data be of equal time interval; the measured data were generally non-isometric. Therefore, before using the two curves to fit the data, measured y_t data must be converted into an isochronous y_t sequence that meets the requirements. In this study, the Lagrange interpolation method was used to perform the isochronous transformation of non-isochronous settlement time series data. The equations of each parameter were calculated using the Bryant method as follows:

$$k = \frac{(n-1) \sum_{t=1}^{n-1} Y_t Y_{t+1} - \sum_{t=1}^{n-1} Y_t \sum_{t=1}^{n-1} Y_{t+1}}{(n-1) \sum_{t=1}^{n-1} Y_t^2 - (\sum_{t=1}^{n-1} Y_t)^2} \quad (11)$$

$$B = \frac{n \sum_{t=1}^n k^t Y_t - \sum_{t=1}^{n-1} k^t \sum_{t=1}^n Y_t}{n \sum_{t=1}^{n-1} k^{2t} - (\sum_{t=1}^{n-1} k^t)^2} \quad (12)$$

$$A = \frac{(\sum_{t=1}^n Y_t - B \sum_{t=1}^n k^t)}{n} \quad (13)$$

OPTIMAL WEIGHTED AVERAGE GEOMETRIC PREDICTION MODEL

If there were m kinds of settlement prediction models for a problem, $\hat{y}_{1t}, \hat{y}_{2t}, \dots, \hat{y}_{mt}$, $t = 1, 2, \dots, N$, then at the same time, \hat{y}_t represents the i type of the prediction model and the predicted value of the t phase, \hat{y}_t represents the weighted geometric average combination prediction model of the above m types of prediction models, and also represents the prediction value of the t phase of the model.

$$\hat{y}_t = \prod_{i=1}^m \hat{y}_{it}^{w_i} \quad (14)$$

$$\text{if } W = (w_1, w_2, \dots, w_m)' \in R^m, \text{ and } \sum_{i=1}^m w_i = 1, w_i \geq 0, i = 1, 2, \dots, m \quad (15)$$

If \hat{y}_t is used to represent the measured values of the actual settlement in the t period, $s_{it} = \ln \hat{y}_{it} - \ln y_t$ and $S_t = \ln \hat{y}_t - \ln y_t$ are used to denote the logarithmic errors of \hat{y}_{it} and \hat{y}_t respectively, then:

$$\begin{aligned} S_t^2 &= (\ln \hat{y}_t - \ln y_t)^2 = (\ln \prod_{i=1}^m \hat{y}_{it}^{w_i} - \ln y_t)^2 = \\ &(\sum_{i=1}^m w_i \ln \hat{y}_t - \ln y_t)^2 = \left[\sum_{i=1}^m w_i (\ln \hat{y}_{it} - \ln y_t) \right]^2 = \\ &(w_1, w_2, \dots, w_m) \begin{vmatrix} \ln \hat{y}_{1t} - \ln y_t \\ \ln \hat{y}_{2t} - \ln y_t \\ \vdots \\ \ln \hat{y}_{mt} - \ln y_t \end{vmatrix} (\ln \hat{y}_t - \ln y_t, \\ &\ln \hat{y}_{2t} - \ln y_t, \dots, \ln \hat{y}_{mt} - \ln y_t) \begin{vmatrix} w_1 \\ w_2 \\ \vdots \\ w_m \end{vmatrix} = W'(s_{it}s_{jt})W \end{aligned} \quad (16)$$

where: $W = (w_1, w_2, \dots, w_m)'$; $(s_{it}s_{jt})$ is an m order square matrix.

Therefore, the sum of the square of logarithmic errors is:

$$S^2 = \sum_{t=1}^N S_t^2 = \sum_{t=1}^N W'(s_{it}s_{jt})W = W' \left[\sum_{t=1}^N (s_{it}s_{jt}) \right] W \quad (17)$$

where matrix $A = \sum_{t=1}^N (s_{it}s_{jt})$ is generally a positive definite matrix. Due to

(1) $\left[\sum_{t=1}^N (s_{it}s_{jt}) \right]' = \sum_{t=1}^N (s_{it}s_{jt})' = \sum_{t=1}^N (s_{it}s_{jt})$, matrix A is a symmetric matrix;

(2) For $X = (x_1, x_2, \dots, x_m)' \in R^m - \{0\}$, there are:

$$X' \left[\sum_{t=1}^N (s_{it}s_{jt}) \right] X = \sum_{t=1}^N X'(s_{it}s_{jt})X = \sum_{t=1}^N (\sum_{k=1}^m x_k s_{kt}) \geq 0 \quad (18)$$

If $X'AX$ is the constant zero, $\sum_{k=1}^m s_{kt}x_k = 0, t = 1, 2, \dots, N$. That is, for any nonzero m dimensional vector X , it is the solution of the equations in (19).

$$\left. \begin{array}{l} s_{11}x_1 + s_{21}x_2 + \dots + s_{m1}x_m = 0, \\ s_{12}x_1 + s_{22}x_2 + \dots + s_{m2}x_m = 0, \\ \vdots \\ s_{1N}x_1 + s_{2N}x_2 + \dots + s_{mN}x_m = 0, \end{array} \right\} \quad (19)$$

If $x_k = 1, x_i = 0, i \neq k, i, k = 1, 2, \dots, m$, there is $s_{kt} = 0, k = 1, 2, \dots, m, t = 1, 2, \dots, N$,

$s_{kt} = \ln \hat{y}_{kt} - \ln y$ is sometimes not zero, therefore:

$$X'AX \geq 0 \quad (20)$$

From equations (1) and (2) the matrix A is a positive definite matrix, so that A is invertible and for any nonzero vector W , $S^2 > 0$. $Q = (1, 1, \dots, 1)' \in R^m$, so the optimal weight coefficient W can be determined by minimizing the sum of the logarithmic error square $S^2 = W'AW$ of the combined prediction model under the constraint conditions of $W'Q = 1$, $W \geq 0$.

Using the result from [20], the solution is:

$$W = \left\{ \left[\sum_{t=1}^N (s_{it}s_{jt}) \right]^{-1} Q \right\} / \left\{ Q^{-1} \left[\sum_{t=1}^N (s_{it}s_{jt}) \right]^{-1} Q \right\} \quad (21)$$

For the weighted geometric combination prediction model composed of Logistic and Gompertz models, the optimal weight coefficients are:

$$\left. \begin{array}{l} w_1 = (\sum_{t=1}^N s_{2t}^2 - \sum_{t=1}^N s_{1t}s_{2t}) / \left[\sum_{t=1}^N (s_{1t}^2 + s_{2t}^2 - 2s_{1t}s_{2t}) \right] \\ w_2 = \sum_{t=1}^N (s_{1t}^2 - s_{1t}s_{2t}) / \left[\sum_{t=1}^N (s_{1t}^2 + s_{2t}^2 - 2s_{1t}s_{2t}) \right] \end{array} \right\} \quad (22)$$

Due to $w_1 + w_2 = 1$, only one of the w_1, w_2 was solved.

ACCURACY OF THE COMBINED PREDICTION MODEL

According to the square sum of absolute errors (SSE), square sum of relative errors (SSRE), standard error (SE), relative standard error (RSE) and mean absolute percentage error (MAPE), the accuracy of the optimal combination prediction model proposed in this study was tested using five parameters. The formulas of each parameter are as follows:

$$\left. \begin{aligned} SSE &= \sum_{t=1}^N (\hat{y}_t - y_t)^2, SSPE = \sum_{t=1}^N \left(\frac{\hat{y}_t - y_t}{y_t} \right)^2 \\ SE &= \left(\frac{SSE}{N} \right)^{0.5}, SPE = \left(\frac{SSPE}{N} \right)^{0.5} \\ MAPE &= \frac{1}{n} \sum_{t=1}^N \left(\frac{|\hat{y}_t - y_t|}{y_t} \right) \times 100\% \end{aligned} \right\} \quad (23)$$

According to the value MAPE, the prediction accuracy can be divided, as shown in Table 2.

Tab. 2 - MAPE classification of prediction accuracy

MAPE %	Prediction accuracy	MAPE %	Prediction accuracy
<10	High accuracy	20~50	Feasible
10~20	Good	>50	Infeasible

ENGINEERING EXAMPLE ANALYSIS

High-filled soil engineering in Wuhan TianHe airport [21]

Located in the Wuhan City, Hubei Province, China, the Wuhan Tianhe Airport Second Channel Expressway has a total length of approximately 15.5 km. Most of the landforms are low mountains and hills with little structural erosion. The topography is undulating and there are more high-filled sections across the whole line. After the completion of the construction, the settlement deformation of the high-filled section of the whole line was monitored in real time. This study focuses on the S2 section, the pile number of the section is K4+200~K5+325 and total length is 1.215 km. Section K4+860 is a special subgrade section and the settlement deformation of this section was analysed and predicted. The embankment filling height of this section was 8.2 m and measurement period was from June 12 to December 15, 2016. Based on the measured settlement data across 153 days, using the Bryant method, logarithmic transformation and linearization equations listed in Table 1, the Logistic and Gompertz models were determined, respectively:

$$\hat{y}_{1t} = \frac{132.2949}{1 + 4.2697 \times e^{-0.0577t}} \text{ and } \hat{y}_{2t} = 133.8612 \times e^{-1.9656e^{-0.0427t}}$$

Therefore:

$$\sum_{t=1}^{20} s_{1t}^2 = 0.0548, \sum_{t=1}^{20} s_{2t}^2 = 0.0581, \sum_{t=1}^{14} s_{1t} s_{2t} = 0.0539$$

The Optimal weight coefficient $w_1 = 0.8204, w_2 = 0.1796$. Therefore, the optimal weighted geometric average combination prediction model was:

$$\hat{y}_t = \hat{y}_{1t}^{0.8204} \cdot \hat{y}_{2t}^{0.1796}$$

Using the Logistic model, Gompertz model and the proposed optimal weighted geometric average combination prediction model, the predicted settlement values and precision index values

were calculated (Tables 3 and 4). The relationship curve of settlement and time of section K4+860 is shown in Figure 1. The curve of relationship between measurement time and relative error of section K4+860 and a diagram of measurement time and residual scatter plot are shown in Figure 2 and Figure 3, respectively.

Tab. 3 - Settlement datas of K4+860 by measured and predicted

Time/d	Measured data /mm	Predicted data/mm		
		Logistic model	Gompertz model	The combined model
10	36.707	38.936	37.126	38.604
13	45.111	43.855	43.316	43.758
18	59.202	52.681	53.808	52.888
31	66.11	77.194	79.334	72.574
35	79.321	84.443	86.125	78.742
38	96.485	89.594	90.815	94.812
45	103.898	100.357	100.390	102.363
47	105.427	103.069	102.783	104.018
52	110.353	109.110	108.138	109.935
56	112.551	113.199	111.822	112.950
57	113.509	114.122	112.666	113.860
68	122.903	121.997	120.186	122.670
88	126.203	128.864	127.859	126.683
94	127.358	129.850	129.191	127.731
99	129.063	130.454	130.076	130.086
115	130.757	131.557	131.936	130.625
123	131.109	131.829	132.490	131.248
130	133.617	131.984	132.843	133.138
145	133.983	132.164	133.324	134.071
153	134.203	132.212	133.479	134.339

Tab. 4 - Comparison of precision index values of each prediction model

Model type	SSE	SSRE	SE	RSE	MAPE%
Logistic model	293.234	0.057	3.829	0.054	3.461
Gompertz model	330.611	0.064	4.066	0.057	3.364
The combined model	96.776	0.025	2.200	0.036	1.866



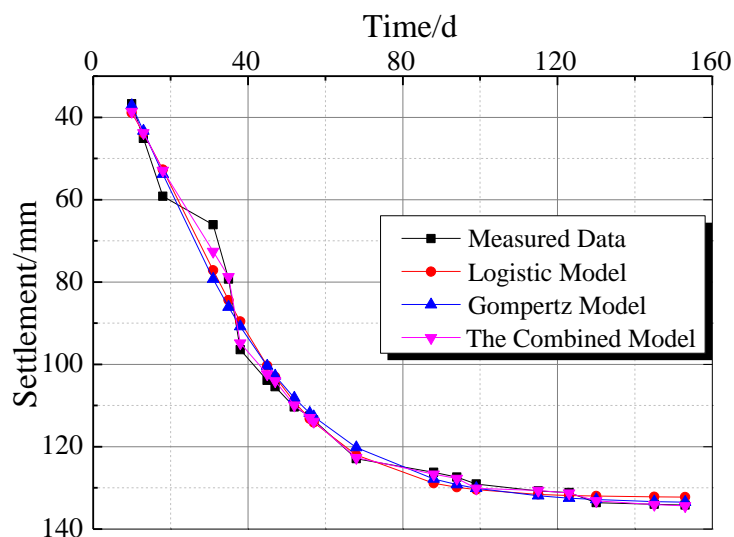


Fig. 1 - Measured settlement and predicted settlement curves

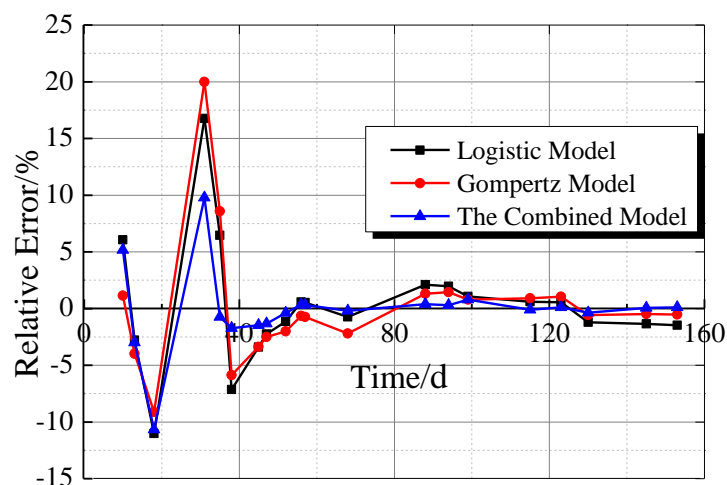


Fig. 2 - Measurement time and relative error curves

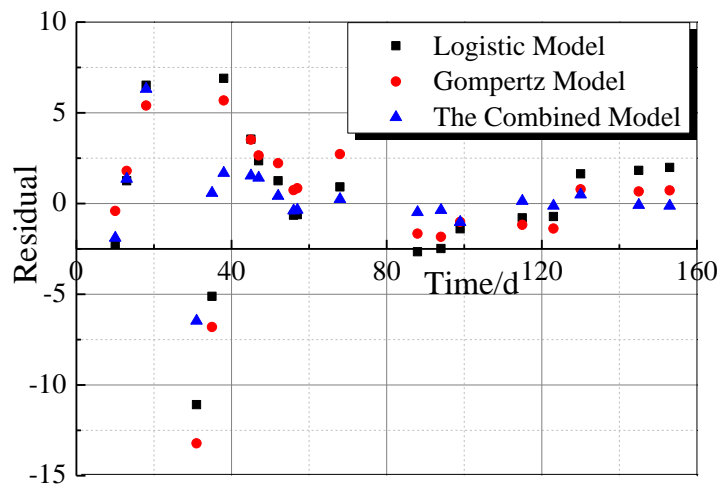


Fig. 3 - Measurement time and residual scatter plots

The high-filled embankment project of Wuhan Tianhe Airport, the regularity of SSE and SE values of the accuracy index of the prediction model, and SSRE values and RSE values of the stability reliability index of the prediction model were similar to that of the high-filled embankment project of Yan Jiafeng Section (Table 8). However, in this study the MAPE values of the Logistic, Gompertz and proposed combined prediction models were 3.461%, 3.364% and 1.866%, respectively. All indicate a high precision prediction and the MAPE values in this study were smaller, suggesting greater accuracy. When the monitoring time was 38 days, the relative error was large, and the variation range was -11.02%-20.00% (Figure 5). However, when the monitoring time was longer than 38 days, the variation range of the relative error was -3.41%-0.07%. The residual diagram was consistent with the randomness and unpredictability of probability theory, and the points described by the combined prediction model were scattered randomly about a line with residuals equal to 0 (Figures 3 and 6), suggesting that the proposed prediction model was effective.

CONCLUSION

- (1) To address the deficiencies in single settlement prediction models in predicting the settlement of high-fill soil, this study combined the Logistic and Gompertz prediction models to solve optimal weighting coefficients. This was achieved taking the sum of the minimum logarithmic error squares of the combined model as the objective function, and then deriving the optimal weighted geometric mean combination prediction model.
- (2) Selecting the engineer measured data for the fitting analysis, the comparative analysis indicated that the accuracy (SSE, SE and MAPE) and reliability (SSRE, RSE) of the optimal combination predicting model was better than any single model, and the adaptability was greater. When the monitoring time exceeded the curve inflection point, it was similar to the measured value, indicating the optimal combination predicting model was good for settlement prediction.
- (3) The proposed combination prediction model could be used to optimize the combination of multiple models and buffer the advantages and disadvantages of each single model. When there is no negative weight ratio, the settlement prediction accuracy was improved significantly.

In this study, linear loading or approximate linear loading only was used for the analysis. The application of a non-linear growth model to settlement prediction of step loading and more complex loading processes requires further study and analysis.

ACKNOWLEDGEMENTS

This work was supported by the National Natural Science Foundation of China (Grant Nos. 41562014 and 41662017). The authors are also very grateful to the editors and anonymous reviewers for valuable suggestions which have improved the quality of this paper.

REFERENCES

- [1] Akira Asaoka., 1978. Observational procedure of settlement prediction. Soils & Foundations, 18(4): 87-101.
- [2] Zheng Jiangguo, Cao Jie, Zhang Jiwen. et al., 2018. Analysis of influencing factors of loess high fill settlement based on centrifuge model test. Journal of Rock Mechanics and Engineering. Vol. 38, 1-13.
- [3] Zhuo Wenze, Zhou Ren., 2015. Study on settlement Prediction of Deep soft Foundation of Henei-Haifang Expressway. Journal of Hebei University of Engineering (Natural Science Edition), Vol. 32, No. 3, 19–24.
- [4] Xue Jie., 2018. Study and Analysis on Prediction of subgrade settlement of Expressway. Traffic North, No. 8, 53–55.

- [5] Feng Huiping, Geng Huiling, Han Bowen.,2017. Prediction Model for subgrade settlement of High Speed Railway in unsaturated soil region. *Journal of Geotechnical Engineering*, Vol. 39, No. 6, 1089–1095.
- [6] Siew-Ann Tan.,1994. Hyperbolic method for settlement in clays with vertical drains. *Can. Geotech.J*, Vol. 31, No. 1, 125–131.
- [7] AKIRAASAOKA.,1978. Observational procedure of settlement predictions[J]. *Soils and Foundations*, Vol. 18, No. 4, 87–101.
- [8] Siew-Ann Tan, Soon-Hoe Chew.,1996. Comparison of the hyperbolic and Asaoka observational method of monitoring consolidation with vertical drains. *Soils and foundation*, Vol. 36, No. 3, 31–42.
- [9] Lei Xuwen, Bai Shiwei, Meng Qingshan.,2000. Application of Grey Prediction in settlement Analysis of soft soil Foundation. *Rock and Soil Mechanics*, Vol. 21, No. 2, 145–147.
- [10] Song Yanhui, Nie Dexin.,2003. Verhuslt model for prediction of foundation settlement. *Rock and Soil Mechanics*, Vol. 24, No. 1, 123–126.
- [11] Zhao Minghua, Zeng Guangxian, Xiang Zhenfeng.,2006. Grey Optimum-Markov Prediction Model for settlement of High fill Embankment. *Road Traffic Technology*, Vol. 23, No. 11, 19–22.
- [12] Akira Asaoka, Koh Misumi.,1988. Analysis and prediction of consolidation settlement of normally consolidated clay foundation under embankment loading. *Soils and foundations*, 28(3):35-49.
- [13] Dalgic, Suleyman, Simsek. et al., 2002. Settlement predictions in the Anatolian motorway, Turkey. *Engineering Geology*, 67(1): 185-199.
- [14] Bergado, Dennes T. Daria, Peter M, Sampaco. et al., 1991. Prediction of embankment settlements by in-situ tests. *Geotechnical Testing Journal*, 14(4): 425-439.
- [15] Gompertz B., 1825. On the Function Expressive of the Law of Human Mortality, and on a new Method of Determining the Value of Life Contingencies: *Philosophical Transactions of the Royal Society*, 513-585.
- [16] Zhang Yuting, Sun Hao, Wang Jinxiang.,2009. Application of Gompertz Curve Model to settlement Prediction of soft soil Foundation of Sea Embankment. *Port of Waterways*, Vol. 30, No. 4, 257–262.
- [17] Wu Qixing, Hu Hui.,2006. Analysis of settlement of soft soil under vacuum preloading based on Gompertz growth curve. *Journal of Rock Mechanics and Engineering*, Vol. 25, No. 2, 3600–3606.
- [18] Xu Hongzhong, Shi Bin, Li Xuehong.,2005. Study on Logistic growth model and its applicability for prediction of total process settlement *Rock and Soil Mechanics*, Vol. 26, No. 3, 387–391.
- [19] Mei Guoxiong, Zai Jinmin, Yin Jinze.,2005. The proof of the "S" shape of the settlement-time curve and its application from the constitutive relation of the soil. *Rock and Soil Mechanics*, Vol. 26, 21–24.
- [20] Tang Xiaowo.,1992. Optimal combination prediction method and its application. *Statistics and Management*, Vol. 11, No. 1, 31–35.
- [21] Wei Daokai, Kou Hailei.,2018. Study on data fitting and Prediction of settlement and deformation of High- fill subgrade on Expressway. *Road Engineering*, Vol. 43, No. 1, 251–256.

COHESION TEST OF A SINGLE IMPREGNATED AR-GLASS ROVING IN HIGH-PERFORMANCE CONCRETE

Tomáš Vlach, Jakub Řepka, Jakub Hájek, Richard Fürst, Zuzana Jirkalová and Petr Hájek

University Center for Energy Efficient Buildings of CTU in Prague, Buštěhrad, Třinecká 1024, Czech Republic; tomas.vlach@cvut.cz; jakub.repka@cvut.cz; jakub.hajek@cvut.cz; richard.furst@cvut.cz; zuzana.jirkalova@cvut.cz; petr.hajek@cvut.cz

ABSTRACT

The development of light and very thin concrete building structures and demand for extremely thin elements in design are inter alia reasons for the development of composite materials as non-traditional reinforcement. Composite materials are currently used as reinforcement mostly in the form of fiber reinforced polymer bars similar to traditional steel reinforcement bars, but the last decade sees also rise in the use of technical textiles. This article is focused on the interaction between impregnated textile reinforcement and high-performance concrete matrix and its easy determination using originally modified pullout test. The second aim of this article is improvement of interaction conditions between reinforcement and cementitious matrix using fine-grained silica sand applied on the surface of the composite reinforcement similarly to the traditional fiber reinforced polymer reinforcement with commonly used diameters. To investigate an effect of this modification a bending test was performed on small thin concrete slabs with different amounts of reinforcement.

KEYWORDS

Concrete, High performance concrete, Textile reinforcement, Cohesion, Interaction, Roving, Alkali resistant glass, Surface treatment

INTRODUCTION

Textile reinforced concrete (TRC) is a new composite material made of high-performance concrete (HPC) reinforced with technical textiles. The properties of this material are still intensively researched and its use is steadily growing. The basic principle is identical to the traditional steel reinforced concrete. HPC has great mechanical properties regarding compression and textile reinforcement has similarly good parameters in tension. With proper utilization of the HPC properties it is possible to use lesser amount of concrete in comparison with traditional concrete for elements with similar load-bearing capacity which in turn leads to more environmentally effective elements [1]. The technical textiles used as reinforcement are chemically resistant and non-corrosive and these characteristics can be further improved by using epoxy resin or materials. The TRC elements therefore do not need as massive concrete cover of reinforcement as in the case of traditional reinforced concrete with steel reinforcement affected by corrosion. The most commonly used technical textiles as reinforcement are alkali-resistant glass, carbon, basalt and aramid.

This article is focused on the interaction of impregnated textile reinforcement in HPC matrix and its easy determination using originally modified pull-out test. In addition, this experiment was supplemented by the bending test performed on thin slabs to further verify and test the different amounts of reinforcement in cross-sectional area. This issue is relatively thoroughly dealt with in the case of fiber reinforced polymer (FRP) reinforcement with conventional diameters. Testing



methods, interaction and methods for its improvement were already successfully proposed and measured. There are many articles and standards all around the world. Impregnated technical textiles using epoxy resin for homogenization are basically also FRP material with considerably smaller diameter, but standards for element design and the effect of interaction with the cement matrix have not been issued yet. There is also no standard with defined procedures to measure the interaction conditions.

Some articles about the interaction conditions of textile reinforcement were already published. This article is focused only on impregnated technical textiles. Portal [2] states that there is no standard methodology for measurement and evaluation of the TRC pull-out test. The pull-out test was set by the Krüger [3] and Lorenz and Ortlepp [4] asymmetric test. In their experiment samples of 400 x 100 x 15 mm were reinforced using one layer of technical textile. Various anchoring lengths were selected for the characterization of interaction conditions and also the moment of breaking point of textile reinforcement in the sample [5].

Banholzer [6] developed a one-sided test that is used for detection of broken light-fiber filaments. A sample is manufactured with dimensions of 10 x 10 mm and length of 30 mm using epoxy resin with a bundle of fibers in the middle of this prism. The fibers inside are therefore sufficiently protected against the steel jaws of the testing machine. The sample with epoxy prism is then embedded into the concrete matrix with dimensions of 50 x 50 mm and length of also 30 mm. During the testing procedure the sample of reinforcement is pulled out of the concrete part using a supported steel plate with displacement speed of 0.1 mm/min until the maximum displacement of 1.7 mm.

Very interesting testing methodology is also described in [5] with whole fabrics, not a single roving. This case also includes the effect of PP and PVA fibers that are used during the weaving of technical textile for yarn joining. These fibrils connect the whole fabric before the process of impregnation. The principle is analogous to the previously described testing methodology with a single roving. A portion of technical textile is inserted into the HPC specimen during the concreting with free length of fabric to be fixed into the testing machine. The fabric fixed into the testing machine is then pulled out from the concrete specimen using a steel frame as a support for the concrete part.

MATERIALS AND PREPARATION OF SPECIMENS

Concrete

The HPC mixture used in this experiment was developed at the Faculty of Civil Engineering, Czech Technical University in Prague (FCE CTU) for various applications [7]. This mixture was designed using mainly local sources of raw materials. It is a self-compacting fine-grained concrete and its composition is presented in Table 1. The HPC mixture used in this experiment was without any types of fibers. Water cement ratio was 0.25 and the water binder ratio was 0.20 for this mixture. Compressive strength tested on cubes with sides of 100 mm was equal to 140.5 MPa according to the standard CSN EN 12390-3. Tensile strength while bending tested on beams with dimensions of 160 x 40 x 40 mm was equal to 15.4 MPa according to standard CSN EN 12390-5. The same HPC recipe has been also used for several applications and research activities at the CTU like waffle and solid experimental facade elements [8] or in [9], [10]. Using the same concrete mixture allows the results to be compared with each other during the continuous process of alternative reinforcement development.

Tab. 1 - High-performance concrete mix composition

Component	Unit	HPC
Cement I 42.5R	[kg/m ³]	680
Technical silica sand	[kg/m ³]	960
Silica flour	[kg/m ³]	325
Silica fume	[kg/m ³]	175
Superplasticizers	[kg/m ³]	29
Water (12°C)	[kg/m ³]	171
Total	[kg/m ³]	2340

Composite reinforcement

The technical textile reinforcement was produced from AR-glass fibers homogenized with epoxy resin. Rovings of AR-glass fibers were chosen from other types of technical textiles such as carbon, basalt or aramid due to the lower elasticity modulus, more visible interaction conditions and also due to economic aspects. Used rovings were from the company Cem-FIL® with a length weight (titer) of 2400 g/km (= 2400 tex), specific gravity of 2680 kg/m³, tensile strength of 1700 MPa and modulus of elasticity of 72 GPa according to the technical data sheet.

Epoxy resin SikaFloor-156 from the company Sika was used for the homogenization of the rovings. Basic parameters of pure resin are tensile strength in bending of 15 MPa and modulus of elasticity of 2.0 GPa. Specific gravity of the material is 1100 kg/m³ according to the technical data sheet. This resin has excellent penetrating properties due to its low viscosity and is therefore very suitable for roving homogenization. The epoxy resin accounted for about 65% of the cross-section of the impregnated roving due to the experimental manual nature of its production in the lab.

Part of the textile reinforcement was produced with a smooth surface formed by the epoxy resin, while the other part was created with surface modification utilizing fine-grained silica sand. This surface treatment ensures better interaction conditions between composite reinforcement and the cementitious matrix and was inspired in surface modification of the FRP bars with higher diameter. The application of this type of surface treatment in the case of textile reinforcement was described by Shi-ping [11] and the suitable size of silica sand grains was defined by previous author's research [12].

Specimen preparation

The specimens were prepared for two types of experimental verification of the composite reinforcement performance. The first experiment designed for determination of basic material interaction conditions was a pull-out test performed with a single impregnated roving with smooth surface in comparison with a roving with surface treatment using fine-grained silica sand. The second experiment was a four-point bending test performed as the most common way of loading for TRC applications. Molds for all TRC specimens were prepared individually using a system of laminated chipboards. One mold was made for five identical specimens for the pull-out test and the other one for three TRC panels for the four-point bending test.

The developed pull-out test method for single impregnated roving was originally inspired by American standard for testing of FRP reinforcements ACI 440.3R-03 "Guide test methods for fiber reinforced polymers (FRPs) for reinforcing or strengthening concrete structures" with modified



specimen dimensions. The concrete part of specimens had constant dimensions of 100 x 100 mm with thickness related to the composite reinforcement diameter. First experiments were performed with the thickness close to the mentioned ACI standard with respect to the ratio to the other two dimensions, so the first thickness was 100 mm [13]. Especially in the case of single thin impregnated roving with the surface treatment the composite roving was usually broken before the start of slipping along the cementitious matrix. That leads to the thickness optimization using easy calculations. The resulting optimal thickness of the specimens for the used AR-glass roving 2400 tex with the diameter of approximately 2.0 mm was calculated to 20 mm.

The single roving homogenized by epoxy resin was fixed in the middle of the mold before the concreting of HPC part. A small cone made of silicone was installed on the composite roving inside the mold on the side where the composite reinforcement was fixed in the testing machine to prevent pulling of a shear cone from the HPC during the test procedure. This HPC shear cone would negatively affect results and cause skips on the measured curve. The anchoring length of each single impregnated roving was measured as the length of the roving inside a mold before concreting without the silicone cone. This length was also controlled after the pull-out test was performed by breaking of the HPC part and measuring the actual length. Mold was not treated with a demolding oil to prevent the contamination of the surface of the composite reinforcement.

The side of composite reinforcement fixed in testing machine was provided with epoxy sleeve enveloping it. Composite reinforcement has high tensile strength but is very fragile, so the epoxy sleeves were there to prevent damage of the impregnated rovings due to them being fixed in the testing machine. The epoxy sleeves replaced previously used steel ones [14], which made preparation of the specimens and manipulation with them much easier.

After initial preparations, the concreting was performed using self-consolidating HPC. The preparation of specimens is presented in Figure 1. Altogether 12 specimens were prepared - 6 specimens with the smooth surface and 6 specimens with the surface modification using fine-grained silica sand. The surface modification is visible in Figure 1.



Fig. 1 – Specimens preparation for the pull-out test.

Specimens for the four-point bending test were prepared in the form of small slabs with the dimensions of 100 x 360 x 18 mm. Reinforcement grids made of the impregnated AR-glass rovings were prepared in two different densities with 5 and 10 rovings per 100 mm specimen width and were cut to fit the intended specimen dimensions. The slabs were prepared in three variants. One with two 5 roving layers (2x5), second with two 10 roving layers (2x10) and third with four 10 roving layers (4x10). The last variant represents the maximum amount of textile reinforcement that allowed for proper concrete distribution throughout the specimens. All variants were prepared with a smooth surface and also with a surface modification, three specimens for each variant.

The casting process was performed layer by layer. That means a layer of HPC with a controlled thickness to ensure the proper concrete cover, then a TR was inserted, then a middle portion of HPC, another TR, and an upper layer of HPC in the case of specimens with two reinforcement grids and similarly in the case with four. The concrete cover layer was designed with a thickness of 4 mm and due to the chosen concreting process, no spacers were used. Specimens were not vibrated to prevent movement of the composite reinforcement to the HPC surface, the concrete HPC mixture was self-consolidating as mentioned above. The preparation of the specimens for the flexural test is presented in Figure 2.

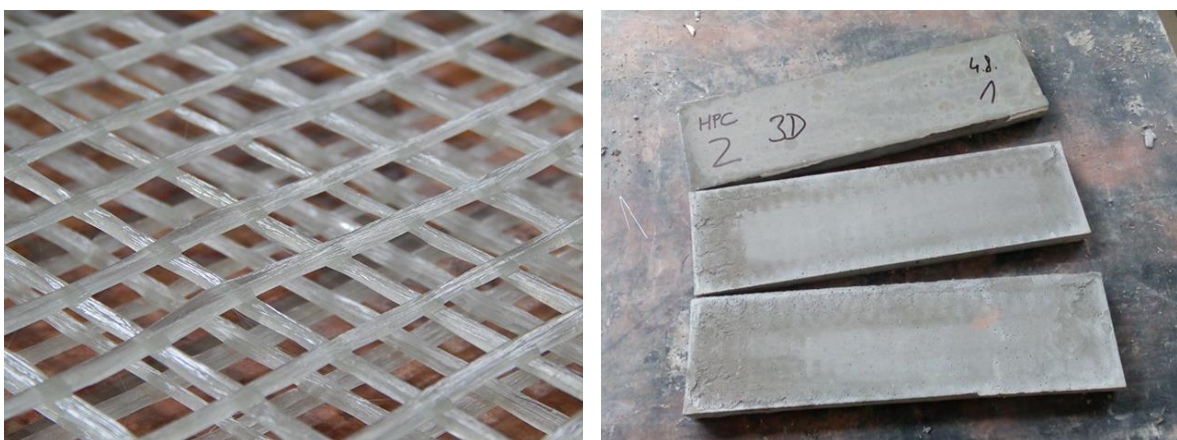


Fig. 2 – Specimens preparation for the four-point bending test.

All specimens were demolded one day after the casting process and were stored in constant conditions for another 27 days. The panels were stored in water tank and constant temperature of 22 °C. The specimens created for pull-out test were placed in air-conditioned environment with constant humidity of 60%. Dimensions and weight of the specimens were measured before testing.

EXPERIMENTS

Cohesion test

The developed pull-out method was focused on the complete curve of bond behaviour with a simple interpretation and application of results in the field of science as well as in the field of engineering and structures designing. As mentioned above this method was inspired by the ACI 440.3R-03 standard, but specimen dimensions were modified due to the small cross-sectional area of the composite reinforcement in comparison with traditional FRP reinforcement. Other aspects of the test set up were very similar to the traditional FRP cohesion test. Epoxy sleeves were installed only on one side of the rovings because of the safe and stable fixing to the testing machine without any damages to the roving filaments. Concrete part had constant dimensions of 100 x 100 mm and optimized thickness of 20 mm for single AR-glass impregnated roving with titer 2400 tex in this experiment. A view of the developed testing set up inspired by ACI standard is presented in Figure 3.

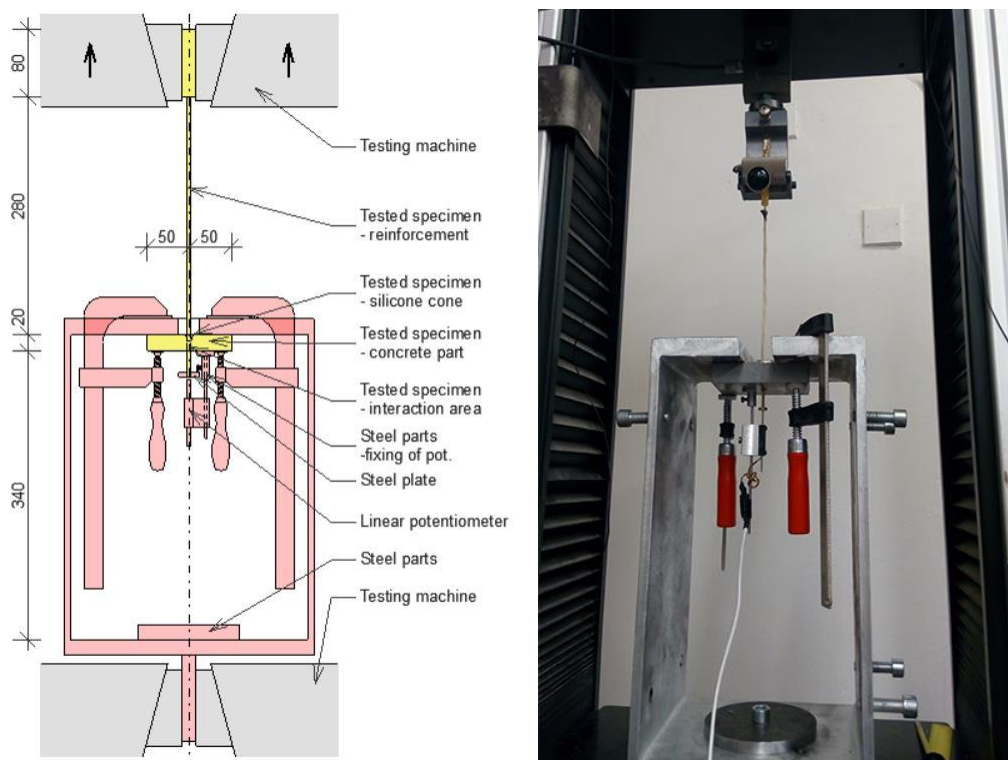


Fig. 3 – Basic scheme of own developed pull out test method inspired by ACI standard and picture of the actual setup.

Time, force, crosshead displacement and pull-out of the reinforcement were measured during the test procedure inspired by the ACI standard for a simple and direct determination of bond behaviour. Pull-out was measured on the free end of the impregnated roving by a potentiometer. The concrete part was equipped with a steel element made precisely by a lathe attached to the concrete by epoxy resin and the potentiometer was fixed in this steel part by a bolt. A circular rigid steel plate was similarly attached at the free end of the reinforcement which protruded from the concrete part by approximately 20 mm to provide stable contact area for the potentiometer. Considering the steel plate, the maximum theoretical pull-out value was around 15 mm. Detailed view of the potentiometer and its fixing on the HPC part is presented in Figure 4. The speed of loading was constant at 2.0 mm/min according to the prescribed tensile stress increment of approximately 2.0 MPa/s in ACI 440.3R-03 standard.



Fig. 4 – Detailed view of the bottom part of the concrete specimen with installed potentiometer and support constructions for the pull-out values measurement.

The results of the pull-out test are presented in Figure 5 and Figure 6 in the form of two graphs. Both graphs show pull out measured by the potentiometer on the X axis and corresponding force on the Y axis. Figure 5 shows overall comparison of specimens with smooth composite reinforcement and those with the surface treatment made of fine-grained silica sand. The test proved that there was little cohesion between HPC matrix and composite reinforcement with smooth surface as all rovings without surface treatment were pulled out of their HPC matrix. Figure 6 presents more detailed view focused on the specimens with impregnated rovings treated with fine-grained silica sand which showed almost perfect bonding with the HPC matrix. All impregnated rovings with surface treatment were broken before they could be pulled out. Another advantage of the surface treatment of the reinforcement is the stability of the results because no sample shows significant deviations as shown in Figure 6. Also, the maximum tensile strength of the impregnated rovings was without any negative caused by the embedded grains of silica sand. The presented curves of pull-out can be used for example for non-linear numerical modelling of crack development and crack opening of TRC elements using analytical methods or other numerical software.

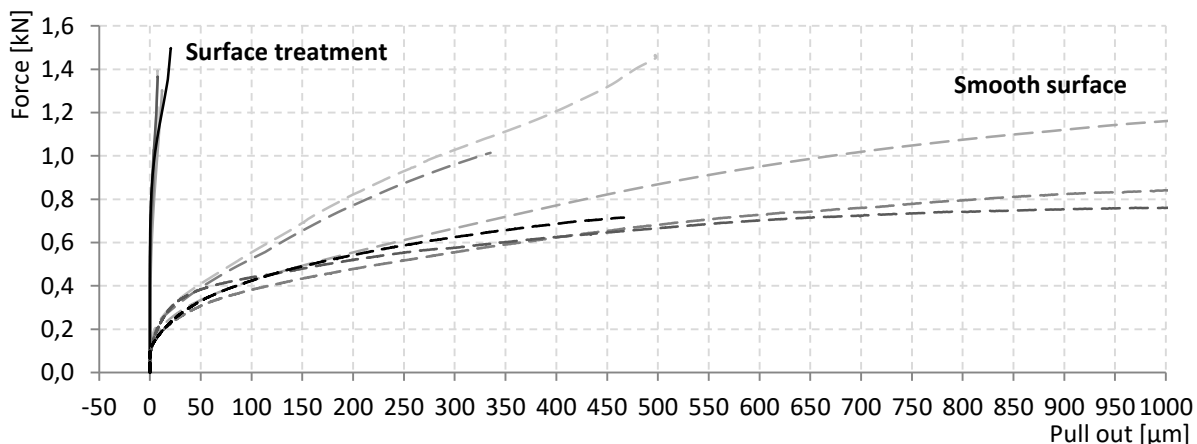


Fig. 5 – Results of pull-out test presented in the form of force – pull-out diagram using data from the testing machine and potentiometer showing rapid difference between the smooth surface and specimens with the surface modification.

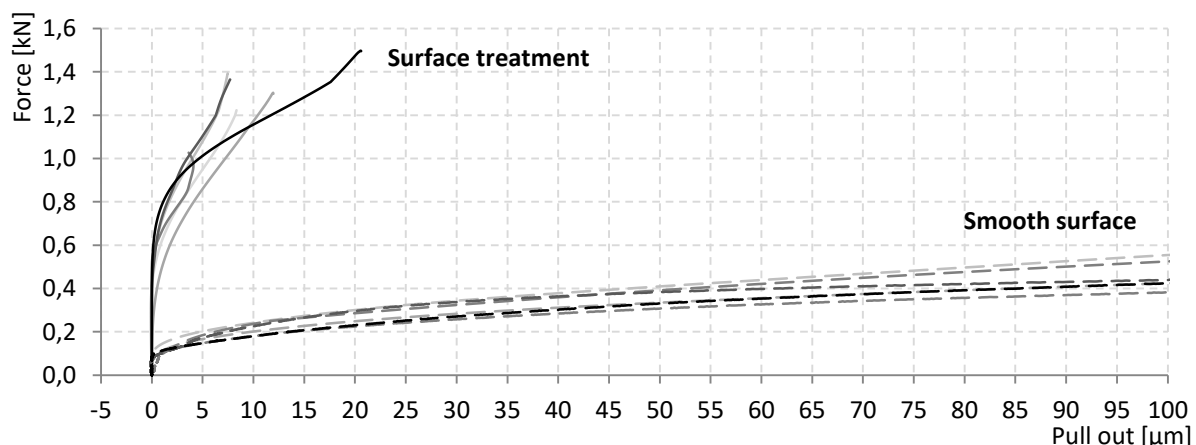


Fig. 6 – Results of pull-out test presented in the form of force – pull-out diagram using data from the testing machine and potentiometer. Detailed view on the beginning of the pull-out test with limited X axis showing rapid difference between the smooth and treated surface.

Four-point bending test

The four-point bending test was performed on small slabs with dimensions of 100 x 360 mm with constant thickness of 18 mm. Concrete cover of the composite reinforcement was designed to only 4 mm and was achieved by controlled application of HPC layers. The specimens were not vibrated to prevent the reinforcement movement to the HPC surface due to the lower density of the composite reinforcement compared to HPC. Three specimens were created for each group with the same designed amount of reinforcement. Six sets of samples were prepared in total.

Three variants with smooth surface and three with surface treatment using fine-grained silica sand were created. The first group contained two identical layers of composite reinforcement. One layer had 5 parallel impregnated rovings in the longitudinal direction with grid spacing of 22 mm. Grid spacing of rovings in transverse direction was 24 mm. The second group was also made with two identical layers of pre-prepared textile reinforcement but with 10 impregnated rovings in longitudinal direction spaced 10 mm from each other. The last third group of specimens was made with four layers of reinforcement with 10 impregnated rovings in longitudinal direction similar to the previous group. This combination of 4 layers with 10 rovings in each layer was the maximum possible amount of composite reinforcement for these specimen dimensions and composite reinforcement production technology, especially for the specimens with surface treatment. A view of the test setup and typical crack development is shown in Figure 7.



Fig. 7 – Typical crack development of 2x5 reinforcement with smooth surface on the left and 4x10 reinforcement treated with fine-grained silica sand on the right side.

Testing was performed with axial distance of supports of 300 mm and 100 mm in the case of loading supports. All supports had curvature with 15 mm radius. Monitored parameters during the testing procedure were magnitude of the reaction on the load cell and displacement of crosshead of the testing machine. Four-point bending test was performed on MTS 100 testing machine with controlled constant load increment of 2.0 mm per minute [12], [15], [16].

The results are presented in Figure 8, Figure 9 and Figure 10 in the form of force – displacement graph, because presentation of flexural stress on the y axis is not relevant after the initiation of the first crack in the HPC part despite the fact that it is commonly used. Always two graphs are presented side by side where the left side represents specimens with smooth composite reinforcement and the right side represents specimens with composite reinforcement with surface treatment.

Specimens with only two layers of textile reinforcement with five rovings in each layer are shown in Figure 8. The first sudden drop on the curve represents the formation of the first crack, creating a plastic joint, followed by an opening of the crack and an activation of the reinforcement. The load-bearing capacity of the specimen before the first crack initiation is given only by the tensile strength of the concrete without the contribution of the reinforcement. The small difference in this value between the samples with smooth reinforcement on the left and the samples with

surface treated reinforcement on the right is due to a slight inconsistency in specimen thickness which varied from the intended 18 mm.

After the initiation of the first crack the specimens with smooth reinforcement typically formed one additional crack, each under one of the loading supports, after which the smooth reinforcement started slipping. Their behaviour under pressure was typical for a slightly reinforced concrete structures with wide cracks opening. The specimens with the surface treated reinforcement formed multiple more narrow cracks, due to significantly better interaction conditions between reinforcement and cementitious matrix. The pull-out was not that significant and much faster reinforcement activation lead to the multiple cracking, which is characteristic for structures with higher amount of reinforcement [12], [16].

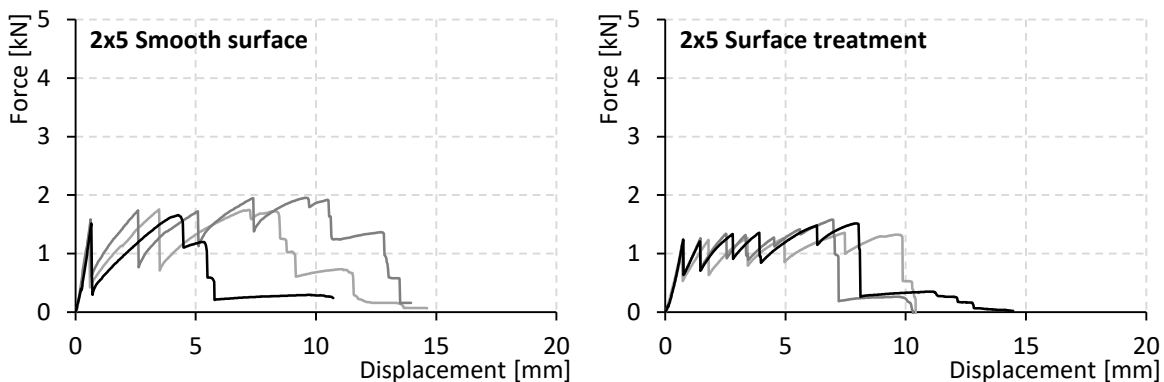


Fig. 8 – Force – displacement curves from the four-point bending test of specimens reinforced with 2x5 impregnated rovings with and without surface modification.

Very similar trend is presented in Figure 9 in the case of more heavily reinforced specimens with 10 rovings in each layer of reinforcement. Higher amount of reinforcement logically led to the higher maximum value of reached force in comparison to the specimens with 2x5 reinforcement. The specimens with smooth reinforcement on the left side show similar crack development as the specimens in Figure 8 on the right side with 2x5 reinforcement treated with fine-grained silica sand. The activation of surface treated 2x10 reinforcement is again much faster than in the case of its smooth counter-part. The specimens with surface modification also show higher ultimate reached force while also having lower displacement in the time of their collapse.

Figure 10 shows that the amount of reinforcement is so high in the cross-sectional area of the specimen that curves look more or less similar. The positive effect of the surface modification of composite textile reinforcement with fine-grained silica sand is much less significant in comparison with Figure 8 and Figure 9.

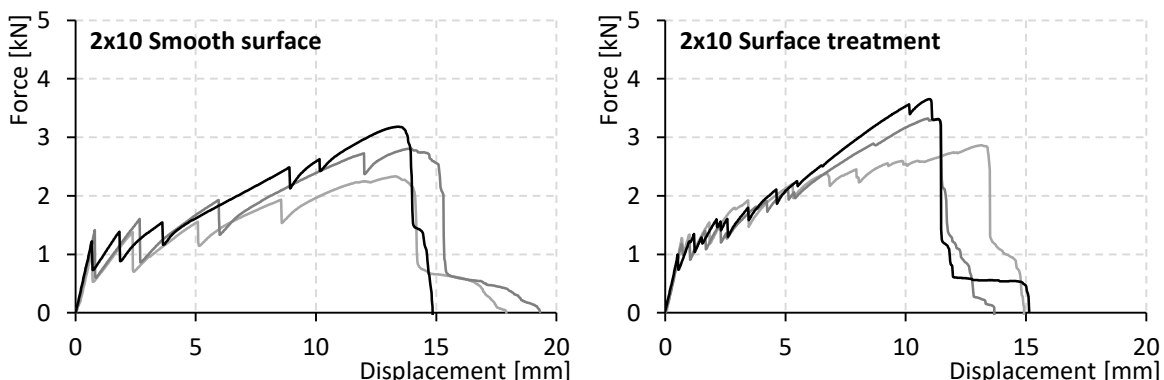


Fig. 9 – Force – displacement curves from the four-point bending test of specimens reinforced with 2x10 impregnated rovings with and without surface modification.

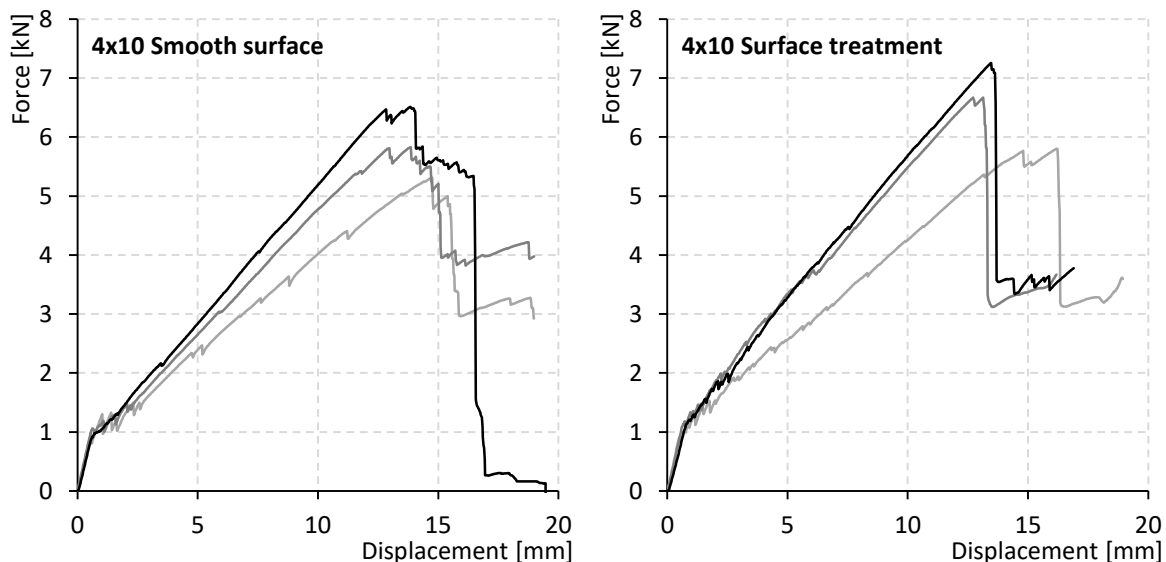


Fig. 10 – Force – displacement curves from the four-point bending test of specimens reinforced with 4x10 impregnated rovings with and without surface modification.

CONCLUSION

During the testing procedure of the own developed pull-out test method, the composite textile reinforcement in the form of a single impregnated roving with surface treatment made with fine-grained silica sand reached the maximum values of tensile stress in the composite reinforcement corresponding to the results of tensile test presented in a previous research. That means that the surface treatment using fine-grained silica sand has no significant negative effect on the tensile strength of the impregnated roving. The impregnated individual rovings were in most cases damaged (in the case of impregnated rovings with smooth surface after significant pull-out) where they were in contact with the surrounding HPC prism due to the fact that the reinforcement was pressed by the irregular contact area of the HPC during the process of reinforcement activation. The fibers near the surface of the textile reinforcement were therefore subjected to higher tensile stress, which leads to the weakening of the reinforcement and subsequent breaking of the roving in this area. Epoxy resin impregnation of the individual rovings however provides sufficient protection of AR-glass fibers in HPC matrix from premature damage for both smooth and modified reinforcement. The HPC part of tested specimens showed no signs of damage.

The difference between specimens with and without surface treatment is also clearly visible. The curves representing typical samples with smooth surfaces show a rapid pull-out of the reinforcement from the part of the HPC sample with higher pull-out values and lower corresponding force. After activation of the reinforcement in its full length, there is a very slow increase in force during the loading process due to poor interaction of both materials. This result signifies the need of large anchorage length of the smooth composite reinforcement required for the load transfer in the actual TRC element. The curves representing typical samples with surface modification provide much better results with higher contact stiffness. Grains of fine silica sand allow almost no slipping due to the high surface roughness.

The contact area of the reinforcement and cementitious matrix is constant in this method, due to the composite reinforcement passing completely through the HPC prism. The pull-out is measured by a potentiometer placed on the free end of the reinforcement protruding from the HPC prism which ensures activation of the reinforcement in its whole length.

Textile reinforcement with surface treatment provides significantly better results regarding the crack formation and development as was also demonstrated by flexural bending test performed on small slabs using different variants and amounts of composite textile reinforcement. Better

bonding conditions lead to a very short anchorage length for reinforcement activation without a significant loss of force due to the loading process controlled by constant increment of displacement. The ultimate bending strength was also a little higher. The most visible difference in the results is at the beginning of the curve during the process of reinforcement activation in the case of 2x10 impregnated rovings with smooth surface and with surface treatment. The surface treatment is therefore very effective and can also have economic benefits by saving reinforcement material.

It is also obvious from the presented figures that with a higher amount of textile reinforcement a bending behaviour similar to that of elements made of traditional materials and with traditional diameters of reinforcement can be achieved. This means that after the first initiation of cracks, there is no massive opening of cracks. This effect was achieved with a roving material made of alkali-resistant glass, which has a modulus of elasticity slightly higher than the HPC used. After impregnation with epoxy resin, the composite reinforcement as a whole even has a similar modulus of elasticity. It explains why such a large amount of composite reinforcement was needed to achieve those results during the bending test.

ACKNOWLEDGEMENTS

This work has been supported by the Ministry of Education, Youth and Sports within National Sustainability Programme I (NPU I), project No. LO1605 - University Centre for Energy Efficient Buildings – Sustainability Phase.

REFERENCES

- [1] L. Laiblová *et al.*, „Environmental Impact of Textile Reinforced Concrete Facades Compared to Conventional Solutions—LCA Case Study”, *Materials*, roč. 12, č. 19, Art. č. 19, led. 2019.
- [2] N. Williams Portal, I. Fernandez Perez, L. Nyholm Thrane, a K. Lundgren, „Pull-out of textile reinforcement in concrete”, *Constr. Build. Mater.*, roč. 71, s. 63–71, lis. 2014.
- [3] M. Krüger, „Vorgespannter textilbewehrter Beton (Prestressed textile reinforced concrete)”, *Philos. Dr. Thesis Stuttg. Univ. Stuttg. Fak. Bau- Umweltingenieurwissenschaften Diss*, 2004.
- [4] E. Lorenz a R. Ortlepp, „Bond Behavior of Textile Reinforcements - Development of a Pull-Out Test and Modeling of the Respective Bond versus Slip Relation”, in *High Performance Fiber Reinforced Cement Composites 6*, G. J. Parra-Montesinos, H. W. Reinhardt, a A. E. Naaman, Ed. Springer Netherlands, 2012, s. 479–486.
- [5] W. Brameshuber, *Report 36: textile reinforced concrete-state-of-the-art report of RILEM TC 201-TRC*, roč. 36. RILEM publications, 2006.
- [6] B. Banholzer, „Bond behaviour of a multi-filament yarn embedded in a cementitious matrix”, PhD Thesis, Bibliothek der RWTH Aachen, 2004.
- [7] M. Kynclova, „Environmentally effective waffle floor structures from fibre concrete”, prezentováno v International PhD Symposium in Civil Engineering, Technical University of Denmark, Lyngby, 2010.
- [8] T. Vlach, P. Hájek, C. Fiala, L. Laiblová, J. Řepka, a P. Kokeš, „Waffle Facade Elements from Textile Reinforced High Performance Concrete”, *Proc. HiPerMat*, 2016.
- [9] C. Fiala *et al.*, „Construction and Static Loading Tests of Experimental Subtle Frame from High Performance Concrete for Energy Efficient Buildings”, *Solid State Phenomena*, 2017.
- [10] A. Chira, A. Kumar, T. Vlach, L. Laiblová, a P. Hajek, „Textile-reinforced concrete facade panels with rigid foam core prisms”, *J. Sandw. Struct. Mater.*, roč. 18, č. 2, Art. č. 2, bře. 2016.
- [11] S. Yin, M. Na, Y. Yu, a J. Wu, „Research on the flexural performance of RC beams strengthened with TRC under the coupling action of load and marine environment”, *Constr. Build. Mater.*, roč. 132, s. 251–261, úno. 2017.
- [12] T. Vlach, L. Laiblová, M. Ženíšek, A. Chira, A. Kumar, a P. Hájek, „The Effect of Surface Treatments of Textile Reinforcement on Mechanical Parameters of HPC Facade Elements”, in *Key Engineering Materials*, 2016, roč. 677, s. 203–206.
- [13] T. Vlach, M. Novotná, C. Fiala, L. Laiblová, a P. Hájek, „Cohesion of Composite Reinforcement Produced from Rovings with High Performance Concrete”, *Appl. Mech. Mater.*, roč. 732, s. 397–402, 2015.

- [14] V. Tomáš *et al.*, „Comparison of Different Methods for Determination of Modulus of Elasticity of Composite Reinforcement Produced from Roving”, *Adv. Mater. Res.*, č. 1054, Art. č. 1054, 2014, Viděno: úno. 27, 2017.
- [15] L. Laiblová, T. Vlach, M. Ženíšek, A. Kumar, a P. Hájek, „Comparison of Different Types of Glass Reinforcement for HPC Facade Elements from Mechanical and Economical Aspects”, *Key Engineering Materials*, 2017.
- [16] T. Vlach, L. Laiblová, M. Ženíšek, J. Řepka, a P. Hájek, „Soft Insert for Support Modeling of Slightly Textile Reinforced Concrete”, *Key Engineering Materials*, 2018.

DEM STUDY ON THE PENETRATION OF JACKED PILES INTO LAYERED SOFT CLAY

Suchun Yang, Mingyi Zhang and Songkui Sang

*Qingdao University of Technology, School of Civil Engineering, Qingdao, China;
18560609732@qq.com; zmy58@163.com; 1542439862@qq.com*

ABSTRACT

In order to explore the variation law of soil particle displacement and pile force around piles during penetration process, the DEM (Discrete Element Method) model is used to test the penetration of pile foundation in layered soft soil foundation. The variation law of pile penetration force, radial pressure at pile-soil interface, friction resistance at pile side, displacement field and force field between particles during penetration process is analyzed. Research shows: (1) The penetration force increases with the increase of penetration depth and pile diameter. The increase of pile diameter is beneficial to overcome the influence of unfavorable strata. (2) At the same penetration depth, with the continuous penetration of the pile body, the radial pressure gradually decreases, showing a significant degradation phenomenon. The reason for the degradation of lateral friction is essentially the degradation of the radial pressure. (3) The distribution of contact force chain in different soil layers is similar, but the range of action is different. The contact force in silt layer is obviously larger than that in silty clay layer. The compressive stress of the soil at the end of the pile transfers radially with tensile stress. With the increase of pile diameter, the compressive stress and tensile stress in soil layer are gradually increasing, and the influence range of compressive stress and tensile stress is also gradually increasing. (4) The displacement of the soil below the pile tip is triangular, and the soil at the pile tip is squeezed around under the action of the pile tip. The influence range of particle displacement in each soil layer is different, and the influence range of particle displacement in silt layer is obviously smaller than that in silty clay layer.

KEYWORDS

DEM; Clay; Pile; Force; Displacement

INTRODUCTION

Jacked pile technology has the advantages of low noise and clean construction, and is widely used in engineering construction. The problem of pile penetration and its influence have been concerned for a long time in engineering and academic fields[1-3]. The mechanical problems of jacked piles can be divided into the penetration stage and the use stage according to the working conditions. The mechanical problems in the two stages are different, but both are complex. During the penetration stage of jacked pile, the pile tip strongly squeezes the soil, the displacement of the soil changes from small deformation to large deformation, and the pore water pressure changes drastically, which causes the mechanical properties of the soil to change. The pile side produces a reaction force, and this force is affected by many factors, such as the compressive modulus of the soil, the composition of soil particles, the depth of the soil layer, etc. The jacked pile



is often subjected to cyclic loads during the use stage. Soils will weaken under the action of cyclic loading, which will affect the bearing capacity of the pile.

There are three main theories that can be used to analyze the mechanics of jacked piles: cavity expansion theory[4], strain path method[5], and limit equilibrium method[6], but each method has its limitations in application. For example, the cavity expansion theory ignores the influence of depth on the bearing capacity, and strain path method can only work on non-deformable soil, the limit equilibrium method uses the assumed slip line as the failure surface, and different assumed slip lines will cause large differences in the calculation results.

Because of the imperfect theory, many scholars[7-8] use experimental methods to explore the penetration force of jacked piles, which are mainly divided into macro-tests and meso-tests. Macro-tests mostly use piles with sensors to perform penetration tests in a model box or on-site and collect data in real time. To study the pile-soil interaction on the meso scale, some scholars[9] used meso-tests methods, such as CT, white light interferometer, etc., to test the porosity and contact area of soil particles under force.

Soil material is neither ideal elastomeric material nor ideal plastic material but is cemented or extruded by granular particles. Due to the granular characteristics of soil, the traditional continuum method and finite element method cannot reveal the microscopic mechanism of soil deformation and the law of force transfer in essence. Compared with the finite element method, the particle flow discrete element method has greater advantages. There are series of independent motions between the particle elements, which can reveal the macro-mechanics mechanism from the micro-particle element level. Particle flow software can effectively simulate discontinuous problems such as separation and cracking of media, and it is more and more widely used in geotechnical engineering. Cundall[10] (1971) put forward the concept of discrete element method for the first time. It is also the earliest application of discrete element method[11] to solve and study rock mechanics problems. At present, numerical simulation of particle flow is widely used in sand and rock[12-15]. However, when simulating clay, it is difficult for particle flow to be used in clay due to the small particle size requirement, the large number of particles in the model and the complexity of parameter calibration. The author repeatedly calibrates clay parameters and simulates the process of static pressure pile penetrating into clay soil by DEM to explore the change law of macro and micro physical quantities.

ESTABLISHMENT AND PENETRATION OF DEM JACKED PILE MODEL

Formation of Layered Soft Clay Foundation

The traditional rainfall method relies on the self-weight balance of particles to form the soil layer. Different self-weight results in different initial stress fields of the soil layer. Therefore, this paper uses the Grid Method proposed by Duan & Cheng[16] to generate soil layers. GM method divides the model of soil sample into many small areas. When the soil particles are generated, they are generated in order from left to right and from bottom to top. Finally, the soil model with controllable compactness and porosity is generated.

The size of the model is 450 mm *700 mm (width *height). Twelve layers of particles are generated, and 119880 soil samples are generated. The height of each layer is 5 cm, and the upper seven layers of simulated clay layers have particle sizes ranging from 0.45 mm to 0.7 mm. The lower five layers are sand layers with particle sizes ranging from 1.22 mm to 1.67 mm, and the



initial porosity of soil samples is 0.25. Considering that the gravity field is affected by size, the acceleration of gravity of soil particles is increased to 40 G. The process of particle formation is shown in Figure 1. $GM_{i,j}$, I are expressed as the number of rows in the grid, J is expressed as the number of columns in the grid. It is convenient to observe particle movement and distinguish the soil layer with horizontal and vertical color bands.

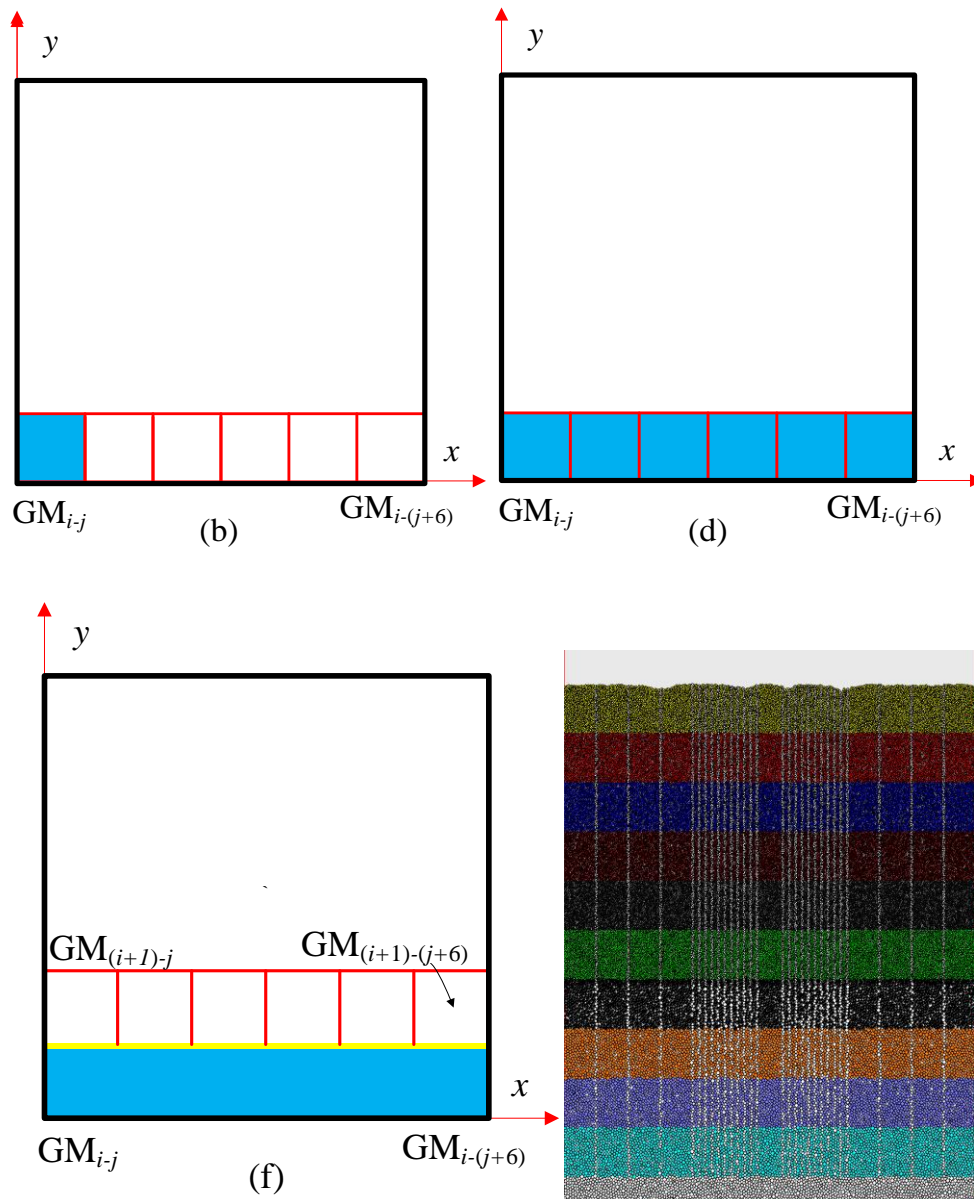


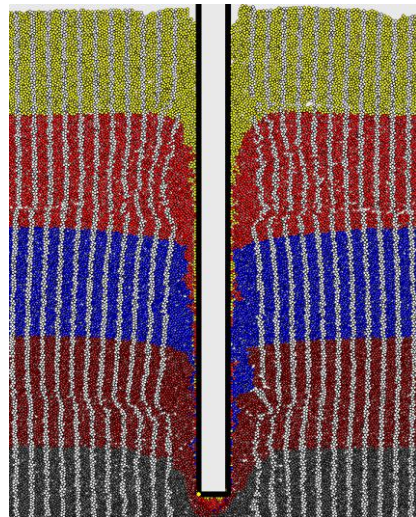
Fig. 1 - Graphics of soil samples generated by GM method

According to the relevant research[17-19], the contact and parameters between particles are assigned. The meso-physical parameters of soil particles are listed in Table 1.

Tab. 1 - Soil meso-parameters

NO.	Density / (kg/m ³)	Soil classification	Normal contact	Tangential contact	Normal bond	Tangential bond	friction coefficient
1	2720	Silty clay	1e7	1e7	500	250	0.27
2	2710	Silty soil	5e7	5e7	500	250	0.756
3	2720	Silty clay	1e7	1e7	1000	500	0.32
4	2720	Silty clay	1e7	1e7	1000	500	0.46
5	2710	Silty soil	5e7	5e7	500	250	0.79
6	2720	Silty clay	1e7	1e7	1000	500	0.502
7	2710	Silty soil	5e7	5e7	500	250	0.78
8-12	2650	Sand	8e8	8e8	/	/	0.5

Pile Penetration


Fig. 2 - Pile driving process

Three sizes of piles are generated in the already formed soil particle model. The length of the pile is 30 cm, and the diameter of the pile is 10 mm, 15 mm and 20 mm. This kind of pile is composed of particles that can extract force and displacement. The penetration force of the pile top is increased from 0kN by 50kN each time, and the changes in force and displacement are monitored. When the pile body is completely penetrated into the soil particles, the loading is stopped.

ANALYSIS OF DEM TEST RESULTS

Pile-pressing Force Analysis

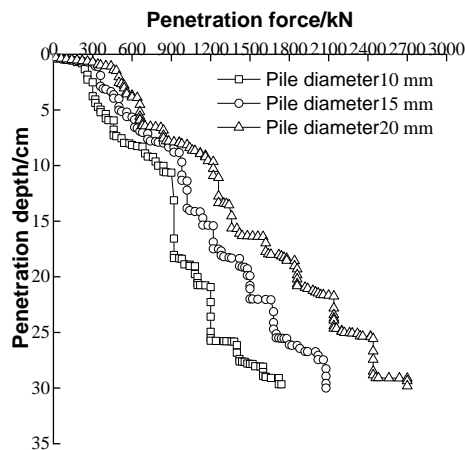


Fig. 3 - Curve of penetration force with penetration depth

From Figure 3, it can be seen that with the increase of penetration depth, the penetration force increases gradually, and with the increase of pile diameter, the pile-pressing force increases gradually. The variation law of the curve also reflects the difference in the soil layer. From the point of view of the specific soil layer, the force of pile end increases rapidly and the displacement hardly changes when the pile end is not penetrated into the soil layer at the initial penetration stage. With the increase of penetration force, the penetration force keeps stable and the displacement increases sharply after piercing the soil layer at the pile end.

When the end of the pile penetrates into the silt layer, the penetration force increases rapidly and the penetration displacement increases slowly. When penetration into the silty clay layer, the penetration force remains stable and the penetration displacement increases rapidly.

When the pile tip is located in the depth of 10 cm~20 cm, 25 cm~30 cm (silty clay layer 3, 4, 6), there is also a phenomenon of the rapid increase of pile driving displacement. Because the penetration force is still large after crossing the overlying soil layer, the displacement of the third, fourth and sixth layers of the soft soil layer increase sharply.

During the penetration process, when the pile tip is located in the soft soil layer, the displacement will increase sharply, which will be restrained with the increase of pile diameter. This shows that with the increase of pile diameter, unfavorable soil can be overcome to a certain extent. The specific reasons are as follows: Figure 4 shows that the increase of pile diameter will cover more soil particles, and part of the particles at the end of the pile is composed of upper soil particles, which have been compressed and consolidated during penetration. When the end of the pile is located in soft soil, the increase of pile diameter will increase the proportion of consolidated soil particles at the end of the pile, which shows that the displacement at the end of the pile decreases.

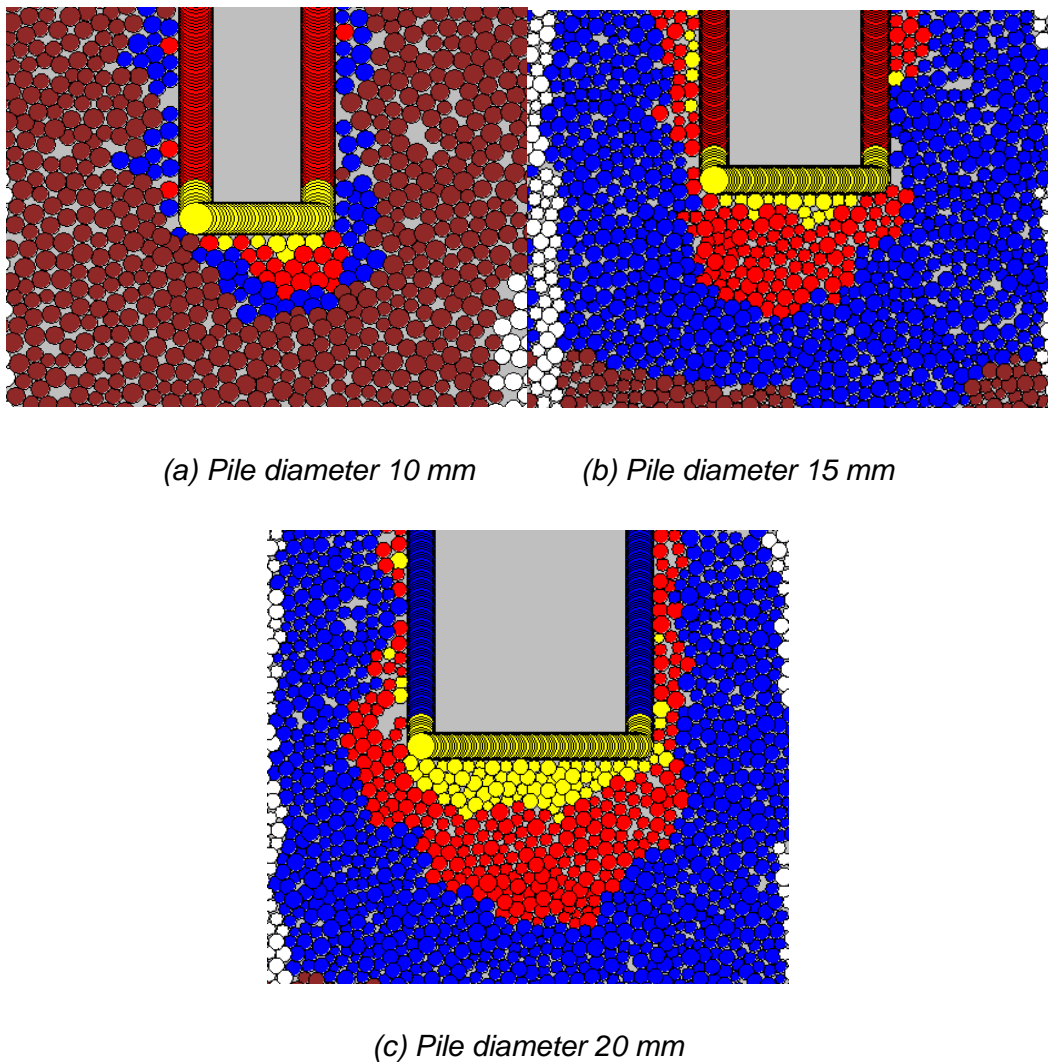


Fig. 4 - Particle forms of incidental soil under different pile diameters

Analysis of Radial Pressure and Pile Side Friction

Each particle composing the pile can monitor the force change in real time, and extract the soil pressure monitored by the pile side particle at each depth from the DEM., the curve of the radial pressure on the pile side with penetration depth is drawn, as shown in Figure 5.

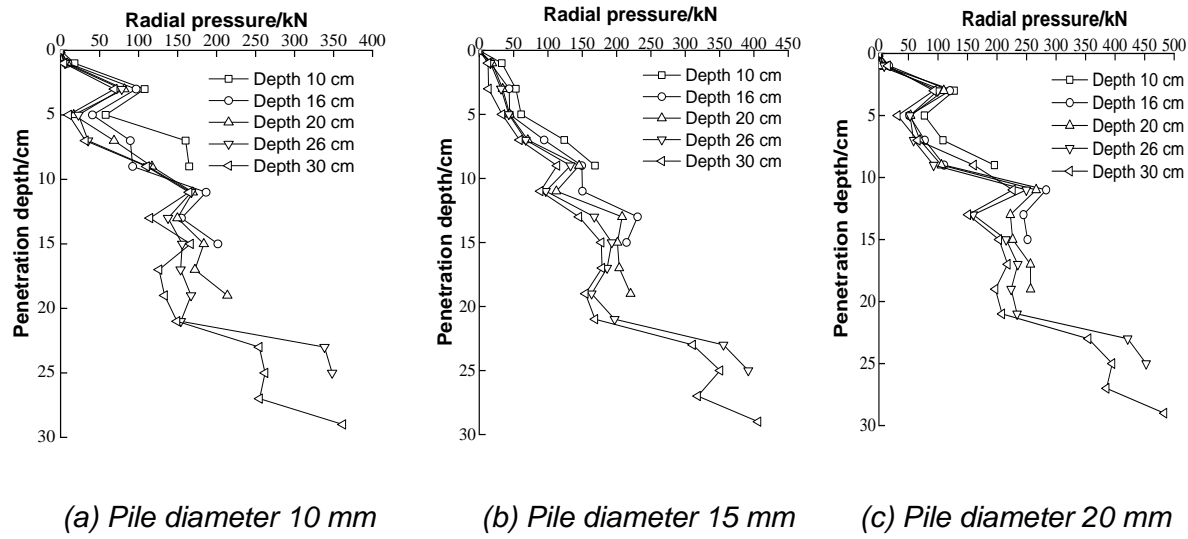


Fig. 5 - Curve of radial earth pressure with penetration depth

From Figure 5, it can be found that with the increase of penetration depth, the soil pressure on the pile side increases gradually; the increase of pile diameter has no significant effect on the trend of soil pressure increase; when the pile side is located at the depth of 10 cm~20 cm, 25 cm~30 cm (silty clay), the soil pressure increases slightly with the depth fluctuation; When the pile side is located in the depth of 5 cm~10 cm and 20 cm~25 cm (silt), the soil pressure increases obviously with the depth. With the increase of penetration depth, the earth pressure at the same depth decreases slightly.

The frictional resistance of each section of the pile side during penetration into the soil is monitored, and the curve of frictional resistance of pile side with penetration depth is drawn as shown in Figure 6.

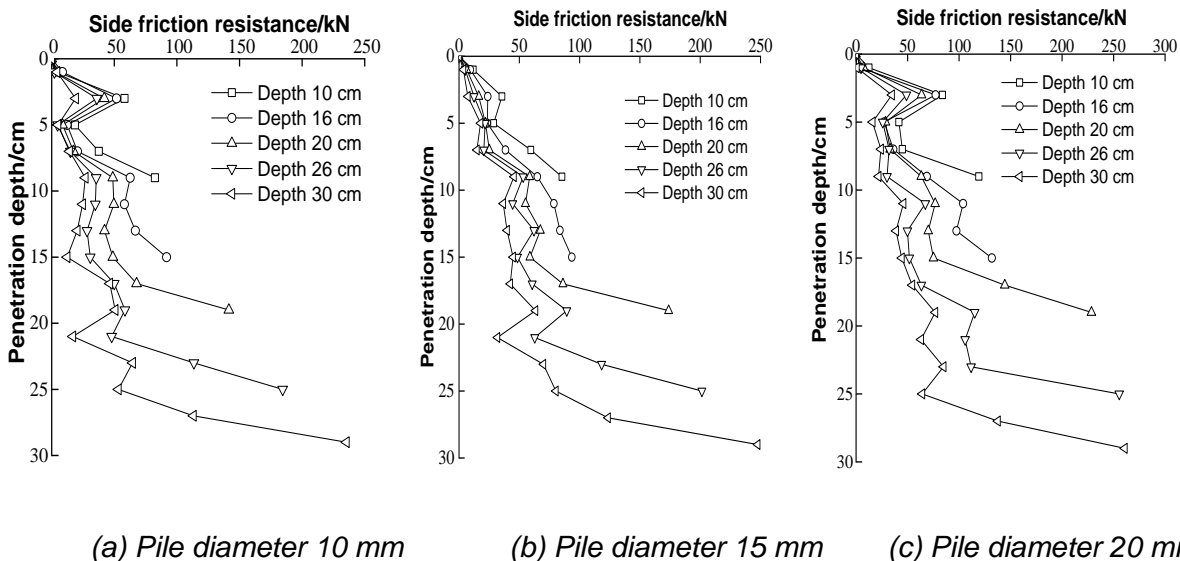
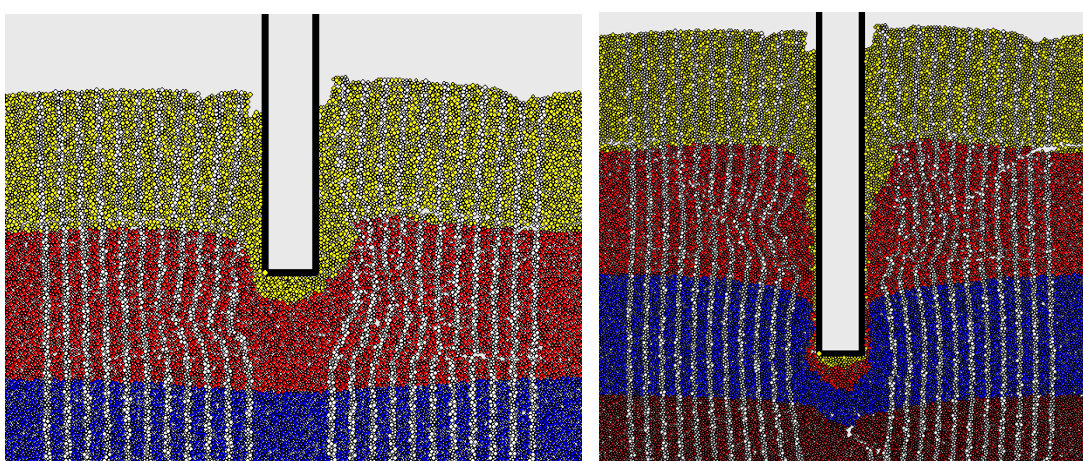


Fig. 6 - Curve of side friction resistance with penetration depth

According to Figure 6, it can be found that the variation of pile side friction with penetration depth is consistent with that of pile side soil pressure with penetration depth. With the increase of pile diameter, the frictional resistance of the pile side also increases gradually. This is because, with the increase of pile diameter, the effect of squeezing soil is more obvious, resulting in an increase of side friction. At the same penetration depth, the variation of lateral friction is the same as that of soil pressure at the pile side. With the increase of penetration depth, the lateral friction decreases gradually, and the obvious weakening phenomenon appears. This phenomenon is called "shear weakening" by Heerma[20], and "h/R" effect by Bondilph[21]. The variation law of side friction is consistent with that of earth pressure, which also shows that the essence of the degradation of side friction is the degradation of earth pressure.

Analysis of soil movement around pile

Taking a model pile with a diameter of 20 mm as an example, the movement of soil around the pile is analyzed when the pile passes through different soil layers during penetration.



(a) Penetration from silty clay layer to silt layer (b) Penetration from silt layer to silty clay layer

Fig. 7 - Changes of soil around pile

From Figure 7, it can be seen that when the pile penetrates into different soil layers, the form of soil breakage is different. Figure 7 (a) shows that the shear band between pile and soil is wider and filled with silty clay when the end of pile is penetrated from silty clay layer (yellow) to silt layer (red), but the width of shear band between pile and soil decreases with the increase of penetration depth. This is because: when the end of the pile is penetrated from soft soil to hard soil, punching failure occurs when the end of the pile penetrates into the soil, resulting in a wider shear band between the soil layer and the pile. As the pile continues to penetrate, the width of the shear band decreases with the increase of the lateral earth pressure of the pile in the hard soil layer.

Figure 7 (b) shows that when the end of the pile is penetrated from silt (red) to silty clay (blue), the shear band between pile and soil is narrower and there are fewer silt particles filled. It shows that when the end of the pile penetrates into the soft soil layer from the hard soil layer, the end of the pile penetrates into the soft soil, resulting in a narrow shear band between the soil layer and the pile.

Particle displacement analysis

In the process of pile driving, the change of contact force is essentially the expression of particle movement and redistribution. DEM software can monitor the displacement of soil particles in real time. The displacement distribution of particles in different soil layers was obtained by DEM. The direction of the black arrow indicates the direction of the particle displacement, and the length of the arrow indicates the size of the displacement.

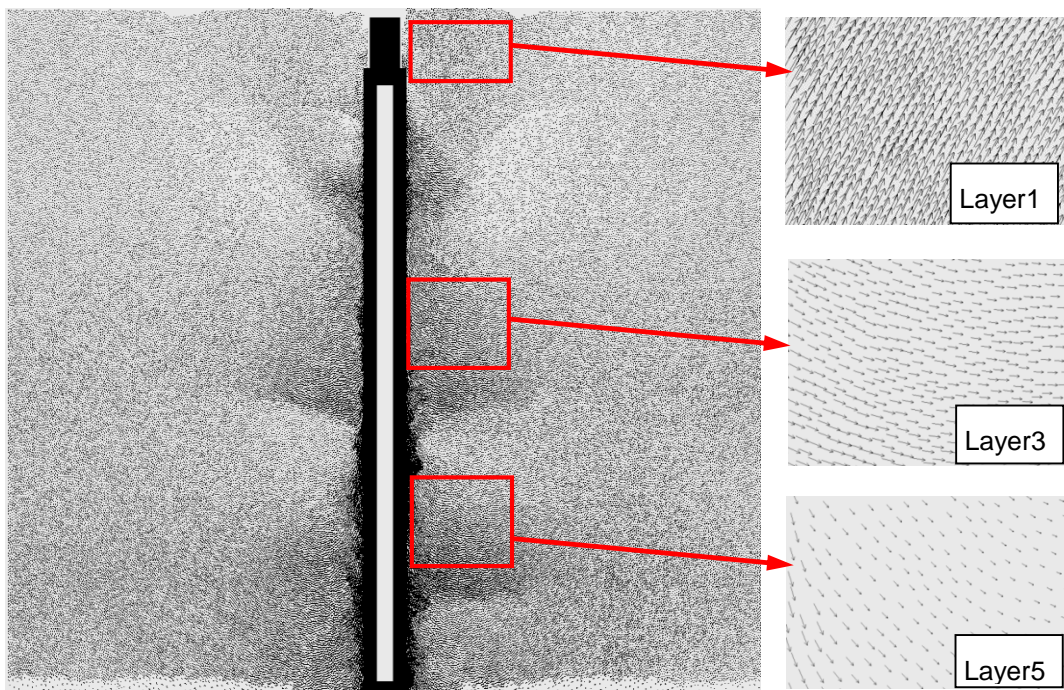


Fig. 8 - Particle Displacement Diagram after Pile Driving

From Figure 8, it can be seen that the displacement of soil around piles in different soil layers is quite different. In the process of penetration, the particles in the first soil layer move upward due to the compaction effect, and the macroscopical behavior is the uplift of the top soil during penetration. This is also one of the reasons why the friction resistance and radial pressure of pile side are smaller in the early stage of penetration. In the third soil layer, the horizontal displacement is the main one, because the third soil layer is silty clay layer, the contact stiffness and friction coefficient are small and the cohesion is large, so the horizontal displacement is easy to occur under the action of soil compaction. The fifth layer is silty soil with larger contact stiffness and friction coefficient. Compared with silty clay, the soil is harder and the effect of particle extrusion is stronger. Under the condition of pile penetration shear, the downward displacement occurs, which shows that the particles move downward obliquely.

Through Figure 8, it is found that the influence range of particle displacement in different soil layers is different after penetration. The influence range of particle displacement of silt layer is obviously smaller than that of silty clay layer, which indicates that the displacement of hard soil layer during penetration is smaller than that of soft soil layer, which corresponds to the conclusion that the sensitivity of soft soil is high, the structure is strong, and the strength of soil decreases more obviously after disturbance.

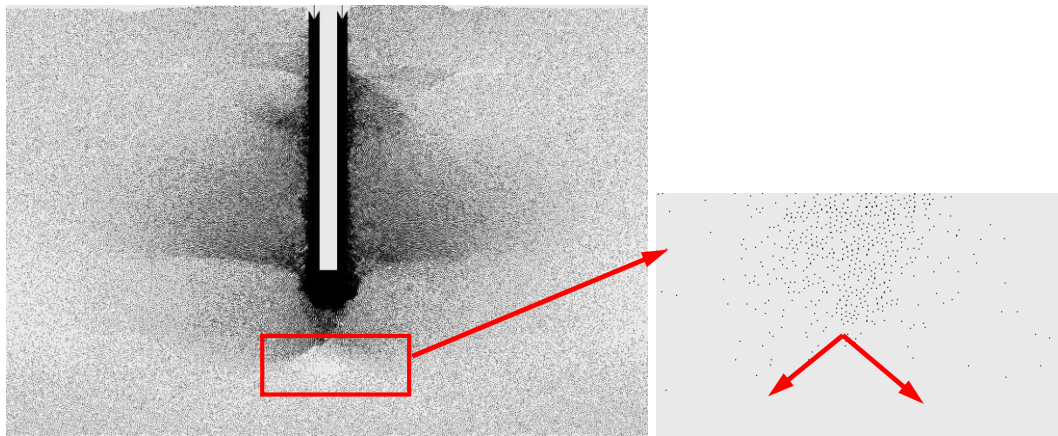


Fig. 9 - Pile tip particle displacement diagram during penetration

Pile diameter 20 mm penetration process is shown in Figure 11. By enlarging the red area at the end of the pile, it can be found that the displacement of the soil at the end of the pile presents a "triangular" distribution, indicating that the soil at the end of the pile is squeezed around under the action of the force at the end of the pile.

Analysis of contact force chain

Contact force chain refers to the average force between particles and the effective stress in soil. After the foundation model is generated and given the contact model, force chains will be generated between particles according to the position and displacement of particles. The thickness of black line in the force chain diagram represents the size of contact force, the direction of black line represents the direction of contact force, and the red force chain represents the tensile stress. In the process of pile penetration, the force chain will change.

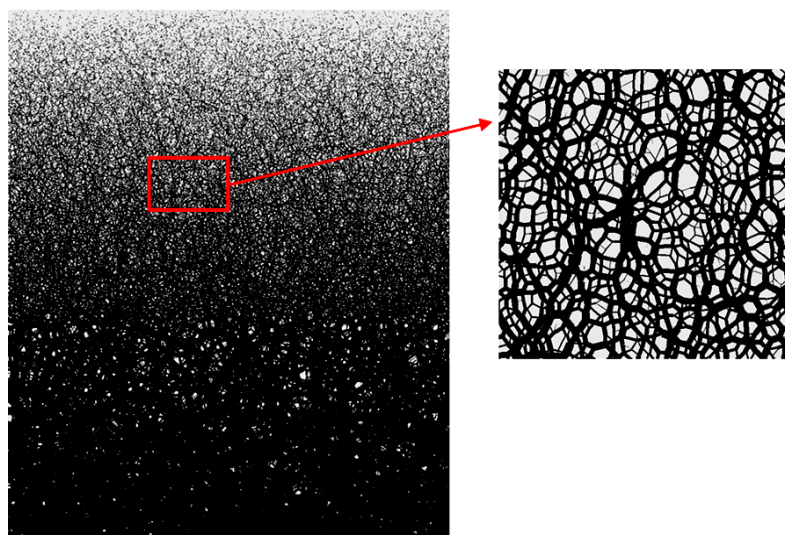
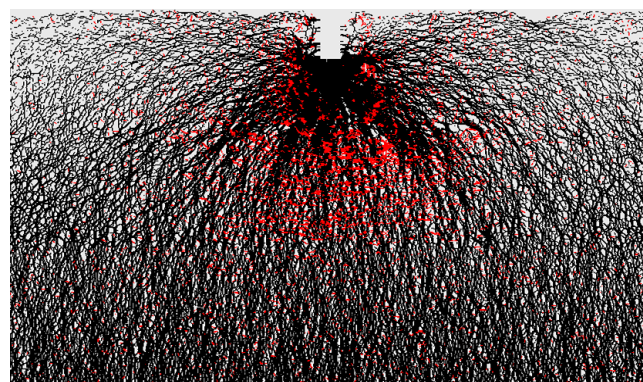
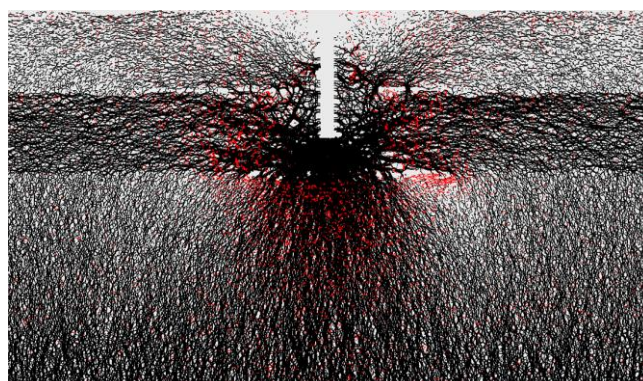


Fig. 10 - Force Chain Diagram after Soil Layer Generation

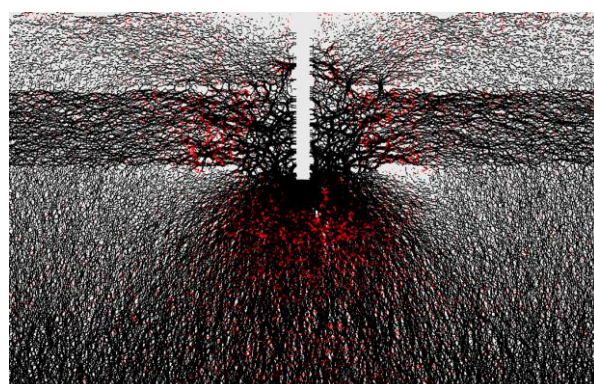
From the Figure 10, it can be seen that the contact force generated by deadweight increases gradually from top to bottom, and the transmission direction of the force chain is mainly vertical, there are also smaller horizontal and inclined bifurcations, showing a clear tree network.



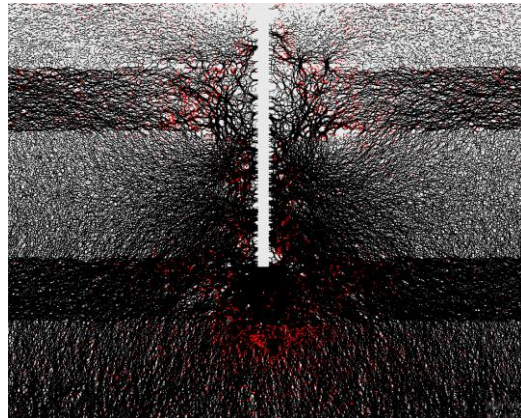
(a) penetration 2 cm



(b) penetration 7 cm



(c) penetration 10 cm



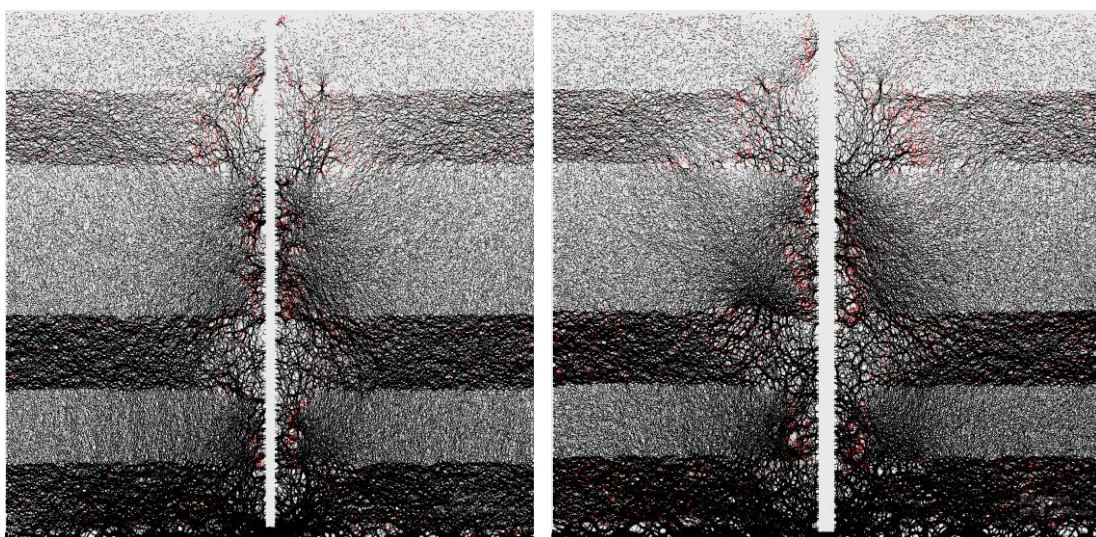
(d) penetration 20 cm

Fig. 11 - Force chain changes at different depths

Figure 11 shows that in the initial stage of penetration, the force chain at the end of the pile is concentrated and radiated around, and the force chain at the side of the pile is sparse, indicating that the soil at the end of the pile bears most of the penetration force and the frictional resistance at the side of the pile is smaller at the initial stage of penetration. With the continuous penetration of the pile and the continuous extrusion of the soil, there is a large horizontal force chain near the pile side. With the increase of the distance between the soil and the pile side, the large horizontal force chain gradually changes into a force chain under self-weight.

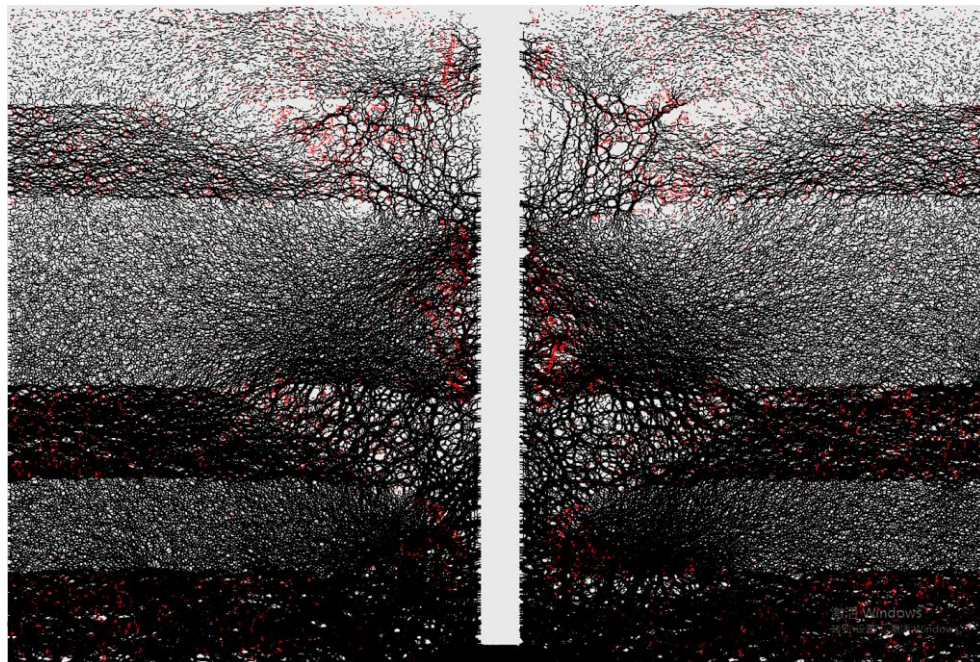
The range of action of force chain in different soil layers is different, and the range of action of hard soil is larger. In silty clay layer, the tension and compression stress concentrates near the pile. With the increase of distance, the tension stress gradually disappears, and the compression stress gradually decreases to the contact force under self-weight.

The contact force of silt layer is obviously greater than that of silty clay layer, and the stress of the soil beside the pile in silt layer also shows a horizontal direction, and the action range of tension and compression stress is larger.



(a) Pile diameter 10 mm

(b) Pile diameter 15 mm



(c) Pile diameter 20 mm

Fig. 12 - Variation of force chain under different pile diameters

From Figure 12, it can be found that with the increase of pile diameter, the compressive stress and tensile stress in the soil layer are gradually increasing, and the influence range caused by soil compaction effect is also gradually increasing. From the comparison of Figures 12 (a) (b) (c), it is found that with the increase of pile diameter, the transmission direction of the force chain becomes vertical and the force chain increases gradually. This is because the cohesion of silt layer is smaller and the contact stiffness is bigger, so horizontal displacement is not easy to occur; while the cohesion of silty clay layer is bigger and the contact stiffness is smaller. Under the extrusion force of pile body and soil, the particles at the interface of silt layer and silty clay layer tend to move in the direction of smaller contact stiffness, resulting in larger vertical compressive stress at the interface between silt layer and silty clay layer.

With the increase of pile diameter, the greater the extrusion force between pile and soil, the greater the movement displacement of soil particles, and the greater the compressive stress between particles at the interface.

CONCLUSION

(1) The penetration force increases with the increase of penetration depth and pile diameter. The increase of pile diameter is beneficial to overcome the influence of unfavorable strata.

(2) At the same penetration depth, with the continuous penetration of the pile body, the radial pressure gradually decreases, showing a significant degradation phenomenon. The reason for the degradation of lateral friction is essentially the degradation of the radial pressure.

(3) The distribution of contact force chain in different soil layers is similar, but the range of action is different. The contact force in silt layer is obviously larger than that in silty clay layer. The compressive stress of the soil at the end of the pile transfers radially with tensile stress. With the increase of pile diameter, the compressive stress and tensile stress in soil layer are gradually increasing, and the influence range of compressive stress and tensile stress is also gradually increasing.

(4) The displacement of the soil below the pile tip is triangular, and the soil at the pile tip is squeezed around under the action of the pile tip. The influence range of particle displacement in each soil layer is different, and the influence range of particle displacement in silt layer is obviously smaller than that in silty clay layer.

ACKNOWLEDGEMENTS

The work presented in this paper was financially jointly supported by the National Natural Science Foundation of China (Grant No. 51778312).

REFERENCES

- [1] YANG Su-chun, ZHANG Ming-yi, WANG Yong-hong, SANG Song-kui, MIAO De-zi. Field test on pile tip resistance of closed-end jacked pipe pile penetrating into layered foundation[J]. Rock and Soil Mechanics, 2018, 39(S2): 91-99.
- [2] Liu, Jun-Wei;Zhang, Ming-Yi;Yu, Feng;Bai, Xiao-Yu.Experimental study on interface shear fatigue between soils and PHC pipe piles[J]. Chinese Journal of Geotechnical Engineering. 2013, 35(S2) : 1037-1040.
- [3] Li, L., Li, J., Sun, D. a., & Zhang, L. Time-dependent bearing capacity of a jacked pile: An analytical approach based on effective stress method. Ocean Engineering, 143, 177-185.
doi:10.1016/j.oceaneng.2017.08.010
- [4] Aleksandar S. Vesic. Expansion of cavities in infinite soil mass[J]. Journal of Soil Mechanics & Foundations Div. 1972. 98 (SM3) : 265-290
- [5] Mohsen M. Baligh. Strain Path Method[J]. Journal of Geotechnical Engineering. 1985. 111 (9) : 1108-1136
- [6] Suchun Yang,Junwei Liu,Ankit Garget al. Analytical Solution for Estimating Bearing Capacity of a Closed Soil Plug: Verification Using An On-Site Static Pile Test[J]. Journal of Marine Science and Engineering. 2020. 8 (7) : 490
- [7] Suchun Yang,Junwei Liu,Mingyi Zhanget al. ANALYTICAL SOLUTION AND FIELD TEST OF CRITICAL BEARING CAPACITY AND SETTLEMENT OF PILE TIP[J]. CIVIL ENGINEERING JOURNAL-STAVEBNÍ OBZOR. 2020. 1: 61
- [8] Guthlac Wilson. THE CALCULATION OF THE BEARING CAPACITY OF FOOTINGS ON CLAY.[J]. Journal of the Institution of Civil Engineers. 1941. 17 (1) : 87-96
- [9] Suchun Yang,Junwei Liu,Longfei Xuet al. A New Approach to Explore the Surface Profile of Clay Soil Using White Light Interferometry[J]. Sensors. 2020. 20 (11) : 3009
- [10] Cundall P A. A computer model for simulating progressive, large-scale movement in blocky rock system[C]. Proceedings of the International Symposium on Rock Mechanics, 1971, 2(8): 129-136.
- [11] Cundall P A. Strack O D L .A discrete numerical model for granular assemblies[J]. Geotechnique , 1979, 29(1): 47-65.
- [12] Zhang Z , Wang Y H . Three-dimensional DEM simulations of monotonic jacking in sand[J]. Granular Matter, 2015, 17(3):359-376.



- [13] Wang J , Zhao B . Discrete-continuum analysis of monotonic pile penetration in crushable sands[J]. Canadian Geotechnical Journal, 2014, 51(10):1095-1110.
- [14] Yin, F., Xiao, Y., Liu, H., Zhou, H., & Chu, J. Experimental Investigation on the Movement of Soil and Piles in Transparent Granular Soils. Geotechnical and Geological Engineering, 36(2), 783-791. doi:10.1007/s10706-017-0353-2
- [15] Yu-nong, L., & Jing-pei, L. Behavior of the penetration process of model jacked pile in layered soil. Electronic Journal of Geotechnical Engineering, 14 P, 1-10.
- [16] Duan, N., Cheng, Y.. A modified method of generating specimens for a 2D DEM centrifuge model [C]. Geo-Chicago, American Society of Civil Engineers, 2016, pp: 610-620.
- [17] Zhou Jian, Wang Jiaquan, Zeng Yuan, et al. Particle flow simulation for slope stability analysis [J]. Rock and Soil Mechanics, 2009, 30 (1): 86-90.
- [18] Zhou Bo, Wang Huabin, Zhao Wenfeng, et al. Study on the correlation between meso-and macro-mechanical parameters of viscous materials [J]. Rock and Soil Mechanics, 2012, 33 (10): 3171-3178.
- [19] Chen Jianfeng, Li Huili, Zhou Jian. Study on correlation between macro and micro parameters of clay [J].Quarterly Journal of Mechanics, 2010, 31(2): 304-309.
- [20] Heerema E. P., De Jong A. An advanced wave equation computer program which simulates dynamic pile plugging through a coupled mass-spring system[M]. Numerical methods in offshore piling. Thomas Telford Publishing, 1980: 37-42.
- [21] Bond A J, Jardine R J. Effects of installing displacement piles in a high OCR clay[J]. Géotechnique, 1991, 41(03): 341-363.

EXPERIMENTAL RESEARCH INTO THE RESPONSE OF HISTORICAL STRUCTURE TO THE EFFECTS OF NATURAL SEISMICITY

Tomáš Čejka and Aneta Libecajtová

*CTU in Prague, Faculty of Civil Engineering, Department of Building Structures,
Prague, Thákurova 7, Czech Republic; cejka@fsv.cvut.cz,
aneta.libecajtova@fsv.cvut.cz*

ABSTRACT

The article presents the evaluation a building technical survey of a damaged historic rectory building in Luby near Cheb, it analyses the damage and proposes conceptual ideas for the rehabilitation design of a historic building damaged by the effects of natural seismicity applying the results and outputs of the NAKI II research project.

KEYWORDS

Natural seismicity; Historic building; Building technical survey; Stiffness of masonry structure; Additional prestressing

INTRODUCTION

The number of prominent historic and heritage buildings (over 40,000 immovable monuments situated on the territory of Bohemia, Moravia and Silesia), their cultural and historical value and the resources that must be spent on their restoration require special care for their protection and restoration.

The restoration and rehabilitation of historic and heritage masonry buildings, in many cases, requires the strengthening and rehabilitation of damaged and degraded masonry of pillars, walls and vaults of stone, brick, mixed or multi-leaf and half-timbered masonry, which is often in varying degrees of degradation and failure. In the case of historic buildings exposed to the effects of extraordinary loads and effects (undermined areas, areas susceptible to flooding and floodplains, mining areas, traffic-intensive areas, seismic areas), their spatial stability and residual structural capacity must be secured.

Severe earthquakes with a focus located on the territory of the Czech Republic or in its immediate vicinity are known from historical sources. Even today, weaker earthquakes are detected mainly in western and north-eastern Bohemia - in border areas with Germany and Poland. The strongest of them, which are also felt by the inhabitants, may be the cause of failure of historic buildings. According to [1], eight regions characterized by seismic hazards of up to the intensity of 7° on the MSK – 64 scale (ca 500 mm.s⁻²) can be delimited in the Czech Republic – Kraslice Region (7°), Český Les (6°), the eastern part of the Krušné Mountains (6°), Silesia (6°), north-eastern Bohemia (7°), the Western Carpathians and the Carpathian Foredeep Basin (7°), South Bohemia (6°), South Moravia (6°). A total of over 18000 cultural monuments and 133 national cultural monuments are situated in these regions [2] (Figure 1).

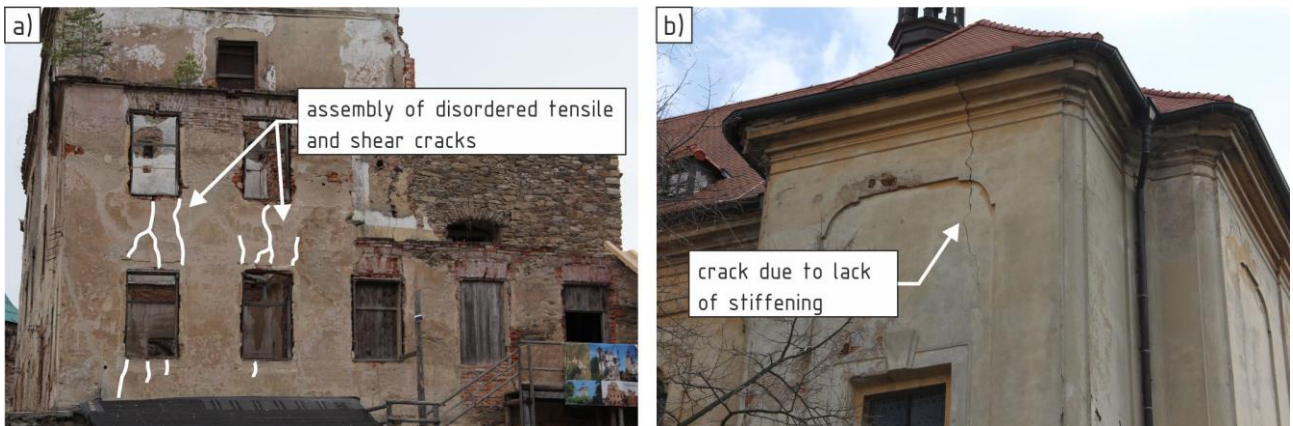


Fig. 1 - Illustration of damage to historic buildings in seismically active regions – a) Hartenberg Castle, Josefov (end of 12th and beginning of 13th century.), b) St. Anna's Church, Karlovy Vary – Sedlec (18th century)

The above facts testify to the need to address the issues related e.g. to the response of historic structures to the effects of natural seismicity, their potential consequences and the influence on their failure and residual structural capacity.

Earthquakes in the Czech Republic are usually concentrated in so-called swarms. An extremely strong swarm with the most active earthquakes was recorded in the Kraslice Region (western Bohemia) during the period of increased seismic activity at the turn of the 19th and 20th centuries. After a following period of rest, a stronger seismic swarm was registered in the area of the settlement of Nový Kostel in 1936 - 1937 and 1985 - 1986 reaching a local magnitude of 4.6 (intensity of 7° on MSK – 64). This earthquake intensity may cause damage to buildings - cracks, damage to plaster layers, falling off roofing, etc. More recently, increased seismic activity has been recorded again since 1997. At the end of 2000, a strong shock reached a local magnitude of 3.4 and was felt by the residents of Cheb, Sokolov, Karlovy Vary and Tachov Regions. A strong earthquake swarm was registered from August 2001, comprising over 1,500 earthquakes recorded in its eight phases, of which more than 5% were also felt by the local population [3]. The last major earthquake that has hit the Czech Republic so far occurred in May 2014. Its epicentre was located in the Cheb Region, in the settlement of Nový Kostel, 8.5 km below the Earth's surface, and the shocks could be felt as far as Central Bohemia and Prague. The earthquake's magnitude of 4.6 made it comparable to the earthquake of December 1985, and it became one of the strongest earthquakes in the last 100 years.

In addition to the above-mentioned areas, the majority of the territory of the Czech Republic is characterized by a seismic hazard of up to the fifth degree, and South Bohemia and Moravia up to the sixth degree MSK - 64 (the influence of Eastern Alpine and West Carpathian earthquakes). According to the seismic hazard map of the Czech Republic (Annex to the National Application Document to Eurocode 8), the manifestations of natural earthquakes with a macroseismic intensity in the range of 6 to 6.5 ° MSK - 64 can be expected mainly along the perimeter of the Bohemian Massif, with quasi-effective acceleration values ranging from 0.06 to 0.4 g.

Structures with insufficient spatial stiffness and insufficiently rigid foundation structures tend to be highly susceptible to dynamic effects caused by technical and natural seismicity [4]. The extreme sensitivity to dynamic effects caused by seismicity are, for example, typical of masonry buildings without bond beams, or beam and wall ties, with ineffective beam ties situated in degraded masonry, with an insufficiently rigid supporting system of vaults, buildings with yielding, e.g. joist and beam ceilings, with vaults without bowstrings and with insufficiently deep rigid foundations, unbonded foundations and inappropriate foundation subsoil [5, 6]. The type of masonry failure under dynamic loading with vibrations corresponds essentially to brittle fracture. At

relatively low vibrations, the masonry breaks due to fatigue not only in joints, but also in masonry units. Vertical cracks occurring in the perimeter walls of castle and church towers are also, in many cases, caused by seismic effects (including low-cyclic temperature effects and dynamic effects of heavy bells) [6].

For the sake of simplicity, the movement during an earthquake can be assumed to be a simple harmonic motion - continuous, similar to the oscillatory motion characterised by an amplitude, period, velocity and acceleration. Building structures in regions with high seismicity are also assessed for the values caused by seismic movements of the foundation soil, for the effect of inertial forces acting at different points of the structure, concentrated at the level of individual floors.

The horizontal movement of the Earth's surface during an earthquake reaches 0.3 to 0.5 times (or more) the gravitational acceleration - this horizontal component has the most severe impacts on buildings. A frequent cause of failures of masonry structures is the relatively low tensile strength of masonry and low ductility, which is the cause of considerable sensitivity of these materials (masonry structures) to the effects of forced deformations. The consequences of this property are, in many cases, manifested locally by stress states with a significant tensile component. The severity and intensity of seismic (dynamic) effects spreading through the soil, caused primarily by natural seismicity, depends, among other things, on the execution method and the properties of the foundation structures of the building. The composition of the geological environment and its mechanical properties affect the magnitude of vibrations from the subsoil, which may be amplified or damped by this composition. Natural frequencies - of soils of the overlying formations on the bedrock - are a major agent in terms of the propagation of vibrations through the subsoil. In the conditions of the Czech Republic, the usual thickness of soils on the bedrock is 2-4 m. In this case, the natural frequencies of the soil on the bedrock may approach the natural frequencies of buildings, and, as a result, the transmission of vibrations from traffic into building structures is amplified by the so-called resonance effect [7]. The failure of masonry structures may also occur due to the secondary excitation of subsoil movements in the vicinity of non-stabilized geological conditions.

The effect of seismic undulation of the subsoil with direct contact is first transmitted to the foundation structure of the building, exerting cyclic horizontal deformations of the foundation in response to the cyclic movements of the subsoil, which are transmitted to higher floors via the underground (lowest) floor depending on the shear and flexural stiffness. The magnitude and type of the horizontal deformation depends mainly on the stiffness of the structure of individual floors or the substructure. The highest values of stresses or horizontal (shear) deformations related to the distribution of the load-bearing system's stiffness along the height of the building are on the lowest floors, situated between the foundations and the superstructure, or in the substructure. In this perspective, systems with a relatively low stiffness on these floors – e.g. spacious halls, temple naves, etc. - represent the weakest, critical point, usually with the lowest resistance to seismic effects [8, 9].

LUBY RECTORY

The in-situ experimental activity aimed at the influence of seismic effects on historic structures carried out in the historic building of the Luby Rectory included the building technical survey, numerical analysis and, based on them, the identification of the likely cause of failures in the building and design of potential rehabilitation measures.

Brief description of the building

The rectory building in the settlement of Luby was built at the end of the 17th and the beginning of the 18th century, and is situated in the immediate vicinity of St. Andrew's Church, which is dated back to the 11th century. In 1739, the rectory was reduced to ashes, and only parts



of load-bearing walls on the 1st overground storey remained. After the fire, the rectory was restored, but in 1865 it burned down again and was newly restored (Figure 2). Up to now, no major construction work has been done in the rectory building. As part of routine maintenance, the roofing and windows were replaced, bathrooms and toilets were gradually installed inside the building, and ceilings were replaced in some rooms. Throughout the whole time of the building's existence, cracks caused by the assumed effects of earthquakes have been repeatedly repaired. The rectory has served its purpose with varying intensity until the present day.



Fig. 2 - Luby Rectory – a) southern elevation, b) eastern elevation

Structure of the rectory building

The rectory building is a two-storey masonry, partially cellared structure with a pitched roof with hips.

The vertical load-bearing structures are founded on strip footings of stone masonry or hand-placed rockfill. According to the information available, the building should be partially based on bedrock and partially on made-up ground and sediments. The underground floor is supported by a stone masonry vaulted structure with a rise of 2.2 m and a span of 4.5 m starting at the floor level. The overground vertical load-bearing structures are made of stone or mixed masonry. The thickness of perimeter walls on the 1st overground storey, including plasters, is ca 1000 mm, on the 2nd overground storey ca 500 mm. The interior load-bearing walls laid out in both directions are 350 and 500 mm thick. The thickness of partitions is 150 and 200 mm. The heads of window sills and door openings in the load-bearing walls are vaulted.

The floor structure over the 1st and 2nd overground storey consists of a wooden beam floor with a soffit (span of ca 3.5 to 5.2 m). The floors in the residential spaces are wooden, the corridors and sanitary facilities are tiled.

The staircase leading from the ground floor to the first floor is a clockwise curvilinear staircase. The stair treads made of stone are mounted in the walls at both ends.

The load-bearing structure of the roof cladding consists of a collar-beam roof supported by purlins. The 160/160 strutting beam is located in each truss. Purlins with dimensions of 140/200 are mounted on 140/200 columns. The columns are anchored by 100/100 braces securing the stiffness of the roof truss in the transverse direction, and 120/120 strips securing the longitudinal stiffness of the roof truss. The 140/200 columns are embedded in tie beams at the floor structure

level. 120/140 rafters are supported by strutting beams and headers. Headers are used in intermediate rafter trusses. The roof truss load-bearing structure applies tie beams, strips and braces for the horizontal reinforcement of the roof structure. Asbestos slate roof cladding is laid on an overall formwork of planks.

The windows are wooden with insulating double glazing. The entrance and most of the interior doors are massive wooden doors, and new modern smooth doors are fitted in the additionally installed sanitary facilities.

ANALYSIS OF FAILURES IDENTIFIED DURING A PRELIMINARY VISUAL BUILDING TECHNICAL SURVEY

Failures identified during a preliminary visual building technical survey

The preliminary building technical survey included the detection of defects and failures of varying relevance in the building. In accordance with the building and historical development and the effect of degradation processes, traces of increased moisture contents are visible on vertical, mainly perimeter structures, parts of horizontal structures, and the most part of vertical load-bearing and non-load-bearing structures are damaged by cracks. The type of visible traces of increased moisture contents corresponds to the missing or non-functional insulation against rising damp. The results of the survey do not point out any biological degradation and weakening of the wooden members of the roof truss structure and ceilings manifested by increased deformations.

The damage to the rectory building in the form of cracks is evident both on the facade and on the internal load-bearing and dividing structures. There are tensile or, to a lesser extent, shear cracks. Looking at the facade cracks occur most often in the corners of openings. The cracks are found on both overground storeys, they have a slightly inclined shape and interconnect the superimposed window or door openings. A typical crack found in the facade begins on the eaves, continues to the window head on the 2nd overground storey, then passes across the window sill to the window head on the 1st overground storey, and from there it continues via the window sill of the 1st overground storey as far as the masonry footing. Some cracks branch into several other cracks. The crack width varies along the building's height. The narrowest cracks are above the foundations and gradually widen towards the roof. Cracks are found both in surface finishes and the masonry. Cracks occur with varying intensity on all facades, but the building has suffered most damage on the north and east facades (Figure 3).

At the entrance to the building on the 1st overground storey, there are prominent cracks in the right and left corners of the room separating the transverse load-bearing walls from the southern perimeter wall of the building. Cracks of a similar type are found in all connections of internal and perimeter vertical structures on the ground floor. The cracks in the corners of rooms are, in some parts, followed by a number of inclined cracks in the load-bearing walls. There are cracks in the vaulted heads of the openings extending into the ceilings of the floor structure where they often copy the connections of individual structural members of the soffit. The cracks on the 1st overground storey are most often found in the places of connections of structural members – e.g. the connection of the interior and perimeter walls, in the cavettos of the floor structure's connection to the load-bearing walls, mounting of the vaulted strip in the masonry, etc.

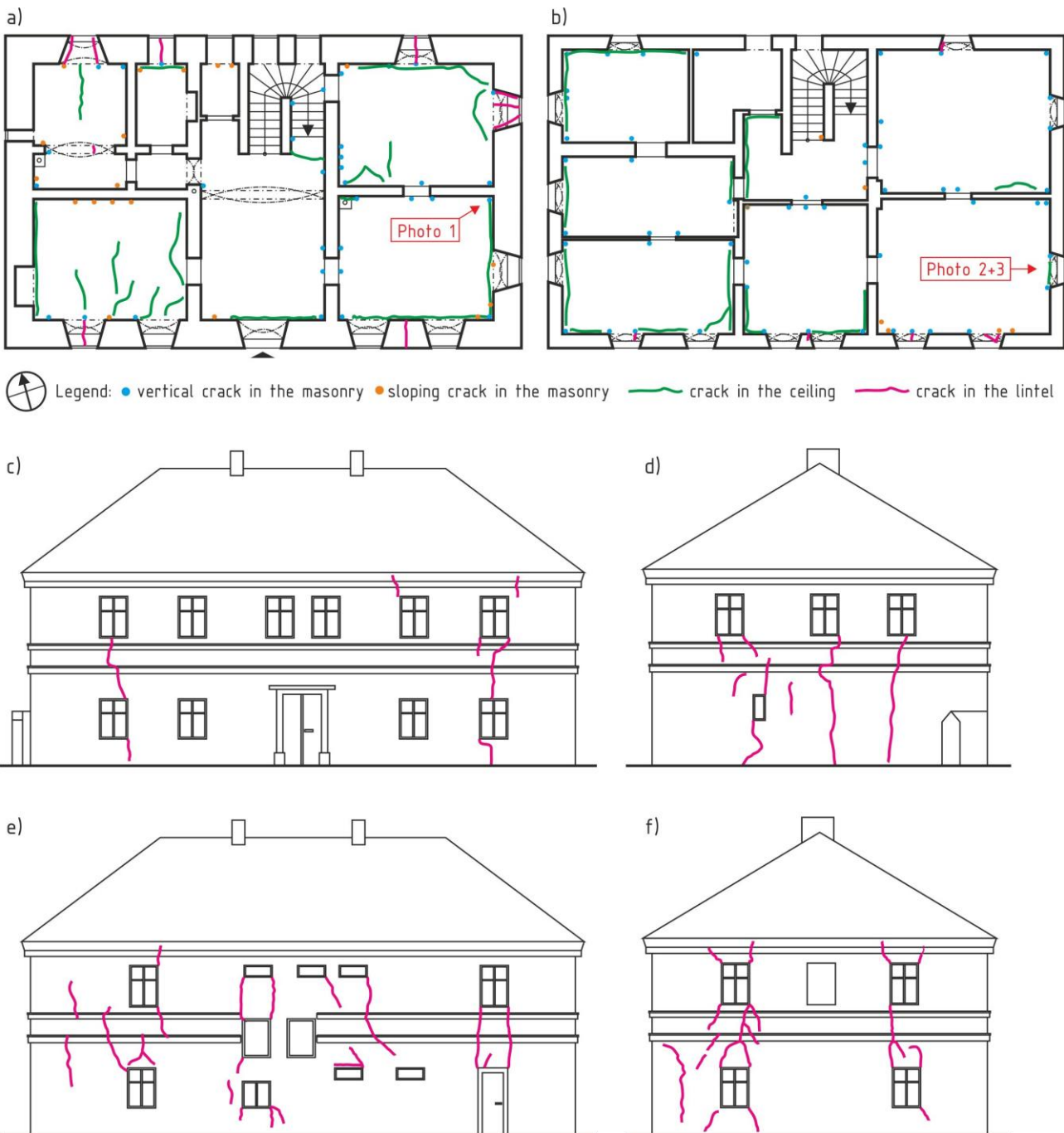


Fig. 3 - Schematic drawings of the rectory with marked failures and points where photographs were taken – a) plan of 1st overground storey, b) plan of 2nd overground storey, c) southern elevation, d) western elevation, e) northern elevation, f) eastern elevation

The type of cracks on the 2nd overground storey is similar to that on the 1st storey. The cracks most commonly occurring there are vertical or slightly inclined cracks in the corners of rooms, cracks in walls and partitions, in the vaulted heads of window and door openings and cracks between individual ceiling elements. On the 2nd overground storey, the rectory building is damaged by more prominent cracks than on the 1st storey. The most prominent - widest cracks are found in the eastern part of the building, where they are 2.5 to 4 mm wide in the perimeter wall. These cracks originate from a horizontal crack separating the floor structure from the perimeter wall, continue all the way to the window recess and then further on across the window sill. Due to

the type and location of these prominent cracks, it can be assumed that unless their further development is prevented, they may become the cause of a significant decrease in the structural capacity of the building as a whole in the future (Figure 4).

No reinforcing structures (visible tie cotsers of beam or wall ties), or marks of additionally installed stiffening structures were found in the building, neither in the interior, nor in the exterior during the preliminary building technical survey.

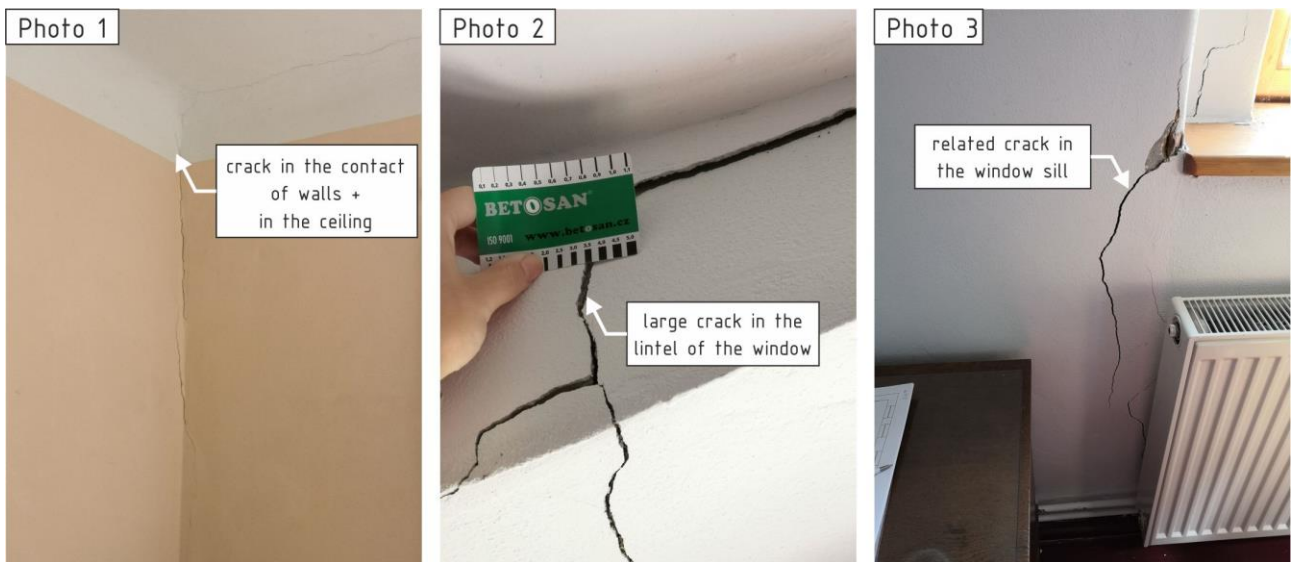


Fig. 4 - Illustration of damage to the building

Numerical model of the structure

To verify the assumption of seismic loading as a possible cause of the detected failures of the masonry structure, a spatial model of the structure was created in the Scia Engineer 19.1 programme on the basis of data obtained during the building technical survey.

The main load-bearing elements of the structure were modelled - load-bearing and reinforcing walls, masonry partitions, floor joists, vaulted arches and truss structures. The walls and partitions were discretized using planar elements with 4 nodes with an edge size of 250 mm. The average number of 1D finite elements on bar members was 10. The total number of elements was 11,077, of which 7,738 were planar elements. Linearly elastic characteristics of the used materials - masonry and wood - were considered. The modulus of elasticity of the masonry considered was 3.1 GPa and Poisson's ratio 0.2. The mechanical characteristics of wood were kept according to the default settings of the computer programme.

Figure 5 displays the computational model and the first mode shape of the structure. The first mode shape corresponds to the theoretically identified first natural frequency of 4.29 Hz. The largest theoretical deformations are located in the eastern gable and correspond to the most extensive damage found on the site. The calculated values of deformations in the places of failures exceed the deformation values for the formation of tensile cracks in the masonry.

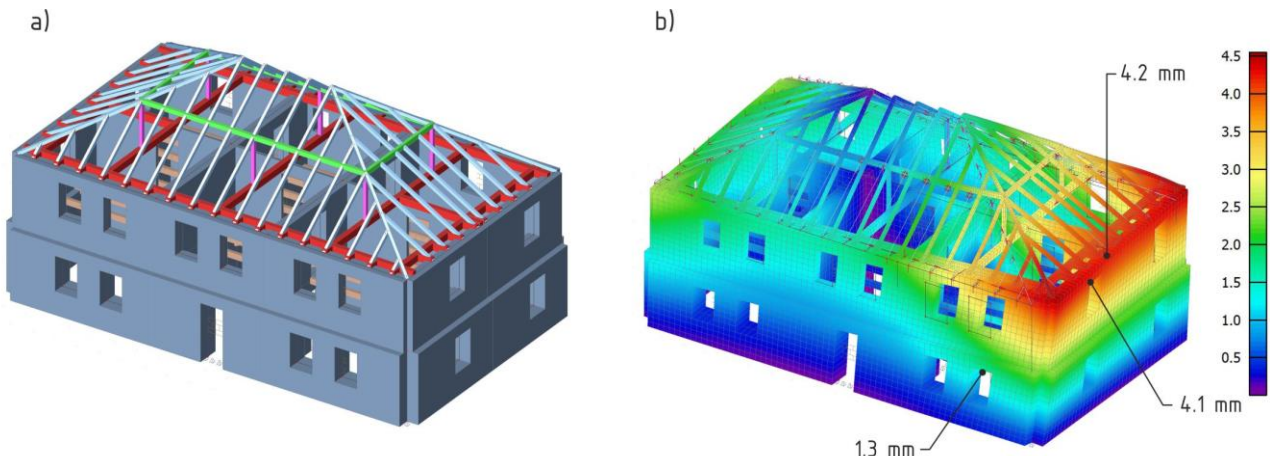


Fig. 5 - a) computational model of the building, b) building's first mode shape

Analysis of the results of a building technical survey and numerical analysis

Due to the type of cracks, we may assume that the change in physical and mechanical properties of the masonry or its components caused by rising damp is not the main cause of cracking. Likewise, the temperature differences in individual structures have a minimal effect on the formation and development of cracks due to their occurrence. The occurrence of cracks in the connections of individual structures indicates their insufficient bonding. The type of structure and its missing adequate reinforcement (at least at the ceiling level) against horizontal loading effects also allow further development and propagation of cracks.

The first mode shape of the structure identified on the basis of numerical analysis and associated deformations confirm the assumption of seismic loading as a possible cause of failure of the masonry structure.

Based on the analysis of the information and findings obtained during the evaluation of the preliminary building technical survey, we may assume that the cause of the occurrence and development of cracks are the effects caused by seismic loads.

DESIGN OF REHABILITATION MEASURES

Due to the probable cause of the occurrence and development of failures in the building and the type of structure (masonry structure of stone and mixed masonry without reinforcing elements or with non-functional reinforcing elements), the most appropriate rehabilitation method is to increase the stiffness of the structure by its additional bracing and prestressing by means of steel ties and prestressing cables, or by carbon fibre-based lamellas. The cracks must be grouted or filled before prestressing the structure. The bracing and prestressing of masonry structures is an effective and reliable protective measure for damaged masonry structures.

A reliable function of beam ties and tie rods, their immediate (not delayed) effectiveness is the most reliable prevention of the appearance or continuing development of tensile and shear cracks in masonry. By using prestressing ropes, cables and lamellas, higher values of masonry prestressing can be achieved compared to steel tie rods. Before mounting tie rods or cables, ropes and lamellas and designing prestressing forces, the stresses in the masonry must be assessed in terms of the prestressing method and the position of e.g. prestressing cables in relation to the prestressed masonry core and the spatial stiffness of the structure (masonry stresses in the direction of masonry bed joints), and it must be ensured that the additional pushing of anchor plates does not cause a significant decrease in the prestressing force and thus a reduction in the masonry prestressing effectiveness. Before grouting the grooves and anchors, it is necessary to check the stability (to avoid a decrease) of the prestressing force in the cables and tie rods.

Additional reinforcement of historic masonry buildings currently mostly applies the bracing of masonry with steel tie rods of circular cross-sections, strip steel, or prestressing patent wires inserted in grooves up to 150 mm deep arranged in both directions of the building (Figure 6). Another solution is an effective and controlled activation of the existing wall or beam ties, tie rods and load distribution anchor plates (e.g. by additional activation of the beam tie attached to the rehabilitated joists).

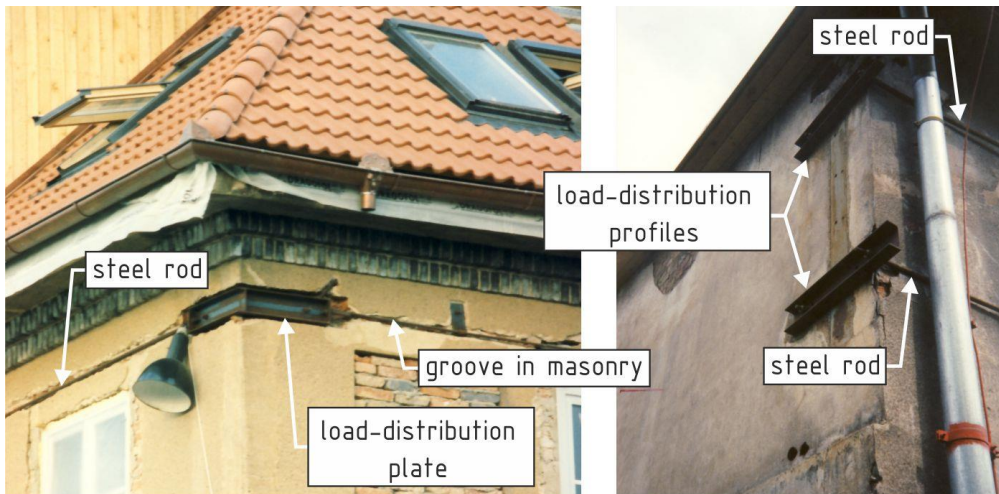


Fig. 6 - a) Bracing walls with circular steel sections, b) temporary bracing of masonry [10]

In some cases, a newly executed bond beam of reinforced concrete or prestressed concrete may serve as "passive" static protection (stiffening) (e.g. during a complex roof truss replacement, extension of a building, etc.).

Rehabilitation with CFRP lamellas

Damaged masonry buildings with insufficiently functioning tie rods and beam ties, or with the absence of wall and beam ties in some historic buildings can be reinforced with lamellas based on carbon or aramid fibres fitted in their end parts with special metal anchoring elements enabling the activation or pre-tensioning of the lamellas to the required force. Steel load distribution plates or special prestressing devices must be mounted in the anchoring parts of the lamellas and the masonry must be reinforced (Figure 7) [11, 12].

A lamella based on carbon or aramid fibres can be attached in a special metal anchor sleeve of enclosed shape with a wedge-shaped hole for passing the lamella through it, which allows its anchoring by metal wedge-shaped plates with a special surface treatment on both sides – a roughened surface at the contact with the lamella and grooves at the contact with the enclosed anchor sleeve similarly provided with grooves enabling reliable clamping of the lamella and preventing its slipping (slacking). The lamella-metal anchor plates contact surfaces should be treated with epoxy resin before adjustment. The lamellas can be prestressed by means of prestressing (spacer) screws fastened to the sleeves using so-called "torque" wrenches.

Lamellas (beam ties) can pass along wooden floor beams or steel floor joists, or on the upper surface of subfloor planks, and must be secured in position by clips at a 1.5 - 2 m spacing. Depending on specific conditions and in accordance with the requirements for fire resistance or protection against mechanical failure, the lamellas based on carbon or aramid fibres can be protected by special fire-resistant cover strips, fire-retardant coatings, etc. In this modification, the prestressing by a lamella is imposed into the structure by a "solitary" force acting on both ends of the lamella in the place of the anchor sleeve and the load distribution plate. Securing the required effectiveness of prestressing cables, prestressing steel tie rods and carbon lamellas requires that

prestressing should be applied to the existing masonry structure along the entire length of the prestressing tie rod, lamella, etc. (Figure 8). In cases where a prestressed lamella, fixed by the prestressing device and laid in a shallow groove is coated with structurally effective plaster, adhesive sealant, an adhesive layer, etc. and the prestressing device is only released after the required strength of this "covering and fixing" layer has been reached, the prestressing force can be applied along the entire length of the lamella (Figure 8). This solution usually removes extreme stresses in the place of prestressing devices and anchor plates [10].

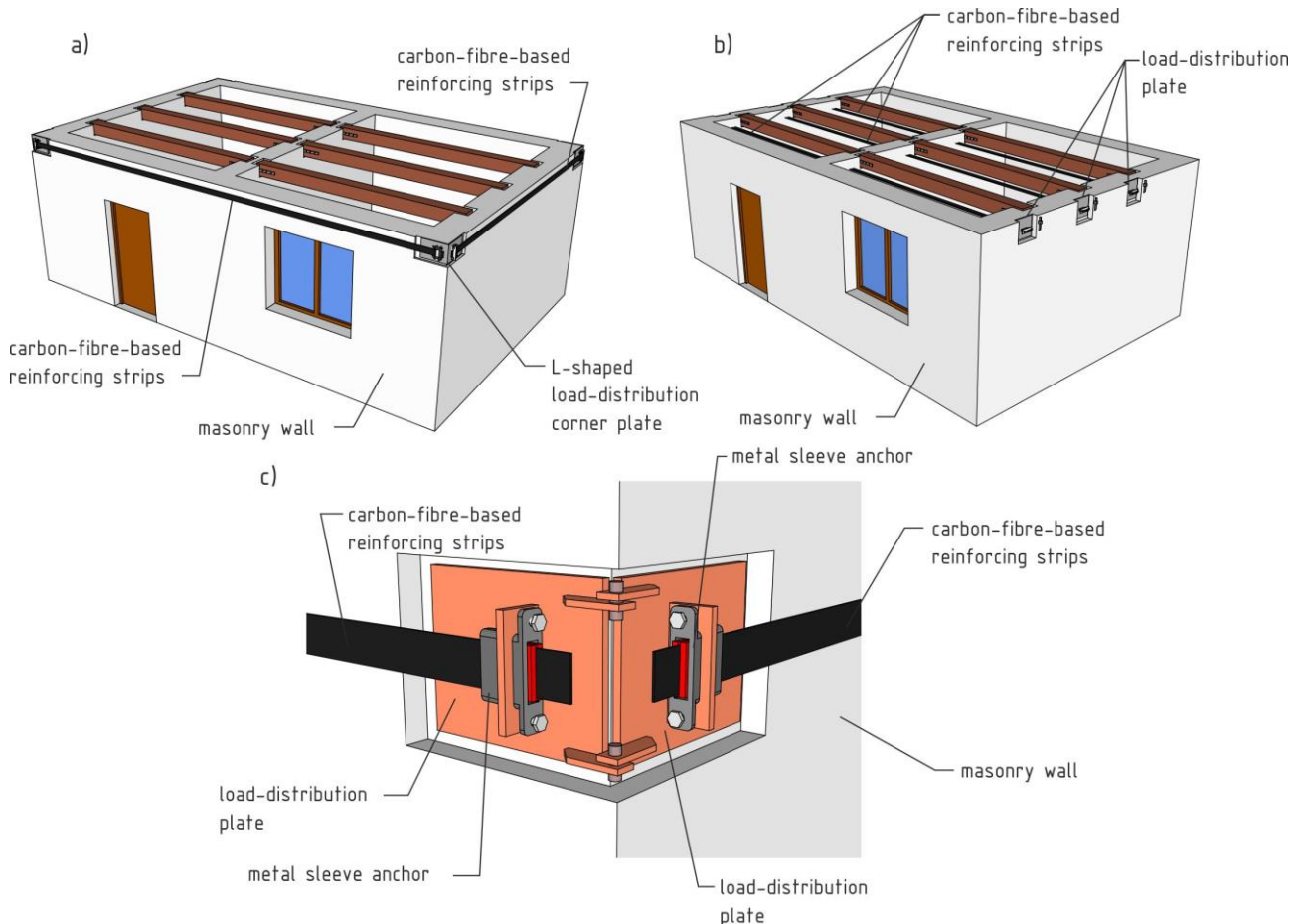


Fig. 7 - Reinforcement of damaged masonry buildings with insufficiently functioning tie rods and beam ties or with their absence by means of lamellas based on carbon or aramid fibres

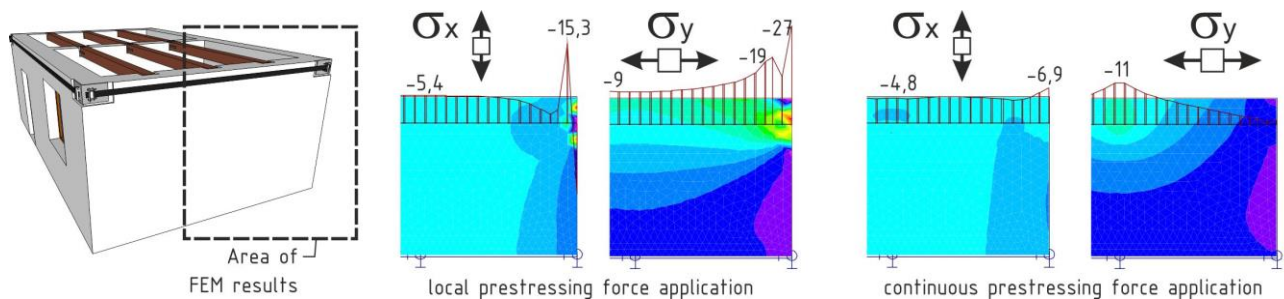


Fig. 8 - Stresses in masonry in the end area of prestressing members

The magnitude of prestressing forces must be identified by a structural calculation in accordance with the time pattern and magnitude of horizontal normal stresses and shear stresses and the condition of masonry.

Special attention must be paid to the treatment of masonry and surfaces in the places of anchor plates (corrosion protection, damaged integrity of surface treatment, effects of moisture and temperature near the anchors, etc.).

Lamellas 60 - 100 mm wide and 2 to 4 mm thick fitted with special anchoring and prestressing elements can be applied directly onto undamaged, treated and ground masonry to create a smooth surface without protrusions. In the case of masonry with damaged surface layers, after removing the damaged and incohesive parts of the masonry, the lamellas are applied onto the masonry surface levelled with a thin layer of polymer modified cement or lime-cement mortar, or onto the treated surface of damaged masonry after its previous grouting and the repair (sealing) of cracks using a similar method as in the case of steel cables and tie rods. Depending on the depth of the lamella sinking in the masonry, the stresses and stability of the wall must be assessed taking into account the masonry thickness, prestressed lamella position, distance of the walls laid out perpendicular to the prestressed wall, the prestressing force magnitude and, as a rule, the large eccentricity of prestressing forces. Also, the perimeter wall must be stabilized against buckling by transverse walls or struts (e.g. pipes into which transverse expansion lamellas – collets are inserted). Proper remediation requires the wall to be braced so that the resultant bracing force passes through the core of the cross-section, i.e. the tie must be placed at the outer and inner face of the wall. For small prestressing forces (small forces caused by the effects of seismicity), it is possible to place prestressing elements only at one wall surface.

The anchoring areas of prestressed reinforcing lamellas must be fitted with metal load distribution plates, mounted on the reinforced masonry, modified for mounting the anchoring metal elements at the ends of reinforcing lamellas.

In cases of active prestressing of lamellas to higher tensile force values, the building must be prestressed around the perimeter by means of lamellas anchored in "L"-shaped corner metal load distribution plates located in the corners of the building at one height level. The prestressing must be performed gradually by alternately applying the prestressing force in both directions (see Figure 7).

Depending on specific conditions and in accordance with the requirements of fire resistance or protection against mechanical failure, the lamellas based on carbon or aramid fibres can be protected by special cover strips made for this purpose, fire protection coatings, plaster or they can be laid in a groove filled with a polymer modified cement screed applied after the mounting of lamellas.

Another possibility of horizontal reinforcement of e.g. perimeter masonry is the stiffening (strengthening) of masonry by means of lamellas based on carbon fibres 40 - 100 mm wide, inserted in a widened groove in the bed joint, or in a groove cut outside the bed joint (in irregular masonry without a continuous bed joint) deeper by min. 20 to 40 mm than the width of the reinforcing lamella. After cutting and cleaning, the horizontal groove is filled with a special mixture based on polymer modified cement with an adequate consistency to enable pushing the lamella into the joint. In another case, the lamella can be inserted into an open joint, and subsequently, after the joint is sealed and the lamella prestressed, the joint is injected (sealed) with a polymer modified cement mixture.

Reinforcing lamellas can be installed in any place depending on the structural requirements, the occurrence of cracks and the extent of damage (e.g. in every 3rd bed joint, in thirds of the masonry height, etc.).

The advantage of the proposed masonry reinforcement, in addition to the variability of the distribution of lamellas along the height of the masonry (building), is mainly limited disturbance of the historic masonry, preservation of the original appearance and dimensions of the masonry structure – after the installation of reinforcing carbon lamellas into the bed joints or horizontal grooves and the mounting of metal anchoring elements, the masonry can be coated with plaster in the original thickness, quality and composition (does not require the execution of demanding covering layers).

Rehabilitation of the rectory building with lamellas based on carbon or aramid fibres

A numerical analysis of reinforcing (prestressing) of the building using lamellas based on carbon or aramid fibres is performed as a part of building's rehabilitation design. The reinforcing was introduced into the computational model of the building in two steps. In the first step, the reinforcing of perimeter walls at the level of the ceiling of the 1st and 2nd floors and reinforcing of the building's corners were modelled. Figure 9a shows the first mode shape of the building with reinforcement. The maximal values of deformation decreased to 70 % of the values of deformation of the building without prestressing (see Figure 5). The calculated first natural frequency increased to 5.12 Hz. In the second step, in addition to the reinforcing of perimeter walls, the reinforcing of inner walls was introduced. The character of the first mode shape has slightly changed and the largest values of calculated deformations also occur on the opposite side of the building (Figure 9b). The maximal value of deformation reaches approximately 60 % of the deformation of the building without prestressing and it decreased by 15 % in comparison with the value of deformation for reinforcing only of the perimeter walls. The theoretically determined first natural frequency of the building with reinforcing of perimeter and inner walls was 6.22 Hz. The numerical analysis confirmed the positive effect of prestressing on increasing the rigidity of the building.

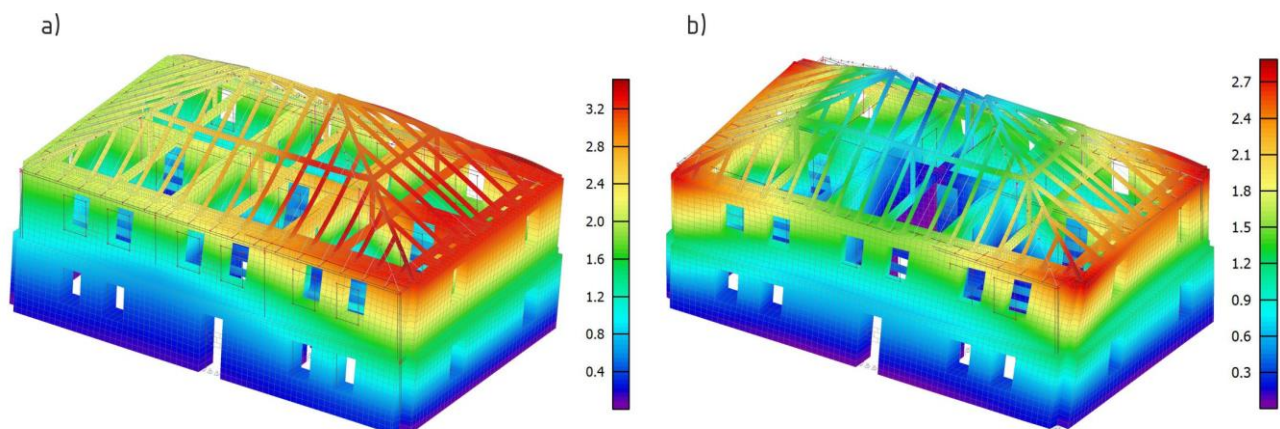


Fig. 9 - Building's first mode shapes: reinforcing of perimeter walls (a), reinforcing of perimeter and inner walls (b)

The proposed rehabilitation method - increasing the stiffness of a two-storey historic rectory building in Luby damaged by the effects of natural seismicity - with the use of lamellas based on carbon, or aramid fibres is displayed in Figure 10.

The rehabilitation method respects the results of executed numerical analysis. Additional reinforcing prestressing elements are designed at the level of the ceilings of 1st and 2nd floor in the perimeter walls and inner load-bearing walls. Due to the absence of beam anchors, the reinforcing system is extended by the reinforcement of wooden beam ceilings in places of missing or non-functional anchors using lamellas based on carbon or aramid fibres and resins. The use of prestressing elements was verified in a performed numerical analysis.

The diagram shows the position of prestressing lamellas, the location of anchoring and load distribution elements. The position of individual elements of the additionally executed reinforcing system of the masonry structure is chosen so as to minimize the interference with the historic structure, but, at the same time, maximize its stiffness gain.

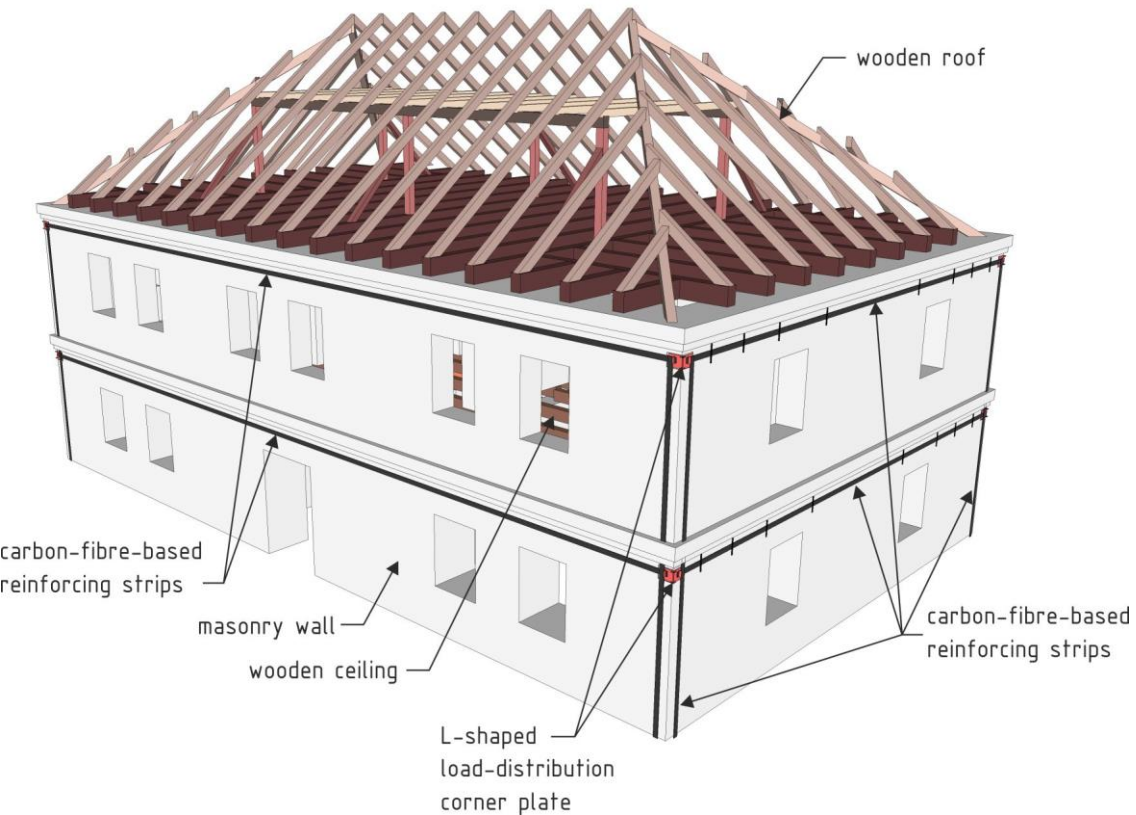


Fig. 10 – Scheme of the rectory building with a marked layout of FRP lamellas and steel anchoring and load distribution sections

SUMMARY

The preliminary building technical survey, the analysis of its results and the numerical analysis allowed identifying the most likely cause of damage to the historic rectory building in Luby near Cheb. The results obtained during the previous research within the NAKI research project were used in the conceptual design of the rehabilitation of a historic building damaged by the effects of natural seismicity consisting in increasing the building's stiffness. Compared to the reinforcement of the structure with steel prestressing elements, the properties of the used prestressing elements enable reducing the negative impacts of the designed rehabilitation method on the historic structure.

ACKNOWLEDGEMENTS

The article was written with support from the NAKI DG16P02M055 project "Development and Research into Materials, Procedures and Technologies for Restoration, Conservation and Strengthening of Historic Masonry Structures and Surfaces and Systems of Preventive Care of Historic and Heritage Buildings Threatened by Anthropogenic and Natural Risks".

REFERENCES

- [1] Schenk, V. and Schenková, Z.: Maps of Seismic Zones in Recent Czech National Codes. Exploration Geophysics, Remote Sensing and Environment, IV.2/97, ČAAG-Praha, 9-11, 1997
- [2] Monument – databáze památek NPU, <http://monumnet.npu.cz>
- [3] Geofyzikální ústav Akademie věd České republiky, Seismické oddělení

- [4] Celep, Z., Icncecek, M., Pakdamar, F.: Structural and earthquake response analysis of the Muradiye mosque, 14 WCEE, Beijing, China Conference: Proceedings of the 14th World Conference on Earthquake Engineering, 12.-17.10.2008,
- [5] Borri, A., Corradi, M., Vignoli, A.: New materials for strengthening and seismic upgrading interventions, International Workshop Ariadne 10, Arcchip, Prague, Czech Republic; 04/2002
- [6] Ravikumar, C.S., Thandavamoorthy, T.S.: Application of FRP for strengthening and Retrofitting of civil engineering structures, International Journal of Civil Structural, Environmental and infrastructure Engineering, Research and Development (IJCSEIERD), ISSN (P) 2249-6866, ISSN (E) 2249-7978, vol. 4, Issue 1, feb. 2014, p. 49 – 60
- [7] Makovička, D., Makovička, D. jr.: Response Analysis and Vibroinsulation of Buildings Subject to Technical Seismicity, In: Earthquake Resistant Engineering Structures VII. Southampton: WIT Press, 2009, pp. 197-205. ISSN 1746-4498. ISBN 978-1-84564-180-1
- [8] Elghazouli, A. (Ed.). Seismic Design of Buildings to Eurocode 8. 2009. London: CRC Press
- [9] Lorant, G., Seismic Design Principles, dostupné z: <https://www.wbdg.org/resources/seismic-design-principles> [citováno 2018-03-21].
- [10] Witzany, J. a kol., Obnova rekonstrukce staveb. Poruchy, degradace, sanace, Praha: CTU. Czech Technical University Publishing House, 2018. ISBN 978-80-01-06360-6.
- [11] Witzany, J. Zigler, R., Předpínací kotva pro zpevnění nosného zdíva, Czech Republic. Utility Model CZ 31090. 2017 (in Czech)
- [12] Witzany J., Čejka T and Zigler R.. Stiffener for bracing of masonry buildings particularly historical. Utility design, Úřad průmyslového vlastnictví, 23023. 2011 (in Czech)

ESTIMATION OF DISPLACEMENT CAPACITY OF RECTANGULAR RC SHEAR WALLS USING EXPERIMENTAL AND ANALYTICAL DATABASE

Florin Pavel¹, Petru Panfilii¹, Ehsan Noroozinejad Farsangi^{2*}

1. Technical University of Civil Engineering Bucharest, Bd. Lacul Tei, 122-124, Sector 2, Bucharest, Romania;
2. Faculty of Civil and Surveying Engineering, Graduate University of Advanced Technology, Kerman, Iran; email: noroozinejad@kgut.ac.ir (*Corresponding)

ABSTRACT

This study is focused on the evaluation of the displacement capacity of RC shear walls using both experimental and analytical results. The first observation of the study is that few experimental results for slender RC shear walls having thicknesses larger than 150 mm are available in the literature. From the experimental database, it was observed that the mean and the median ultimate drift of squat RC shear walls is about half of that obtained for slender RC shear walls. Considering the limitation of the experimental database, the simple empirical model for the ultimate drift ratio of slender RC shear walls proposed in this study is also based on available analytical results from the literature. The model provides a good fit with the observed results and besides, due to the fact that it does not require sectional analysis of the element, it allows a rapid assessment of the displacement capacity of slender RC shear walls as a function of the seismic design code parameters. The proposed formula can be inserted in future revisions of the seismic assessment guidelines for RC structures for rapid seismic evaluation purposes.

KEYWORDS

Regression analysis; Correlation coefficient; Experimental database; Numerical modelling; RC shear wall; Displacement capacity

INTRODUCTION

The assessment of the strength and displacement capacity of structural elements is a key step in the seismic performance assessment of structures. Among the structural elements used for earthquake resistant structures, the shear walls are commonly used in regions of medium and high seismicity for medium and high-rise structures. The ultimate displacement capacity of structural elements is a key part in the assessment of the seismic performance which is, at its turn, a key part of the seismic risk assessment.

Eurocode 8-3 proposes two different models for the evaluation of the ultimate rotation capacity of beams, columns, and shear walls. However, the two relations proposed in Eurocode 8-3 require data obtained from sectional analysis which requires a significant amount of computation time [1]. The strength, deformation, and failure modes of RC shear walls under cyclic loading are also analysed in the paper of Grammatikou et al. in which updated models similar to the ones in Eurocode 8-3 are also proposed [2]. The cyclic shear and displacement capacity of squat or slender RC shear walls are analysed in a number of papers in the literature [3-14]. In the paper of Wallace, the observed seismic behaviour of shear walls structures during the Chile and New Zealand earthquakes is discussed. Based on the seismic performance of code-compliant thin RC shear walls, several changes were recommended by [15]. The seismic behaviour of a RC shear-wall building that



collapsed during the 2003 Bingöl earthquake was investigated by nonlinear static analysis and nonlinear dynamic analysis in the study of Çavdar et al. [16]. The study of Ugalde and Lopez-Garcia notes that only 2% of the residential building inventory consisting mainly of RC shear walls structures suffered significant damage as a result of the Maule 2010 earthquake [17]. The study of Pavel and Vacareanu discusses the seismic performance of RC shear walls structures during the Vrancea earthquake of March 1977 and analyses the seismic performance of a building similar with one that collapsed in 1977 [18]. Segura and Wallace [19] and Abdullah and Wallace [20] have also proposed relations for the computation of the drift capacity of reinforced concrete structural walls based on experimental data. Shegay et al. have developed a relation for the computation of the curvature ductility of structural walls [21]. Cando et al. have analysed the effect of the stiffness on the seismic performance of residential shear wall buildings designed according to current Chilean regulation [22]. The study of Arteta et al. [23] has shown that ductile behaviour of thin boundary elements of special structural walls under pure compression is not achievable by only complying with the detailing provisions given in ACI 318-08 [24]. The study of Marzok et al. analysed the results in terms of displacements and bending moment capacities for RC shear walls given by various commonly-used codes [25]. The displacement capacity of unreinforced masonry or confined masonry shear walls has been analysed by [26-29].

A critical aspect related to the cyclic seismic behaviour of rectangular RC shear walls is the occurrence of significant out-of-plane displacement and which can induce a significant reduction of the deformation capacity. This aspect is discussed in the studies of [30-33]. These studies show that the onset of buckling instability occurs earlier in the case of boundary elements of higher longitudinal reinforcement ratios. Moreover, it was observed that the maximum tensile strain corresponding to initiation of out-of-plane deformation and out-of-plane instability was lower in squat wall models when compared to the slender ones.

Thus, in this paper, we analyse the ultimate drift ratio of slender RC shear walls using an experimental database, and besides, using analytical results from the study of Pavel [34]. As previously mentioned, the use of analytical results is due to the scarcity of experimental results of RC shear walls having thicknesses larger than 150 mm. The limited numbers of such tests are also confirmed by the test data collected by Abdullah [35]. In addition, a simple empirical model for evaluating the ultimate drift ratio of slender RC shear walls is also proposed in this study using both experimental and analytical results. The model is recommended to be used for rapid seismic assessments.

EXPERIMENTAL DATABASE

The first database used in this study is the experimental one developed by Zhou et al. which consists of 226 tests on rectangular RC shear walls [36]. The database contains test results for both squat (ratio between the wall height and its length $H_w/l_w < 2$) and slender ($H_w/l_w \geq 2$) RC shear walls. It is true that the database compiled by Abdullah contains a much larger number of experimental results, however, the database is not public and the authors did not have access to the test results [35].

The experimental results have the following characteristics:

- concrete strength (f_c): 12.3 – 63.4 MPa;
- section length (l_w): 0.15 – 5.50 m;
- height of the wall (H_w): 0.42 – 3.96 m;
- thickness of the wall (t_w): 20 – 160 mm;
- axial load ratio (ALR): 0 – 0.25;
- H_w/l_w : 0.35 – 5.86;
- l_w/t_w : 5.31 – 57;
- web horizontal reinforcement ratio ρ_{wh} : 0 – 0.037;
- web vertical reinforcement ratio ρ_{wv} : 0 – 0.037;
- boundary element horizontal reinforcement ratio: ρ_{bh} : 0 – 0.021;



- boundary element vertical reinforcement ratio: ρ_{bv} : 0.005 – 0.099.

The ultimate drift ratios obtained experimentally for squat and slender RC shear walls are compared in Figure 1. The statistical indicators of the ultimate drift ratios for the two types of RC shear walls are reported in Table 1. It can be easily observed that the mean and median ultimate drift of squat RC shear walls is about half of that obtained for slender elements. The limited number of experimental results for RC slender shear walls can also be observed from Figure 1.

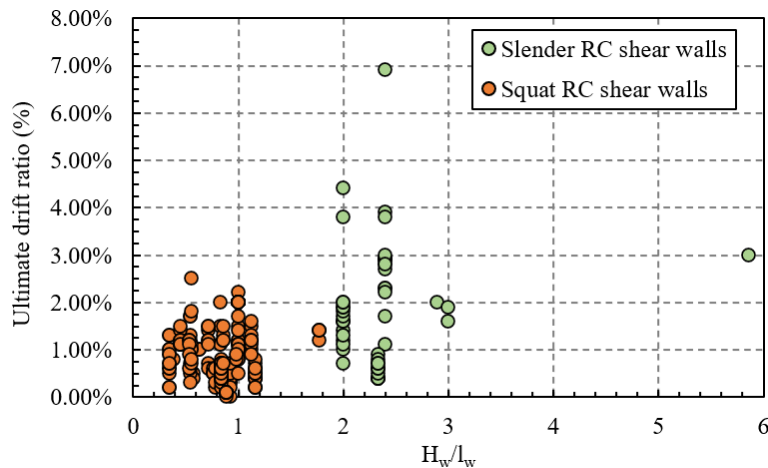


Fig. 1 – Comparison of the ultimate drift ratios obtained experimentally for slender and squat RC shear walls

Tab. 1: Statistical indicators of the experimental ultimate drift ratio for squat and slender RC shear walls

Statistical indicator of the experimental ultimate drift ratio	Squat RC shear walls	Slender RC shear walls
Mean value	0.009	0.019
Median value	0.007	0.017
Standard deviation	0.005	0.013
Skewness	0.673	1.430
Kurtosis	-0.046	3.568
5 th percentile	0.001	0.004

Subsequently, a correlation analysis between the experimental ultimate drift ratios for squat and slender RC shear walls and some of the characteristics of the database shown previously is performed. The results of the correlation analysis are shown in Table 2. The largest correlation coefficient is observed between the ultimate drift of slender RC shear walls and the thickness of the web. It can be observed from Figure 2 that, as the thickness of the web increases so does the ultimate drift. The limited number of experimental results for RC shear walls with thicknesses in excess of 100 mm is noteworthy.



Tab. 2: Correlation coefficient between the experimental ultimate drift ratio for squat and slender RC shear walls and the characteristics of the test characteristics

Statistical indicator of the experimental ultimate drift ratio	Squat RC shear walls	Slender RC shear walls
concrete strength (f_c)	-0.21	0.28
section length (l_w);	0.43	0.62
height of the wall (H_w)	0.56	0.62
thickness of the wall (t_w)	0.60	0.71
axial load ratio (ALR)	0.31	-0.11
h_w/l_w	0.04	0.15
h_w/t_w	-0.19	-0.13
web horizontal reinforcement ratio (ρ_{wh})	0.09	0.30
web vertical reinforcement ratio (ρ_{wv})	0.10	-0.19
boundary element horizontal reinforcement ratio (ρ_{bh})	0.46	0.66
boundary element vertical reinforcement ratio (ρ_{bv})	-0.11	0.15
yield strength of the web horizontal reinforcement ($f_{y,wh}$)	0.56	0.14
yield strength of the web vertical reinforcement ($f_{y,wv}$)	0.53	0.19
yield strength of the boundary element horizontal reinforcement ($f_{y,bh}$)	0.39	0.40
yield strength of the boundary element vertical reinforcement ($f_{y,bv}$)	0.28	0.44

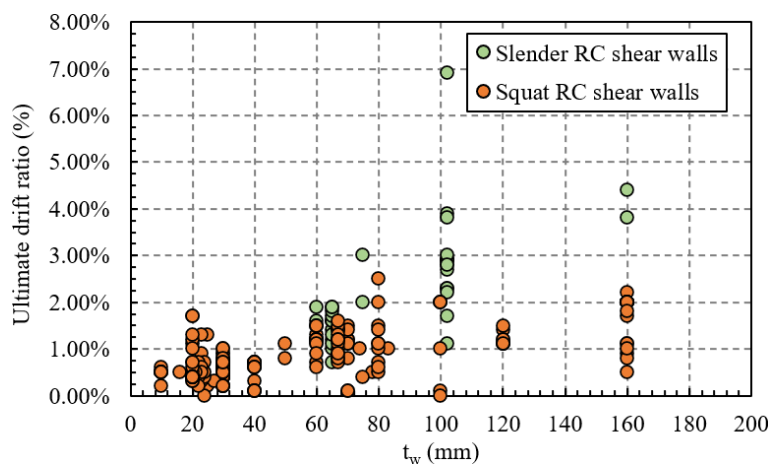


Fig. 2 – Variation of the ultimate drift ratio as a function of the thickness of the RC shear walls

Figure 3 shows a comparison between the empirical and the normal CDF (cumulative distribution function) for the experimental ultimate drift ratio of slender RC shear walls. One can notice that the normal CDF provides a good fit of the experimental results. The adequacy of the fit is confirmed by statistical testing (Kolmogorov-Smirnov, Anderson-Darling and Chi-squared) performed on the sample. The null hypothesis is not rejected for any significance level α ranging between 0.01 and 0.20. The lognormality assumption is accepted for all significance when using the Kolmogorov-Smirnov and Anderson-Darling statistical tests and is rejected for three significance levels (out of five) when employing the Chi-squared statistical test.

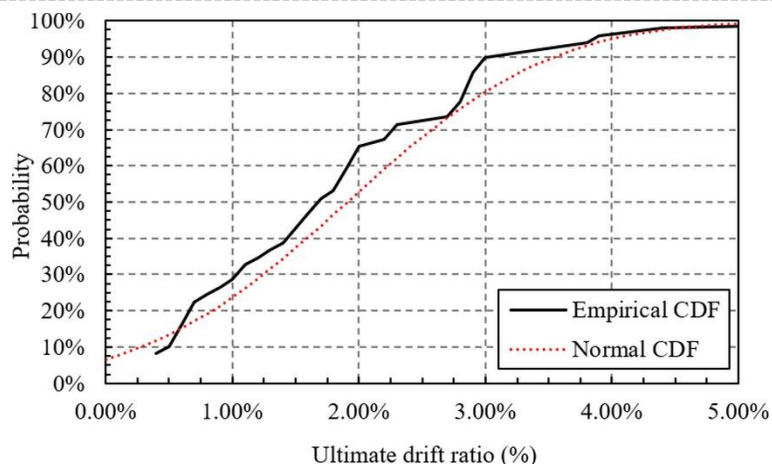


Fig. 3 – Comparison of the empirical and normal CDF for the experimental ultimate drift ratio of slender RC shear walls

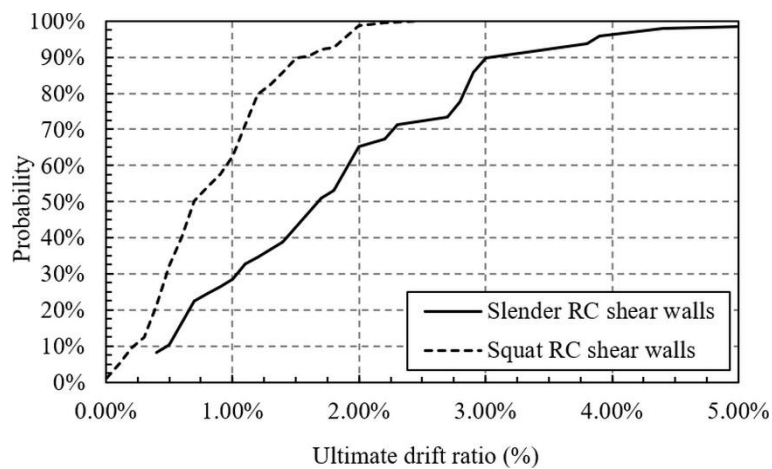


Fig. 4 – Comparison between the CDFs for the experimental ultimate drift ratio of slender and squat RC shear walls

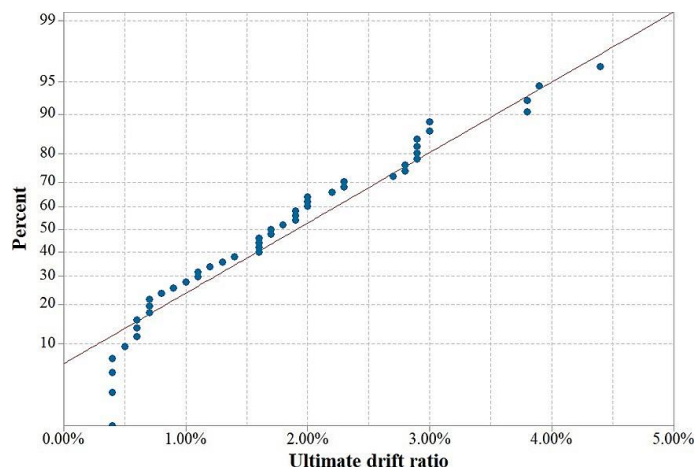


Fig. 5 – Normality test check for the experimental ultimate drift ratio of slender RC shear walls

The CDFs in terms of the experimental ultimate drift ratio for the squat and slender RC shear walls are compared in Figure 4. One can notice the much larger ultimate drift ratios of slender RC shear walls. The normality assumption is further checked in Figure 5 using a normal probability plot. The distribution can be regarded as normal starting from an ultimate drift ratio of about 0.7%.

ANALYTICAL DATABASE

Due to the scarcity of available date for slender RC shear walls having thicknesses larger than 150 mm, as observed from the experimental database compiled by Abdullah, we decided to employ in this study a second database [35]. The second database used in this study is the analytical one developed by Pavel [34] which comprises 81 cyclic analyses of rectangular RC shear walls performed using the code VecTor4 [37]. The shear walls were designed according to the current seismic design regulations from Romania. All the shear walls analysed in this study are slender with the ratio $H_w/l_w \geq 2$. The analytical database of Pavel [34] has the following characteristics:

- concrete strength (f_c): 30 MPa, 40 MPa, 50 MPa;
- section length (l_w): 3.60 m, 4.50 m, 5.40 m;
- height of the wall (h_w): 12.5 m, 13.8 m, 18.8 m;
- thickness of the wall (t_w): 0.25 m, 0.30 m, 0.35 m;
- axial load ratio (ALR): 0.02 – 0.08;
- H_w/l_w : 3.07, 3.47, 3.48;
- l_w/t_w : 14.4, 15.0, 15.42;
- web horizontal reinforcement ratio ρ_{wh} : 0.006 – 0.010;
- web vertical reinforcement ratio ρ_{wv} : 0.004 – 0.007
- boundary element horizontal reinforcement ratio: ρ_{bh} : 0 – 0.0201;
- boundary element vertical reinforcement ratio: ρ_{bv} : 0.007 – 0.008.

The ultimate drift ratios obtained analytically in the study of Pavel [34] are illustrated in Figure 6. It is noticeable from Figure 5 that the analytical results have a much smaller spread as compared to the experimental ones. The statistical indicators of the ultimate drift ratios for the analytical RC slender shear walls are reported in Table 3. It can also be observed that only the mean and median analytical ultimate drifts are close to the statistical indicators obtained from experimental results.

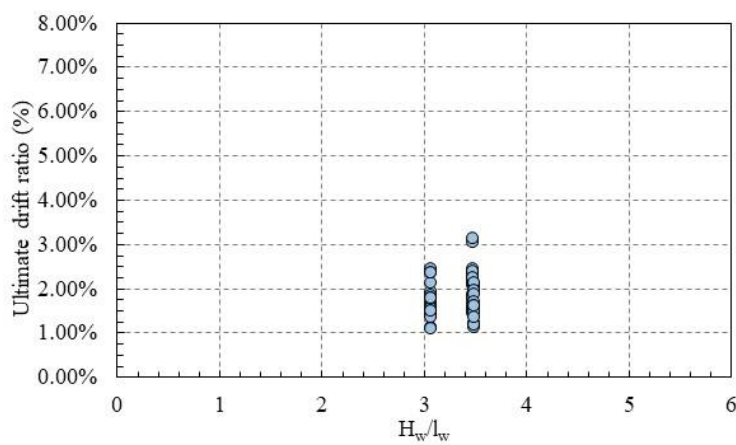


Fig. 6 – Ultimate drift ratios obtained analytically for slender RC shear walls [34]



Tab. 3: Statistical indicators of the analytical ultimate drift ratio for slender RC shear walls [34]

Statistical indicator of the experimental ultimate drift ratio	Slender RC shear walls
Mean value	0.018
Median value	0.017
Standard deviation	0.004
Skewness	0.754
Kurtosis	0.741
5 th percentile	0.012

The correlation analysis between the analytical ultimate drift ratios for slender RC shear walls and some of the characteristics of the database shown previously is performed. The results of the correlation analysis are shown in Table 4. The yield strength for both horizontal and vertical reinforcement in the web and in the boundary elements for all the shear walls analysed in the study of Pavel [34] is 550 MPa. Thus, these parameters are disregarded from the correlation analysis shown in table 4. It can be observed that the correlation coefficient between the analytic ultimate drift ratio and the first four parameters in Table 4 are negative, which is exactly the opposite to what can be observed from Table 2.

Tab. 4: Correlation coefficient between the analytic ultimate drift ratio for squat and slender RC shear walls and the characteristics of the analytical models [34]

Statistical indicator of the experimental ultimate drift ratio	Slender RC shear walls
concrete strength (f_c)	-0.09
section length (l_w);	-0.33
height of the wall (H_w)	-0.22
thickness of the wall (t_w)	-0.33
axial load ratio (ALR)	-0.45
h_w/l_w	0.27
h_w/t_w	-0.36
web horizontal reinforcement ratio	0.25
web vertical reinforcement ratio	-0.12
boundary element horizontal reinforcement ratio	-0.31
boundary element vertical reinforcement ratio	0.04

Figure 7 shows a comparison between the empirical and the normal CDF for the empirical ultimate drift ratio of slender RC shear walls. In this case, too, it can be observed that the normal CDF provides a good fit of the experimental results. The normality assumption of the analytic ultimate drift ratio is further checked in Figure 8 using a normal probability plot. The distribution can be regarded as normal starting from an ultimate drift ratio of about 1.2%. The adequacy of the fit is evaluated by statistical testing (Kolmogorov-Smirnov, Anderson-Darling, and Chi-squared) performed on the sample. The Kolmogorov-Smirnov and Anderson-Darling statistical tests confirm the hypotheses for all significance levels, while in the case of the Chi-squared statistical test, the hypothesis is rejected. As in the case of the normality assumption test, the lognormality assumption is accepted for all significance when using the Kolmogorov-Smirnov and Anderson-Darling statistical tests and is rejected for all significance levels when employing the Chi-squared statistical test.



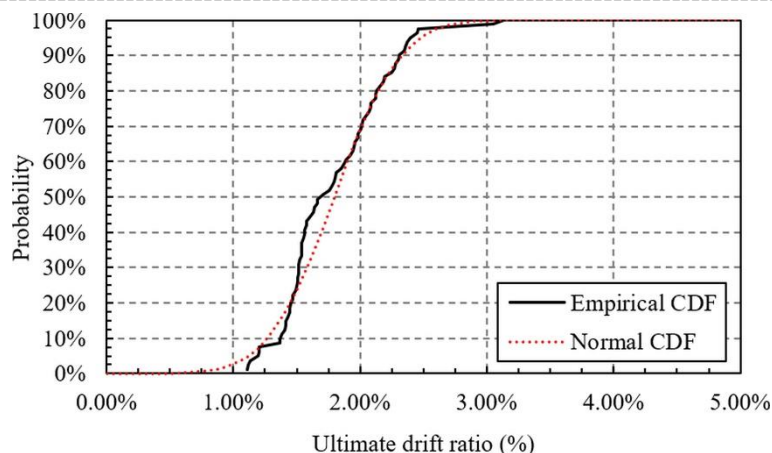


Fig. 7 – Comparison of the empirical and normal CDF for the analytical ultimate drift ratio of slender RC shear walls

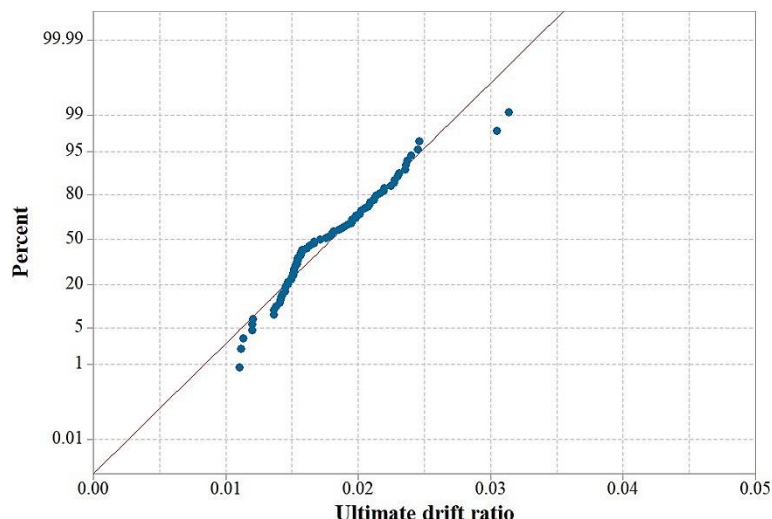


Fig. 8 – Normality test check for the analytic ultimate drift ratio

AN EMPIRICAL MODEL FOR THE ULTIMATE DRIFT RATIO

Subsequently, an empirical model for the displacement capacity of RC slender shear walls is obtained by combining the experimental and analytical results. Unlike models given in Eurocode 8-3 [1] or by Segura and Wallace [19] or Abdullah and Wallace [20], the model proposed in this study uses a much smaller number of input parameters and is readily available to any designer. In addition, the parameters of the proposed empirical model do not require any sectional analysis of the reinforced concrete structural wall, as necessary in the above-mentioned empirical models. Moreover, this model, unlike other models available in the literature also provides uncertainty in evaluating the median drift capacity. The empirical model obtained from the least-squares regression for the ultimate drift ratio (Y) has the following functional form:

$$\log Y = -1.537 - 1.719 \cdot ALR - 0.026 \frac{H_w}{l_w} - 0.023 \frac{l_w}{t_w} + 5.08 \cdot \rho_{wh} + 35.14 \cdot \rho_{bh} \quad (1)$$

The standard error of the estimate obtained from regression analysis is 0.136. The comparison between the observed and predicted values is illustrated in Figure 9. The mean ratio between the observed and the predicted values is 1.05, while the median value is 0.98, the standard



deviation is 0.38 and the correlation coefficient is 0.63. The empirical model proposed in this study employs directly the ALR as a parameter, while the model proposed by Abdullah and Wallace [20] uses the ALR indirectly through the neutral axis depth parameter. Netrattana et al. [11] state that the ALR is the most influential parameter for the displacement capacity of RC shear walls.

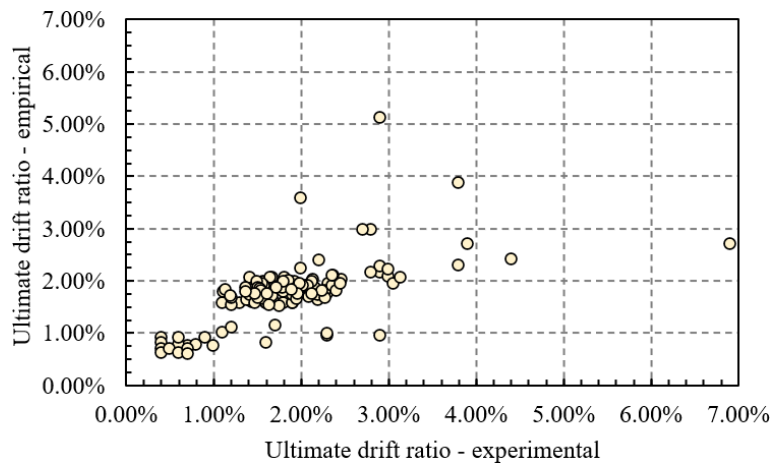


Fig. 9 – Comparison between experimental and empirical ultimate drift ratios of slender RC shear walls

The histogram of residuals (the difference between the observed and the predicted values) is illustrated in Figure 10. In addition, the normal distribution computed for the mean and standard deviation of the residuals is superimposed on the histogram shown in Figure 9. It is visible the fact that the distribution of the residuals follows a normal distribution.

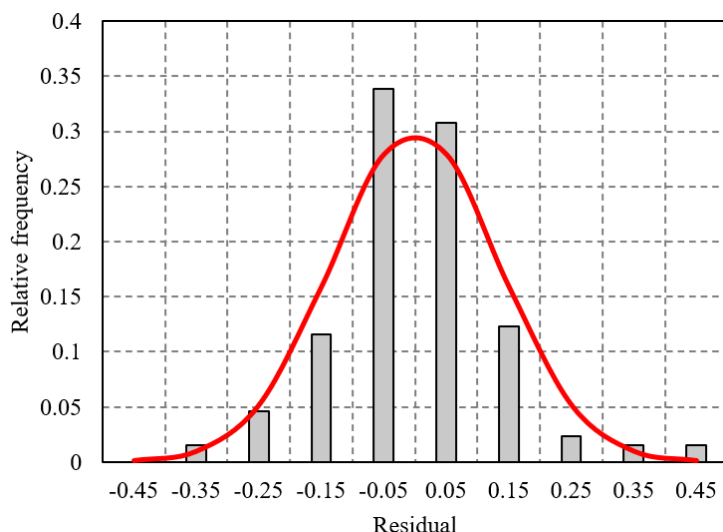


Fig. 10 – Histogram of residuals for the proposed empirical model and fitted normal distribution (red line)

SENSITIVITY ANALYSIS

Finally, in order to validate the empirical model obtained in this study, a sensitivity analysis is performed by varying the parameters of the proposed empirical model (ALR , H_w/l_w , l_w/t_w , ρ_{bh} and ρ_{wh}). The results of the sensitivity analysis are illustrated in Figure 11.

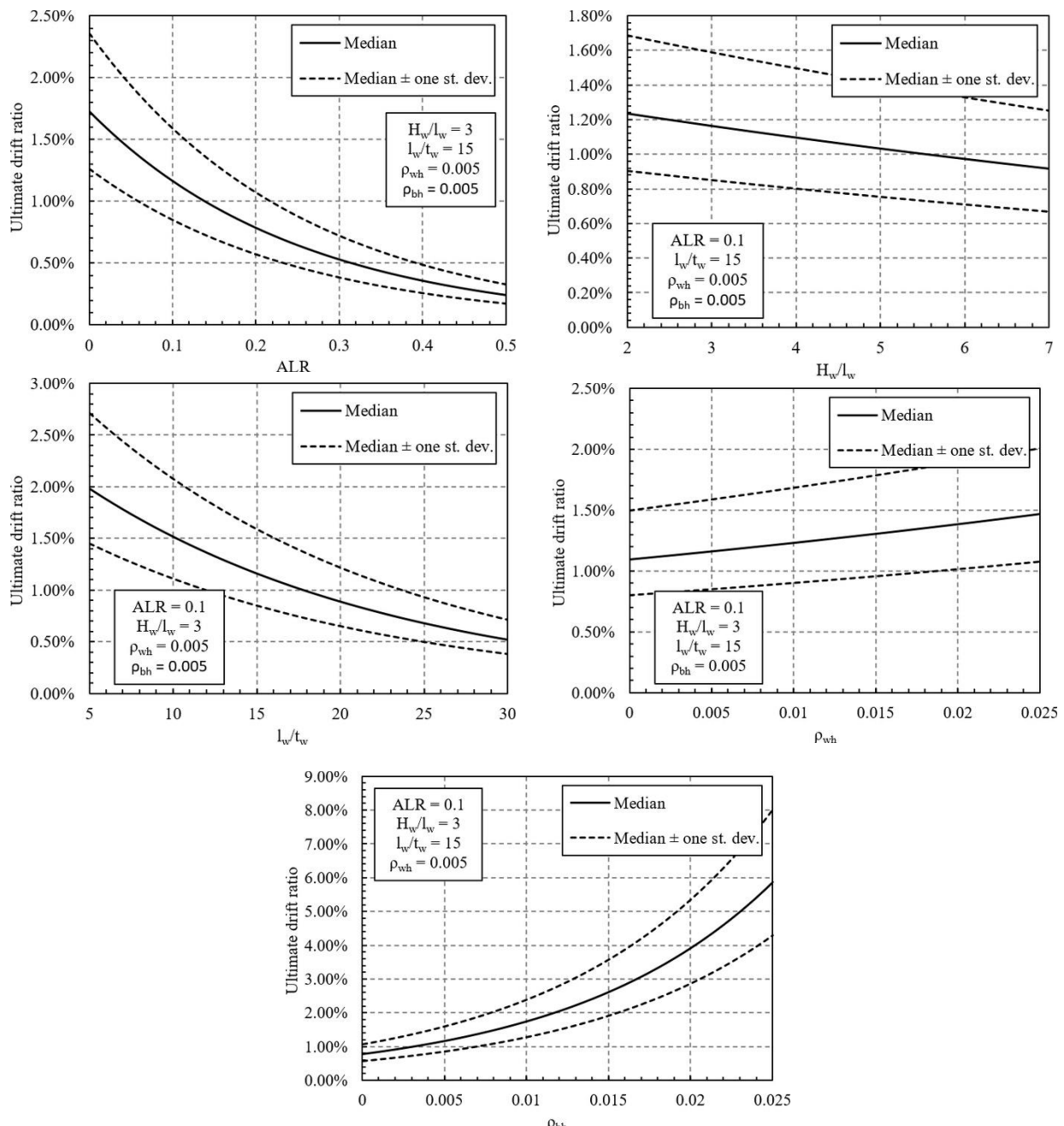


Fig. 11 – Sensitivity analysis for the proposed empirical model

It can be observed that among the parameters of the empirical model, the horizontal reinforcement in the boundary elements is the most important. It can also be observed that the ultimate drift ratios have a similar order of magnitude to the limits proposed by Ghobarah [38]. The current Romanian seismic design code P100-1/2013 [39] which follows the format of the Eurocode 8 [1] proposes a drift limit of 0.025 associated with the Ultimate Limit State (ULS) for all types of structures and limits in the range 0.005 – 0.01 for the Serviceability Limit State (SLS). Based on the results obtained using the proposed empirical model, it might appear as necessary that the drift limits for both SLS and ULS in the case of slender RC shear walls should be adjusted.

The first application of the proposed empirical model is performed for a case-study RC shear wall shown in Figure 12. The thickness of the web is in all cases 20 cm, while its height is 30.25 m. The case-study RC shear wall was designed according to four generations of seismic design



regulations in Romania and its main characteristics, as well as the median ultimate drift ratios, are summarized in Table 5.

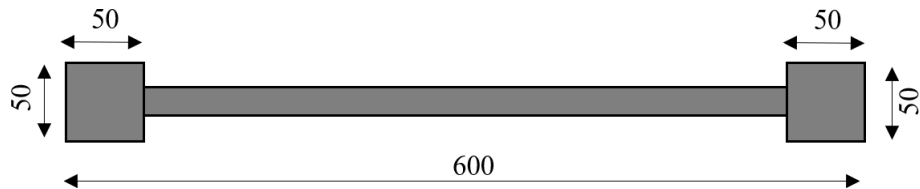


Fig. 12 – Case-study RC shear wall

Tab. 5: Characteristics of the first case-study RC shear wall shown in Figure 12

Seismic code level	ALR	H_w/l_w	l_w/t_w	ρ_{wh}	ρ_{bh}	Median ultimate drift
1	0.156	5.04	24	0.0015	0.0010	0.0035
2	0.117	5.04	24	0.0025	0.0025	0.0047
3	0.117	5.04	24	0.0030	0.0025	0.0047
4	0.078	5.04	24	0.0050	0.0050	0.0069

The probability that the median ultimate drift of the RC shear wall is in excess of 0.005 ranges from 0.54% for the first specimen to 99.2% for the last one which is designed according to the current seismic design regulations in Romania. Thus, based on this analysis, we can expect at least a double displacement capacity of modern RC shear walls in Romania as opposed to the ones designed during the '60s and '70s. The ultimate drifts were also evaluated using SeismoStruct [40] code and according to the relation proposed by Abdullah and Wallace [20] are reported in Table 6. The results in Table 6 show that the results obtained using the relation of Abdullah and Wallace [20] and using SeismoStruct [40] code are superior to the ones computed with the relation from this study. SeismoStruct [40] code provides the largest drift capacities, with the exception of the last RC shear wall. The ultimate drifts computed in SeismoStruct were obtained considering a tension strain limit of 0.05 as recommended in the study of Segura and Wallace [19]. It can be observed that the proposed empirical model provides values which are lower than the ones provided by the relation of Abdullah and Wallace [20] or by using SeismoStruct [40], which is an advantage considering the fact that the model is to be used for rapid seismic assessments.

Tab. 6: Comparison of drift capacities for the analysed RC shear walls

Seismic code level	Median ultimate drift – (this study)	Median ultimate drift – Abdullah and Wallace [20]	Median ultimate drift – SeismoStruct [40]
1	0.0035	-	0.0049
2	0.0047	0.0061	0.0073
3	0.0047	0.0070	0.0076
4	0.0069	0.0129	0.0093

The second application is related to the probability of exceedance of the ultimate drift for a case-study RC shear wall structure consisting of four slender RC shear walls with the characteristics given in Table 7 [41]. The incremental dynamic analysis curve (IDA) is illustrated in Figure 13. The exceedance probability is computed considering a lognormally distributed ALR having the mean value = 0.13 and a coefficient of variation of 0.31. The results obtained using FORM (first-order reliability method) by Melchers [42] in terms of probabilities of exceedance of the ultimate drift capacity as a function of the spectral acceleration level ($SA(T_1)$) are summarized in Figure 14. It can be observed that the median fragility corresponds to $SA(T_1) = 1.15$ g, a value about 50% larger than the elastic design spectral acceleration (equal to 0.75 g) used for this structure. Thus, it can be



observed that the slender RC shear walls designed according to modern seismic regulations offer an adequate level of protection.

Tab. 7: Characteristics of the second case-study RC shear wall

H_w (cm)	l_w (cm)	t_w (cm)	ρ_{wh}	ρ_{bh}
3500	300	35	0.005	0.006

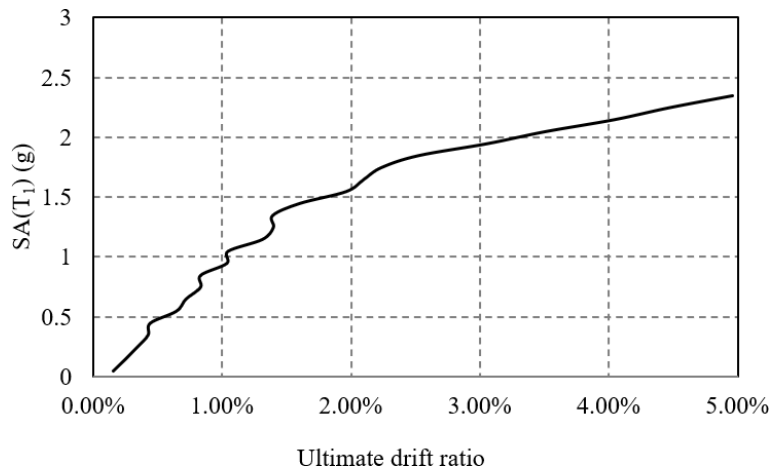


Fig. 13 – IDA curve for the second case-study RC shear wall structure [41]

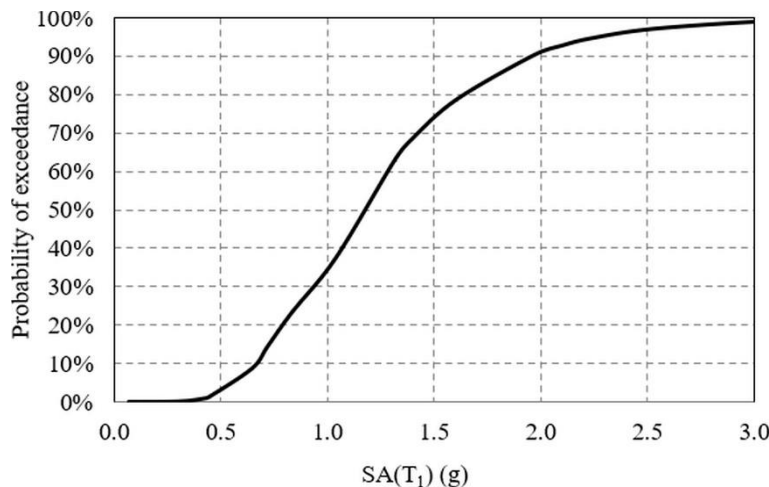


Fig. 14 – Probability of exceedance of the ultimate drift capacity for the second case-study RC shear wall structure [41]

CONCLUSIONS

In this study, we have evaluated the displacement capacity of RC shear walls using both experimental and analytical results. The main reason for using both analytical results is due to the scarcity of test data for slender RC shear walls having thicknesses larger than 150 mm. This situation is also confirmed by the recent test database compiled by Abdullah [35]. An empirical model for the assessment of the ultimate drift ratio is proposed in this study using input parameters readily available for each designer and which does not require the results of sectional analyses, unlike other models proposed in the literature. The proposed model allows a rapid assessment of the displacement capacity of slender RC shear walls as a function of the seismic design code and can

be used for rapid seismic assessments. The most important observation of the study can be summarized as follows:

- few experimental results for slender RC shear walls having thicknesses larger than 150 mm are available in the literature. Thus, the use of empirical models based purely on experimental data, especially for slender RC shear walls is subjected to a significant degree of uncertainty;
- the mean and median ultimate drift of squat RC shear walls is about half of that obtained for slender RC shear walls;
- the mean and median ultimate drift obtained experimentally and analytically for slender RC shear walls are almost identical;
- both the normal and the lognormal CDF provide a good fit of both the experimental and analytic ultimate drift ratios;
- opposite correlation coefficients have been observed between the same RC shear walls characteristics and the ultimate drift ratios obtained experimentally and analytically;
- the mean ratio between the observed and the predicted values using the proposed empirical model is 1.05, while the median value is 0.98, the standard deviation is 0.38 and the correlation coefficient is 0.63;
- the proposed empirical model provides lower-bound seismic capacities when compared with the results of the model proposed by Abdullah and Wallace [20] and with the results from SeismoStruct [40];
- modern RC shear walls in Romania have at least a double displacement capacity as opposed to the ones designed during the '60s and '70s. This is an important observation, especially since there are more than 3000 high-rise RC shear wall structures designed and built-in that period;
- based on the results obtained using the proposed empirical model, it might appear as necessary to adjust the drift limits for both SLS and ULS given in the current Romanian seismic design code P100-1/2013 in the case of slender RC shear walls;
- the median fragility in terms of spectral accelerations obtained for a case-study structure by applying the empirical model proposed in this study is about 50% larger than the elastic design spectral acceleration.

The proposed model, after further testing, can be incorporated in future versions of the seismic assessment guidelines for RC structures for rapid evaluation purposes. By no means the proposed model aims at replacing detailed nonlinear analyses for predicting the force and displacement capacities of RC shear walls.

ACKNOWLEDGEMENTS

The constructive feedback from two anonymous Reviewers is greatly appreciated as it has helped us to considerably improve the quality of the original manuscript.

REFERENCES

- [1] CEN., 2005. Eurocode 8: Design of structures for earthquake resistance-Part 3: Assessment and retrofitting of buildings.
- [2] Grammatikou S., Biskinis D., Fardis, M.N., 2015. Strength, deformation capacity and failure modes of RC walls under cyclic loading. *Bulletin of Earthquake Engineering*, vol. 13(11): 3277-3300.
- [3] Oh Y.H., Han S.W., Lee L.H., 2002. Effect of boundary element details on the seismic deformation capacity of structural walls. *Earthquake Engineering & Structural Dynamics*, vol. 31(8): 1583-1602.
- [4] Thomsen J.H., Wallace J.W., 2004. Displacement-based design of slender reinforced concrete structural walls—experimental verification. *Journal of Structural Engineering*, vol. 130(4): 618-630.
- [5] Krolicki J., Maffei J., Calvi, G.M., 2011. Shear strength of reinforced concrete walls subjected to cyclic loading. *Journal of Earthquake Engineering*, vol. 15(S1): 30-71.
- [6] Lowes L.N., Lehman D.E., Birely A.C., Kuchma D.A., Marley K.P., Hart C.R., 2012. Earthquake response of slender planar concrete walls with modern detailing. *Engineering Structures*, vol. 43: 31-47.



-
- [7] Takahashi S., Yoshida K., Ichinose T., Sanada Y., Matsumoto K., Fukuyama H., Suwada H., 2013. Flexural drift capacity of reinforced concrete wall with limited confinement. *ACI Structural Journal*, vol. 110: 95-104.
- [8] Zhou Y., Zhang D., Huang Z., Li D., 2014. Deformation capacity and performance-based seismic design for reinforced concrete shear walls. *Journal of Asian Architecture and Building Engineering*, vol. 13(1): 209-215.
- [9] Kassem W., 2015. Shear strength of squat walls: A strut-and-tie model and closed-form design formula. *Engineering Structures*, vol. 84: 430-438.
- [10] Beyer K., Hube M., Constantin R., Niroomandi A., Pampanin S., Dhakal R., Sritharan S., Wallace J.W., 2017. Reinforced concrete wall response under uni-and bi-directional loading. In: *Proceedings of the 16th World Conference on Earthquake Engineering*, paper no. 2373.
- [11] Netrattana C., Taleb R., Watanabe H., Kono S., Mukai D., Tani M., Sakashita M., 2017. Assessment of ultimate drift capacity of RC shear walls by key design parameters. *Bulletin of the New Zealand Society for Earthquake Engineering*, vol. 50(4): 482-493.
- [12] Terzioglu T., Orakcal K., Massone L.M., 2018. Cyclic lateral load behavior of squat reinforced concrete walls. *Engineering Structures*, vol. 160: 147-160.
- [13] Biskinis D., Fardis M.N., 2020. Cyclic shear resistance for seismic design, based on monotonic shear models in fib Model Code 2010 and in the 2018 draft of Eurocode 2. *Structural Concrete*, vol. 21(1): 129-150.
- [14] Panfilii P., 2020. Evaluation of the strength and displacement capacity of RC columns and RC structural walls (in Romanian). Master Thesis, Technical University of Civil Engineering Bucharest, Bucharest.
- [15] Wallace J.W., 2012. Behavior, design, and modeling of structural walls and coupling beams—Lessons from recent laboratory tests and earthquakes. *International Journal of Concrete Structures and Materials*, vol. 6(1): 3-18.
- [16] Çavdar Ö., Çavdar A., Bayraktar E., 2018. Earthquake performance of reinforced-concrete shear-wall structure using nonlinear methods. *Journal of Performance of Constructed Facilities*, vol. 32(1): 04017122.
- [17] Ugalde, D., Lopez-Garcia D., 2017. Behavior of reinforced concrete shear wall buildings subjected to large earthquakes. *Procedia Engineering*, vol. 199: 3582-3587.
- [18] Pavel F., Vacareanu R., 2020. Assessment of the seismic performance for a low-code RC shear walls structure in Bucharest (Romania). *The Open Construction & Building Technology Journal*, vol. 14: 111-123.
- [19] Segura Jr C.L., Wallace J.W., 2018. Impact of geometry and detailing on drift capacity of slender walls. *ACI Structural Journal*, vol. 115(3): 885-895.
- [20] Abdullah S.A., Wallace J.W., 2019. Drift capacity of reinforced concrete structural walls with special boundary elements. *ACI Structural Journal*, vol. 116(1): 183-194.
- [21] Shegay A.V., Motter C.J., Elwood K.J., Henry, R.S., 2019. Deformation capacity limits for reinforced concrete walls. *Earthquake Spectra*, vol. 35(3): 1189-1212.
- [22] Cando M.A., Hube M.A., Parra P.F., Arteta C.A., 2020. Effect of stiffness on the seismic performance of code-conforming reinforced concrete shear wall buildings. *Engineering Structures*, vol. 219: 110724.
- [23] Arteta C.A., To D.V., Moehle J.P., 2014. Experimental response of boundary elements of code-compliant reinforced concrete shear walls. In: *Proceedings of the 10th national conference in earthquake engineering*. Anchorage: Earthquake Engineering Research Institute.
- [24] ACI Committee 318, 2008. Building code requirements for structural concrete (ACI 318-08) and commentary. American Concrete Institute, Farmington Hills, MI, 509 pp.
- [25] Marzok A., Lavan O., Dancygier A.N., 2020, August. Predictions of moment and deflection capacities of RC shear walls by different analytical models. *Structures*, Vol. 26: 105-127.
- [26] Ruiz-García J., Negrete, M., 2009. Drift-based fragility assessment of confined masonry walls in seismic zones. *Engineering Structures*, vol. 31(1): 170-181.
- [27] Petry S., Beyer K., 2014. Influence of boundary conditions and size effect on the drift capacity of URM walls. *Engineering Structures*, vol. 65: 76-88.
- [28] Casapulla C., Maione A., Argiento L.U., 2017. Seismic analysis of an existing masonry building according to the multi-level approach of the Italian guidelines on cultural heritage. *Ingegneria Sismica*, vol. 34(1): 40-60.
- [29] Casapulla C., Argiento L.U., Maione A., 2018. Seismic safety assessment of a masonry building according to Italian Guidelines on Cultural Heritage: simplified mechanical-based approach and pushover analysis. *Bulletin of Earthquake Engineering*, vol. 16(7): 2809-2837.
- [30] Rosso A., Almeida J.P., Beyer K., 2016. Stability of thin reinforced concrete walls under cyclic loads: state-of-the-art and new experimental findings. *Bulletin of Earthquake Engineering*, vol. 14(2): 455-484.
- [31] Blandon C.A., Arteta C.A., Bonett R.L., Carrillo J., Beyer K., Almeida J.P., 2018. Response of thin lightly-reinforced concrete walls under cyclic loading. *Engineering Structures*, vol. 176: 175-187.



- [32] Dashti F., Dhakal R.P., Pampanin S., 2018. Evolution of out-of-plane deformation and subsequent instability in rectangular RC walls under in-plane cyclic loading: Experimental observation. *Earthquake Engineering and Structural Dynamics*, vol. 47(15): 2944-2964.
- [33] Haro A.G., Kowalsky M., Chai Y.H., 2019. Out-of-plane buckling instability limit state for boundary regions of special RC structural walls. *Bulletin of Earthquake Engineering*, vol. 17(9): 5159-5182.
- [34] Pavel F., 2020. Investigation on the seismic fragility of in-plane loaded low-and medium-rise rectangular RC structural walls. *Asian Journal of Civil Engineering*, vol. 21: 775-783.
- [35] Abdullah S.A., 2019. Reinforced concrete structural walls: test database and modeling parameters. Doctoral dissertation, University of California Los Angeles.
- [36] Zhou Y., Qian J., Song C. Wang Y., 2010. NEES shear wall database. available at <https://datacenterhub.org/resources/260/>
- [37] Hrynyk T.D., Vecchio F., 2019. VecTor4 user's manual. Vector Analysis Group. <http://www.vectoranalysisgroup.com/software.html>
- [38] Ghobarah A., 2004. On drift limits associated with different damage levels. In: Proceedings of international workshop on performance-based seismic design, edited by P. Fajfar & H. Krawinkler, 321-332.
- [39] MDRAP, 2013. P100-1/2013 - Code for seismic design—Part I—Design prescriptions for buildings. Bucharest, Romania.
- [40] SeismoSoft, 2019. SeismoStruct—A computer program for static and dynamic nonlinear analysis of framed structures. Available at: available from <http://www.seismosoft.com>
- [41] Pavel F., Vacareanu R., 2018. Applications of probabilistic methods in structural reliability and risk assessment – lecture notes. Conspress, Bucharest, Romania.
- [42] Melchers R.E., Beck A.T., 2018. Structural reliability analysis and prediction. John Wiley & Sons.